Nanoscale model systems of the permeability barrier of nuclear pore complexes

Dissertation

for the award of the degree
"Doctor rerum naturalium" (Dr. rer. nat.)
Division of Mathematics and Natural Sciences
of the Georg-August-Universität Göttingen

submitted by
Nico Benjamin Eisele

born in
Weingarten, Germany

Göttingen, 2013

Members of the thesis committee:

Prof. Dr. Dirk Görlich (Thesis mentor and Reviewer)	Max Planck Institute for Biophysical Chemistry Department of Cellular Logistics Göttingen, Germany
Prof. Dr. Claudia Steinem (Reviewer)	Georg August University Göttingen Institute for Organic and Biomolecular Chemistry Göttingen, Germany
Dr. Ralf Richter (Thesis mentor)	CIC biomaGUNE Biosurface Unit San Sebastian, Spain

Additional members of the examination board:

Prof. Dr. Detlef Doenecke	Georg August University Göttingen Department of Biochemistry I Göttingen, Germany
Prof. Dr. Jörg Enderlein	Georg August University Göttingen III. Institute of Physics- Biophysics Göttingen, Germany
Prof. Dr. Sarah Köster	Georg August University Göttingen Nano-Spectroscopy and X-Ray Imaging Nanoscale Imaging of Cellular Dynamics Göttingen, Germany

Date of thesis submission: 31.03.2013
Date of the oral examination: 02.05.2013

This PhD project was carried out as a part of an international collaboration between the laboratories of Prof. Dirk Görlich at the Max Planck Institute for Biophysical Chemistry, Göttingen, Germany and Dr. Ralf Richter at the CIC biomaGUNE, San Sebastian, Spain.

I hereby declare that my thesis entitled ”**Nanoscale model systems of the permeability barrier of nuclear pore complexes**” has been written independently and with no other sources and aids then quoted.

N. Eisele

Nico Eisele
March, 2013, San Sebastian, Spain

What we observe is not nature itself, but nature exposed to our method of questioning.

(Werner Heisenberg, 1901–1976)

Contents

1 Scope and outline 1

1.1 Scope of this thesis 1

1.2 Outline of this thesis 1

2 Introduction 5

2.1 Nucleocytoplasmic transport in eukaryotic cells 5

2.1.1 Nucleocytoplasmic transport is gated by nuclear pore complexes . 5

2.1.2 Transport across the NPC 6

2.1.3 The permeability barrier of NPCs is built of FG repeat domains . 10

2.1.4 Hypotheses about the selectivity mechanism 11

2.1.4.1 The selective phase model 13

2.1.4.2 The virtual gating model 14

2.1.4.3 The nanomechanical reversible collapse model 14

2.1.4.4 The forest model 15

2.1.4.5 The reduction of dimensionality model 16

2.1.5 Biological issues which will be addressed in this thesis 16

2.2 Basic concepts of polymer theory 18

2.2.1 A single polymer in solution 18

2.2.2 Polymer solutions 22

2.2.3 Polymers end-grafted to a surface 26

2.3 Main techniques 27

  2.3.1 Quartz crystal microbalance with dissipation monitoring 27

    2.3.1.1 The working principle 27

    2.3.1.2 Viscoelastic modeling 30

  2.3.2 Spectroscopic ellipsometry 31

    2.3.2.1 Polarization of light 32

    2.3.2.2 Changes in polarization upon reflection 33

  2.3.3 Confocal laser scanning microscope 36

References 38

3 Ultrathin nucleoporin FG repeat films and their interaction with NTRs 45

4 Viscoelasticity of thin biomolecular films 71

5 Cohesiveness tunes assembly and morphology of FG repeat domain meshworks 85

5.1 Abstract 87

5.2 Results 91

  5.2.1 FG domain film assembly and its kinetics 91

  5.2.2 Thickness, concentration, and mechanical properties of FG domain meshworks 92

  5.2.3 Lateral homogeneity of and chain mobility in FG domain meshworks 95

  5.2.4 Energy of film compaction 98

5.3 Discussion 100

  5.3.1 Impact of cohesiveness on the morphology and implications for the size selectivity of the permeability barrier 100

  5.3.2 FG domains can form nanoscopic hydrogels 103

  5.3.3 Impact of cohesiveness on NPC biogenesis and stability 103

5.3.4 Impact of heterogeneities on the performance of the permeability barrier 104
5.4 Methods 106
5.4.1 Proteins and buffer 106
5.4.2 Surfaces 106
5.4.3 Preparation of lipids and lipid vesicles 107
5.4.4 Quartz crystal microbalance with dissipation monitoring (QCM-D) 107
5.4.5 Spectroscopic ellipsometry (SE) 107
5.4.6 Quantification of mass transport limited FG domain adsorption rates 108
5.4.7 Atomic force microscopy (AFM) 109
5.4.8 Fluorescence recovery after photobleaching (FRAP) 110
5.5 Supplementary Information 111
References 115

6 Towards construction of FG repeat domain pores as a model system 121

6.1 Introduction 121
6.2 Theoretical predictions for the diffusion across a porous membrane . . . 124
6.2.1 Simple chamber with stagnant solutions 125
6.2.2 Microfluidic flow chamber 131
6.3 Creation of a setup with unfunctionalized pores 135
6.3.1 Characterization of porous polycarbonate membranes 135
6.3.2 Setup alignment and testing of the data processing routine 138
6.3.3 Construction of a simple chamber 140
6.3.4 Permeability experiments with the simple chamber 140
6.3.5 Construction of a prototype of a microfluidic chamber 144
6.3.6 Permeability experiments with the microfluidic chamber 147

6.4 Functionalization of porous polycarbonate membranes 149
6.4.1 Characterization of SiO_2 coated polycarbonate membranes 149
6.4.2 Functionalization of the SiO_2 layer on polycarbonate membranes . 150
6.4.3 Drying of an Nsp1 film 154
6.5 Discussion 156
6.5.1 The porous substrate 157
6.5.2 Discrepancy between the experimentally measured and the theoretically predicted characteristic time scales 159
6.5.3 Permeability experiments with the microfluidic chamber 159
6.5.4 Functionalization strategy of the substrate 161
6.5.5 Drying of the FG repeat domain film 161
6.6 Conclusions 162
6.7 Materials and methods 163
6.7.1 Materials and buffer preparation 163
6.7.2 Substrate functionalization 163
6.7.3 Construction of simple chambers (stagnant solutions) 164
6.7.4 Construction of microfluidic chambers 165
6.7.5 Confocal microscopy imaging 168
6.7.6 Data processing and analysis routine 168
6.7.7 Protein purification and labeling 168
References 169

7 Concluding remarks and perspectives 171
7.1 Achievements 171
7.1.1 Creation of planar model systems 171
7.1.2 FG repeat domain films resemble the permeability barrier in the NPC 171
7.1.3 NTR binding to FG repeat domain films 172

7.1.4 Connecting biological function of the FG repeat domain meshwork with theoretical predictions from polymer physics 172
7.1.5 First steps towards creating a model system comprising the NPC topology 173
7.2 Outlook 175
7.2.1 Affinity studies 175
7.2.2 Role of NTRs for the morphology of the meshwork 175
7.2.3 Role of spacers for cohesiveness 176
7.2.4 Different types of FG repeat domains at different locations 176
7.2.5 Exploiting the compartmentalization in the artificial FG repeat domain pore system 177
References 178

Author's contribution 181

List of publications 183

Acknowledgment 185

List of Figures

2.1 Sketch of an NPC 6
2.2 Mode of selectivity and mode of transport 7
2.3 Simplified scheme of the classical nuclear import cycle 9
2.4 FG-repeat domains as a key feature of the permeability barrier 11
2.5 Models for the selectivity mechanism 12
2.6 Characteristic parameters describing a coiled polymer chain 19
2.7 A polymer under tension – the blob model 21
2.8 Dilution regimes for flexible polymers 23
2.9 Time and size dependence of the mobility of a permeation probe in a polymer solution 25
2.10 Scheme of QCM-D operation 28
2.11 Polarization of light 33
2.12 Reflection of polarized light 34
2.13 Working principle of confocal laser scanning microscopy 37

5.1 Supramolecular assembly of FG domains, and predictions by polymer theory 89
5.2 Kinetics of FG domain film assembly and maximal grafting density depend strongly on FG domain type 91
5.3 The strength of inter-FG repeat interactions affects the thickness and concentration of FG domain films 93
5.4 Cohesiveness leads to stiffer FG domain films 94

5.5 Grafting density and cohesiveness influence the morphology of FG domain assemblies 96
5.5 Grafting density and cohesiveness influence the morphology of FG domain assemblies 97
5.6 Lateral mobility of FG domain films 98
5.7 Quantification of the energy for FG domain film compaction from binding rates 99
5.8 Impact of cohesiveness on the supramolecular FG domain assembly in the NPC topology 101
5.9 FG domains are anchored specifically and stably through their terminal His-tags to NTA-functionalized SLBs 111
5.10 All FG domains in the films are anchored to the SLB 112
5.11 Tuning FG domain surface density 113
5.12 FG domain film thickness determination from QCM-D data 114

6.1 Schematic illustration of a measurement setup with artificial FG-repeat domain pores 122
6.2 Schematic illustration of two designs for measurement chambers 123
6.3 Illustration of permeation probe distribution in a simple chamber 126
6.4 Illustration of the flux in the microfluidic chamber 131
6.5 Simulated intensity profiles for the current design of the microfluidic chamber 133
6.6 Dependance of the intensity profiles on the top channel with and κ . . . 134
6.7 Beam damage of polycarbonate membranes induced by SEM: 135
6.8 SEM images of the two side of a polycarbonate membrane 136
6.9 SEM images of polycarbonate membranes 137
6.10 Correlation between intensity and concentration of fluorescent probes . . 139
6.11 Scheme for the construction of a simple chamber 141

6.12 Permeation control experiments with the simple chamber 142
6.13 Construction of a microfluidic flow chamber 145
6.14 Characterization of a constructed microfluidic chamber 146
6.15 Flux experiment with microfluidic chamber 148
6.16 Electron microscopy images of SiO_2 coated polycarbonate membranes . . 150
6.17 Binding of FG-repeat domains to functionalized SiO_2 wafers 151
6.18 Estimation of Nsp1-WT grafting density on functionalized polycarbonate membranes by LSM 153
6.19 Effect of drying and rehydrating an Nsp1 film 155
6.20 Scheme for the construction of a master wafer 166
6.21 Scheme for the construction of top and bottom compartments of the microfluidic chamber 167

List of Tables

2.1 Characteristic time scales in a polymer solution 24

6.1 Areal pore density and void fraction of unsputtered polycarbonate membranes 137
6.2 Characteristic time scales τ_{m} determined experimentally and by theory. . 143
6.3 Results from visco-elastic modeling 156

1 Scope and outline

1.1 Scope of this thesis

Nuclear pore complexes (NPCs) are intricate, biological machineries which are embedded in the double membrane envelope of eukaryotic cells. Their function is to control the macromolecular exchange between nucleus and cytoplasm. However, little is known about their working mechanism. The aim of this thesis was to create bio-mimetic model systems of the key feature for the NPC's selectivity, i.e. its permeability barrier. The model systems should resemble the native conditions in various aspects and should allow to obtain fundamental insights into the working mechanism of the native system in the cell.

This PhD project was a truly interdisciplinary and exciting task in which we edged on many scientific areas (such as biology, polymer physics, surface science, chemistry, mathematics, and informatics). The main areas that we connected with this thesis, however, stem from biology and polymer physics. Yet, to achieve our objectives, substantial technical development in the preparation and characterization of surface-confined biomacromolecular films was also part of this thesis.

1.2 Outline of this thesis

Chapter 2 The background information for this thesis will be provided. In section 2.1 the biological background information about the transport of macromolecules across the NPC will be summarized. Since polymer theory is important in this thesis, a short introduction into basic concepts of polymer physics will be given in section 2.2. The main techniques, which were used in this thesis, will be briefly explained in section 2.3.

Chapter 3 In this chapter, we will present the development of a model system of the NPC's permeability barrier which is based on planar films of FG repeat domains end-grafted to a supported lipid bilayer (SLB). We studied the FG repeat domain films by quartz crystal microbalance with dissipation monitoring (QCM-D), ellipsometry and atomic force microscopy (AFM). The presented results provide evidence that the FG repeat domains are mimicking the conditions in the permeability barrier by mode of surface confinement, scale, and FG repeat domain grafting density. We exploited this system to study quantitatively the interaction of nuclear transport receptors (NTRs) with the FG repeat domain films.

Chapter 4 In this chapter, we present our results on a model system of the permeability barrier based on FG repeat domains end-grafted to His-Tag Capturing QCM-D sensors. The model system was studied by QCM-D, ellipsometry and AFM. Here, we applied concepts from polymer theory and rheology to gain insights into the morphology and the dynamics of the FG repeat domain film. This study also provides a detailed description of the quantitative analysis of QCM-D data by means of a viscoelastic model.

Chapter 5 In this chapter, the effect of cohesiveness between FG repeat domains is studied. To this end, we created FG repeat domain films, on SLBs, consisting of different types of FG repeat domains. The FG repeat domain types varied in their degree of cohesiveness. The films were analyzed by QCM-D, ellipsometry, AFM, and confocal laser scanning microscopy (CLSM). Our findings show that the morphology of the supramolecular assembly of the FG repeat domain films is strongly affected by the cohesiveness of the FG repeat domains. Based on concepts from polymer theory, we propose that cohesiveness of FG repeat domains is tuned in the NPC to promote aspects of the permeability barrier's selectivity mechanism.

Chapter 6 On the long run, we would like to create a model system of the permeability barrier which resembles the pore-like topology of the NPC, which has not yet been achieved. In this chapter, we present important intermediate steps towards this goal. This includes the creation of two different measurement chambers in which two compartments are separated by a porous polycarbonate membrane. We developed a measurement setup which allows us to measure the net flux of fluorescent permeation probes across the porous substrate. A mathematical framework was developed and implemented in a self-written computer skript to analyze the data. Moreover, in order to fill the pores in the future with FG repeat domains, a substantial part of this section deals with the development of a functionalization strategy for the polycarbonate membrane.

Chapter 7 This chapters provides overall conclusions of the work presented in this thesis, as well as an outlook.

On a note about the style and presentation of the succeeding chapters A part of this work led to the publication of two articles in peer-reviewed journals and a manuscript which is currently in preparation for submission. They are implemented in the thesis as individual chapters (chapter 3, 4, and 5) in their original style.

2 Introduction

2.1 Nucleocytoplasmic transport in eukaryotic cells

2.1.1 Nucleocytoplasmic transport is gated by nuclear pore complexes

The nucleus of eukaryotic cells

Eukaryotic cells generally comprise functionally distinct compartments, which are separated from the cytosol by at least one membrane layer (reviewed in Ref. [1]). The usually biggest sub-compartment is the nucleus, which is the defining feature of eukaryotes. It is surrounded by a double membrane envelope and constitutes the place where the cellular DNA is stored during the interphase. In the nucleus, the biosynthesis of mRNA, tRNA, or ribosomal subunits takes place, whereas the translation of mRNA into proteins occurs in the cytoplasm. As a consequence, the cell needs to exchange a considerable amount of macromolecules between the cytoplasm and the nucleoplasm.

The nuclear pore complex (NPC)

This macromolecular transport is gated by nuclear pore complexes (NPCs) which perforate the nuclear envelope [2, 3]; in figure 2.1 an artistic view of an NPC is shown. NPCs are built up of about 30 different proteins [4, 5], called nucleoporins (or nups), in manifold copies. The NPC mass yields up to approximately 66 MDa in *Saccharomyces cerevisiae* [6] and 125 MDa in higher eukaryotes [7, 8]. The structural proteins of the NPC are arranged in an octagonal axial symmetry around an aqueous pore [9, 10]. This pore connects cytoplasm and nucleoplasm and serves as the NPC's transport channel for

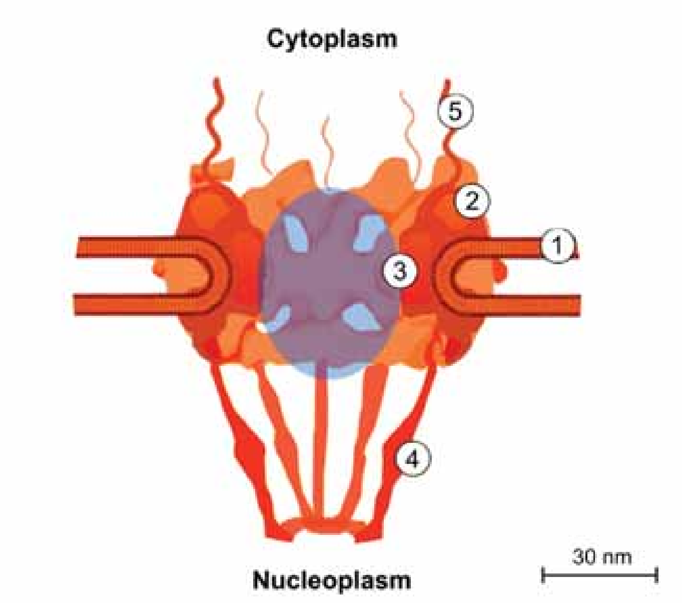

Figure 2.1: Sketch of an NPC: *Shown is a sketch of an NPC embedded in the nuclear envelope (1). The NPC is built of proteins called nucleoporins. Structural units such as the outer ring (2), spokes (3), the nuclear basket (4), and cytosolic filaments (5) are indicated. In the center of the NPC is an aqueous pore with diameter and length of about 30 – 50 nm which serves as the transport channel for macromolecular exchange between cytoplasm and nucleoplasm. The transport channel is equipped with a permeability barrier (indicated by a blue ellipse) which prevents random intermixing of macromolecular content between the two compartments. Image adapted from Ref. [13].*

macromolecules, The dimensions of the transport channel is 30 – 50 nm in both length and width [11]. This is amazingly wide compared to the typical size of most proteins (which have a Stokes radius, R_S, of 3 – 5 nm). As a consequence, proteins that travel through the NPC can stay fully folded during transport and, in addition, tremendous protein fluxes 1000 translocation events per second can be reached [12].

2.1.2 Transport across the NPC

Mode of selectivity and mode of transport

Despite the wide opening of the NPC transport channel, random intermixing of nuclear and cytoplasmic macromolecular content is prevented. To this end, the NPC is equipped with a permeability barrier (discussed in detail later), that allows for a remarkable selectivity of macromolecular transport across the pore (summarized in figure 2.2). Molecules with a molecular weight below 20 – 40 kDa [14] or a diameter smaller than 5 nm [15] can freely travel across the NPC by passive diffusion. In contrast, diffusion of molecules exceeding this size is delayed or blocked unless they are bound to special shuttle proteins, called nuclear transport receptors (NTRs) or karyopherins. This transport route is referred to as facilitated translocation. In this thesis, the term size-selectivity will be used to describe the permeability barrier's ability to allow or block passage of inert molecules (i.e., molecules that are not NTRs) according to their size. For the permeability barrier's ability to block passage of (large) inert molecules while allowing the passage of NTRs and NTRs coupled to cargo, we will use the term type-selectivity.

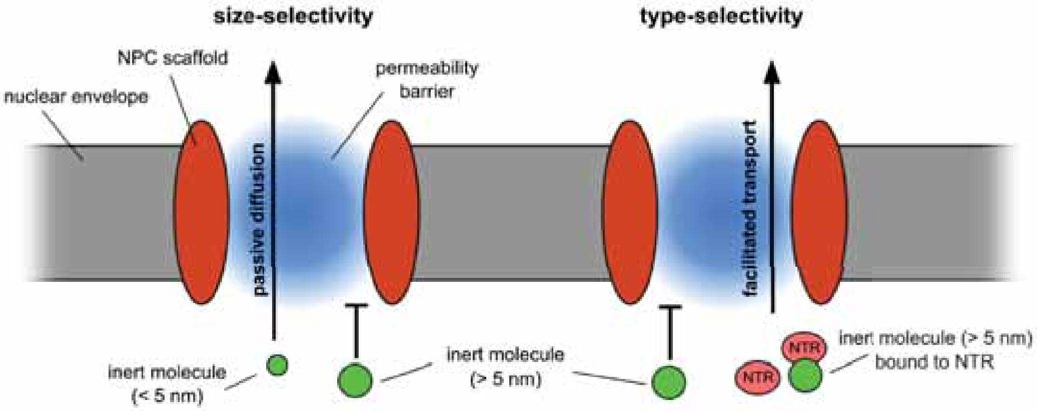
size-selectivity
type-selectivity
NPC scaffold
nuclear envelope
permeability barrier
passive diffusion
facilitated transport
inert molecule (< 5 nm)
inert molecule (> 5 nm)
NTR
NTR
inert molecule (> 5 nm) bound to NTR

Figure 2.2: Mode of selectivity and mode of transport: *Left side: The permeability barrier is size-selective for inert molecules. Small molecules ($R_S < 2.5$ nm) can diffuse through the NPC's permeability barrier by passive diffusion, while large inert molecules are blocked. Right side: Despite their size, large proteins can travel through the NPC if they are NTRs or are coupled to NTRs. This phenomenon is called type-selectivity in this thesis.*

The direction of transport

The NTRs recognize cargo to be shuttled across the NPC by a recognition signal on the cargo to which the NTR binds, either directly or *via* an adapter protein. The direction of transport is determined by the type of recognition signal, which is either a nuclear localization signal (NLS) for nuclear import or a nuclear export signal (NES) for nuclear export. NTRs which bind to NLS to import the cargo into the nucleus are referred to as importins, while NTRs binding to NES to export their cargo out of the nucleus are called exportins.

Classical pathway

Different types of NTRs exist which are involved in different transport cycles (reviewed in Refs. [16, 17]). Here, only the classical pathway (depicted in figure 2.3), which is most examined and therefore best understood, will be explained in more detail, as an example.

In the cytoplasm, importin α (Impα) binds to a cargo with a classical NLS, which is typically a basic sequence, often rich in lysine [18]. In a next step, the NTR importin β (Impβ) binds to the Impβ binding domain (IBB) of Impα [19, 20, 21], thereby forming a protein complex which can travel into the nucleus. In the nucleus, the small GTPase Ran, associated to GTP, binds to Impβ and triggers disassembly of the protein complex and cargo release into the nucleus [20, 22, 23]. Impβ complexed with Ran$\bullet$GTP can directly travel back to the cytoplasm. Impα, however, needs to form a complex with an exportin called CAS and Ran$\bullet$GTP, in order to be shuttled back to the cytoplasm. In the cytoplasm, the RanGTPase-activating protein RanGAP [24, 25] and the Ran-binding proteins RanBP1 and RanBP2 [26, 27, 28] interact with Imp$\beta\bullet$Ran$\bullet$GTP and Imp$\alpha\bullet$CAS$\bullet$Ran$\bullet$GTP complexes, respectively, thereby triggering GTP hydrolysis to GDP and the disassembly of the complexes. To complete the cycle, Ran$\bullet$GDP binds to nuclear transport factor-2 (NTF2) and is transported back to the nucleus [29, 30]. In the nucleus, the GDP in Ran$\bullet$GDP is exchanged with GTP by Ran guanine nucleotide-exchange factor (RanGEF) [31].

Energy for directed transport

Importantly, the transport processes across the NPC are driven by Brownian motion. No energy in form of ATP or GTP is needed for the translocation *per se* [29, 32, 33, 34]. The direction of net-transport and the accumulation of cargo in the nucleoplasm or

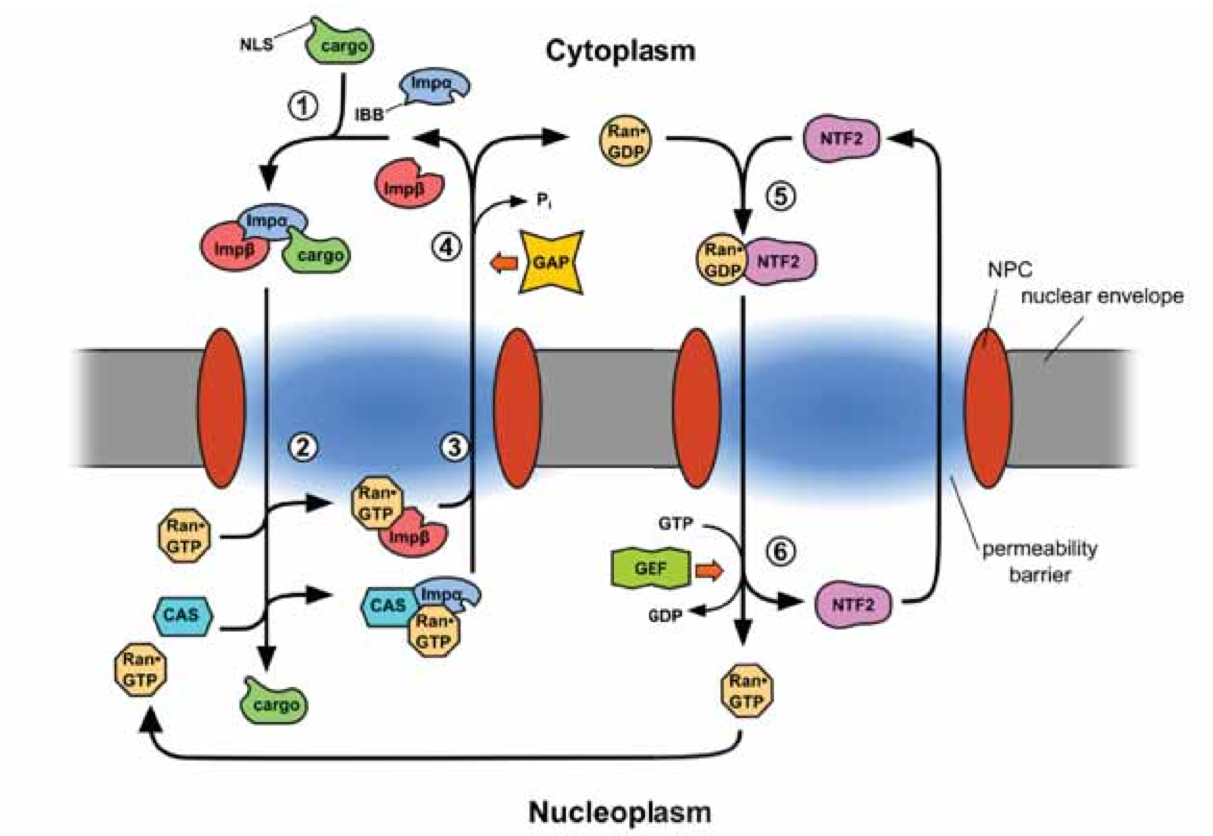
Cytoplasm
NLS
cargo
①
Impα
IBB
Impβ
Ran•
GDP
NTF2
⑤
P$_i$
④
GAP
NPC
nuclear envelope
②
③
Ran•
GTP
CAS
GTP
GEF
GDP
⑥
permeability
barrier
Nucleoplasm

Figure 2.3: Simplified scheme of the classical nuclear import cycle: *(1) The adapter protein Impα binds to the (basic) NLS of a cargo protein while Impβ binds to the IBB domain of Impα. This complex can then travel across the NPC into the nucleoplasm. (2) Here, Ran• GTP binds to Impβ while Ran•GTP and CAS bind to Impα triggering disassembly of the transport complex and cargo release into the nucleoplasm. (3) Impβ•Ran• GTP and Impα•CAS•Ran• GTP travel back to the cytoplasm. (4) In the cytoplasm, GAP is located and triggers GTP hydrolysis by Ran which leads to disassembly of the complexes. Impα and Impβ are now ready for a new import cycle. (5) Ran• GDP is then brought back to the nucleoplasm by NTF2. (6) In the nucleoplasm, GEF is located which exchanges the Ran associated GDP with GTP. Fine details of the import cycle (such as RanBP1/2) were omitted for the sake of clarity. More information can be found in the text.*

cytoplasm is driven only by the asymmetric distribution of cytoplasmic RanGAP and nucleoplasmic RanGEF which generate a Ran• GTP gradient between nucleoplasm and cytoplasm. The energy source for directed transport in the system is the hydrolysis of GTP to GDP by Ran.

2.1.3 The permeability barrier of NPCs is built of FG repeat domains

FG-repeat domains

As pointed out earlier, NPCs are equipped with a permeability barrier which prevents random intermixing of macromolecular material between the cytoplasm and the nucleoplasm. There is strong evidence that this permeability barrier is made of nucleoporin domains, which are natively unfolded [35, 36]. These nucleoporin domains are rich in hydrophobic FG, GLFG, or FxFG (where x stands for any amino acid) repeat motives which are inter-spaced by typically 15 – 20 amino acid long hydrophilic spacers (illustrated in figure 2.4) [37, 38]. Due to these characteristic FG motives, they are called FG repeat domains, FG domains, or FG nups. There are about 10 different types of FG-repeat domains in yeast [4] and vertebrates [5] which are end-grafted in multiple copies to the walls of the NPC. It is estimated that there are in total about 150 FG-repeat domains per pore contributing to about 12 % of the NPC mass [4, 38]. There is also increasing evidence that some of the FG-repeat domains are cohesive [39, 40, 41, 42, 43, 44], i.e. they interact with each other, and that some of them form thereby FG repeat subcomplexes (reviewed in Ref. [45]).

NTRs can interact with FG-repeat domains

NTRs can interact with the FG-repeats of FG-repeat domains, while inert molecules cannot. In addition, evidence exists for some NTRs that they bind specifically to the phenylalanine side chain of FG-repeats [46, 47, 48, 49].

The morphology of the supramolecular assembly of the FG repeat domains

There is consensus that the permeability barrier emerges from the supramolecular assembly of FG repeat domains. Yet, little is known about its native morphology, due to a lack of characterization techniques, which can extract this information from *in vivo* assays. In addition, there is also a lack of model systems which could allow to study the morphology *in situ*.

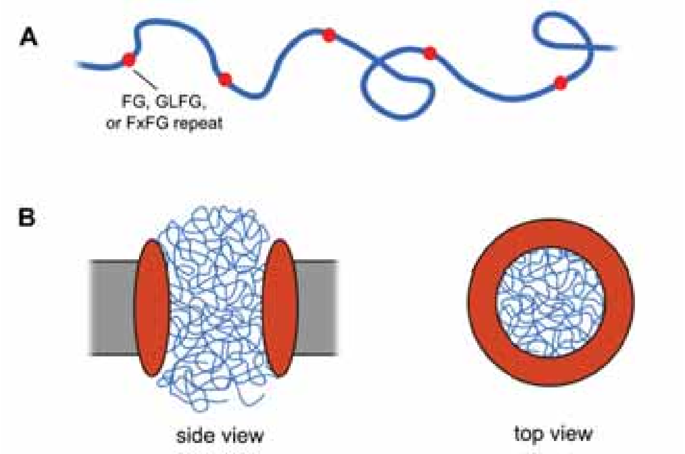

Figure 2.4: FG-repeat domains as key feature of the permeability barrier: *(A) FG-repeat domains are natively unfolded, flexible domains. Characteristically, they bear hydrophobic FG, GLFG, FxFG repeats which are separated by a spacer sequence. (B) The FG-repeat domains are end-grafted to the walls of the NPC. The underlying concept of this thesis is a meshwork like morphology.*

The underlying concept of this thesis is that FG repeat domains form a supramolecular assembly with a morphology of a meshwork, since the natively unfolded, flexible FG repeat domains are likely to interpenetrate each other (see figure 2.4). Some of the hypothesis about the selectivity mechanism of the permeability barrier, which are summarized in the next section, share this concept explicitly (see *selective phase*), or implicitly (see *virtual gating*), or not at all (see *reduction of dimensionality*).

2.1.4 Hypotheses about the selectivity mechanism

The mechanism behind the permeability barrier's selectivity is poorly understood and intensely discussed. Obviously, the traditional structure-function paradigm, for instance often used to explain the function of an enzyme, cannot be applied to the permeability barrier. The FG-repeat domains are natively unfolded, i.e. they do not adopt a fixed structure which action could be understood by the lock-and-key principle. Instead, the selectivity arises from a (dynamic) supramolecular assembly of the FG repeat domains in the NPC transport channel.

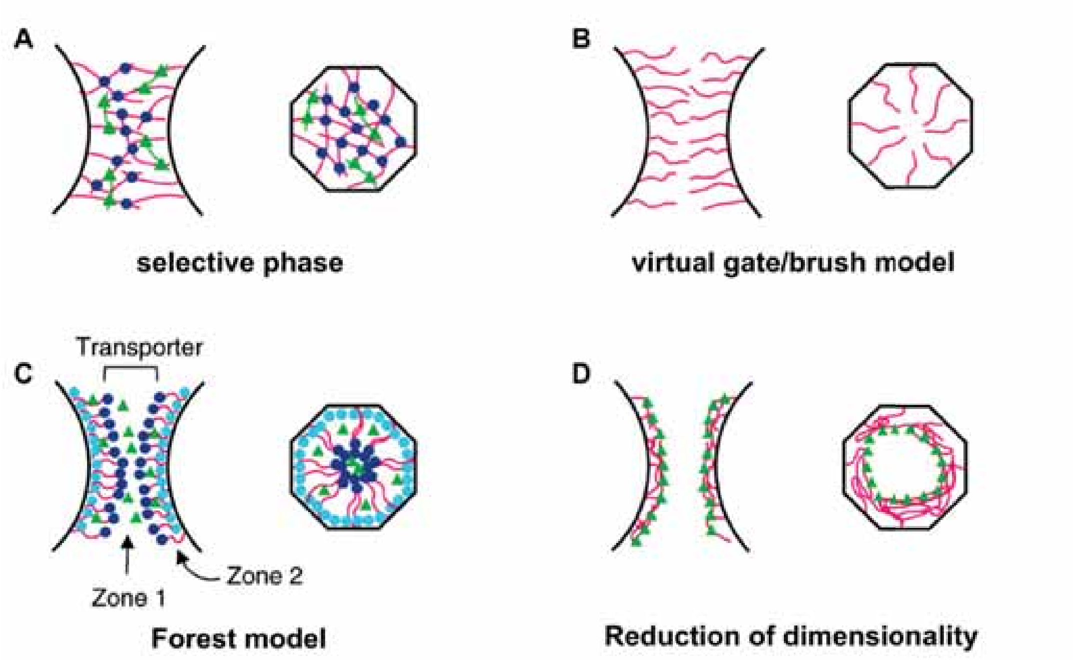

Figure 2.5: Models for the selectivity mechanism: *(A) The selective phase model. FG repeat domains (pink) form a sieve-like structure that functions as a physical permeability barrier. FG-FG contacts (blue dots) form the meshes of the sieve. NTRs (green triangles) can bind to FG domains and partition into the barrier. (B) The virtual gating model. Largely non-cohesive FG repeat domains arrange as "repulsive bristles" or "polymer brushes" (pink) forming an entropic barrier, as translocation of large molecules is energetically unfavorable. (C) The forest model. Cohesive parts of FG repeat domains are in a globular, collapsed conformation (light and dark blue dots) while repulsive parts form brushes (pink). Small inert molecules can pass through the less crowded pink zone while NTRs can pass through the entire NPC transport channel. (D) The reduction of dimensionality model. Transport receptors (green) coat the wall of the transport channel as they bind to FG repeat domains. Passive diffusion of small molecules can occur through the inner tube of the channel. Transport complexes move by a random, two-dimensional walk on the inner wall of the channel. (A-D), side views (left) and top views (right) of the NPC. Taken from Ref. [50].*

Little is known about the morphology of the supramolecular assembly of FG repeat domains and how NTR binding to the FG repeat domains catalyzes their transition through the pore. On account of these gaps of knowledge, several hypotheses for the selectivity mechanism have emerged (see Ref. [51] and references therein, and more recently Ref. [50]). They are based on different putative morphologies of the FG-repeat domain assembly and different effects upon NTR binding. In figure 2.5, the most relevant hypotheses in the context of this PhD thesis are summarized.

2.1.4.1 The selective phase model

The *selective phase model* [12, 52] proposes that the FG repeat domains are cohesive and that the supramolecular assembly of the FG repeat domains is meshwork like (see figure 2.5 A). An important feature are FG-motives, which are supposed to interact with each other thereby forming transient cross-links. This cross-linking gives the FG repeat domain assembly properties of a hydrogel. A collapse of the meshwork is prevented by repulsive parts of hydrophilic spacers between the cohesive elements. Within the permeability barrier, the trajectory of an inert permeation probe is limited to open spaces between meshes. The probe is blocked from passage if its size exceeds the size of a mesh. In contrast, an NTR can compete with inter-FG-interactions and, thereby, temporarily open the mesh [52] and pass through it. This reversible opening allows even large probes connected to an NTR a quick passage through the meshwork.

The model was substantially supported by experimental studies, a few of which will be mentioned here. Frey et al. (2006) showed that the wild type FG-repeat domain Nsp1 from yeast forms a macroscopic hydrogel in *in vitro* assays [39]. A mutant of Nsp1, in which all Fs were replaced by the hydrophilic S, was incapable of gel formation, demonstrating that (hydrophobic) interactions between the FG-repeats are crucial for gel formation. The results of a later study suggested that amyloid-like interactions between spacers contribute additionally to the gel formation [42]. Strikingly, the Nsp1-WT gel could reproduce some of the selectivity properties of the permeability barrier – inert permeation probes with a diameter smaller than 5 nm could enter the gel and diffuse through it, while larger, inert permeation probes were excluded unless bound to an NTR [52].

The selective phase model relies strongly on the presence of cohesive elements distributed along the FG repeat domains. The existence and importance of such elements on the length scale of the NPC is, however, controversially discussed since effects from the surface confinement and other interfacial phenomena may play a role in the native system [40, 53, 54, 55].

2.1.4.2 The virtual gating model

The *virtual gating model* [56], which was formerly named *brownian affinity gating model* [4], assumes that FG repeat domains form ”repulsive bristles” in the NPC and around its entrances (see figure 2.5 B). These bristles exclude inert permeation probes from transport due to an entropic penalty for volume exclusion, which increases with the size of the probe. In contrast to the *selective phase model* (hydrophobic) inter FG-repeat interactions, or cohesiveness, are not considered important for the function of the permeability barrier. As a consequence, the translocation of an NTR across the permeability barrier is not connected with a local change of the morphology of the meshwork (i.e. meshes are not reversibly opened) upon interaction with an NTR. Instead, NTR translocation is considered to be a purely stochastic process. The likelihood of traversing the pore is merely increased by the enrichment of NTRs close to the pore due to binding to FG-repeat domains.

At present, a theoretical framework is lacking that would enable quantitative testing of the model. Some questions which arise, for instance, are: (1) at which grafting density would FG repeat domains form a sufficient permeability barrier for inert probes due to entropic repulsion; (2) could the proposed model consistently explain why inert permeation probes of a size of 5 nm are excluded while large permeation probes with a dimension of 10 – 30 nm (such as pre-ribosomes [57] or intact viral particles [58]) can be translocated efficiently, provided they are bound to NTRs?

2.1.4.3 The nanomechanical reversible collapse model

The *nanomechanical reversible collapse model* [59] is based on the *virtual gating model*, in the sense that the FG-repeat domains are supposed not to cohesively interact with each other and to form a purely repulsive brush. In contrast to the *selective phase model* and to the *virtual gating model*, NTR interaction with the FG-repeat domain brush is proposed to trigger a substantial change in the morphology of the meshwork, i.e. a collapse of the FG-repeat domains towards the wall of the NPC is assumed.

This model is based on atomic force microscopy (AFM) studies carried out on the FG-repeat domain Nup153 which was end-grafted *via* their terminal cysteines to a gold surface [53, 59, 60]. A shrinking of the film (i.e. a collapse) upon addition of Impβ at nanomolar bulk concentrations was reported [59, 61].

A valuable point of these studies [59, 61] is the employed model system, which resembles the NPC in dimensions and mode of FG-repeat domain attachment. A conceptual question concerning collapse-enhanced translocation [59] is how a collapse catalyzes the translocation of NTR bound molecules without allowing inert molecules (not bound to NTRs) to permeate as well? In addition, we show in chapter 3 data that contrasts the experimental findings from Ref. [59] and discuss possible reasons for this discrepancy.

2.1.4.4 The forest model

The *forest model* is based on the finding that FG repeat domains can be often separated into parts with a high cohesiveness and parts with low or no cohesiveness [43]. Computer simulations predicted that the cohesive parts of FG repeat domains may adapt a globular or collapsed coil configuration, while the non-cohesive parts of FG repeat domains form an extended coil [43]. If the position of the globular or collapsed coil is close to the NPC wall it is called a ”shrub” and if an extended coil is between the NPC wall and a collapsed coil (which is then located in the center) it is called a ”tree”. These units are supposed to form a ”forest like morphology” in the NPC (see figure 2.5 C). The forest landscape would have two zones: in the center are collapsed coils and around them are extended coils. NTRs with a small cargo are supposed to travel through the extended-coil zone while NTRs with a large cargo can also travel through the central zone by principles described by the *selective phase model*.

2.1.4.5 The reduction of dimensionality model

The *reduction of dimensionality model* assumes that FG repeat domains coat the inner wall of the NPC (see figure 2.5 D) [51, 62]. Binding of NTRs to the FG repeat domains might further condensate the FG repeat domains to the wall by inducing a collapse (see *nanomechanical reversible collapse*). Thereby, a small channel is created in the center of the NPC which is free of FG repeat domains. through which molecules smaller than the diameter of this channel can diffuse. NTRs (with cargo) can bind to the FG repeat domains at the entrance and start a two-dimensional random walk along the wall of the transport channel which is supposed to allow for a faster translocation through the pore than a three-dimensional walk.

However, since the morphology of the supramolecular assembly of FG repeat domains is not known, the formation of a narrow, FG repeat domain channel is pure speculation. In addition, it is unclear in how far a two-dimensional random walk would increase the translocation across the pore.

2.1.5 Biological issues which will be addressed in this thesis

All of the proposed models make an intimate connection between the selectivity mechanism of the permeability barrier and the morphology of its supramolecular assembly. Studying this morphology in NPCs is technically challenging. A goal of this thesis was hence to create nanoscale model systems of the permeability barrier of NPCs. These model systems should model key features of the native system: (1) the FG repeat domains are end-grafted to the walls of the transport channel; and (2) the thickness of the assembly is in the range of a few ten nanometers. One of our model system is a continuous film of end-grafted FG repeat domains. This model system allowed for an *in situ* characterization of the supramolecular assembly of FG repeat domains. We exploited this model system to quantitatively characterize the interaction between NTRs and FG repeat domains (see chapter 3) and to investigate whether binding of NTRs induces a collapse [59] (see chapter 3). In addition, we studied the morphology of the supramolecular assembly of FG repeat domains in our film and could provide estimates for the size of a mesh by analyzing our data with concepts from polymer theory (see chapter 4). A substantial difference between the proposed models is whether FG repeat domains are cohesive and which role cohesiveness plays. We shed light onto this question by investigating films consisting of FG repeat domain types which differ in their cohesiveness and discuss how cohesiveness can contribute to the permeability barrier's selectivity mechanism (see chapter 5).

2.2 Basic concepts of polymer theory

An important aspect of this thesis was to apply basic concepts of polymer theory to understand some of the properties of the permeability barrier. In this section, we will briefly introduce the concepts which are most important in the context of this thesis. Although we studied FG-repeat domains grafted to a solid support, it is instructive to start with polymers in solutions before going to surface confined polymers, since many concepts apply to both systems. A more comprehensive introduction to polymer theory can be found, for instance, in Refs. [63, 64].

2.2.1 A single polymer in solution

Definition of a polymer

A polymer (chain) consists of repeating elementary units, called monomers, which are covalently connected to each other. Here, we are only considering the case of unbranched and flexible polymer chains, that take the conformation of a coil.

The freely jointed chain model

The freely jointed chain model assumes that the polymer consists of N linear, elemental units, called Kuhn segments of length b, which are interconnected through their ends and can freely rotate around their junctions even if this leads to an overlap of chain segments. A polymer chain, that can be described by the freely jointed chain model is called an ideal chain (illustrated in figure 2.6). The contour length, L_c, of the polymer chain is given by:

$$L_\mathrm{c} = bN. \tag{2.1}$$

The path of the Kuhn segments can be considered to be a random walk (since the segments can rotate freely around their joints). There a two parameters which are usually used to describe the extension of the polymer coil. One is the mean end-to-end distance, called Flory radius [65], R_{F}, which is:

$$R_{\mathrm{F}} = bN^{\frac{1}{2}}, \tag{2.2}$$

for an ideal chain. The other parameter to describe the polymer's extension is the root mean square distance between the chain segments and the polymer's center of mass, called radius of gyration R_{g}. The radius of gyration correlates linearly with R_{F} as:

$$R_{\mathrm{g}} = \frac{1}{\sqrt{6}} bN^{\frac{1}{2}} = \frac{1}{\sqrt{6}} R_{\mathrm{F}}. \tag{2.3}$$

In the following, we will use R_{g} as a measure of the polymer's effective size.

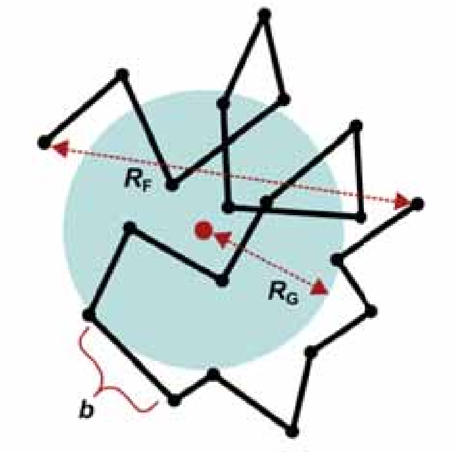

Figure 2.6: ***Characteristic parameters describing a coiled polymer chain:*** *Shown is the projection of a coiled polymer described by the freely jointed chain model. This polymer consists of* $N = 19$ *Kuhn segments, with length* b*. There are two parameters, which can be used as measure for the size of the polymer coil. One is the mean end-to-end distance, the so called Flory radius,* R_F*. The other is the average distance from the center of mass, called radius of gyration,* R_g*. Adapted from Ref. [63].*

The real chain and solvent qualities

In an ideal chain, interactions between monomers separated by many bonds along the chain are ignored. However, in a real chain, monomers may either attract or repel each other. If the polymer is submersed in a solvent, the solvent quality will influence this monomer-monomer interaction. If the net monomer-monomer interaction is repulsive we call the solvent a good solvent. If the monomer makes no energetic distinction between other monomers and solvent, the solvent is called a Θ-solvent. In the case of a poor solvent, the monomer-monomer interaction is attractive. As a consequence, the solvent qualities determine the extension of the polymer coil. The scaling of R_g can be more generally expressed [63] as:

$$R_\mathrm{g} = \alpha b N^\nu \propto N^\nu. \tag{2.4}$$

The exponent ν is called the Flory exponent. In the limit of a very poor solvent, ν is 1/3; in the limit of a very good solvent, ν is about 3/5; and in the limit of a Θ-solvent, ν is 1/2. The numerical prefactor α is of order unity and *a priori* not known. α is usually dropped and the (in the following) derived laws are, hence, scaling laws with an inaccuracy of a numerical factor of order unity.

A polymer under tension – the blob model

If a polymer is brought under tension by applying external constraints (such as the confinement to a surface, or pulling at the two ends of the chain as illustrated in figure 2.7), its conformation will change. In order to correlate the change in conformation with the force and energy needed to induce this change, the so-called blob model can be used [64, 66].

The blob model effectively enables the separation of two different length scales. At a scale larger than the size of a blob, ξ, externally applied force will determine the conformation (e.g. stretching in figure 2.7). At scales smaller than the blob size, the thermal motion of the polymer segments will dominate over the external constraints. The chain within a blob behaves effectively as a free chain in solution and in its conformation the energy of about one $k_\mathrm{B}T$ is stored. The number of Kuhn segments within a blob is assigned the variable N_b.

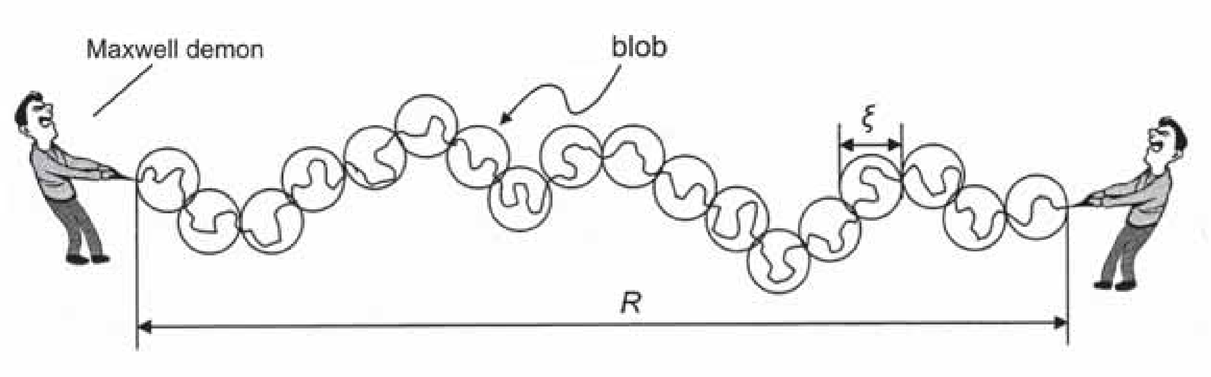

Figure 2.7: ***A polymer under tension – the blob model:*** *If a polymer is under tension, it will extend to the size R. The chain can be subdivided into so-called blobs, of size ξ. The conformation of the Kuhn segments within a blob is not influenced by external applied constrains. Each blob stores the energy of one $k_{\mathrm{B}}T$. Taken from Ref. [63].*

The size of the blob, ξ, (with N_{b} Kuhn segments) scales according to equation (2.4):

$$\xi \propto {N_{\mathrm{b}}}^{\nu} \quad \Leftrightarrow \quad N_{\mathrm{b}} \propto \xi^{\frac{1}{\nu}}. \tag{2.5}$$

For the following it is handy to rewrite equation (2.4) to $N \propto {R_{\mathrm{g}}}^{\frac{1}{\nu}}$ and to be aware that the number of blobs can be calculated by N/N_{b} and scales with R/ξ.

The end-to-end distance of the polymer under tension, R, correlates with R_{g} and ξ as:

$$R \propto \xi \frac{N}{N_{\mathrm{b}}} \propto \xi \frac{{R_{\mathrm{g}}}^{\frac{1}{\nu}}}{\xi^{\frac{1}{\nu}}} \propto {R_{\mathrm{g}}}^{\frac{1}{\nu}} \xi^{\frac{\nu-1}{\nu}} \quad \Leftrightarrow \quad \xi \propto \frac{{R_{\mathrm{g}}}^{\frac{1}{1-\nu}}}{R^{\frac{\nu}{1-\nu}}}. \tag{2.6}$$

The energy, E, of the chain under tension scales with the sum of the energy of all blobs (and the energy per blob is approximately $k_{\mathrm{B}}T$), which leads us to:

$$E \propto k_{\mathrm{B}}T \frac{R}{\xi} \propto k_{\mathrm{B}}TR \frac{R^{\frac{\nu}{1-\nu}}}{{R_{\mathrm{g}}}^{\frac{1}{1-\nu}}} \propto k_{\mathrm{B}}T \left(\frac{R}{R_{\mathrm{g}}}\right)^{\frac{1}{1-\nu}}. \tag{2.7}$$

The stretching force, F, can be straight forwardly calculated. Each time the chain is stretched about one ξ, we add another $k_\mathrm{B}T$ to the energy stored in the chain:

$$F \propto \frac{k_\mathrm{B}T}{\xi} \propto \frac{k_\mathrm{B}T}{R_\mathrm{g}} \left(\frac{R}{R_\mathrm{g}}\right)^{\frac{\nu}{1-\nu}} . \tag{2.8}$$

As a remark, the force necessary to stretch an ideal chain (Θ-solvent, i.e. $\nu = 1/2$) correlates linearly with chain stretching R which is the same force law as for the extension of a spring (Hook's law).

2.2.2 Polymer solutions

The volume fraction

Many properties of a solution of polymers depend on the polymer concentration in the solvent. Instead of expressing the polymer concentration as mass concentration, c (i.e. mass per volume), the polymer concentration is commonly expressed as volume fraction, Φ, i.e. the ratio of occupied volume of the polymers in solution and the volume of the solution. c and Φ are related to each other through the polymer density ρ:

$$\Phi = \frac{c}{\rho} = c\frac{V_\mathrm{mon}N_\mathrm{A}}{M_\mathrm{mon}} \propto c\frac{b^3 N_\mathrm{A}}{M_\mathrm{mon}}, \tag{2.9}$$

where V_mon and M_mon are the volume occupied by a Kuhn segment and its molecular weight, respectively. To derive the right side of equation (2.9), we assumed that the volume of a Kuhn segment scales cubically with its length.

Concentration regimes

A solution of polymers can be divided into different regimes (see figure 2.8) according to the polymer concentration. In the dilute regime, the average distance between polymer coils is larger than the size of the coils. If the concentration of the polymers in solution is increased, such that the average distance between coils becomes shorter than the size of a single coil in solution, the coils start to overlap. This concentration regime is called

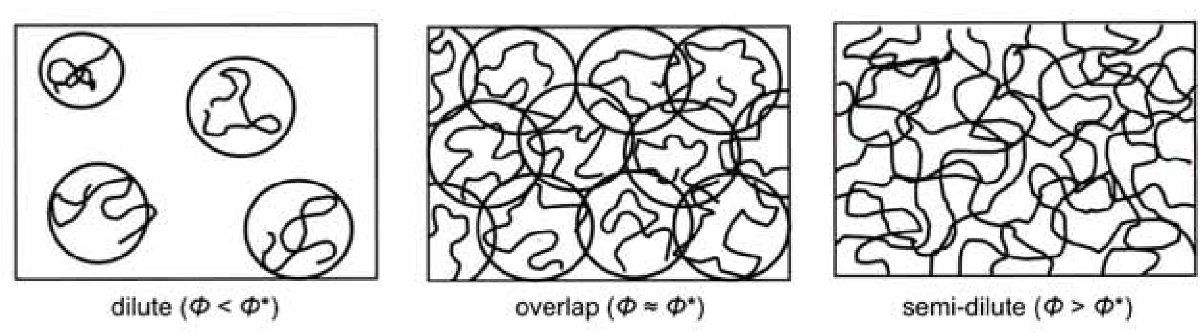
dilute ($\Phi < \Phi^*$)
overlap ($\Phi \approx \Phi^*$)
semi-dilute ($\Phi > \Phi^*$)

Figure 2.8: ***Dilution regimes for flexible polymers:*** *According to the polymer concentration, different dilution regimes emerge. If the concentration is below the overlap concentration* c^**, the distance between polymer coils in solution is larger than the size of the polymers, and the solution is in the dilute regime. As the concentration approaches* c^**, the polymer coils overlap, and the solution is in the overlap regime. For concentrations exceeding* c^**, the regime is called semi-dilute, as long as the solvent still occupies most of the volume. Adapted from Ref. [63].*

semi-dilute regime. The volume fraction when overlapping starts is called overlap volume fraction, Φ^*, and equals the volume fraction of a single polymer inside its own volume, V, as:

$$\Phi^* = \frac{N V_{\mathrm{mon}}}{V} \propto \frac{N b^3}{{R_{\mathrm{g}}}^3} \tag{2.10}$$

The physical behavior of semi-dilute solutions is dominated by the overlapping polymer coils. Most of the volume, however, is still occupied by the solvent. This is the regime that is relevant for most of the bio-polymer assemblies considered in this thesis. If the polymers are further concentrated, the regime is called concentrated-regime and the chains will behave like ideal chains (the crossover concentration between semi-dilute regime and concentrated regime is Φ^{**}). If the concentration is further increased, such that there is no or only very little solvent volume ($\Phi \approx 1$), we have a polymer melt

Characteristic length and time scales

Polymer chains in a semi-dilute solution interpenetrate and exert constraints, and thereby tension, to each other. The blob model, introduced in section 2.2.1, can also be applied to polymers in a semi-dilute solution. The size ξ of a blob with energy $k_{\mathrm{B}}T$ here corresponds to the average distance from a monomer on one chain to the nearest monomer on another chain [63]. It can be shown that ξ, also called correlation length, decreases as a power of the volume fraction [63]:

$$\xi \propto \Phi^{\frac{\nu}{3\nu-1}}. \tag{2.11}$$

For sufficiently large chains, interpenetration leads to a distinct physical phenomenon called entanglement, with another characteristic length scale, the entanglement length (or tube diameter) [63, 67]. a correlates with ξ depending on the quality of the solvent:

$$a(\Phi) \propto \begin{cases} a(\Phi=1)\Phi^{\frac{\nu}{3\nu-1}} \propto \xi, & \nu > 1/2 \text{ (i.e. for a good solvent);} \\ a(\Phi=1)\Phi^{-\frac{2}{3}} \propto \xi^{-\frac{2}{3}}, & \nu = 1/2 \text{ (i.e. for a } \Theta\text{-solvent).} \end{cases} \tag{2.12}$$

a is typically a few times larger than ξ [67]. The parameters to describe the dynamics of the polymer solution are the relaxation times of the characteristic length scales. They are summarized in table 2.1 [67].

Table 2.1: *Characteristic time scales in a polymer solution*

relaxation time of:	parameter		scaling law
a Kuhn segment	τ_0	$\propto$	$\eta_\mathrm{s} b^3/(k_\mathrm{B}T)$
a correlation blob	τ_ξ	$\propto$	$\eta_\mathrm{s}\xi^3/(k_\mathrm{B}T)$ or $\tau_0(\xi/b)^3$
a chain segment with size d (with $\xi < d < a$)	τ_d	$\propto$	$\tau_\xi(d/\xi)^4$
entanglement strand	τ_e	$\propto$	$\tau_\xi(a/\xi)^4$
an entire polymer chain	τ_rep	$\propto$	$\tau_\mathrm{rep}(N/N_\mathrm{e})^3$

η_s is the viscosity of the solvent and N_e is the number of Kuhn segments per entanglement strand.

Permeation probes within a polymer solution

The mobility of an inert permeation probe within a polymer solution in the semi-dilute regime depends on the morphology and dynamics of the polymer solution and on the time-scale of observation. A detailed description of this dependence can be found in Ref. [67].

The dependence is illustrated in figure 2.9 where the probe's mobility is expressed as the product of its size, d, and its mean-square displacement, $\langle r^2(t)\rangle$. In principle, the mobility of the permeation probe can be explained by the following argumentation: When the permeation probe is smaller than ξ, it can diffuse unhampered through the polymer solution. However, if the permeation probe's size, d, is between ξ and a, $d\,\langle r^2(t)\rangle$ will be affected at time scales between τ_ξ and τ_d . If d exceeds the size of an entanglement strand, the permeation probe will be arrested within a volume of ξa^2 at time-scales smaller than τ_rep.

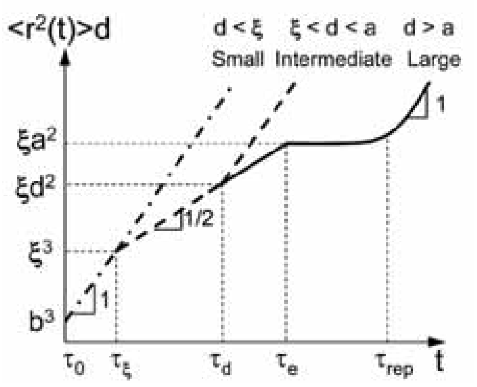

Figure 2.9: *Time and size dependence of the mobility of a permeation probe in a polymer solution:* *A permeation probe with size $d < \xi$ (dash-dotted line) can diffuse freely within a polymer solution, in the semi-dilute regime. If its size is between ξ and a (dashed line), its diffusion is hindered at time scales above between τ_ξ and τ_d. Large permeation probes with $d > a$ (solid line) are even blocked for time scales between τ_e and τ_rep. Scales are logarithmic. Taken from Ref. [67].*

How would cross-links between polymer strands influence the mobility of the permeation probe? Cross-linking of the polymer would introduce an addition characteristic length-scale, namely the average distance between cross-links, γ, and its relaxation time τ_γ. If we consider the extreme case of a homogeneous, tightly cross-linked polymer solution, i.e. $\gamma < \xi$, with stable cross-links, the morphology of the polymer solution would be completely dominated by the cross-links. As a consequence, permeation probes larger than γ would be arrested in a volume of about γ^3.

2.2.3 Polymers end-grafted to a surface

The concepts from polymers in solution can be easily transferred to polymers end-grafted to a surface.

Mushroom and brush regime

If the polymers are end-grafted with an average distance of the grafting points above their size, R_g, there will be individual chains on the surface. This regime is called the mushroom regime. As soon as the grafting density is increased, such that the mean distance of the grafting points is smaller than R_g, the polymers will overlap and be forced to stretch away from the surface (due to repulsion between the chains). This regime is called the brush regime.

Characteristic length scales and mobility of permeation probes in a brush

To a first approximation, we can consider a brush to be a polymer solution located in a restricted volume above the surface. This allows us to straight forwardly transfer the relationships between Φ and ξ (see equation (2.11)) and a (see equation (2.12)), respectively. Also, the relaxation times remain the same, except τ_rep, the time-scale for the relaxation of an entire polymer chain, will be dramatically increased since it is confined to a surface (especially when its anchor point is laterally immobile).

Furthermore, the introduced concepts for the mobility of a permeation probe within a polymer solution can be straight forwardly transferred to a polymer brush, to a first approximation. Bearing in mind that relaxation of an entire chain does not or hardly occur, a permeation probe with a size larger than an entanglement strand would be trapped within a volume of ξa^2.

This approach is relevant to the context of the results presented in this thesis. We would like to stress, here, that ξ and a depend on the volume fraction (i.e. the concentration of the polymer, see equation (2.11) and (2.12)).

2.3 Main techniques

In this section, the surface characterization techniques which I used and further developed during this PhD project will be introduced. The fundamental working principle of Quartz crystal microbalance with dissipation monitoring (QCM-D), spectroscopic ellipsometry, and confocal laser scanning microscopy (CLSM) are briefly explained. Techniques which were used by my collaborators (such as atomic force microscopy (AFM)), are covered in the materials and methods parts of the chapters where results from these techniques are presented.

2.3.1 Quartz crystal microbalance with dissipation monitoring

Quartz crystal microbalance with dissipation monitoring (QCM-D) is an acoustic technique that measures the (wet) solvated surface mass of an adsorbed layer, e.g. the (dry) biomolecular mass of the layer plus the hydrodynamically coupled water. In addition, under certain conditions, QCM-D data can be fitted to a viscoelastic model to extract information about the viscoelastic properties and the thickness of the adsorbed film.

In the frame of this PhD project, QCM-D was one of the main techniques to follow the formation of FG repeat domain films. In addition, the viscoelastic model was applied to our data to extract information about the thickness and the viscoelastic properties of the FG repeat domain films (see in particular chapter 4).

Here, we will briefly outline its working principle (a detailed description can be found in Refs. [68, 69] and references therein).

2.3.1.1 The working principle

An oscillating piezoelectric quartz crystal

The core of a QCM-D is a piezoelectric quartz crystal which is used as a sensor for the adsorbate (see figure 2.10). The sensor is electrically excited at resonance frequency, thus creating a standing wave with two open ends. The resonant frequency, f_n, is related to the thickness of the crystal, d_q, by:

$$d_\mathrm{q} = n\frac{\lambda}{2} = n\frac{v_\mathrm{q}}{2f_n} \quad \Leftrightarrow \quad f_\mathrm{n} = n\frac{v_\mathrm{q}}{2d_\mathrm{q}} \tag{2.13}$$

where n are the overtone modes, or harmonics ($n = 1, 3, 5...$), and v_q is the speed of sound in quartz.

When cutting the driving circuit, the oscillation will decay (see figure 2.10 C). The envelope of the decaying oscillation, u_n, is decaying exponentially over time:

$$u_n \propto e^{-\pi f_n D_n t}. \tag{2.14}$$

The damping factor, D_n, is called dissipation. It is obvious from equation (2.14), that the dissipation will increase if the sensor quickly dissipates the energy of oscillation into the system.

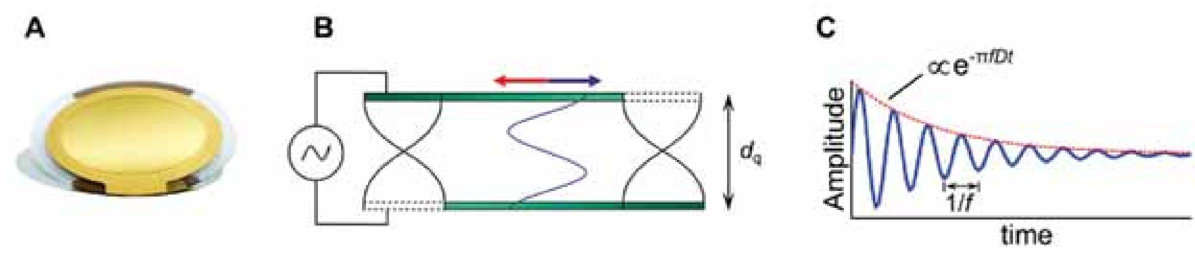

Figure 2.10: Scheme of QCM-D operation: *(A) A picture of a QCM-D quartz crystal sensor. (B) Side view of the crystal. Application of oscillatory voltage results in a cyclical deformation, where top and bottom surfaces move tangentially in an anti parallel fashion. The fundamental frequency (black waves at the edges of the crystal) and the third overtone (blue wave in the middle) are illustrated (not to scale). (C) QCM-D uses a so-called ring-down method. The driving voltage is switched off and the decay in time of the oscillation is monitored. From the decay curve, the resonance frequency f and the energy dissipation D can be extracted. Adapted from Ref. [68].*

The frequency and dissipation are the parameters that the QCM-D is measuring in real time. They are technically measured by the reverse piezo-electrical effect, i.e. the oscillation of the quartz crystal translates into an oscillating voltage. The presented way to extract frequency and dissipation from a decaying curve after cutting voltage is called ring-down approach and is characteristic for QCM-D.

QCM-D can be used as sensor for adsorption processes. If mass adsorbs to the sensor surface, the thickness of the sensor will effectively increase. It can be seen from equation (2.13) that this will lead to a decrease of the resonance frequency. In addition, if the mass is soft (e.g., a film of polymers), the dissipation increases due to frictional losses.

Mass determination for thin and rigid films – Sauerbrey equation

The mass per unit area of the crystal surface, m_q, can be determined from the product of d_q and the density of the quartz crystal, ρ_q. Together with equation (2.13), the following expression can be derived:

$$m_\mathrm{q} = d_\mathrm{q}\rho_\mathrm{q} = n\frac{v_\mathrm{q}\rho_\mathrm{q}}{2f_n}. \tag{2.15}$$

As already pointed out above, if mass adsorbs, the effective thickness of the sensor will increase. This leads to a change in frequency, Δf_n. The changes in frequency are typically small compared to the resonance frequency ($\Delta f_n << f_n$). The first derivative of m_q with respect to f_n can be, hence, used to approximate the adsorbed mass sensed by QCM-D, m_QCM:

$$m_\mathrm{QCM} = \Delta m = -n\frac{v_\mathrm{q}\rho_\mathrm{q}}{2f_n^2}\Delta f_n = -\frac{v_\mathrm{q}\rho_\mathrm{q}}{2nf_0^2}\Delta f_n = -C\frac{\Delta f_n}{n}, \tag{2.16}$$

where f_0 is the fundamental frequency with $f_n = nf_0$ and C is the mass sensitivity constant. If not stated otherwise, we used crystals with $f_0 \approx 4.95\,\mathrm{MHz}$ and a mass sensitivity constant of $C = 18.1\,\mathrm{ng\,cm^{-2}Hz^{-1}}$.

Equation (2.16) is called Sauerbrey equation [70]. It is only valid if the adsorbed mass is (*i*) small (compared to the mass of the crystal), (*ii*) evenly distributed, (*iii*) rigid and (*iv*) coupled with no slip conditions.

The effect of the solvent's viscosity and density

The presence of air has only a very small effect on f and D. Immersion in liquid, however, affects the sensor response considerably and can be approximated [71, 72] by:

$$\Delta f_n = \frac{1}{\sqrt{\pi} v_\mathrm{q} \rho_\mathrm{q}} \sqrt{n f_0^3 \eta_\mathrm{s} \rho_\mathrm{s}} = 0.64 \cdot 10^{-7} \frac{\mathrm{m}^2\mathrm{s}}{\mathrm{kg}} \times \sqrt{n f_0^3 \eta_\mathrm{s} \rho_\mathrm{s}}, \tag{2.17}$$

$$\Delta D_n = \frac{1}{\sqrt{\pi} v_\mathrm{q} \rho_\mathrm{q}} \sqrt{\frac{f_0}{n} \eta_\mathrm{s} \rho_\mathrm{s}} = 1.27 \cdot 10^{-7} \frac{\mathrm{m}^2\mathrm{s}}{\mathrm{kg}} \times \sqrt{\frac{f_0}{n} \eta_\mathrm{s} \rho_\mathrm{s}}. \tag{2.18}$$

Here, ρ_s and η_s are the solvents density and viscosity, respectively.

The role of hydrodynamically trapped solvent

In contrast to optical mass-sensitive techniques (such as ellipsometry or surface plasmon resonance), the mass that is sensed by QCM-D, m_QCM corresponds to all mass that is coupled to the surface [73, 74]. Thus, QCM-D measures the mass of the (dry) biomolecular mass of the adsorbate, m_ads, and the hydrodynamically coupled solvent together, m_sovlent:

$$m_\mathrm{QCM} = m_\mathrm{ads} + m_\mathrm{solvent}. \tag{2.19}$$

As a consequence, structural changes of the adsorbed layers that are accompanied by a change of the hydrodynamically trapped liquid can be easily monitored by QCM-D. An example is the transition from a vesicle layer to an SLB [75], or cross-linking and collapse of polymer films [76].

2.3.1.2 Viscoelastic modeling

Above, we showed that the Sauerbrey qquation (equation (2.16)) can be used to analyze thin and rigid (small ΔD) films. However, if a film is sufficiently soft ($\Delta D > 0$) and thick, the QCM-D will become sensitive to the viscoelastic properties of the film [68]. In this case, the QCM-D data can be fitted to an appropriate viscoelastic model to extract information about the film's viscoelasticity and thickness [68, 77]. The viscoelastic properties are usually expressed as storage modulus, G', which correlates to the materials elasticity and the loss modulus, G'', which describes the viscous energy dissipation in the film. For example, if the viscoelastic film is laterally homogeneous and thinner than the shear-acoustic penetration wave of the QCM-D, Δf and ΔD correlate approximately with the film thickness, d, G' and G'' as:

$$\begin{aligned} \Delta f_n &\approx -\frac{n}{C} m_{\mathrm{QCM}} \left(1 - n 2\pi f_0 \rho_{\mathrm{s}} \eta_{\mathrm{s}} \frac{G''_{\mathrm{n}}}{\rho_{\mathrm{film}} \left({G'_{\mathrm{n}}}^2 + {G''_{\mathrm{n}}}^2 \right)} \right), \\ \Delta D_n &\approx \frac{2n}{f_{\mathrm{n}} C} m_{\mathrm{QCM}} n 2\pi f_0 \rho_{\mathrm{s}} \eta_{\mathrm{s}} \left(\frac{G'_{\mathrm{n}}}{\rho_{\mathrm{film}} \left({G'_{\mathrm{n}}}^2 + {G''_{\mathrm{n}}}^2 \right)} \right), \end{aligned} \tag{2.20}$$

where ρ_{film} is the density of the film. G'_{n} and G''_{n} are frequency dependent. Within the frequency range covered by the harmonics of QCM-D, they follow approximately power laws: $G'_{\mathrm{n}} \approx G'_0 n^{\alpha'}$ and $G''_{\mathrm{n}} \approx G''_0 n^{\alpha''}$, where G'_0 and G''_0 are the storage and loss modulus at the fundamental resonance frequency, respectively, and α' and α'' characteristic exponents. The relation between the film thickness, its density, and "wet-mass" is: $m_{\mathrm{film}}/\rho_{\mathrm{film}} = d$. ρ_{film} needs to be either measured by (a combination of) complementary techniques. In practice, however, ρ_{film} can be assumed to equal ρ_{s}, if the film is highly hydrated which is often the case. These relationships together with equation (2.20) allow to extract information about the viscoelastic properties and the thickness of the film.

2.3.2 Spectroscopic ellipsometry

Ellipsometry is an optical technique which measures changes in the polarization of light upon reflection at a surface. Spectroscopic ellipsometry measures this over a spectrum of wavelengths. If molecules adsorb to the surface, the optical properties of the interface will change. This induces a change in the polarization of the reflected light. From this change the (dry) biomolecular mass, m_{SE}, the thickness, d, and the refractive index, N, of the adsorbed layer can be extracted.

In this PhD project, we used spectroscopic ellipsometry mainly to determine the biomolecular mass of our FG repeat domain films, complementary to the information from QCM-D. It was also used to measure NTR binding to the FG repeat domain films and NTR permeation through the films (see in particular chapter 3). Since ellipsometry measure changes in mass in a time-resolved manner (with a resolution of about 1 s), we could also use it to provide estimates for adsorption and desorption kinetics of proteins to the surface (see chapter 3 and 5).

In the following, we will give a short overview about this method (a more detailed description can be found, for instance, in Refs. [78, 79, 80]).

2.3.2.1 Polarization of light

According to Maxwell's theory light, with a wavelength λ, can be described as an electromagnetic wave with two perpendicular vectors; one for the electric field and one for the magnetic field. In the following, we are only considering the electric field vector, $\vec{E}$, and describe the space by an Cartesian coordinate system such that the direction of propagation is z. The electric field vector can be expressed as a superposition of two orthogonal components, E_x and E_y:

$$\begin{aligned} E_x &= E_x^0 \cos(qz - \omega t + \delta_x), \\ E_y &= E_y^0 \cos(qz - \omega t + \delta_y) \end{aligned} \tag{2.21}$$

where q is the wave number ($2\pi/\lambda$), ω is the angular frequency, t is the time, δ_x and δ_y are phase constants, and E_x^0 and E_y^0 amplitudes of the components E_x and E_y (see figure 2.11).

The polarization of the light depends on the phase shift between E_x and E_y and their ratio.

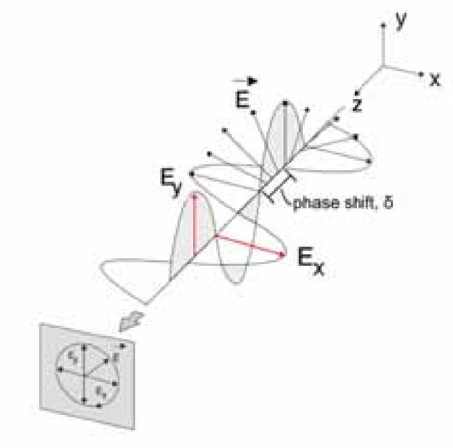

Figure 2.11: Polarization of light: *The electric field vector of the light, $\vec{E}$, can be described as superposition of two electric field vectors perpendicular to each other, E_x and E_y. The polarization of the light depends on the ratio of E_x and E_y, and on the phase shift between them. Here, circular polarized light is depicted, i.e. E_x and E_y have the same amplitude and the phase shift is a multiple of $\pi/2$. Adapted from [79].*

2.3.2.2 Changes in polarization upon reflection

Light will be reflected upon incidence on an interface, as illustrated in figure 2.12. Incident and reflected light span the plane of incidence (POI). The vector of the electric field can then be expressed as superposition of a component parallel, E_p, and a component perpendicular, E_s, to the POI. The polarization of the light will change upon reflection. This change in polarization can be measured by ellipsometry and related to the two ellipsometric angles Ψ and Δ by the fundamental equation of ellipsometry [78]:

$$\tan\Psi \exp(i\Delta) = \frac{E_\mathrm{rp}/E_\mathrm{ip}}{E_\mathrm{rs}/E_\mathrm{is}}. \tag{2.22}$$

Ψ and Δ express the amplitude ratio and phase difference between p- and s-polarizations, respectively (parameters explained in figure 2.12):

$$\Delta = \delta_\mathrm{rp} - \delta_\mathrm{rs}, \tag{2.23}$$

$$|\tan\Psi| = \left|\frac{E_\mathrm{rp}/E_\mathrm{ip}}{E_\mathrm{rs}/E_\mathrm{is}}\right|. \tag{2.24}$$

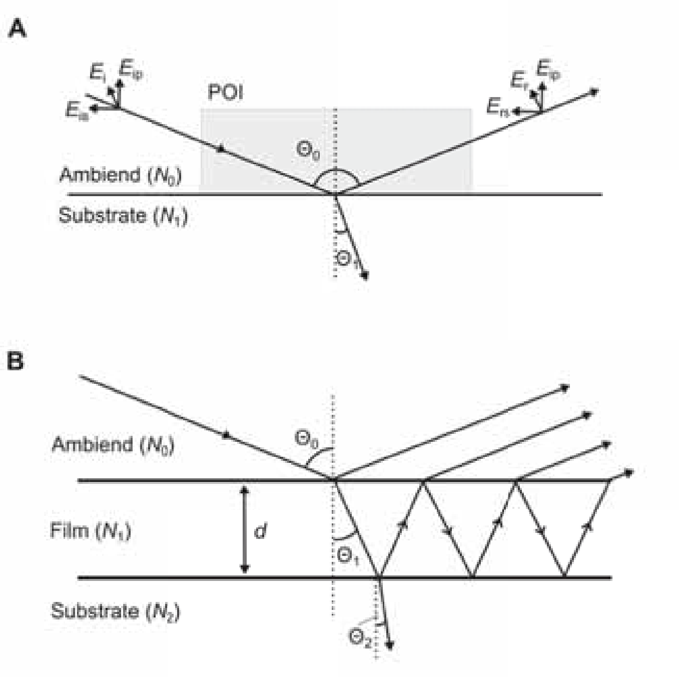

Figure 2.12: Reflection of polarized light: *(A) When a light beam hits a bare surface it will be partly adsorbed and partly reflected according to Snell's law. (B) When a light beam is reflected by a film-covered surface, its reflection can be described by Fresnel's law (see text). In both cases, a change in the phase shift and in the amplitudes of its parallel (E_p) and perpendicular (E_s) components will occur. These changes depend on the surface properties and can be measured by ellipsometry. Complex refractive index of ambient (N_0), complex refractive index of film (N_1), complex refractive index of substrate (N_2), angle of incidence (Θ_0), angle of transmission (Θ_1), angle of adsorption (Θ_2). Adapted from Ref. [79].*

The optical properties of the surface will strongly influence this change in polarization. This is quantitatively described by the Fresnel formalism. We will start with the case of a bare surface before going to a surface covered with a thin, transparent film.

A bare surface

We consider the simple case of reflection at a bare surface with infinite thickness, as illustrated in figure 2.12 (A). In this case the ratios $\mathrm{E_{rp}}/\mathrm{E_{ip}}$ and $\mathrm{E_{rs}}/\mathrm{E_{is}}$ equal the Fresnel reflection coefficients, r_{pp} and r_{s}, which can be calculated by:

$$\frac{E_{rp}}{E_{ip}} = r_{01_p} = \frac{N_1 \cos\, \Theta_0 - N_0 \cos\, \Theta_1}{N_1 \cos\, \Theta_0 + N_0 \cos\, \Theta_1}, \tag{2.25}$$

$$\frac{E_{rs}}{E_{is}} = r_{01_s} = \frac{N_0 \cos\ \Theta_0 - N_1 \cos\ \Theta_1}{N_0 \cos\ \Theta_0 + N_1 \cos\ \Theta_1}. \tag{2.26}$$

The parameters in equation (2.25) and (2.26) are defined in figure 2.12. These equations together with equation (2.22) allow to extract the optical properties (i.e. the refractive indeces) from the ellipsometric data.

A surface covered with a thin, transparent film

If the surface is covered with a thin, transparent film (see figure 2.12 B) the ratios $\mathrm{E_{rp}/E_{ip}}$ and $\mathrm{E_{rs}/E_{is}}$ equal the total Fresnel reflection coefficients, R_{pp} and R_{s}, which can be calculated by:

$$\frac{E_{\mathrm{rp}}}{E_{\mathrm{ip}}} = R_{\mathrm{s}} = \frac{r_{01\mathrm{p}} + r_{12\mathrm{p}} \exp(-4\pi i N_1 \cos\Theta_1 d_1/\lambda)}{1 + r_{01\mathrm{p}}\, r_{12\mathrm{p}} \exp(-4\pi i N_1 \cos\Theta_1 d_1/\lambda)}, \tag{2.27}$$

$$\frac{E_{\mathrm{rs}}}{E_{\mathrm{is}}} = R_{\mathrm{pp}} = \frac{r_{01\mathrm{s}} + r_{12\mathrm{s}} \exp(-4\pi i N_1 \cos\Theta_1 d_1/\lambda)}{1 + r_{01\mathrm{s}}\, r_{12s} \exp(-4\pi i N_1 \cos\Theta_1 d_1/\lambda)}. \tag{2.28}$$

The parameters in equations (2.27) and (2.28) are defined in figure 2.12. By substituting $\mathrm{E_{rp}/E_{ip}}$ and $\mathrm{E_{rs}/E_{is}}$ in equation (2.22), we arrive at:

$$\tan\Psi \exp(i\Delta) = \frac{R_{\mathrm{s}}}{R_{\mathrm{pp}}}. \tag{2.29}$$

In theory, solving equation (2.29), allows to extract the thickness of the film and the optical parameters of the layers from ellipsometric data. In practice, an appropriate model of stacked layers (each with its own thickness and refractive index) is fitted to the data (and reference measurements) to obtain this information.

In this thesis, the (dry) biomolecular surface mass, Γ, of the film was calculated by the deFejter's equation [81]:

$$\Gamma = \frac{d(N_1 - N_0)}{\mathrm{d}N/\mathrm{d}c}, \tag{2.30}$$

where $\mathrm{d}N/\mathrm{d}c$ is the refractive-index increment (which depends on the adsorbing biomolecule).

Typically, we obtained a mass resolution of about 1 ng/cm^2 with our spectroscopic ellipsometer.

A detailed information about the models and data analysis that we employed can be found in the materials and methods part of the individual chapters.

2.3.3 Confocal laser scanning microscope

Confocal laser scanning microscopy (CLSM) is an optical imaging technique that benefits from the feature, that only the light of a thin slice is collected (down to 500 nm). The resolution of thicker samples is increased, since out-of-focus light is effectively excluded. This also facilitates the three dimensional reconstruction of samples.

In this thesis, we used confocal laser scanning microscopy for fluorescence recovery after photobleaching (FRAP) measurements (see chapter 5) and to monitor the depletion of fluorescence probes in a measurement cell by acquiring a time-series of z-stacks (see chapter 6).

In figure 2.13, a scheme of the CLSM working principle is presented. The light source is a laser system. The emitted light is reflected by a dichroic mirror and focused onto a defined focal plane which is conjugated to a second pinhole aperture positioned in front of the detector. The sample is labeled with fluophores which are excited by the laser light leading to emission of fluorescence light. This light (solid line in figure 2.13 A) passes through the dichromatic mirror and is focused as confocal point at the detector pinhole aperture.

Fluorescence emission from fluophores above and below the objective focal plane (dotted and dashed lines, respectively, in figure 2.13 A) is not confocal with the pinhole (i.e. out-of-focus). It forms, hence, extended disks in the aperture plane. As a consequence, most of this light cannot pass through the pinhole aperture and is not detected.

In order to obtain a 2D image, the laser beam scans the focal plane across a defined area in a raster pattern. This is executed by two high speed oscillating mirrors with precisely tunable tilt regarding the incident laser beam. One of the mirrors directs the beam from left to right, along the x-axes (illustrated in figure 2.13 B). Once a line scan

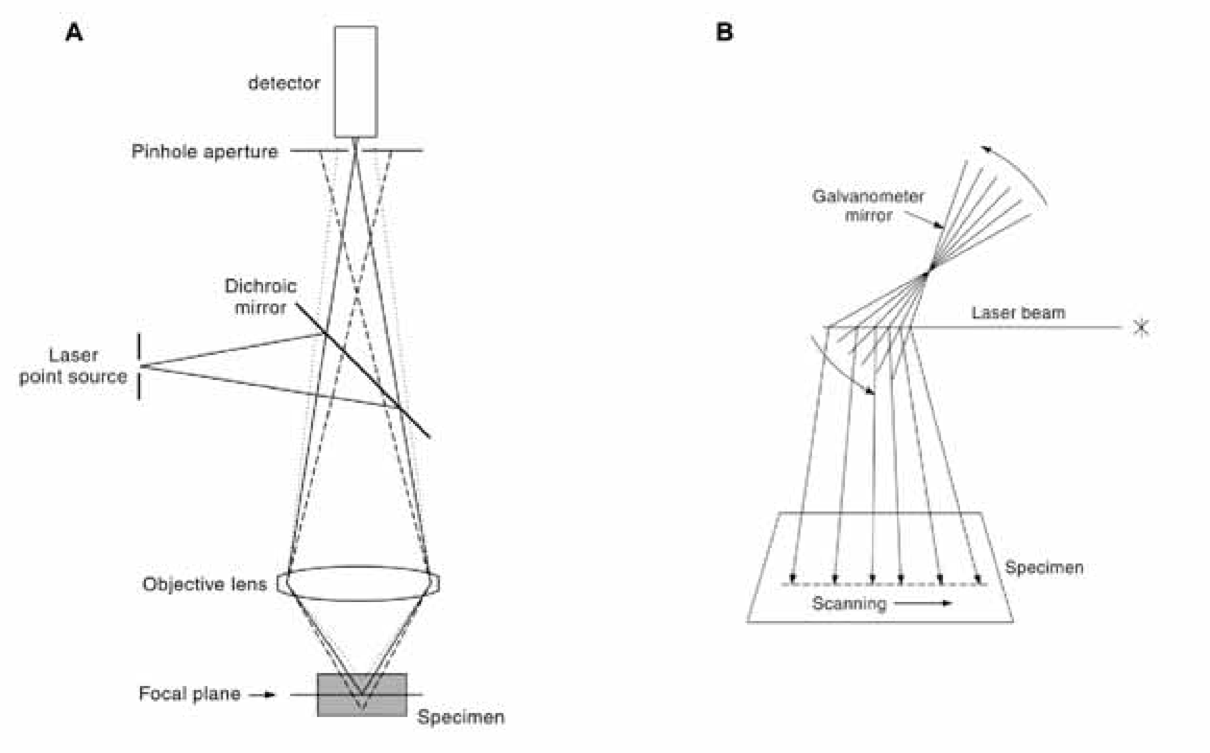
A
detector
Pinhole aperture
Dichroic mirror
Laser point source
Objective lens
Focal plane
Specimen
B
Galvanometer mirror
Laser beam
Specimen
Scanning

Figure 2.13: Working principle of confocal laser scanning microscopy: *(A) Shown is a simplified scheme of a CLSM. Excitation light from a laser point source is focused on point in a confocal plane of the specimen. Fluorescent light from this point (solid line) is focused back on the pinhole of a aperture plane and collected by the detector behind the pinhole. Fluorescent light emitted at points above and below the plane of focus of the objective lens (dotted and dashed lines, respectively) is not confocal with the pinhole and forms extended disks in the plane of the pinhole. Hence, most of the out-of-focus information is excluded from the detector. (B) Shown is one of the galvanometer mirrors of the CLSM. The excitatory laser beam can be delivered to different position of the specimen by tilting the mirror. A second mirror with a perpendicular scan axis to the first mirror, allows to scan an area. Taken from Ref. [82].*

is finished, the other mirror moves the beam one pixel in y-direction. Then, a new line is scanned, and so forth.

3D images can also be obtained, by collecting a z-stack of images. To this end, a series of images is taken. Each time an image is collected, the objective, and hence the focal plane, is moved appropriately in z-direction. Each image corresponds then to one slice in the z-stack.

References

[1] C. de Duve. 2007. “The origin of eukaryotes: a reappraisal”. In: *Nat. Rev. Genet.* 8 (5), pp. 395–403.

[2] H. G. Callan and S. G. Tomlin. 1950. “Experimental studies on amphibian oocyte nuclei. I. Investigation of the structure of the nuclear membrane by means of the electron microscope.” In: *Proc. Roy. Soc. London* 137, pp. 367–378.

[3] G. F. Bahr and W. Beermann. 1954. “The fine structure of the nuclear membrane in the larval salivary gland and midgut of Chironomus”. In: *Exp. Cell Res.* 6 (2), pp. 519–522.

[4] M. P. Rout, J. D. Aitchison, A. Suprapto, K. Hjertaas, Y. Zhao, and B. T. Chait. Feb. 2000. “The yeast nuclear pore complex: composition, architecture, and transport mechanism.” In: *J. Cell Biol.* 148 (4), pp. 635–651.

[5] J. M. Cronshaw, A. N. Krutchinsky, W. Zhang, B. T. Chait, and M. J. Matunis. Sept. 2002. “Proteomic analysis of the mammalian nuclear pore complex”. In: *J. Cell Biol.* 158 (5), pp. 915–27.

[6] M. P. Rout and G. Blobel. Nov. 1993. “Isolation of the yeast nuclear pore complex.” In: *J. Cell Biol.* 123 (4), pp. 771–783.

[7] R. Reichelt, A. Holzenburg, E. L. Buhle, M. Jarnik, A. Engel, and U. Aebi. Apr. 1990. “Correlation between structure and mass distribution of the nuclear pore complex and of distinct pore complex components.” In: *J. Cell Biol.* 110 (4), pp. 883–894.

[8] C. W. Akey and M. Radermacher. July 1993. “Architecture of the Xenopus nuclear pore complex revealed by three-dimensional cryo-electron microscopy.” In: *J. Cell Biol.* 122 (1), pp. 1–19.

[9] S. Wischnitzer. 1958. “An electron microscope study of the nuclear envelope of amphibian oocytes”. In: *J. Ultrastruct. Res.* 1 (3), pp. 201–222.

[10] J. G. Gall. Feb. 1967. “Octagonal nuclear pores.” In: *J. Cell Biol.* 32 (2), pp. 391–399.

[11] Q. Yang, M. P. Rout, and C. W. Akey. Jan. 1998. “Three-dimensional architecture of the isolated yeast nuclear pore complex: functional and evolutionary implications.” In: *Mol. Cell* 1 (2), pp. 223–234.

[12] K. Ribbeck and D. Görlich. Mar. 2001. “Kinetic analysis of translocation through nuclear pore complexes.” In: *EMBO J.* 20 (6), pp. 1320–1330.

[13] M. Jones. 2007. “Side-view Diagram of a Nuclear Pore”. Artwork electronically published under the Creative Commons Attribution-Share Alike 2.5 Generic license.

[14] W. M. Bonner. Feb. 1975. “Protein migration into nuclei. I. Frog oocyte nuclei in vivo accumulate microinjected histones, allow entry to small proteins, and exclude large proteins.” In: *J. Cell Biol.* 64 (2), pp. 421–430.

[15] D. Mohr, S. Frey, T. Fischer, T. Güttler, and D. Görlich. Sept. 2009. “Characterisation of the passive permeability barrier of nuclear pore complexes.” In: *EMBO J.* 28 (17), pp. 2541–2553.

[16] D. Görlich and U. Kutay. 1999. “Transport between the cell nucleus and the cytoplasm.” In: *Annu. Rev. Cell. Dev. Biol.* 15, pp. 607–660.

[17] H. Fried and U. Kutay. Aug. 2003. “Nucleocytoplasmic transport: taking an inventory”. In: *Cell. Mol. Life Sci.* 60 (8), pp. 1659–1688.

[18] D. Kalderon, W. D. Richardson, A. F. Markham, and A. E. Smith. 1984. “Sequence requirements for nuclear location of simian virus 40 large-T antigen”. In: *Nature* 311, pp. 33–38.

[19] D. Görlich, S. R. Prehn, R. A. Laskey, and E. Hartmann. 1994. “Isolation of a protein that is essential for the first step of nuclear protein import”. In: *Cell* 79, pp. 767–778.

[20] D. Görlich, N. Panté, U. Kutay, U. Aebi, and F. R. Bischoff. Oct. 1996. “Identification of different roles for RanGDP and RanGTP in nuclear protein import.” In: *EMBO J.* 15 (20), pp. 5584–5594.

[21] K. Weis, U. Ryder, and A. I. Lamond. Apr. 1996. “The conserved amino-terminal domain of hSRP1 alpha is essential for nuclear protein import.” eng. In: *EMBO J.* 15 (8), pp. 1818–1825.

[22] M. Fornerod, M. Ohno, M. Yoshida, and I. W. Mattaj. Sept. 1997. “CRM1 is an export receptor for leucine-rich nuclear export signals.” eng. In: *Cell* 90 (6), pp. 1051–1060.

[23] H. P. Bogerd, R. E. Benson, R. Truant, A. Herold, M. Phingbodhipakkiya, and B. R. Cullen. Apr. 1999. “Definition of a consensus transportin-specific nucleocytoplasmic transport signal.” eng. In: *J. Biol. Chem.* 274 (14), pp. 9771–9777.

[24] F. R. Bischoff, C. Klebe, J. Kretschmer, A. Wittinghofer, and H. Ponstingl. Mar. 1994. “RanGAP1 induces GTPase activity of nuclear Ras-related Ran.” eng. In: *Proc. Natl. Acad. Sci. U.S.A.* 91 (7), pp. 2587–2591.

[25] F. R. Bischoff, H. Krebber, T. Kempf, I. Hermes, and H. Ponstingl. Feb. 1995. “Human RanGTPase-activating protein RanGAP1 is a homologue of yeast Rna1p involved in mRNA processing and transport.” eng. In: *Proc. Natl. Acad. Sci. U.S.A.* 92 (5), pp. 1749–1753.

[26] F. R. Bischoff and D. Görlich. Dec. 1997. "RanBP1 is crucial for the release of RanGTP from importin beta-related nuclear transport factors." eng. In: *FEBS Lett.* 419 (2-3), pp. 249–254.

[27] R. H. Kehlenbach, A. Dickmanns, A. Kehlenbach, T. Guan, and L. Gerace. May 1999. "A role for RanBP1 in the release of CRM1 from the nuclear pore complex in a terminal step of nuclear export." eng. In: *J. Cell Biol.* 145 (4), pp. 645–657.

[28] M. Koyama and Y. Matsuura. June 2010. "An allosteric mechanism to displace nuclear export cargo from CRM1 and RanGTP by RanBP1." eng. In: *EMBO J.* 29 (12), pp. 2002–2013.

[29] K. Ribbeck, G. Lipowsky, H. M. Kent, M. Stewart, and D. Görlich. Nov. 1998. "NTF2 mediates nuclear import of Ran." In: *EMBO J.* 17 (22), pp. 6587–6598.

[30] A. Smith, A. Brownawell, and I. G. Macara. 1998. "Nuclear import of Ran is mediated by the transport factor NTF2." In: *Curr. Biol.* 8 (25), pp. 1403–1406.

[31] F. R. Bischoff and H. Ponstingl. Nov. 1991. "Catalysis of guanine nucleotide exchange on Ran by the mitotic regulator RCC1." eng. In: *Nature* 354 (6348), pp. 80–82.

[32] S. Kose, N. Imamoto, T. Tachibana, T. Shimamoto, and Y. Yoneda. Nov. 1997. "Ran-unassisted nuclear migration of a 97-kD component of nuclear pore-targeting complex." eng. In: *J. Cell Biol.* 139 (4), pp. 841–849.

[33] K. Ribbeck, U. Kutay, E. Paraskeva, and D. Görlich. Jan. 1999. "The translocation of transportin-cargo complexes through nuclear pores is independent of both Ran and energy." eng. In: *Curr. Biol.* 9 (1), pp. 47–50.

[34] M. V. Nachury and K. Weis. Aug. 1999. "The direction of transport through the nuclear pore can be inverted." In: *Proc. Natl. Acad. Sci. U.S.A.* 96 (17), pp. 9622–9627.

[35] D. P. Denning, V. Uversky, S. S. Patel, A. L. Fink, and M. Rexach. Sept. 2002. "The Saccharomyces cerevisiae nucleoporin Nup2p is a natively unfolded protein." In: *J. Biol. Chem.* 277 (36), pp. 33447–33455.

[36] D. P. Denning, S. S. Patel, V. Uversky, A. L. Fink, and M. Rexach. Mar. 2003. "Disorder in the nuclear pore complex: the FG repeat regions of nucleoporins are natively unfolded." In: *Proc. Natl. Acad. Sci. U.S.A.* 100 (5), pp. 2450–2455.

[37] M. P. Rout and S. R. Wente. Oct. 1994. "Pores for thought: nuclear pore complex proteins." eng. In: *Trends Cell Biol.* 4 (10), pp. 357–365.

[38] L. A. Strawn, T. Shen, N. Shulga, D. S. Goldfarb, and S. R. Wente. Mar. 2004. "Minimal nuclear pore complexes define FG repeat domains essential for transport." In: *Nat. Cell Biol.* 6 (3), pp. 197–206.

[39] S. Frey, R. P. Richter, and D. Görlich. Nov. 2006. “FG-rich repeats of nuclear pore proteins form a three-dimensional meshwork with hydrogel-like properties.” In: *Science* 314 (5800), pp. 815–817.

[40] S. S. Patel, B. J. Belmont, J. M. Sante, and M. F. Rexach. Apr. 2007. “Natively unfolded nucleoporins gate protein diffusion across the nuclear pore complex.” In: *Cell* 129 (1), pp. 83–96.

[41] S. Frey and D. Görlich. 2009. “FG/FxFG as well as GLFG repeats form a selective permeability barrier with self-healing properties”. In: *EMBO J.* 28 (17), pp. 2554–2567.

[42] C. Ader, S. Frey, W. Maas, H. B. Schmidt, D. Görlich, and M. Baldus. 2010. “Amyloid-like interactions within nucleoporin FG hydrogels”. In: *Proc. Natl. Acad. Sci. U.S.A.* 107 (14), pp. 6281–6285.

[43] J. Yamada, J. L. Phillips, S. Patel, G. Goldfien, A. Calestagne-Morelli, H. Huang, R. Reza, J. Acheson, V. V. Krishnan, S. Newsam, A. Gopinathan, E. Y. Lau, M. E. Colvin, V. N. Uversky, and M. F. Rexach. 2010. “A bimodal distribution of two distinct categories of intrinsically disordered structures with separate functions in FG nucleoporins”. In: *Molecular & Cellular Proteomics* 9 (10), pp. 2205–2224.

[44] S. Milles and E. A. Lemke. 2011. “Single molecule study of the intrinsically disordered FG-repeat nucleoporin 153”. In: *Biophys. J.* 101 (7), pp. 1710–1719.

[45] T. U. Schwartz. 2005. “Modularity within the architecture of the nuclear pore complex”. In: *Curr. Opin. Struct. Biol.* 15 (2), pp. 221–226.

[46] M. K. Iovine, J. L. Watkins, and S. R. Wente. Dec. 1995. “The GLFG repetitive region of the nucleoporin Nup116p interacts with Kap95p, an essential yeast nuclear import factor.” eng. In: *J. Cell Biol.* 131 (6), pp. 1699–1713.

[47] R. Bayliss, K. Ribbeck, D. Akin, H. M. Kent, C. M. Feldherr, D. Görlich, and M. Stewart. Oct. 1999. “Interaction between NTF2 and xFxFG-containing nucleoporins is required to mediate nuclear import of RanGDP.” In: *J. Mol. Biol.* 293 (3), pp. 579–593.

[48] R. Bayliss, T. Littlewood, and M. Stewart. July 2000. “Structural basis for the interaction between FxFG nucleoporin repeats and importin-beta in nuclear trafficking.” In: *Cell* 102 (1), pp. 99–108.

[49] T. A. Isgro and K. Schulten. Dec. 2005. “Binding dynamics of isolated nucleoporin repeat regions to importin-beta.” In: *Structure* 13 (12), pp. 1869–1879.

[50] S. Wälde and R. H. Kehlenbach. 2010. “The Part and the Whole: functions of nucleoporins in nucleocytoplasmic transport”. In: *Trends Cell Biol.* 20 (8), pp. 461–469.

[51] R. Peters. Mar. 2005. “The nanopore connection to cell membrane unitary permeability.” In: *Traffic* 6 (3), pp. 199–204.

[52] S. Frey and D. Görlich. Aug. 2007. “A saturated FG-repeat hydrogel can reproduce the permeability properties of nuclear pore complexes.” In: *Cell* 130 (3), pp. 512–523.

[53] R. Y. H. Lim, N.-P. Huang, J. Köser, J. Deng, K. H. A. Lau, K. Schwarz-Herion, B. Fahrenkrog, and U. Aebi. June 2006. “Flexible phenylalanine-glycine nucleoporins as entropic barriers to nucleocytoplasmic transport.” In: *Proc. Natl. Acad. Sci. U.S.A.* 103 (25), pp. 9512–9517.

[54] S. S. Patel and M. F. Rexach. Jan. 2008. “Discovering novel interactions at the nuclear pore complex using bead halo: a rapid method for detecting molecular interactions of high and low affinity at equilibrium.” In: *Mol. Cell. Proteomics* 7 (1), pp. 121–131.

[55] V. V. Krishnan, E. Y. Lau, J. Yamada, D. P. Denning, S. S. Patel, M. E. Colvin, and M. F. Rexach. Aug. 2008. “Intramolecular cohesion of coils mediated by phenylalanine–glycine motifs in the natively unfolded domain of a nucleoporin.” In: *PLoS Comput. Biol.* 4 (8), e1000145.

[56] M. P. Rout, J. D. Aitchison, M. O. Magnasco, and B. T. Chait. Dec. 2003. “Virtual gating and nuclear transport: the hole picture.” In: *Trends Cell Biol.* 13 (12), pp. 622–628.

[57] W. W. Franke and U. Scheer. 1974. “Pathways of nucleocytoplasmic translocation of ribonucleoproteins.” eng. In: *Symp. Soc. Exp. Biol.* (28), pp. 249–282.

[58] N. Panté and M. Kann. Feb. 2002. “Nuclear pore complex is able to transport macromolecules with diameters of about 39 nm.” eng. In: *Mol. Biol. Cell* 13 (2), pp. 425–434.

[59] R. Y. H. Lim, B. Fahrenkrog, J. Köser, K. Schwarz-Herion, J. Deng, and U. Aebi. Oct. 2007a. “Nanomechanical basis of selective gating by the nuclear pore complex.” In: *Science* 318 (5850), pp. 640–643.

[60] R. Y. H. Lim, J. Köser, N.-P. Huang, K. Schwarz-Herion, and U. Aebi. Aug. 2007b. “Nanomechanical interactions of phenylalanine-glycine nucleoporins studied by single molecule force-volume spectroscopy.” In: *J. Struct. Biol.* 159 (2), pp. 277–289.

[61] R. L. Schoch, L. E. Kapinos, and R. Y. Lim. 2012. “Nuclear transport receptor binding avidity triggers a self-healing collapse transition in FG-nucleoporin molecular brushes”. In: *Proc. Natl. Acad. Sci. U.S.A.* 109 (42), pp. 16911–16916.

[62] R. Peters. Oct. 2009. “Functionalization of a nanopore: the nuclear pore complex paradigm.” In: *Biochim. Biophys. Acta* 1793 (10), pp. 1533–1539.

[63] M. Rubinstein and R. H. Colby. 2003. “Polymer Physics”. Oxford: Oxford University Press.

[64] P.-G. de Gennes. 1979. “Scaling Concepts in Polymer Physics”. Ithaca and London: Cornell University Press.

[65] P. J. Flory. 1953. “Principles of polymer chemistry”. Ithaca, NY: Cornell University Press.

[66] P. G. de Gennes. July 1987. “Polymers at an interface; a simplified view”. In: *Adv. Colloid Interface Sci.* 27 (3-4), pp. 189–209.

[67] L. H. Cai, S. Panyukov, and M. Rubinstein. Oct. 2011. “Mobility of Nonsticky Nanoparticles in Polymer Liquids”. In: *Macromolecules* 44 (19), pp. 7853–63.

[68] I. Reviakine, D. Johannsmann, and R. P. Richter. Dec. 2011. “Hearing what you cannot see and visualizing what you hear: interpreting quartz crystal microbalance data from solvated interfaces”. In: *Anal. Chem.* 83 (23), pp. 8838–48.

[69] F. Höök, C. Larsson, and Fant. 2002. “Biofunctional surfaces studied by quartz crystal microbalance with dissipation monitoring”. In: *Encyclopedia of Surface and Colloid Science*, pp. 774–791.

[70] G. Sauerbrey. 1959. “Verwendung von Schwingquarzen zur Wägung dünner Schichten und zur Mikrowägung.” In: *Zeitschrift für Physik A* 155, pp. 206–222.

[71] K. K. Kanazawa and J. G. Gordon. July 1985. “Frequency of a quartz microbalance in contact with liquid”. In: *Anal. Chem.* 57 (8), pp. 1770–1771.

[72] M. Rodahl and B. Kasemo. June 1996. “On the measurement of thin liquid overlayers with the quartz-crystal microbalance”. In: *Sensors and Actuators A: Physical* 54 (1-3), pp. 448–456.

[73] E. Reimhult, C. Larsson, B. Kasemo, and F. Höök. Dec. 2004. “Simultaneous surface plasmon resonance and quartz crystal microbalance with dissipation monitoring measurements of biomolecular adsorption events involving structural transformations and variations in coupled water.” In: *Anal. Chem.* 76 (24), pp. 7211–7220.

[74] P. Bingen, G. Wang, N. F. Steinmetz, M. Rodahl, and R. P. Richter. Oct. 2008. “Solvation Effects in the Quartz Crystal Microbalance with Dissipation Monitoring Response to Biomolecular Adsorption. A Phenomenological Approach.” In: *Anal. Chem.* 80, p. 8880.

[75] R. Richter, A. Mukhopadhyay, and A. Brisson. Nov. 2003. “Pathways of Lipid Vesicle Deposition on Solid Surfaces: A Combined QCM-D and AFM Study”. In: *Biophys. J.* 85 (5), pp. 3035–3047.

[76] F. Höök, B. Kasemo, T. Nylander, C. Fant, K. Sott, and H. Elwing. Dec. 2001. “Variations in Coupled Water, Viscoelastic Properties, and Film Thickness of a Mefp-1 Protein

Film during Adsorption and Cross-Linking: A Quartz Crystal Microbalance with Dissipation Monitoring, Ellipsometry, and Surface Plasmon Resonance Study". In: *Anal. Chem.* 73 (24), pp. 5796–5804.

[77] D. Johannsmann. 1999. "Viscoelastic analysis of organic thin films on quartz resonators". In: *Macromolecular Chemistry and Physics* 200 (3), pp. 501–516.

[78] H. Fujiwara. 2007. "Spectroscopic Ellipsometry: Principles and Applications". West Sussex, England: John Willey & Sons Ltd.

[79] D. Gonçalves and E. A. Irene. Sept. 2002. "Fundamentals and applications of spectroscopic ellipsometry". en. In: *Química Nova* 25, pp. 794–800.

[80] R. P. Richter, K. B. Rodenhausen, N. B. Eisele, and M. Schubert. in press. "Coupling Spectroscopic Ellipsometry and Quartz Crystal Microbalance to Study Organic Films at the Solid-Liquid Interface". Ed. by K.-J. Eichhorn and K. Hinrichs. Springer.

[81] J. A. De Feijter, J. Benjamins, and F. A. Veer. 1978. "Ellipsometry as a tool to study the adsorption behavior of synthetic and biopolymers at the air-water interface". In: *Biopolymers* 17 (7), pp. 1759–1772.

[82] D. B. Murphy. 2001. "Fundamentals of Light Microscopy and Electronic Imaging". Wiley-Liss, Inc.

3 Ultrathin nucleoporin FG repeat films and their interaction with NTRs

This chapter was published in EMBO Reports, 2010, 11: 366–372, as:

Ultrathin nucleoporin phenylalanine-glycine repeat films and their interaction with NTRs

Authors: **Nico B. Eisele**[a,b], Steffen Frey[b], Jacob Piehler[c], Dirk Görlich[b], Ralf P. Richter[a,d]

[a] Biosurfaces Unit, CIC biomaGUNE, Paseo Miramon 182, 20009 San Sebastian, Spain
[b] Department of Cellular Logistics, Max Planck Institute for Biophysical Chemistry, Am Faßberg 11, 37077 Göttingen, Germany
[c] Department of Biology, University of Osnabrück, Barbarastraße 11, 49076 Osnabrück, Germany
[d] Max Planck Institute for Metals Research, Heisenbergstraße 3, 70569 Stuttgart, Germany

Contribution of authors: Nico B. Eisele, Steffen Frey, Dirk Görlich and Ralf P. Richter designed research. Nico B. Eisele performed QCM-D and ellipsometry measurements and analyzed data. Steffen Frey purified proteins. Jacob Piehler contributed bis-NTA functionalized lipids. Ralf P. Richter performed AFM measurements and analyzed data.

EMBO reports

EMBO open

scientific report

Ultrathin nucleoporin phenylalanine–glycine repeat films and their interaction with nuclear transport receptors

Nico B. Eisele[1,2]*, Steffen Frey*[2]*, Jacob Piehler*[3]*, Dirk Görlich*[2] *& Ralf P. Richter*[1,4+]

[1]Biosurfaces Unit, Centre for Cooperative Research in Biomaterials, Donostia—San Sebastian, Spain, [2]Department of Cellular Logistics, Max Planck Institute for Biophysical Chemistry, Göttingen, Germany, [3]Department of Biology, University of Osnabrück, Osnabrück, Germany, and [4]Max Planck Institute for Metals Research, Stuttgart, Germany

This is an open-access article distributed under the terms of the Creative Commons Attribution License, which permits distribution, and reproduction in any medium, provided the original author and source are credited. This license does not permit commercial exploitation without specific permission.

Nuclear pore complexes (NPCs) are highly selective gates that mediate the exchange of all proteins and nucleic acids between the cytoplasm and the nucleus. Their selectivity relies on a supramolecular assembly of natively unfolded nucleoporin domains containing phenylalanine–glycine (FG)-rich repeats (FG repeat domains), in a way that is at present poorly understood. We have developed ultrathin FG domain films that reproduce the mode of attachment and the density of FG repeats in NPCs, and that exhibit a thickness that corresponds to the nanoscopic dimensions of the native permeability barrier. By using a combination of biophysical characterization techniques, we quantified the binding of nuclear transport receptors (NTRs) to such FG domain films and analysed how this binding affects the swelling behaviour and mechanical properties of the films. The results extend our understanding of the interaction of FG domain assemblies with NTRs and contribute important information to refine the model of transport across the permeability barrier.

Keywords: FG repeat domain; nuclear pore complex; nuclear transport receptor; nucleoporins; permeability barrier

EMBO *reports* (2010) **11**, 366–372. doi:10.1038/embor.2010.34

INTRODUCTION

All eukaryotic cells rely on nuclear pore complexes (NPCs) as the unique path to shuttle macromolecules across their nuclear envelope. Translocation through the central channel, with a diameter and length of 35–40 nm in the case of yeast (Yang *et al*, 1998), is selective: molecules smaller than 5 nm in diameter (Mohr *et al*, 2009) can diffuse efficiently through the pore, whereas larger molecules are delayed or blocked—unless they are bound to nuclear transport receptors (NTRs). The permeability barrier, and its selectivity, arises from an assembly of natively unfolded protein domains that are rich in phenylalanine–glycine repeats (FG repeat domains; Denning *et al* (2003) and references therein) and that are grafted at a high density on to the channel walls. These NTRs can interact with the FG repeat domains, thereby facilitating the translocation of NTR-bound cargo.

Several models have been proposed to explain the mechanism of function of the permeability barrier (Peters, 2009, and references therein). They are distinct in the putative nanoscale organization of FG repeats and in how NTRs are thought to interact with FG repeats to confer selective permeability to such a dynamic supramolecular assembly. In the 'virtual gating' (Rout *et al*, 2003) and 'selective phase' (Ribbeck & Görlich, 2001, 2002) models, for example, NTRs are thought to interact locally with a homogeneous distribution of FG repeat domains. The 'reversible collapse' model (Lim *et al*, 2007), by contrast, assumes transient morphological changes over distances as large as the contour length of entire FG repeat domains. The 'reduction of dimensionality' (Peters, 2005) model postulates the presence of a distinct structure, a surface lined with FG repeats, for efficient translocation of NTRs.

Inspired by these models, we sought to create *in vitro* nanoscopic assemblies of FG repeat domains to provide detailed insight into the interaction between NTRs and FG repeat-domain meshworks, and the concomitant morphological changes that are

---

[1]Biosurfaces Unit, Centre for Cooperative Research in Biomaterials, Paseo Miramon 182, Donostia—San Sebastian 20009, Spain
[2]Department of Cellular Logistics, Max Planck Institute for Biophysical Chemistry, Am Fassberg 11, Göttingen 37077, Germany
[3]Department of Biology, University of Osnabrück, Barbarastrasse 11, Osnabrück 49076, Germany
[4]Max Planck Institute for Metals Research, Heisenbergstrasse 3, Stuttgart 70569, Germany
[+]Corresponding author. Tel: +34 943 00 5329; Fax: +34 943 00 5315; E-mail: rrichter@cicbiomagune.es

Received 27 August 2009; revised 28 January 2010; accepted 12 February 2010;
published online 9 April 2010

©2010 EUROPEAN MOLECULAR BIOLOGY ORGANIZATION

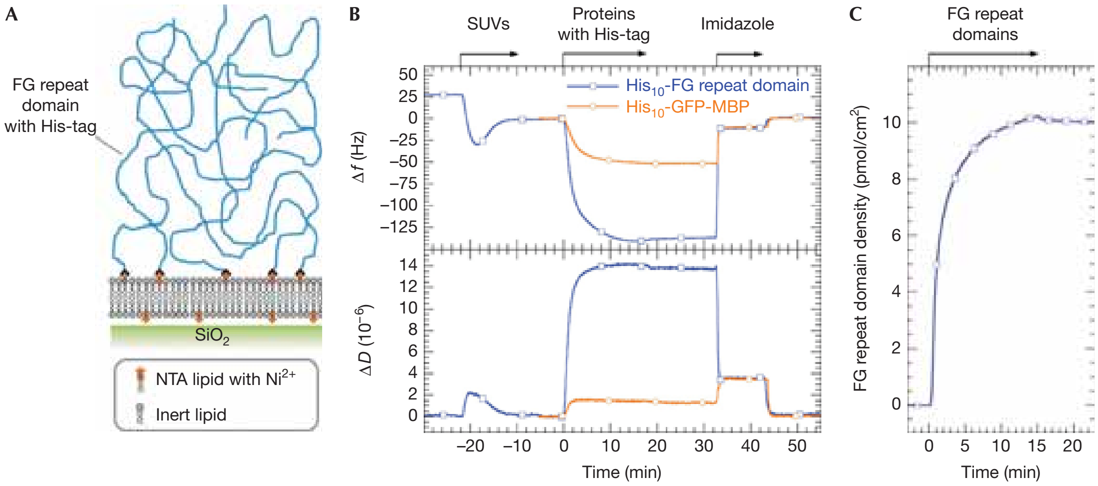

Fig 1 | Formation of membrane-anchored monolayers of phenylalanine–glycine repeat domains. (**A**) Scheme illustrating the film architecture. The FG repeat domain of Nsp1p (amino acids 2–601) was grafted through an amino-terminal His$_{10}$ tag to a *bis*-NTA-functionalized SLB. (**B**) Construction of an FG repeat film, followed by quartz crystal microbalance with dissipation monitoring. The start and duration of the incubation with different samples is indicated (arrows); remaining times correspond to buffer washes. The SLB was formed by exposure of 50 μg/ml SUVs, containing 10 mol% *bis*-NTA-functionalized lipids, to a silica surface. The two-phase behaviour together with the final changes in frequency and dissipation, $\Delta f = -28$ Hz and $\Delta D < 0.3 \times 10^{-6}$, characterize the formation of an SLB of good quality. Strong changes in frequency and dissipation on the addition of 1.5 μM His-tagged FG repeat domains reflect the formation of a flexible and hydrated film. Binding of 1.4 μM His-tagged GFP–MBP is shown for comparison. This fusion of globular proteins with a comparable molecular weight and an identical His-tag to the FG repeat domains induced about one-third of the frequency shift of the FG repeats and a low dissipation shift, as expected for a rigid monolayer of about 8 nm in thickness. At the end of the film formation processes, $\Delta D/-\Delta f$ ratios of 0.1×10^{-6}/Hz for FG repeat domains and 0.028×10^{-6}/Hz for GFP–MBP were reached. The more than threefold higher value for FG repeat domains reflects the increased softness of this film. All His-tagged proteins bound with high affinity but could be removed by washing with 500 mM imidazole. Changes in Δf and ΔD at about 43 min do not reflect any changes on the surface but result from a change in the viscosity or density of the surrounding solution owing to the presence of imidazole. (**C**) Ellipsometric analysis of the FG repeat domain density during film formation, with 3 μM His-tagged FG repeat domains in solution. FG, phenylalanine–glycine; GFP, green fluorescent protein; MBP, maltose-binding protein; NTA, nitrilotriacetic acid; SLB, supported lipid bilayer; SUV, small unilamellar vesicle.

induced by NTRs. We found continuous planar monolayers of end-grafted FG repeat domains (Fig 1A) to be suitable for this goal. Their macroscopic extension in two dimensions and their confinement to a solid support make such films amenable to characterization by surface-sensitive biophysical methods. By using such methods, the construction and morphology of the films can be controlled tightly and their interaction with NTRs quantified.

RESULTS AND DISCUSSION

Formation of FG repeat-domain films

We used supported lipid bilayers (SLBs; Richter *et al*, 2006) as a platform for the construction of FG repeat-domain films (Fig 1A). The SLBs provide a tuneable density of anchorage sites—here 10 mol% of *bis*-nitrilotriacetic-acid (NTA)-functionalized lipids (Lata *et al*, 2006)—together with a background of low unspecific binding. A His-tagged construct of the FG repeat domain (amino acids 2–601) of Nsp1p, a yeast nucleoporin that is essential for viability and located in the central region of the pore channel, was used as building material for the model films.

Step-by-step assembly of the films was monitored by quartz crystal microbalance with dissipation monitoring (QCM-D; Fig 1B). Strong shifts in resonance frequency, Δf, and dissipation, ΔD, on incubation of the FG repeat construct provide evidence for successful formation of a soft and hydrated film. The FG repeat domains remained stably bound upon rinsing in buffer. They could be fully eluted with imidazole and did not bind to SLBs that lacked NTA functionality (supplementary Fig S5 online), indicating specific anchorage through their amino-terminal His tags. This ‘end on’ attachment is reminiscent of the anchorage of FG repeat domains to the NPC channel walls, although the orientation is upside down. The thickness of the film, 34 ± 4 nm, estimated from QCM-D data (supplementary Fig S2 online and supplementary Table S2 online), represents only a fraction of the contour length of the FG repeat domain (~250 nm) but is similar to the dimensions of the central NPC channel. We note that an FG repeat monolayer of such a thickness would readily fill the cross-section of the central NPC channel. Imaging by atomic force microscopy (AFM; supplementary Fig S4 online) revealed the surface of the film to be flat, indicating that the film is laterally homogeneous, at least, down to a length scale of a few 10 nm.

Adsorbed amounts were quantified by ellipsometry (Fig 1C; supplementary Fig S3 online). The final film density of 10.0 ± 0.5 pmol FG repeat domains per cm^2 corresponds to a mean distance of 4.4 ± 0.1 nm between neighbouring anchor points. By adjusting the incubation time for FG repeat domains,

©2010 EUROPEAN MOLECULAR BIOLOGY ORGANIZATION

lower and higher anchor densities could be achieved readily (data not shown). With each FG repeat domain of Nsp1p containing 36 FG repeat units, the surface density corresponds to an average concentration of 106 ± 18 mM FG repeat units inside the film. For comparison, we expect a similar repeat density in yeast NPC, when assuming that its approximately 3,500 FG repeat units (Strawn *et al*, 2004) fill a volume that extends slightly beyond the boundaries of the pore channel, covering a total distance of about 50 nm along the channel axis. The FG repeat concentration is also comparable to macroscopic, *in vitro*-assembled FG repeat hydrogels that were shown recently to exhibit a selectivity of transport similar to that of intact NPCs (Frey & Görlich, 2007, 2009).

Binding of NTRs to FG repeat-domain films

Having established that our model films match the thickness, the FG repeat concentration and the 'end on' mode of chain attachment that are pertinent to NPCs, we considered how NTRs interact with such FG repeat meshworks. Ellipsometric assays (Fig 2A) with a selected NTR, importin-β from *Saccharomyces cerevisiae* (scImpβ/Kap95p), revealed binding in a concentration-dependent manner. The titration data (Fig 2D) could not be fitted well by a single Langmuir isotherm (data not shown), indicating that the film contains more than one type of binding site. The simplest model providing a good fit was a two-component Langmuir isotherm (Fig 2D), with apparent dissociation constants of $K_D^{(1)} = 0.32\,\mu M$ and $K_D^{(2)} = 5.3\,\mu M$ (Table 1). One might be tempted to attribute these dissociation constants to two discrete types of binding site. Our findings are, however, also consistent with the presence of a spectrum of binding sites that cover a range of affinities. We note that the lower dissociation constant is remarkably similar to those reported previously for the interaction of scImpβ (Pyhtila & Rexach, 2003) or mammalian Impβ (Ben-Efraim & Gerace, 2001) with FG Nups from the central region of the NPC. It should also be noted that the dissociation constants are unlikely to reflect the binding strength between NTRs and individual FG repeat units. Rather, they are the result of multivalent interactions.

Assuming independent binding sites, the two-component Langmuir isotherm predicts a saturation limit of 4.0 ± 0.4 pmol/cm^2, which is 2.5-fold less than the concentration of FG repeat domains, or about 90-fold less than the concentration of FG repeat units in the film. Given that Impβ has about nine binding sites for FG repeat units (Isgro & Schulten, 2005), this number suggests that the binding capacity of the film for NTRs is not limited by the concentration of FG motifs. We propose that volume exclusion and entropic effects are the limiting parameters.

Our experimental approach also enabled—for the first time, to the best of our knowledge—the quantification of the effect of Gsp1p•GTP, the yeast homologue of RanGTP, and cargo on NTR binding close to equilibrium (Fig 2; Table 1). Titration data for scImpβ•Gsp1p•GTP could be fitted well by using a simple Langmuir isotherm, and revealed a tenfold-increased dissociation constant as compared with $K_D^{(1)}$ for scImpβ alone, in qualitative agreement with earlier studies on various FG Nups (Allen *et al*, 2001; Ben-Efraim & Gerace, 2001). By contrast, binding was enhanced 3–5-fold when scImpβ was in complex with a model cargo, a fusion protein made of a nuclear import signal and monomeric enhanced green fluorescent protein (importin-β-binding domain (amino acids 2–63) of yeast Srp1p–mEGFP; schImpβ•IBB–mEGFP). We suggest that an allosteric mechanism enhances the docking of the cargo complex to FG repeats, and thereby counteracts the repulsion of large cargoes by the permeability barrier (Ribbeck & Görlich, 2002).

The binding of NTR was fast and fully reversible, except for scImpβ•Gsp1p•GTP, for which a minor fraction (<20%) remained bound after rinsing. The latter might reflect some tendency of the complex to precipitate at the high concentrations reached in the FG repeat film, and as a result, the determined affinity might represent a slight overestimate. The relaxation times for reaching binding equilibria were similar to the resolution of our experimental setup, which provides a lower bound of 0.1/s for the off-rates (Fig 2A–C; Table 1). Off-rates of the same order of magnitude have already been reported (Rabut *et al*, 2004). We note that the intrinsic off-rates could be considerably higher, as mass transport to and from the surface is likely to limit the binding reaction (supplementary information online). Control experiments with an inert probe (maltose-binding protein–mCherry) on FG repeat films and with scImpβ on both FG repeat-free SLBs and films of FG/FxFG repeat domains, in which all phenylalanines in the FG context have been replaced by serines, confirmed that the assays are specific for the interaction of NTRs with the film (supplementary Figs S6–S8 online).

NTRs can permeate FG repeat-domain films

To test whether the NTR can travel across FG repeat-domain films, we doped SLBs with an additional functionality of 2% biotinylated lipids and immobilized a submonolayer (~1.4 pmol/cm^2) of avidin on the SLB (Bingen *et al*, 2008) before forming an FG repeat film (Fig 3). The film was affected only marginally by the presence of avidin: the FG repeat mass was reduced by less than 5% (data not shown) and non-biotinylated scImpβ bound in similar amounts (Fig 3B). Noticeably, biotinylated scImpβ showed increased binding, with saturation levels reached at similar times. The additional fraction of biotinylated NTR, about 0.5 pmol/cm^2, remained irreversibly bound, presumably by docking to the surface-immobilized avidin. These observations provide evidence that scImpβ could not only bind to but also efficiently permeate the FG repeat film.

Effect of NTR influx on the morphology of FG repeat films

The NTR-induced structural changes in FG repeats have been suggested to explain the transport selectivity of NTRs (Lim *et al*, 2007; Peters, 2009), and we sought to characterize the effect of scImpβ influx on the morphology of the FG repeat film by AFM. Controlled indentation of FG repeat films with a nanoscopic probe (Fig 4A) revealed a repulsive interaction over a range of 30–40 nm, in agreement with the film thickness inferred from QCM-D. Interestingly, the presence of 1 μM scImpβ in solution, or about 0.5 mM in the film, did not significantly change the onset of repulsion and the shape of the force–distance curve (Fig 4A), indicating that scImpβ does not markedly affect the thickness and mechanical properties of the film. This finding was corroborated by supplementary QCM-D measurements covering a large range of NTR solution concentrations (Fig 4B). The QCM-D data are consistent with a minor increase in the thickness of the film, by a few nanometres, and a moderate increase in its rigidity

©2010 EUROPEAN MOLECULAR BIOLOGY ORGANIZATION

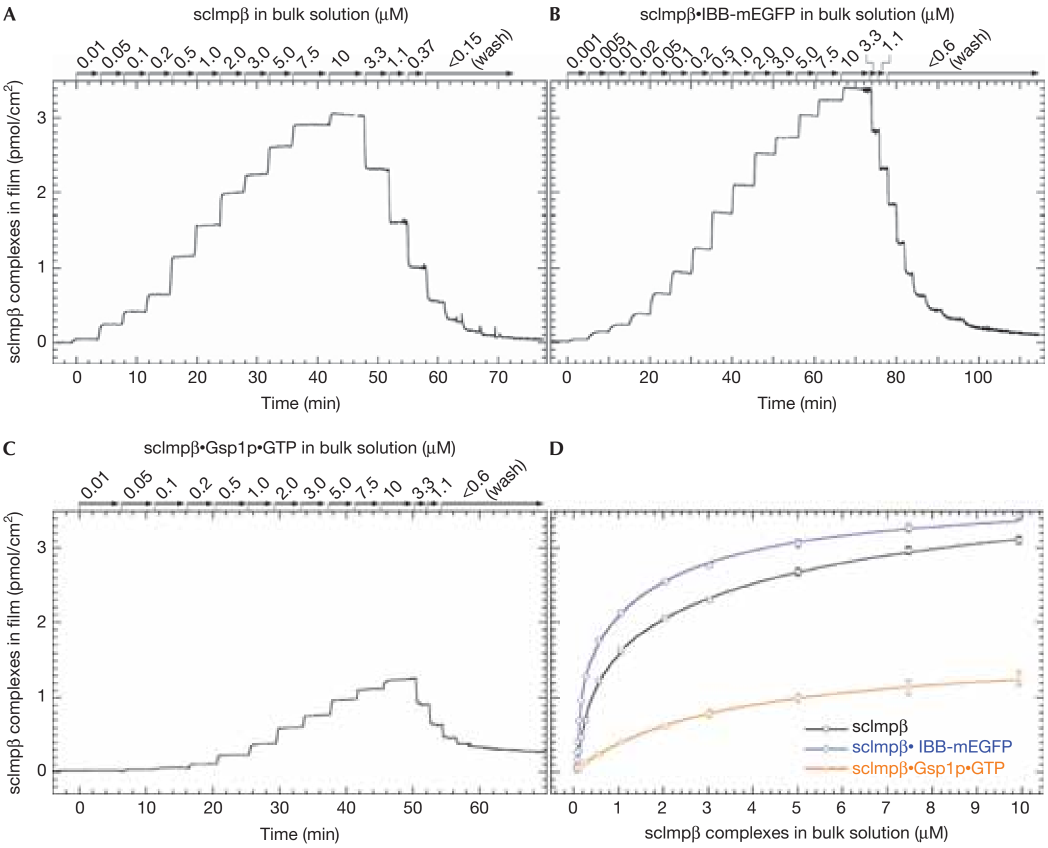

Fig 2 | Interaction of a nuclear transport receptor with phenylalanine–glycine repeat-domain films. Titration curves, determined by ellipsometry, for the binding of (**A**) free scImpβ, (**B**) scImpβ•IBB–mEGFP and (**C**) scImpβ•Gsp1p•GTP (in the presence of 100 μM excess GTP) to FG repeat films. (**D**) Absorbed amounts of scImpβ and its complexes at the equilibrium, with fits (solid lines) by single (scImpβ•Gsp1p•GTP) or two-component Langmuir isotherms (scImpβ, scImpβ•IBB–mEGFP). FG, phenylalanine–glycine; mEGFP, monomeric enhanced green fluorescent protein.

Table 1 | Binding parameters for the interaction of scImpβ and its complexes with phenylalanine–glycine repeat films

	$K_D^{(1)}$ (μM)	$K_D^{(2)}$ (μM)	$\Gamma_{max}^{(1)}$ (pmol/cm²)	$\Gamma_{max}^{(2)}$ (pmol/cm²)	Γ_{max}^{total} (pmol/cm²)	PC (10³)	k_{off} (per s)
scImpβ	0.32 ± 0.04	5.3 ± 1.7	1.6 ± 0.2	2.4 ± 0.2	4.0 ± 0.4	1.5 ± 0.6	> 0.1
scImpβ•IBB–mEGFP	0.057 ± 0.004	1.8 ± 0.2	1.29 ± 0.06	2.40 ± 0.06	3.69 ± 0.12	6.7 ± 1.6	> 0.1
scImpβ•Gsp1p•GTP	3.5 ± 0.5	—	1.63 ± 0.13	—	1.63 ± 0.13	0.14 ± 0.05	> 0.1

mEGFP, monomeric enhanced green fluorescent protein; PC, partition coefficient.

(supplementary Table S2 online). Importantly, they firmly exclude a collapse of the film.

Implications for permeability barrier function

Binding of scImpβ considerably increases the total protein mass of the film. At 10 μM scImpβ level in solution, which approximates the total cellular NTR concentration (U. Jäkle and D.G., unpublished observations), the mass increases by about 45%. It might at first seem surprising that such a massive influx barely affects the thickness of the film. Our finding can be rationalized, however, by simple arguments related to the physical behaviour of flexible polymers that are either crosslinked transiently or are entangled (polymer meshworks). With an approximate 100 mM FG repeat density, the FG repeat film contains on average about 12 FG repeat units within a volume that is occupied by a single scImpβ molecule. By contrast, not more than nine FG-binding sites have so far been suggested for mammalian Impβ (Isgro & Schulten, 2005). The NTR would thus find enough FG repeat units in the volume it displaces to saturate its binding sites. Recruitment of FG repeats from a distance is therefore not required, and a

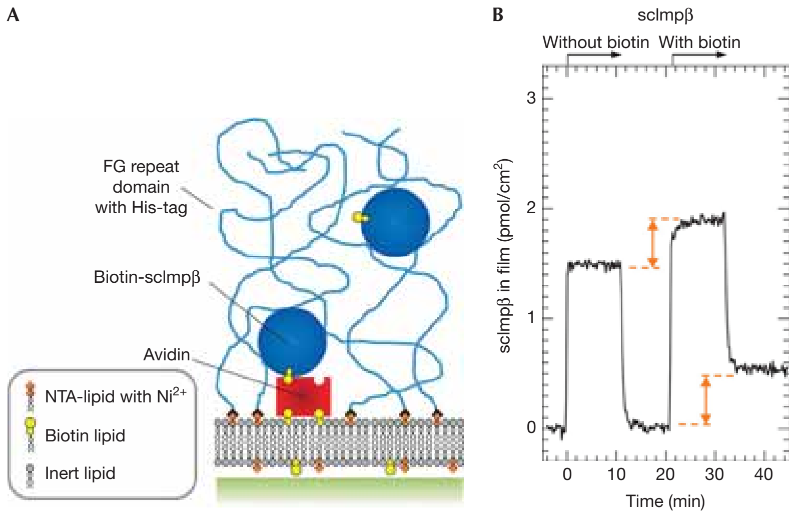

Fig 3 | Nuclear transport receptors can permeate phenylalanine–glycine repeat-domain films. (**A**) To assay permeation, SLBs were doped with an additional functionality of 2 mol% biotinylated lipids, and a submonolayer of avidin (1.4 pmol/cm^2) was immobilized on the SLB before the FG repeat-domain film was formed (data not shown). The size of the globular proteins (also see supplementary Fig S10 online) and the thickness of the SLB and the FG repeat film are drawn to scale. (**B**) Binding assay by ellipsometry: adsorption of 1 μM tag-free scImpβ was fully reversible and similar in magnitude as in Fig 2. The same concentration of biotin-tagged scImpβ exhibited significantly enhanced binding. The additional binding (indicated in orange) was irreversible. FG, phenylalanine–glycine; NTA, nitrilotriacetic acid; SLB, supported lipid bilayer.

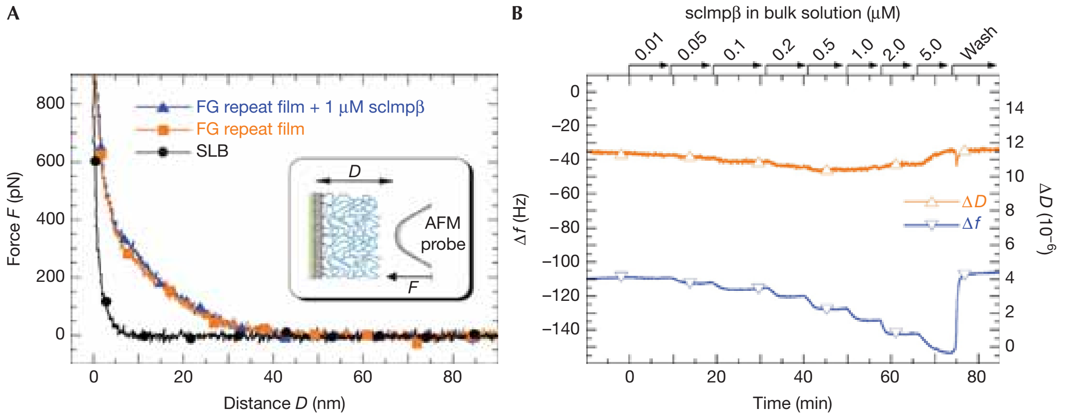

Fig 4 | Nuclear transport receptors moderately increase the thickness and rigidity of dense phenylalanine–glycine repeat films. (**A**) AFM indentation assay on FG repeat-domain films (schematic inset). Repulsive forces were detectable on FG repeat-domain films up to distances of 30–40 nm from the hard-wall compression limit. The onset of repulsion and the shape of the force–distance curve did not change significantly in the presence of 1 μM scImpβ in the solution. Controls on SLB-covered silica before and after the indentation assay demonstrate that the interaction of these surfaces with the AFM probe remained rather short-ranged (around 6 nm). (**B**) The titration curve, measured by quartz crystal microbalance with dissipation monitoring, provides information about the changes in the mechanical properties of the film on scImpβ binding. Changes in dissipation were small (<10% of the FG repeat film), whereas the changes in frequency were considerable (~45% at 5 μM). These data are consistent with a minor increase in the thickness of the film and a moderate increase in its rigidity, but exclude a collapse of the film (supplementary Table S2 online). AFM, atomic force microscopy; FG, phenylalanine–glycine; SLB, supported lipid bilayer.

collapse of the film is unlikely. At the same time, the inclusion of scImpβ would require some FG repeat chains to be displaced from the volume that it occupies. The concomitant increase in film thickness would at most correspond to the total added protein volume. Using a molecular volume of scImpβ of 200 nm^3 and a surface density of 3.1 pmol/cm^2, this thickness increase amounts to approximately 4 nm. Film swelling would hence be moderate at best, consistent with our experiments.

This simple consideration of the physical behaviour of polymer meshworks has two notable implications. First, as it is not based on any details of the molecular structure of scImpβ, it is likely to apply to many, if not all, NTRs. Second, it predicts that on entering an FG repeat meshwork, NTRs would affect only their immediate environment, whereas more distant meshwork regions would remain unaffected. We suggest that such a separation of local and global morphology is important for the selectivity of the permeability barrier of the NPC. It allows two apparently contradictory functions to be accomplished simultaneously: local interactions between the NTR and FG repeats promote efficient translocation, while the rest of the permeability barrier remains unaffected and can continuously block inert molecules of similar size. This conjecture is consistent with both the 'virtual gating' and the 'selective phase' models.

The data obtained in our experimental setup, however, contrast with those described by Lim *et al* (2007), who reported a more than twofold decrease in thickness, from 30 nm down to 13 nm, on incubation of nanoscale islands of FG repeat meshworks with mammalian Impβ. On the basis of the argumentation above, such a collapse would only be plausible if the number of FG repeats available in the immediate environment of an approaching NTR is too small to saturate all of its FG repeat binding sites and if the interaction between NTR and FG repeats is sufficiently strong. Indeed, Lim *et al* (2007) used Nup153, a nucleoporin that is located in the nucleoplasmic region of the NPC and that exhibits an affinity for mammalian Impβ, which is at least one order of magnitude higher (Ben-Efraim & Gerace, 2001; Bednenko *et al*, 2003) than what is encountered typically for nucleoporins in the central region. Furthermore, estimates provided by Lim *et al* (2006) suggest that the density of FG repeat domains on the nanoscale islands was 5–30 times lower than in our study. We note that Lim *et al* (2007) found considerable collapse at a bulk concentration of 0.1 pM Impβ, several orders of magnitude below the affinity of Nup153 for Impβ (~10 nM) and the total cellular NTR concentration (~10 μM). The discrepancy could be explained by direct binding of Impβ to the nanoscale gold islands to which the terminal cysteines of Nup153 FG repeat domains had been bonded. In such a case, it would not be surprising that the FG repeat domains appear collapsed while bound to surface-immobilized receptor molecules. This interpretation is supported by the fact that Impβ contains 23 cysteines and that excess binding sites on the gold islands had not been quenched in that study.

On the basis of our experimental findings and the average density of FG repeats in the NPC, we conclude that a 'nanomechanical collapse' is unlikely to occur in the central region of the NPC. Its noteworthy that the density of FG repeats is not homogeneous but might tend to decrease towards the peripheral regions of the NPC. Thus, at present, we cannot exclude the possibility that NTRs might affect the morphology of FG repeat domains at the boundary of the NPC. We stress that our data, and considerations of the behaviour of polymer meshworks, suggest that efficient entry, permeation and exit of NTRs can be accomplished without invoking any specific structures and pathways, such as a narrow tube along the axis of the NPC or channel walls, as required in some of the existing transport models (Macara, 2001; Peters, 2009).

Conclusions and Perspectives

Despite their simplicity in concept and composition, our model films provided hitherto inaccessible insight into the structure–function interrelationship of FG repeat-rich nucleoporin assemblies. Their two-dimensional extension made the FG repeat films accessible to label-free and quantitative analysis by a toolbox of surface-sensitive biophysical methods. We observed that scImpβ can efficiently enter, permeate and leave FG repeat films, and quantified the impact of cargo and Gsp1p•GTP on binding. Correlation of the binding of NTRs with concomitant changes in the swelling behaviour and mechanical properties of the FG repeat films revealed that the presence of scImpβ does not affect the global morphology of the FG repeat assemblies. This finding can be explained plausibly if we assume that the FG repeat domains form a dense meshwork, either cross-linked transiently or entangled, as postulated by the 'selective phase' model.

Our methodological approach can easily be extended to other FG repeats, or mixtures of them, and thus provides a simple tool for the screening of interactions with NTRs in a relevant and well-controlled nano-environment. Future studies will aim, in particular, at understanding the role of inter-FG repeat interactions in selective transport and at elucidating the parameters that govern the exclusion of inert or weakly interacting molecules from translocation.

METHODS

See the supplementary information online for materials, expression and purification of proteins, substrate preparation, the details of the implementation of QCM-D, ellipsometry, AFM indentation assays and imaging.

QCM-D. QCM-D measures the changes in the resonance frequency, Δf, and dissipation, ΔD, of a sensor crystal on interaction of soft matter with its surface. The QCM-D response is sensitive to the mass (including coupled water) and the mechanical properties of the surface-bound layer. Adsorption and interfacial processes were monitored *in situ* with sub-second time resolution, under continuous flow of sample solution. The thickness of FG repeat-domain monolayers was estimated by numerical fitting of the QCM-D data to a viscoelastic model.

Ellipsometry. Ellipsometry estimates the changes in the ellipsometric angles, Δ and ψ, of polarized light on reflection at a planar surface. We used ellipsometry *in situ*, using silicon wafers as substrates that were installed in an open cuvette with continuously stirred sample solution, to quantify adsorbed/absorbed masses in a time-resolved manner. Samples were injected directly into the cuvette and excess sample was removed by repeatedly diluting the cuvette content in buffer. Bound masses were determined by numerical fitting of the ellipsometric data.

Nanoindentation assays by AFM. Force–displacement curves were acquired by using Si_3N_4 probes with a nominal apex radius below 10 nm. The SLBs and FG repeat films were prepared on silicon wafers and probed in buffer with maximal loads of 1 nN.

Supplementary information is available at *EMBO reports* online (http://www.emboreports.org).

ACKNOWLEDGEMENTS
This study was supported financially by funds from the Department of Industry of the Basque Government (to N.E. and R.P.R.), the Max Planck Society, and Deutscher Akademischer Austausch Dienst (to N.E.).

CONFLICT OF INTEREST

The authors declare that they have no conflict of interest.

REFERENCES

Allen NPC, Huang L, Burlingame A, Rexach M (2001) Proteomic analysis of nucleoporin interacting proteins. *J Biol Chem* **276:** 29268–29274

Bednenko J, Cingolani G, Gerace L (2003) Importin-β contains a COOH-terminal nucleoporin binding region important for nuclear transport. *J Cell Biol* **162:** 391–401

Ben-Efraim I, Gerace L (2001) Gradient of increasing affinity of importin-β for nucleoporins along the pathway of nuclear import. *J Cell Biol* **152:** 411–417

Bingen P, Wang G, Steinmetz NF, Rodahl M, Richter RP (2008) Solvation effects in the QCM-D response to biomolecular adsorption—a phenomenological approach. *Anal Chem* **80:** 8880–8890

Denning DP, Patel SS, Uversky V, Fink AL, Rexach M (2003) Disorder in the nuclear pore complex: the FG repeat regions of nucleoporins are natively unfolded. *Proc Natl Acad Sci USA* **100:** 2450–2455

Frey S, Görlich D (2007) A saturated FG-repeat hydrogel can reproduce the permeability properties of nuclear pore complexes. *Cell* **130:** 512–523

Frey S, Görlich D (2009) FG/FxFG as well as GLFG repeats form a selective permeability barrier with self-healing properties. *EMBO J* **28:** 2554–2567

Isgro TA, Schulten K (2005) Binding dynamics of isolated nucleoporin repeat regions to importin-β. *Structure* **13:** 1869–1879

Lata S, Gavutis M, Piehler J (2006) Monitoring the dynamics of ligand–receptor complexes on model membranes. *J Am Chem Soc* **128:** 6–7

Lim RYH, Huang N-P, Köser J, Deng J, Lau KHA, Schwarz-Herion K, Fahrenkrog B, Aebi U (2006) Flexible phenylalanine–glycine nucleoporins as entropic barriers to nucleocytoplasmic transport. *Proc Natl Acad Sci USA* **103:** 9512–9517

Lim RY, Fahrenkrog B, Koser J, Schwarz-Herion K, Deng J, Aebi U (2007) Nanomechanical basis of selective gating by the nuclear pore complex. *Science* **318:** 640–643

Macara IG (2001) Transport into and out of the nucleus. *Microbiol Mol Biol Rev* **65:** 570–594

Mohr D, Frey S, Fischer T, Güttler T, Görlich D (2009) Characterisation of the passive permeability barrier of nuclear pore complexes. *EMBO J* **28:** 2541–2553

Peters R (2005) Translocation through the nuclear pore complex: selectivity and speed by reduction-of-dimensionality. *Traffic* **6:** 421–427

Peters R (2009) Translocation through the nuclear pore: Kaps pave the way. *Bioessays* **31:** 466–477

Pyhtila B, Rexach M (2003) A gradient of affinity for the karyopherin Kap95p along the yeast nuclear pore complex. *J Biol Chem* **278:** 42699–42709

Rabut G, Doye V, Ellenberg J (2004) Mapping the dynamic organization of the nuclear pore complex inside single living cells. *Nat Cell Biol* **6:** 1114–1121

Ribbeck K, Görlich D (2001) Kinetic analysis of translocation through nuclear pore complexes. *EMBO J* **20:** 1320–1330

Ribbeck K, Görlich D (2002) The permeability barrier of nuclear pore complexes appears to operate via hydrophobic exclusion. *EMBO J* **21:** 2664–2671

Richter RP, Bérat R, Brisson AR (2006) The formation of solid-supported lipid bilayers—an integrated view. *Langmuir* **22:** 3497–3505

Rout MP, Aitchison JD, Magnasco MO, Chait BT (2003) Virtual gating and nuclear transport: the hole picture. *Trends Cell Biol* **13:** 622–628

Strawn LA, Shen T, Shulga N, Goldfarb DS, Wente SR (2004) Minimal nuclear pore complexes define FG repeat domains essential for transport. *Nat Cell Biol* **6:** 197–206

Yang Q, Rout MP, Akey CW (1998) Three-dimensional architecture of the isolated yeast nuclear pore complex: functional and evolutionary implications. *Mol Cell* **1:** 223–234

SOME RIGHTS RESERVED **_EMBO reports_ is published by Nature Publishing Group on behalf of European Molecular Biology Organization. This article is licensed under a Creative Commons Attribution-Noncommercial-Share Alike 3.0 License. [http://creativecommons.org/licenses/by-nc-sa/3.0/]**

Supplementary Information

Ultrathin nucleoporin FG repeat films and their interaction with nuclear transport receptors

Nico B. Eisele,[1,2] *Steffen Frey,*[2] *Jacob Piehler,*[3] *Dirk Görlich,*[2] *and Ralf P. Richter* [1,4]*

[1] Biosurfaces Unit, CIC biomaGUNE, Paseo Miramon 182, 20009 Donostia - San Sebastian, Spain

[2] Department of Cellular Logistics, Max Planck Institute for Biophysical Chemistry, Am Fassberg 11, 37077 Göttingen, Germany

[3] Department of Biology, University of Osnabrück, Barbarastraße 11, 49076 Osnabrück, Germany

[4] Max Planck Institute for Metals Research, Heisenbergstraße 3, 70569 Stuttgart, Germany

*Corresponding author. E-mail: rrichter@cicbiomagune.es. Phone: +34 943 00 5329. Fax: +34 943 00 5315

Materials and Methods

Buffer: A buffer solution of 150 mM NaCl, and 10 mM HEPES, pH 7.4, in ultrapure water was used to prepare lipid vesicles, to dilute protein stock solutions, and in all experiments reported. 5 to 25 mM $NiCl_2$ were added for the incubation step leading to the formation of a supported lipid bilayer.

Preparation of lipids and lipid vesicles: Lyophilised dioleoylphosphatidylcholine (DOPC) and dioleoylphospatidylethanolamine-CAP-biotin (DOPE-CAP-Biotin) were purchased from Avanti Polar Lipids (Alabaster, AL, USA). A lipid analogue based on a chelator headgroup comprising two nitrilotriacetic acid moieties (bis-NTA) was prepared as described earlier (Lata et al, 2006). The divalent presentation of NTA improves the binding stability of histidine-tagged proteins, with dissociation constants in the lower nM range (Lata et al, 2005).

Lipids were mixed in chloroform, dried, re-suspended in buffer and homogenised as described earlier (Richter et al, 2003). Small unilamellar vesicles (SUVs) were obtained by sonication (30 min) with a tip sonicator (Branson, USA), operated in pulsed mode at 30% duty cycle with refrigeration, followed by centrifugation in an Eppendorf centrifuge (10 min at 14,000 *g*) to remove titanium particles. SUV suspensions were stored at 4ºC under nitrogen. Concentrations and mixing ratios were estimated from the dry masses of employed lipid material. Before use vesicle suspensions were diluted to 50 µg/ml.

E. coli expression vectors: Plasmids allowed for recombinant expression of indicated proteins in *E. coli*. Complete plasmid sequences are available on request (Table S1).

Table S1: E.coli expression vectors.[a)]

Name	protein name	expressed protein	resistance conferred by plasmid	Reference
pSF345	$\text{Nsp1}^{2\text{-}601}$	$\text{His}_{10}\text{-TEV-Nsp1}^{2\text{-}601}\text{-Cys}$	Ampicillin	(Frey et al, 2006)
pSF362	$\text{Nsp1}^{2\text{-}601}(\text{F}\rightarrow\text{S})$	$\text{His}_{10}\text{-TEV-Nsp1}^{2\text{-}601}(\text{F}\rightarrow\text{S})\text{-Cys}$	Ampicillin	(Frey et al, 2006)
pSF1106	PrA-TEV-scImpβ	ProteinA-TEV-scImpβ	Kanamycin	this study
pSF970	Bio-scImpβ	His_{14}-TEV-Bio-scImpβ	Kanamycin	this study
pSF966	MBP-TEV-BirA	MBP-TEV-BirA	Spectinomycin	this study
pSF844	MBP-mCherry	His_{14}-TEV-MBP-mCherry	Kanamycin	(Frey & Görlich, 2009)
pSF807	IBB-mEGFP	His_{14}-TEV-IBB-mEGFP-Cys	Kanamycin	this study
pSF814	Gsp1p (yeast Ran)	His_{14}-TEV-Gsp1p	Kanamycin	this study
pSF815	Prp20p (yeast RCC1)	His_{14}-TEV-Prp20p	Kanamycin	this study
pSF488	His_{10}-GFP-MBP	His_{10}-GFP-MBP-Cys	Ampicillin	this study

[a)] Abbreviations: His_{10}/ His_{14}, histidine tag; TEV, TEV-protease recognition site; PrA, ProteinA; Bio, AviTag (GLNDIFEAQKIEWHE; (Schatz, 1993)); IBB, importin β-binding domain (corresponding to amino acids 2-63 of *S. cerevisiae* Srp1p).

Expression and purification of proteins: To produce His_{10}-tagged Nsp1 FG/FxFG repeat domain ($M_w = 64.6$ kDa) or its F→S mutant (61.3 kDa), *E. coli* transformed with pSF345 or pSF362, respectively, was grown at 37°C to $OD_{600} = 2.0$ in TB medium supplemented with 200 µg/ml ampicillin. The culture was cooled down to 25°C, induced with 1 mM IPTG, and further incubated for 3 h. Before cell harvest, 1 mM PMSF (phenylmethylsulfonyl fluoride) and 5 mM EDTA were added directly to the culture. Cells were resuspended in 8.3 M guanidinium-hydrochloride (Gua-HCl) containing 2 mM EDTA and 20 mM DTT and lysed by a single round of freezing and thawing. After centrifugation for 60 min at 38000 rpm, the cleared lysate was supplemented with 100 mM Tris/HCl (pH 8.5) and 1 mM imidazole and applied to a nickel-chelate column. The column was washed with 7.5 Gua-HCl, 100 mM Tris/HCl (pH 8.5), 1 mM EDTA, 1 mM imidazole followed by a second wash step with 6 M Gua-HCl, 20 mM Tris/HCl (pH 8.0), 1 mM EDTA, 1 mM imidazole. Bound protein was eluted with 4.5 M Gua-HCl, 15 mM Tris/HCl (pH 8.0), 1 mM EDTA, 500 mM imidazole and applied to a thiopyridine-activated, SH-reactive matrix. The matrix was washed with 6 M Gua-HCl, 20 mM Tris/HCl (pH 8.0), 1 mM EDTA, 1 mM imidazole followed by a second washing step with deionised water. Proteins were eluted with 6 M Gua-HCl, 20 mM Tris/HCl (pH 7.5), 1 mM iminodiacetic acid, 10 mM DTT, applied to a preparative C18 reverse phase HPLC column, eluted with increasing concentrations of acetonitrile in 0.15 % TFA, and lyophilised. Pure proteins were dissolved in 6 M Gua-HCl, 1 mM iminodiacetic acid, 10 mM acetic adic, 5 mM sodium acetate at 460 µM (WT) and 320 µM (F→S mutant), respectively.

To produce the respective untagged proteins, the eluates from the SH-reactive matrix were transferred into 2 M urea, 50 mM Tris/HCl (pH 7.5), 2 mM EDTA, 5 mM DTT, and the His_{10}-tag was cleaved off using his-tagged TEV-protease. TEV-protease, the tag and remaining non-cut proteins were separated from the pure repeat domain by two successive passages over a nickel-chelate column. The flow-through was adjusted to 6 M Gua-HCl and applied to RP-HPLC as described before.

To produce untagged scImpβ (95.2 kDa), *E. coli* strain BLR transformed with pSF1106 was grown at 25°C to $OD_{600} = 1.0$ in TB medium supplemented with 50 µg/ml kanamycin. The culture was cooled down to 18°C, induced with 0.5 mM IPTG, and further incubated over night. Before cell harvest, 1 mM PMSF (phenylmethylsulfonyl fluoride) and 5 mM EDTA were added directly to the culture. Cells were resuspended in buffer HS (2 M NaCl, 50 mM Tris-HCl (pH 8.0), 5 mM $MgCl_2$, 1 mM imidazole, 0.5 mM EDTA, 10 mM DTT) and lysed by sonication. After centrifugation for 60 min at 37000 rpm, the cleared lysate was applied to IgG sepharose (GE healthcare). After extensively washing with buffer HS and buffer A (44 mM Tris-HCl (pH 7.5), 290 mM NaCl, 4.4 mM $MgCl_2$, 0.44 mM EDTA, 10 mM β-ME), bound protein was eluted by incubation with TEV protease, concentrated and further purified by gel filtration on a Superdex200 column (GE Healthcare) equilibrated with buffer A. To remove trace amounts of residual TEV protease, the peak fractions were pooled and passed through a nickel-sepharose column. The final protein preparation was supplemented with 1/9 volume 2.5 M sucrose, concentrated to 100 µM and frozen in liquid nitrogen.

To produce biotinylated scImpβ (97.3 kDa), plasmids encoding His_{14}-TEV-Bio-scImpβ and MBP-TEV-BirA were co-transformed in *E.coli* strain BLR. The cells were grown in TB medium supplemented with 50 µg/ml kanamycin, 50 µg/ml spectinomycin and 20 µg/ml biotin at 25°C. At $OD_{600} = 0.4$, the cultures were induced with 0.2 mM IPTG and the temperature was shifted to 20°C for 15 hours. Before harvesting the cells, 1 mM PMSF and 5 mM EDTA were added to the culture. After centrifugation and resuspension of the cell pellet in buffer HS, cells were disrupted by sonication and the lysate was cleared by centrifugation at 37000 rpm for 60 min. Cleared lysates were applied to a nickel-sepharose column equilibrated with buffer HS. After washing off unbound proteins with buffer HS followed by buffer A, proteins were eluted with buffer A supplemented with 300 mM imidazole. The his-tag was cut off with TEV protease (1:50 enzyme to substrate ratio) at room temperature. Cut proteins were further purified by gel filtration on a Superdex200 16/60 column (Pharmacia) equilibrated with buffer A followed by a second passage over nickel-sepharose. The purified protein was supplemented with 1/9 volume 2.5 M sucrose, concentrated to 100 µM and frozen in liquid nitrogen.

Expression of MBP-mCherry (67.3 kDa) was described previously (Frey & Görlich, 2009). Purification was performed as described above for biotinylated scImpβ. The stock solution had a concentration of 100 µM. IBB-mEGFP, Gsp1p and Prp20p were expressed and purified following the identical protocol.

Expression and purification of His_{10}-GFP-MBP (69.1 kDa) was performed analogous to MBP-mCherry, however, the cleavage with TEV-protease and the second passage over the nickel-sepharose column were omitted.

The scImpβ•IBB-mEGFP complex (129.6 kDa) was pre-formed using an 1.5-fold excess of IBB-mEGFP over scImpβ and purified by gel filtration on a Superdex200 16/60 column equilibrated with buffer A. The complex was concentrated, supplemented with 1/9 volume of 2.5 M sucrose and frozen in liquid nitrogen. The stock had a concentration of 100 µM.

The scImpβ•Gsp1p•GTP (120.3 kDa) complex was formed by incubating a mixture of 45 µM Gsp1p, 20 µM scImpβ, 2 µM Prp20p, 0.4 µM pyruvate kinase, 0.5 mM GTP and 10 mM phosphoenolpyruvate in buffer A for 1.5 h at room temperature. The complex was purified by gel filtration on a Superdex200 16/60 column equilibrated with buffer A, followed by a passage over a nickel-sepharose column to remove trace amounts of his-tagged proteins. The complex was concentrated, supplemented with 1/9 volume of 2.5 M sucrose and frozen in liquid nitrogen. The stock had a concentration of 100 µM.

Lyophilised avidin (Av, 66 kDa) was purchased from Sigma, and reconstituted in ultrapure water to a concentration of approximately 15 µM, as described by the manufacturer. Before use the solution was diluted to about 0.05 µM.

Substrate preparation: Silica-coated QCM-D sensors (QSX303, Q-Sense, Gothenburg, Sweden) and silicon wafers with a native oxide layer of less than 2 nm thickness (University Wafers, South Boston, MA, USA) were cleaned by immersion in a 2% sodium dodecyl sulfate solution for 30 min, rinsing with ultrapure water, blow-drying with nitrogen, and exposure to UV/ozone (BioForce Nanosciences, Ames, IA, USA) for 30 min. Cleaned substrates were stored in air and again exposed to UV/ozone (30 min) prior to use.

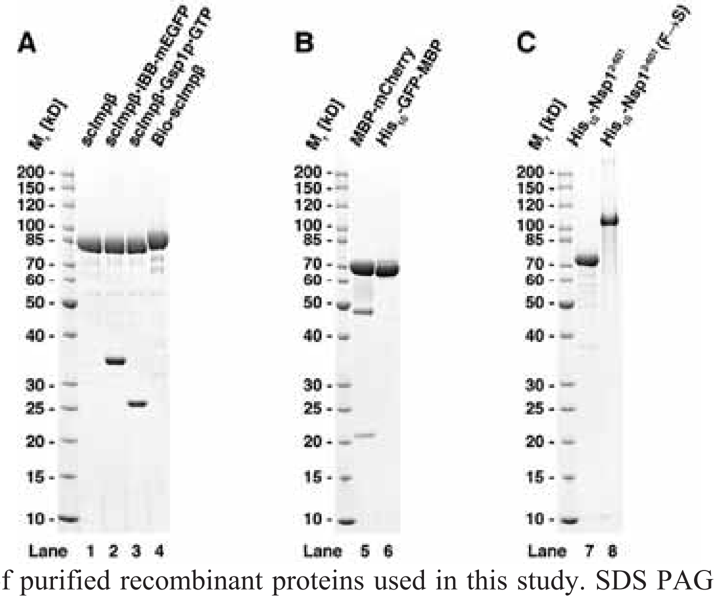

Figure S1: Quality of purified recombinant proteins used in this study. SDS PAGE of scImpβ, scImpβ complexes and biotinylated scImpβ (A), MBP fusion proteins (B) and His_{10}-tagged Nsp1 repeat domains (C). All preparations contain more than 90% full length protein. Major bands at 35 kD in lane 2 and 26 kD in lane 3 correspond to IBB-mEGFP or Gsp1p, respectively, which stoichiometrically associate with scImpβ. Minor bands at 48 kD and 21 kD in lane 5 are indicative for a specific backbone break observed during maturation of the mCherry fluorophore. This break does not influence the integrity of the MBP-mCherry fusion or its Stokes radius as judged from size exclusion chromatography.

Quartz crystal microbalance with dissipation monitoring

QCM-D measures changes in resonance frequency, Δf, and dissipation, ΔD, of a sensor crystal upon interaction of (soft) matter with its surface. The QCM-D response is sensitive to the mass (including coupled water) and the mechanical properties of the surface-bound layer. Adsorption and interfacial processes were monitored *in situ* with sub-second time resolution.

QCM-D measurements were performed with a Q-Sense E4 system (Q-Sense AB, Västra Frölunda, Sweden). The system was operated in flow mode with a rate of typically 20 µl/min, using a syringe pump (KD Scientific, Holliston, MA, USA). The working temperature was 23°C. Δf and ΔD were measured at 6 overtones ($n = 3, 5 \ldots 13$, corresponding to resonance frequencies of $f_n \approx 15, 25 \ldots 65$ MHz) simultaneously. Changes in dissipation and normalised frequency, $\Delta f = \Delta f_n / n$, of the fifth overtone are presented.

Quantification of FG repeat film thickness by QCM-D: The thickness of FG repeat monolayers was estimated by fitting the QCM-D data to a viscoelastic model (Domack et al, 1997; Voinova et al, 1999) as implemented in the software QTM (D. Johannsmann, Technical University of Clausthal, Germany). The model relates the measured QCM-D responses, Δf and ΔD as a function of n, to the viscoelastic properties of the adsorbed layer(s) and the surrounding solution. The small load approximation was employed (see (Johannsmann, 2007) for further information). The FG repeat film was represented by a viscoelastic layer with thickness d, density ρ, storage modulus G', and loss modulus G''. The storage modulus is a measure for the elasticity of the film. The loss modulus is related to the film's viscosity, η, by $G'' = 2\pi f \eta$. A material is called elastic (viscous), if $G' >> G''$ ($G' << G''$). If $G' \approx G''$, it is called viscoelastic.

The layer's density was coupled to the thickness via

$$\rho = \rho_{\text{Solution}} + \frac{m_{\text{Protein}}}{d}\left(1 - \frac{\rho_{\text{Solution}}}{\rho_{\text{Protein}}}\right), \qquad \text{(S1)}$$

with ρ_{Protein} and m_{Protein} being the protein density (1.35 g/cm^3) and the protein mass per surface area in the film, respectively. m_{Protein} was estimated by ellipsometry. The viscoelastic properties, G' and G'', were allowed to be frequency dependent, following power laws with exponents α' and α'', respectively. The exponents were allowed to vary within ranges that are physically reasonable for polymer solutions and gels, i.e., $0 \leq \alpha' \leq 2$ and $-1 \leq \alpha'' \leq 1$ (Ferry, 1980). The semi-infinite bulk solution was assumed to be Newtonian with a viscosity of 0.89 mPa·s, and a density of $\rho_{\text{Solution}} = 1.0$ g/cm^3. The SLB exhibited very low dissipation and was therefore treated as a rigid layer ("Sauerbrey layer"). All measured overtones were included in the fitting routine.

For the investigated FG repeat films, a unique fit of good quality was obtained. Fig. S2 displays the best fit to the data in Fig. 1B, and Table S2 (measurement #1) shows the corresponding results. The film thickness of 34 nm was rather well determined, with changes of less than ±15% leading to more than twofold increases in χ^2. All other parameters were also rather well constrained by the QCM-D data (Table S2). The loss modulus of about 100 kPa corresponds to a viscosity of 3.2 mPa·s, which is 3.6-fold the viscosity of water. The storage modulus of 150 kPa is similar to the elasticity of polydimethylsiloxane (PDMS) at medium cross-linker density (Brown et al, 2005). It should be noted that the viscous and/or elastic behaviour of a given material depends on the frequency at which it is deformed (Ferry, 1980). The QCM-D operates at considerably higher frequencies (MHz) than common bulk rheometers (mHz to kHz). The viscoelastic properties reported here may thus differ from those obtained by other methods.

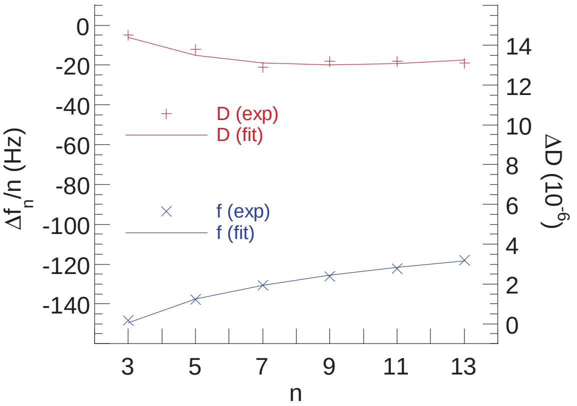

Figure S2: Experimental and fitted QCM-D responses for an FG repeat film. The data correspond to Fig. 1B (at 20 min).

Effect of scImpβ influx on the FG repeat film: The response of FG repeat films to selected bulk concentrations of scImpβ was measured by QCM-D (Fig. 4B). The thickness and viscoelastic properties of the films were quantified with the viscoelastic model, and are displayed in Table S2 (measurement #2). Note that the FG repeat film that was used in the titration assay (measurement #2) was slightly less dense than the film displayed in Fig. 1 (measurement #1), resulting in a slightly lower thickness. Upon addition of scImpβ, the thickness increased weakly, by a few nanometers at most, with increasing scImpβ concentrations. At the same time, the storage and loss moduli increased, by a few 10%, indicating moderate film rigidification. The data in Table S2 illustrate that the pronounced increase in the absolute frequency shift that is observed upon incubation of 5 µM scImpβ (Fig. 4B) stems from a combination of moderate increases in the film's hydrated mass ($d \times \rho$), elasticity (G') and viscosity (expressed in G'').

Table S2: Properties of FG repeat domain films, as determined from fits to the viscoelastic model.

measurement	$c_{\text{scImp}\beta}$ (µM)	d [a)] (nm)	ρ (g/cm^3)	G' [a), b)] (kPa)	α' [a)]	G'' [a), b)] (kPa)	α'' [a)]
#1	-	34±4	1.05±0.01	150±60	0.15±0.15	103±15	0.94±0.03
#2	-	29±4	1.05±0.01	96±50	0.2±0.2	93±20	0.93±0.04
	0.2	30±4	1.06±0.01	82±50	0.2±0.2	103±20	0.93±0.04
	1.0	32±4	1.07±0.01	89±50	0.2±0.2	116±30	0.93±0.04
	5.0	34±4	1.09±0.01	117±50	0.2±0.2	129±30	0.93±0.04

[a)] Errors correspond to the range within which χ^2 does not increase by more than two-fold from the value obtained for the best fit.

[b)] G' and G'' are given at $f = 5$ MHz.

***In situ* ellipsometry**

Ellipsometry measures changes in the ellipsometric angles, Δ and Ψ, of polarised light upon reflection at a planar surface. We employed ellipsometry *in situ*, using silicon wafers as substrates that were installed in an open cuvette with continuously stirred sample solution, to quantify adsorbed/absorbed masses in a time-resolved manner.

Data were acquired with a spectroscopic rotating compensator ellipsometer (M2000V, Woollam, NE, USA), operating in a wavelength range from $\lambda = 380$ to 1000 nm, at 70º angle of incidence and a time resolution of ~5 s, using a custom-designed open glass cuvette at ambient temperature. The cuvette setup was inspired by Corsel et al. (Corsel et al, 1986). Samples were injected directly into the buffer-filled cuvette at desired concentrations, and continuously stirred with a magnetic stirrer (~200 rpm). To remove samples, the cuvette content was diluted, by repeated addition of at least a 2-fold excess of buffer and removal of excess liquid, until the concentration of soluble sample was below 10 ng/ml. The stirrer ensured homogenisation of the cuvette content within a few seconds.

Quantitative evaluation of in situ ellipsometric data: Bound masses were determined by numerical fitting of the ellipsometric data to a multi-layer model. Ellipsometric data were fitted over the accessible wavelength spectrum, using the software CompleteEASE (Wollam, NE, USA). The model relates the measured ellipsometric responses, Δ and Ψ as a function of λ, to the optical properties of the substrate, the adsorbed layer(s) and the surrounding solution.

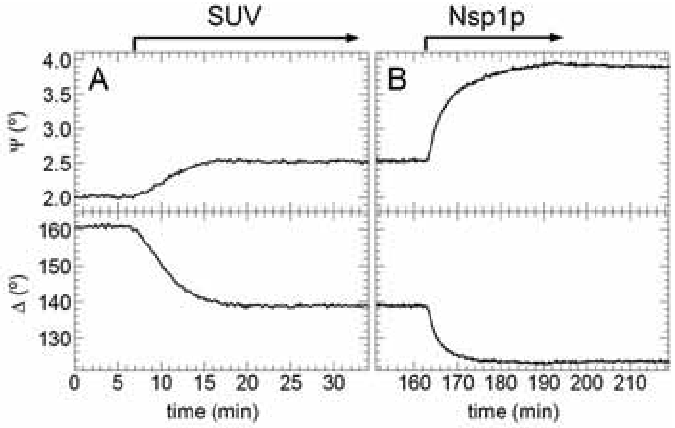

Figure S3: Representative ellipsometric data, Δ and Ψ at $\lambda = 633$ nm, for the formation of a supported lipid bilayer (*A*), and an FG repeat film (*B*).

Calibration: The cuvette was verified to exhibit negligible window effects. To this end, a calibration wafer with a silica overlayer of ~20 nm thickness (Wollam) was employed, as described by the manufacturer. Only cells were used that induced an absolute offset in Δ smaller than 0.5º.

The cleaned silicon wafers were characterised in buffer in the cuvette prior to each *in situ* measurement. The thickness and the optical properties of the silica overlayer were determined, based on a three-layer model (solvent, native silicon oxide, silicon) and tabulated optical constants for silicon (CompleteEASE, Wollam). The native oxide layer was treated as a transparent Cauchy medium, with a refractive index of $n_{\mathrm{oxide}}(\lambda) = A_{\mathrm{oxide}} + B_{\mathrm{oxide}} / (\lambda/\mu\mathrm{m})^2$. The semi-infinite bulk solution was also treated as a transparent Cauchy medium. Its refractive index, $n_{\mathrm{solvent}}(\lambda) = 1.325 + 0.00322 / (\lambda/\mu\mathrm{m})^2$, was calculated from tables in the literature (Daimon & Masumura, 2007; Lide, 2004). The measured thickness of the native oxide layer was found to be 1.9±0.2 nm. Its optical properties were $A_{\mathrm{oxide}} = 1.472 \pm 0.013$ and $B_{\mathrm{oxide}} = 0.020 \pm 0.003$. The χ^2-value for the best fit was typically smaller than 1.4, indicating an excellent fit.

Quantification of adsorbed amounts: To extract the properties of the adsorbed biomolecular layer from the ellipsometric response, a four-layer model (solvent, biomolecular layer, native silicon oxide, silicon) was used. The SLB and the protein film were treated as a single biomolecular layer. We assumed this layer to be transparent and homogeneous (Cauchy medium), with a given thickness, d_{bml}, and a wavelength-dependent refractive index $n_{\mathrm{bml}}(\lambda) = A_{\mathrm{bml}} + B_{\mathrm{bml}} / (\lambda/\mu\mathrm{m})^2$. B_{bml} was fixed to 0.00322, while d_{bml} and A_{bml} were fitted simultaneously. The properties of all other layers were fixed to the values determined during calibration. The χ^2-value for the best fit was typically smaller than 2.0.

Adsorbed amounts were determined according to (De Feijter et al, 1978):

$$\Gamma = \frac{m}{M_{\mathrm{W}}} = \frac{1}{M_{\mathrm{W}}} \frac{d_{\mathrm{bml}}^{(2)}\left(n_{\mathrm{bml}}^{(2)} - n_{\mathrm{solvent}}\right) - d_{\mathrm{bml}}^{(1)}\left(n_{\mathrm{bml}}^{(1)} - n_{\mathrm{solvent}}\right)}{\mathrm{d}n/\mathrm{d}c}, \qquad \text{(S2)}$$

with m being the adsorbed mass per unit area, and M_{W} the molecular weight of the adsorbate. The indices (1) and (2) refer to determined values prior to and during a given incubation step, respectively. For most proteins, and within an error of less than 5%, the refractive index increment, dn/dc, is constant over the range of concentrations encountered in the reported measurements (0 to 500 mg/mL) (Bingen et al, 2008). In Eq. S2, we employed the refractive indices of the biomolecular layers at $\lambda = 633$ nm, and used a value of dn/dc = 0.180 cm^3/g for all proteins (Brandrup et al, 1989; Fasman, 1973). In practice, the errors associated with d_{bml} and n_{bml}-n_{solvent} can be rather high for the nanometre-thin films investigated here. The errors are though covariant, i.e., the product $d_{\mathrm{bml}}(n_{\mathrm{bml}}\text{-}n_{\mathrm{solvent}})$ and thus the adsorbed mass can be determined with good accuracy (Cuypers et al, 1983).

Quantification of mean anchor distances: To calculate the mean distance, s, between neighbouring sites of FG repeat domain anchorage we assumed hexagonal order of the anchors:

$$s^2 = \frac{2}{\sqrt{3}} \frac{1}{N_{\mathrm{A}}\Gamma}, \qquad \text{(S3)}$$

with N_{A} being Avogadro's number, and Γ the amount of adsorbed FG repeat domains (in mol/cm^2).

Determination of dissociation constants: The dissociation constant, K_{D}, and the saturation limit, $\Gamma_{\max}$, for the binding of scImpβ to FG repeat films was obtained from the equilibrium absorbed amounts, Γ, as a function of NTR bulk concentration, by numerical fitting to a single-component Langmuir isotherm:

$$\Gamma = \Gamma_{\max} \frac{[\mathrm{scImp}\beta]}{K_{\mathrm{D}} + [\mathrm{scImp}\beta]}, \qquad \text{(S4)}$$

or to a two-component Langmuir isotherm:

$$\Gamma = \Gamma_{\max}^{(1)} \frac{[\mathrm{scImp}\beta]}{K_{\mathrm{D}}^{(1)} + [\mathrm{scImp}\beta]} + \Gamma_{\max}^{(2)} \frac{[\mathrm{scImp}\beta]}{K_{\mathrm{D}}^{(2)} + [\mathrm{scImp}\beta]}. \qquad \text{(S5)}$$

Estimation of partition coefficients: The partition coefficient, i.e., the relative distribution of scImpβ in the film and in the bulk solution at low scImpβ concentrations, was calculated as:

$$PC = \frac{\Gamma_{\max}}{K_{\mathrm{D}} d}. \qquad \text{(S6)}$$

$\Gamma_{\max}$ and K_{D} were taken from the high affinity contribution of the Langmuir isotherm, and d from the QCM-D data (Table S2).

Estimation of dissociation rate constants: Association and dissociation of scImpβ to FG repeat films occurred fast: the relaxation times for reaching binding equilibria were typically smaller than 10 s (Fig. 2A). From this observation, we deduce a lower bound for the dissociation rate constant:

$k_{\mathrm{off}} > 0.1\ \mathrm{s}^{-1}$. For high affinity interactions ($K_{\mathrm{D}}^{(1)} = 0.36\ \mu\mathrm{M}$), this corresponds to a lower bound of $k_{\mathrm{on}} > 3\times10^{5}\ \mathrm{M}^{-1}\mathrm{s}^{-1}$ for the association rate constant.

Adsorption and desorption of scImpβ may be limited (i) by the transport of the molecules to the film, (ii) by the intrinsic association/dissociation rate between scImpβ and FG repeat films, and (iii) by the diffusion of scImpβ inside the film.

- *Transport limitations:* In our experimental setup (flat surface opposite a rotating stirrer), transport of molecules to the film can be adequately described by diffusion through an unstirred layer next to the surface (Hermens et al, 2004). In our setup, and for the typical size of the proteins used here, the thickness of this layer is about 20 μm. The mass transport limited adsorption rate of scImpβ can be estimated from a reference measurement of an adsorption process that is limited by mass transport and that occurs under identical stirring conditions, according to (Hermens et al, 2004):

  $$\left(\frac{\partial\Gamma}{\partial t}\right)_{\mathrm{scImp}\beta} = \left(\frac{D_{\mathrm{scImp}\beta}}{D_{\mathrm{ref}}}\right)^{2/3} \frac{[\mathrm{scImp}\beta]}{[\mathrm{ref}]} \left(\frac{\partial\Gamma}{\partial t}\right)_{\mathrm{ref}} . \tag{S7}$$

  We chose the adsorption of Av to a biotinylated supported lipid bilayer as the reference (data not shown). The diffusion constants, *D*, of scImpβ and Av were estimated from their Stokes radius to be about 55 and 70 $\mu\mathrm{m}^2$/s, respectively. The estimated adsorption rate for [scImpβ] = 1 μM was 0.29 pmol/cm^2/s. For comparison, the initial adsorption rate determined from the data in Fig. 3B was 0.23 pmol/cm^2/s. Within the uncertainties in the employed concentrations and diffusion constants, the two values are equal, indicating that mass transport does affect binding rates of scImpβ.

- *Diffusion inside the film:* Assuming a diffusion constant of 0.1 $\mu\mathrm{m}^2$/s inside the film (Frey & Görlich, 2007), it would take less than 10 ms for scImpβ to diffuse across a film of 35 nm thickness. This is several orders of magnitude faster than the measured off-rate, and hence negligible.

Atomic force microscopy (AFM)

Nanoindentation and imaging were performed with a NanoWizard II AFM (JPK, Berlin, Germany) using oxide-sharpened Si_3N_4 probes (NP-S, Veeco, CA, USA) with a nominal spring constant of 0.06 N/m and a nominal apex radius below 10 nm. The AFM probes were coated with a layer of PLL(20)-g[3.5]-PEG(2) (Susos AG, Dübendorf, Switzerland), in order to limit unspecific interactions between the AFM tip and the sample (Richter & Brisson, 2005).

SLBs and FG repeat films were prepared on silicon wafers, following the same incubation steps as those established by QCM-D (Fig. 1B). Incubation was performed in still solution, with twofold increased concentrations and incubation times.

Nanoindentation assays: Force versus displacement curves were acquired in buffer solution, at approach speeds and maximal loads of typically 100 nm/s and 1 nN, respectively. We compared only force curves that were acquired with the same tip, in order to minimise the effects that variations in the shape of the AFM probe may have on indentation. Reference force curves were acquired on a control surface - an SLB that lacked FG repeat coating – before and after indentation of each FG repeat film. Only indentation series which reproducibly showed a small interaction distance (~5 nm) on naked SLBs were accepted.

Force curves were reproducible upon repeated indentation at the same spot and at different spots on the same sample. Variations in the approach speed over more than two orders of magnitude, from 100 nm/s to 20 μm/s, did not change the force curves (data not shown), indicating that viscous lateral flow of FG repeat domains on these timescales does not affect the indentation assay.

Imaging: AFM images were acquired in solution and in tapping mode, using the NanoWizard II. We employed the same type of cantilever that was used in the nanoindentation assays. The drive frequency was typically around 13 kHz, and the free amplitude of the cantilever was set to 1 V. To ensure soft approach to the sample, the setpoint amplitude was decreased manually, in steps of a few mV, until the surface could be tracked. Scan speeds of 4 to 20 μm/s were employed.

Lateral homogeneity of FG repeat films:

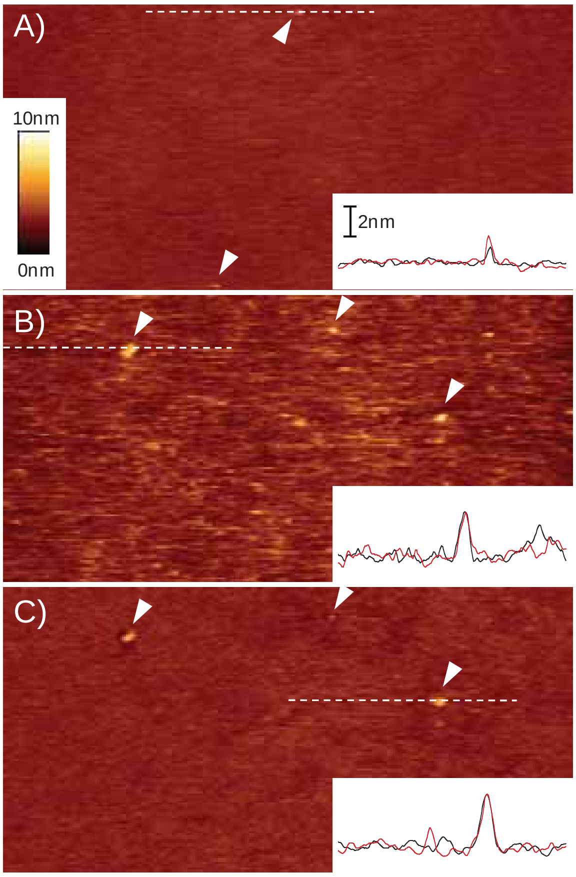

Figure S4: Representative AFM images of the surface topography of a supported lipid bilayer (*A*) and a monolayer of FG repeat domains (*B*-*C*). (*A*) Supported lipid bilayer prior to the immobilisation of FG repeat domains. Overall, the surface appears smooth. The apparent root mean square (rms) roughness is 0.2 nm. The *inset* shows the height profile of a part of a selected scan line (*white dashed line*). The Ångström-scale variations in height in the trace (*red*) and retrace (*black*) directions do not superpose well, indicating that they do not represent stable surface features but most likely experimental noise. A few defects, however, were resolved (*arrowheads*). They protruded by 2 to 5 nm out of the film, and could be stably detected upon repeated imaging of the same surface area (*not shown*). Their apparent diameter of down to 20 nm provides an upper limit for the lateral imaging resolution. These defects may represent residual vesicles that are trapped in the SLB (Richter et al, 2003). (*B*) Image of a monolayer of FG repeat domains, acquired at minimum load required for tracking the surface. The surface appears rougher than the SLB (rms roughness = 0.7 nm), although still very smooth compared to the thickness of the FG repeat film (30 to 40 nm, Fig. 4A). A comparison of trace and retrace data of a selected scan line (*inset*) shows that most of the roughness does not originate from stable surface features. Instead, it may either originate from noise and/or limited surface tracking, or from highly dynamic surface features. A few stable defects were present in the film (*arrowheads*). (*C*) Same surface area as in (*B*), imaged with slightly increased load. The apparent roughness decreases and approaches that of an SLB (rms roughness = 0.3 nm). The stable defects (*arrowheads*) remain visible, independent of the imaging load. We conclude that the FG repeat monolayers are laterally homogeneous, at least down to a length scale of a few 10 nm. Image size: 5 µm × 2.5 µm. Colour bar: false colour coding of relative heights.

Controls for the specificity of binding assays

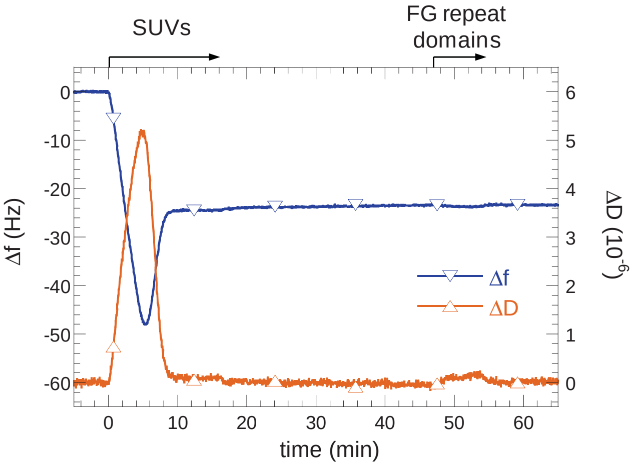

Figure S5: FG repeat domains do not bind to SLBs that lack NTA functionality. SLBs were made from 50 µg/ml SUVs containing exclusively DOPC. The QCM-D responses at the end of the incubation process were $\Delta f = -25$ Hz and $\Delta D < 0.3\times10^{-6}$, as typically observed for DOPC SLBs of good quality (Richter et al, 2003). His-tagged FG repeat domains, exposed at 3 µM concentration, induced only very small responses, $|\Delta f| < 1$ Hz and $\Delta D < 0.3\times10^{-6}$.

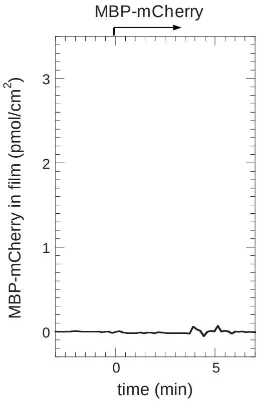

Figure S6: Binding of MBP-mCherry to an FG repeat film, monitored by ellipsometry. The FG repeat film was produced as described in Fig. 1, but with a slightly lower film density (9.1 pmol/cm^2). MBP-mCherry was incubated at a concentration of 1.1 µM. No interaction could be detected.

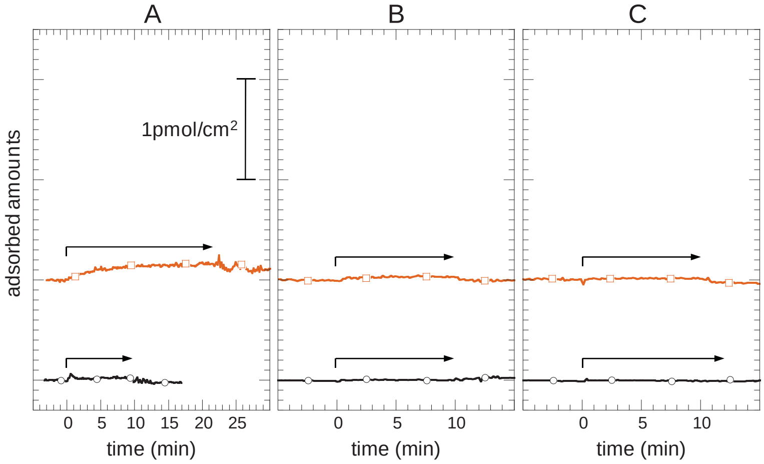

Figure S7: Controls for binding of scImpβ (*A*), scImpβ•IBB-mEGFP (*B*), and scImpβ•Gsp1p•GTP (*C*) to SLBs made of DOPC alone (black circles) and of DOPC and 10% NTA-functionalised lipids (orange rectangles). The SLBs were formed as described in Fig. S6 and Fig. 1, respectively; scImpβ, free or as a complex, was incubated at a concentration of 1 μM for the indicated durations (*arrows*). In most cases, binding was below or close to the detection limit. Some residual binding (~0.1 pmol/cm^2) was detected for scImpβ on NTA-functionalized SLBs. It is unlikely to affect the titration curve in Fig. 2 appreciably, since most of the NTA groups will be occupied by his-tags upon FG repeat film formation.

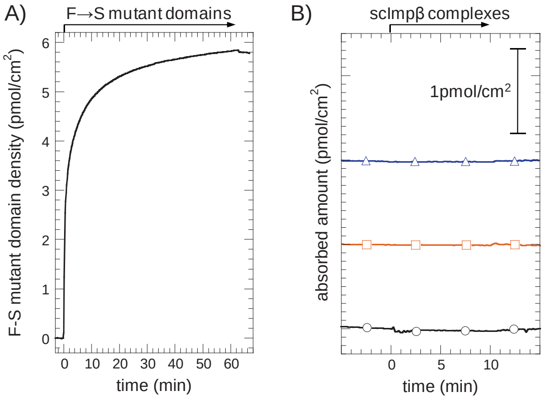

Figure S8: Interaction of scImpβ and its complexes with films that are made of a mutant form of Nsp1 FG/FxFG repeat domains in which all phenylalanines in FG context have been replaced by serines (F→S mutant, see (Frey et al, 2006) for details), monitored by ellipsometry. A NTA-functionalised SLB was formed as described in Fig. 1. His$_{10}$-tagged F→S mutant repeat domains were incubated at a concentration of 2 μM (*A*). scImpβ (*black circles*), scImpβ•IBB-mEGFP (*orange squares*), and scImpβ•Gsp1p•GTP (*blue triangles*), incubated at 1 μM concentration in solution, did not bind to the mutant film (*B*). These data confirm that the observed binding of scImpβ to FG repeat domains is specific.

All FG repeat domains in the FG repeat films are bound to the SLB

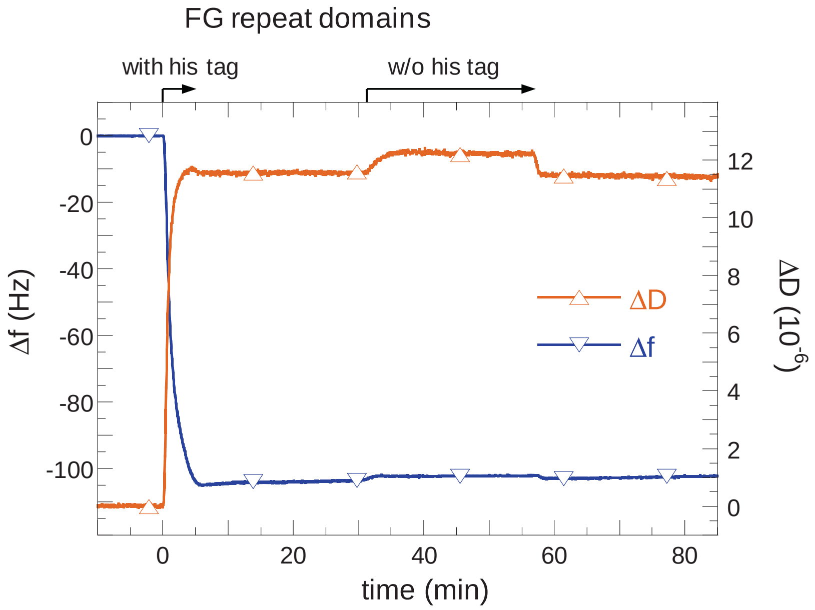

Figure S9: Interaction of his-tag free FG repeat domains with FG repeat domain films, monitored by QCM-D. A NTA-functionalised SLB was formed as described in Fig. 1. His_{10}-tagged FG repeat domains were incubated at a concentration of 3 µM, until a frequency shift of about -100 Hz was reached. Small changes in Δf and ΔD upon exposure to 3 µM his-tag free FG repeat domains may reflect changes in the film morphology due to binding of FG repeat domains. At present, we can though not exclude that they stem from minor changes in the viscosity or density of the bulk solution. Upon washing in buffer, the Δf and ΔD signals return quickly to the values prior to incubation of his-tag free FG repeat. We conclude that homophilic interactions or entanglement are not sufficient to entrap individual FG repeat domains stably in the FG repeat film. All stably bound FG repeat domains must hence be connected directly to the SLB.

Thickness of monolayers of avidin and biotinylated scImpβ

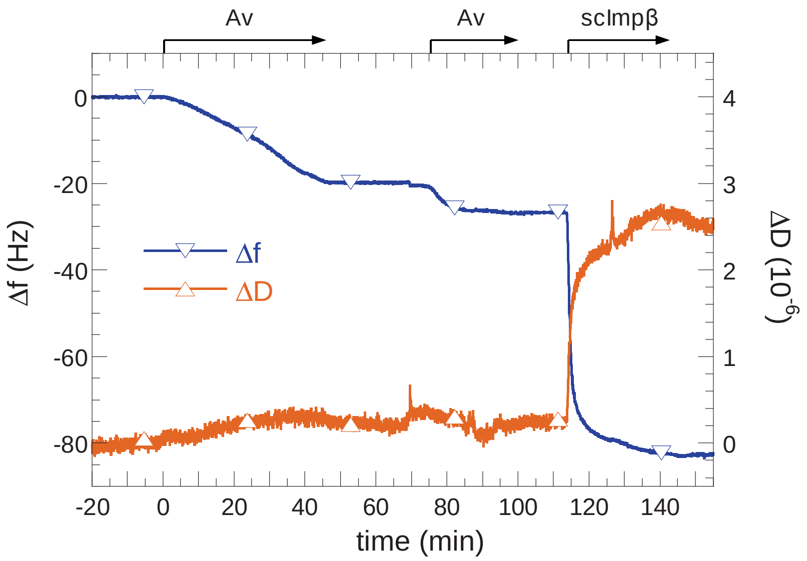

Figure S10: Formation of monolayers of avidin (Av) and biotinylated scImpβ on SLBs containing biotinylated lipids, monitored by QCM-D. The SLB was formed from 50 µg/ml SUVs containing 88 mol-% DOPC, 10% bis-NTA functionalised lipids and 2% biotin-functionalised lipids (*not shown*). Avidin was incubated in two steps, at a concentration of about 0.1 µM, until saturation. Biotinylated scImpβ was incubated at a concentration of 0.5 µM. From the final frequency shifts of -27 Hz for Av and -56 Hz for scImpβ, layer thicknesses of 4 nm and 8 nm, respectively, can be estimated, in agreement with the molecular dimensions of both molecules. For this estimate, a mean density of 1.2 g/cm^3 inside the protein layer was assumed (Bingen et al, 2008).

References

Bingen P, Wang G, Steinmetz NF, Rodahl M, Richter RP (2008) Solvation effects in the QCM-D response to biomolecular adsorption - a phenomenological approach. *Anal Chem* **80:** 8880-8890

Brandrup J, Immergut EH, Grulke EA (1989) *Polymer Handbook*, 3rd edn. New York: Wiley-Interscience.

Brown XQ, Ookawa K, Wong JY (2005) Evaluation of polydimethylsiloxane scaffolds with physiologically-relevant elastic moduli: interplay of substrate mechanics and surface chemistry effects on vascular smooth muscle cell response. *Biomaterials* **26:** 3123-9

Corsel JW, Willems GM, Kop JMM, Cuypers PA, Hermens WT (1986) The Role of Intrinsic Binding Rate and Transport Rate in the Asorption of Prothrombin, Albumin and Fibrinogen to Phospholipid Bilayers. *J Colloid Interface Sci* **111:** 544-554

Cuypers PA, Corsel JW, Janssen MP, Kop JMM, Hermens WT, Hemker HC (1983) The Adsorption of Prothrombin to Phosphatidylserine Multilayers Quantitated by Ellipsometry. *J Biol Chem* **258:** 2426-2430

Daimon M, Masumura A (2007) Measurement of the refractive index of distilled water from the near-infrared region to the ultraviolet region. *Applied Optics* **46:** 3811-3820

De Feijter JA, Benjamins J, Veer FA (1978) Ellipsometry as a Tool to Study the Adsorption Behavior of Synthetic and Biopolymers at the Air-Water Interface. *Biopolymers* **17:** 1759-1772

Domack A, Prucker O, Rühe J, Johannsmann D (1997) Swelling of a polymer brush probed with a quartz crystal resonator. *Physical Review E* **56:** 680-689

Fasman GD (1973) *Handbook of Biochemistry*, Cleveland, OH, USA: CRC Press.

Ferry JD (1980) *Viscoelastic Properties of Polymers*, 3rd edn. New York: Wiley & Sons.

Frey S, Görlich D (2007) A Saturated FG-Repeat Hydrogel Can Reproduce the Permeability Properties of Nuclear Pore Complexes. *Cell* **130:** 512-523

Frey S, Görlich D (2009) FG/FxFG as well as GLFG repeats form a selective permeability barrier with self-healing properties. *EMBO J* **28:** 2554-2567

Frey S, Richter RP, Görlich D (2006) FG-rich repeats of nuclear pore proteins form a three-dimensional meshwork with hydrogel-like properties. *Science* **314:** 815-817

Hermens WT, Benes M, Richter RP, Speijer H (2004) Effects of flow on solute exchange between fluids and supported biosurfaces. An overview. *Biotechn Appl Biochem* **39:** 277-284

Johannsmann D (2007) Studies of Viscoelasticity with the QCM. In *Piezoelectric Sensors*, Steinem C, Janshoff A (eds), Vol. 5, pp 49-110. Berlin Heidelberg: Springer

Lata S, Gavutis M, Piehler J (2006) Monitoring the Dynamics of Ligand-Receptor Complexes on Model Membranes. *J Am Chem Soc* **128:** 6-7

Lata S, Reichel A, Brock R, Tampé R, Piehler J (2005) High-Affinity Adaptors for Switchable Recognition of Histidine-Tagged Proteins. *J Am Chem Soc* **127:** 10205-10215

Lide DR (2004) *Handbook of Chemistry and Physics*, 85 edn. Boca Raton, FL, USA: CRC Press.

Richter RP, Brisson A (2005) Following the formation of supported lipid bilayers on mica - a study combining AFM, QCM-D and ellipsometry. *Biophys J* **88:** 3422-3433

Richter RP, Mukhopadhyay A, Brisson A (2003) Pathways of lipid vesicle deposition on solid surfaces: a combined QCM-D and AFM study. *Biophys J* **85:** 3035-3047

Schatz PJ (1993) Use of Peptide Libraries to Map the Substrate Specificity of a Peptide-Modifying Enzyme: A 13 Residue Consensus Peptide Specifies Biotinylation in Escherichia coli. *Nat Biotechnol* **11:** 1138-1143

Voinova MV, Rodahl M, Jonson M, Kasemo B (1999) Viscoelastic Accoustic Response of Layered Polymer Films at Fluid-Solid Interfaces: Continuum Mechanics Approach. *Physica Scripta* **59:** 391-396

4 Viscoelasticity of thin biomolecular films

This chapter was published in Biomacromolecules, 2012, 11: 2322–2332 as:

Viscoelasticity of Thin Biomolecular Films: A Case Study on Nucleoporin Phenylalanine-Glycine Repeats Grafted to a Histidine-Tag Capturing QCM-D Sensor

Authors: **Nico B. Eisele**[a,c], Fredrik I. Andersson[b], Steffen Frey[c], Ralf P. Richter[a,d]

[a] Biosurfaces Unit, CIC biomaGUNE, Paseo Miramon 182, 20009 San Sebastian, Spain
[c] Biolin Scientific AB, Hängpilsgatan 7, 426 77 Västra Frölunda, Sweden
[c] Department of Cellular Logistics, Max Planck Institute for Biophysical Chemistry, Am Faßberg 11, 37077 Göttingen, Germany
[d] Max Planck Institute for Intelligent Systems, Heisenbergstraße 3, 70569 Stuttgart, Germany

Contribution of authors: Nico B. Eisele and Ralf P. Richter designed research. Nico B. Eisele performed QCM-D and ellipsometry measurements and analyzed data. Fredrik I. Andersson provided (expertise on) His-tag capturing sensors. Steffen Frey purified proteins. Ralf P. Richter performed AFM measurements and analyzed data.

BIOMACROMOLECULES
Article
pubs.acs.org/Biomac

Viscoelasticity of Thin Biomolecular Films: A Case Study on Nucleoporin Phenylalanine-Glycine Repeats Grafted to a Histidine-Tag Capturing QCM-D Sensor

Nico B. Eisele,[†,‡] Fredrik I. Andersson,[§] Steffen Frey,[‡] and Ralf P. Richter*[,†,∥]

[†]Biosurfaces Unit, CIC biomaGUNE, Paseo Miramon 182, 20009 Donostia - San Sebastian, Spain
[‡]Department of Cellular Logistics, Max Planck Institute for Biophysical Chemistry, Am Faßberg 11, 37077 Göttingen, Germany
[§]Biolin Scientific AB, Hängpilsgatan 7, 426 77 Västra Frölunda, Sweden
[∥]Max Planck Institute for Intelligent Systems, Heisenbergstraße 3, 70569 Stuttgart, Germany

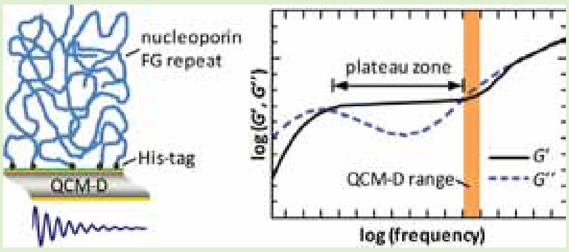

ABSTRACT: Immobilization of proteins onto surfaces is useful for the controlled generation of biomolecular assemblies that can be readily characterized with in situ label-free surface-sensitive techniques. Here we analyze the performance of a quartz crystal microbalance with dissipation monitoring (QCM-D) sensor surface that enables the selective and oriented immobilization of histidine-tagged molecules for morphological and interaction studies. More specifically, we characterize monolayers of natively unfolded nucleoporin domains that are rich in phenylalanine–glycine repeats (FGRDs). An FGRD meshwork is thought to be responsible for the selectivity of macromolecular transport across the nuclear pore complex between the cytosol and the nucleus of living cells. We demonstrate that nucleoporin FGRD films can be formed on His-tag Capturing Sensors with properties comparable to a previously reported immobilization platform based on supported lipid bilayers (SLB). Approaches to extract the film thickness and viscoelastic properties in a time-resolved manner from the QCM-D response are described, with particular emphasis on the practical implementation of viscoelastic modeling and a detailed analysis of the quality and reliability of the fit. By comparing the results with theoretical predictions for the viscoelastic properties of polymer solutions and gels, and experimental data from an atomic force microscopy indentation assay, we demonstrate that detailed analysis can provide novel insight into the morphology and dynamics of FG repeat domain films. The immobilization approach is simple and versatile, and can be easily extended to other His-tagged biomolecules. The data analysis procedure should be useful for the characterization of other ultrathin biomolecular and polymer films.

INTRODUCTION

Solid-phase assays have become commonplace to study biomolecular interactions, in biosensors and microarrays, for fundamental biochemical or molecular biological studies and in applied biomedicine or biotechnology. They are attractive because they enable sensitive readout via a variety of detection techniques, controlled positioning of one of the binding partners, and easy separation of interacting material from the remaining solution phase. A crucial aspect in the assay design is the preparation of the functionalized surface. Ideally, the surface should accommodate the molecules of interest in a stable and active manner, with controlled orientation, conformation, and density, and at the same time be inert to the nonspecific binding of any other molecular species.

In the case of recombinant proteins, a sequence of typically between 6 and 20 histidine residues (His) is commonly used as a so-called His-tag to facilitate purification from the cell lysate by affinity chromatography. When produced recombinantly or synthetically, the His-tag can be placed at a well-defined position within the polypeptide chain. Anchorage through a site-specific His-tag to a surface that selectively captures multihistidine moieties would hence by design lead to a highly oriented immobilization of proteins or peptides. Such an approach has indeed been successfully used in various biochemical and biophysical studies.[1−5]

Quartz crystal microbalance with dissipation monitoring (QCM-D) is a popular surface-sensitive technique for the analysis of surface-bound molecules or thin films. The technique not only provides information about the amount of surface-bound material. Because of its mechano-acoustic transducer principle, it is also exquisitely sensitive to the mechanical properties of the adsorbate (reviewed by ref 6). Here, we present an easy approach for the specific, stable, and oriented immobilization of His-tagged biomolecules to QCM-D sensor surfaces. The method is based on a reusable His-tag Capturing Sensor and should have broad applicability for interaction studies involving proteins, peptides, or other molecules that can be equipped with a His-tag.

Received: April 14, 2012
Revised: June 5, 2012
Published: July 10, 2012

ACS Publications © 2012 American Chemical Society

dx.doi.org/10.1021/bm300577s | *Biomacromolecules* 2012, 13, 2322−2332

Driven by our own research interests, we chose a nucleoporin domain containing phenylalanine-glycine repeats (FG repeat domain or FGRD) as a model protein to demonstrate the performance of the His-tag Capturing Sensor. FGRDs are thought to be key for the selectivity in macromolecular transport between the cytosol and the nucleus of eukaryotic cells. They are natively unfolded[7] and densely grafted with one end to the channel walls of nuclear pore complexes (NPCs) that perforate the nuclear envelope. Molecules above a certain size (approximately 5 nm in diameter[8]) need to be attached to dedicated shuttle proteins, nuclear transport receptors (NTRs), for efficient transport through the channel (reviewed in refs 9 and 10). FGRDs comprise multiple hydrophobic FG, GLFG, or FxFG motives separated by more hydrophilic spacers,[7,11] and binding of NTRs to phenylalanines in the FG context is crucial for facilitated transport of NTRs and their cargo complexes.[12−14] The physical mechanism behind transport selectivity remains poorly understood and several models have been proposed (see ref 15 and references therein). Most of them share the idea that the permeability barrier of NPCs arises from the supramolecular assembly of FGRDs. The structure of the FGRD meshwork inside the NPC remains elusive, presumably because it is highly dynamic and exhibits a low degree of order. In vitro assays on the macroscopic scale have shown that FGRDs can form hydrogels.[16−19] An open question is, to what extent the attractive intermolecular interactions that promote gel formation are present and functionally relevant if the system is reduced to the nanometer scale. The rheological analysis of nanoscale systems would provide an indirect way to access their morphological and dynamical features.

In the case of a laterally homogeneous film, quantitative information about the linear rheological properties and thickness can be extracted from the QCM-D response through a continuum viscoelastic model. In an earlier study, we had introduced ultrathin films of FGRDs as model systems of the nuclear pore permeability barrier.[3] Here, we analyze what type of information can be gained from the analysis of viscoelastic properties of such films by QCM-D. Particular emphasis is put on the procedure of modeling QCM-D data with explicit consideration of the frequency dependence of viscoelastic properties, and the analysis of the resulting data with regard to the information that they can provide about the nanoscale morphology and dynamics of entangled or cross-linked polymer meshworks. Although we focus on a specific type of FGRD film, our methodological approach should be useful for other thin polymer films. These occur in a broad range of (bio)technological applications, such as antifouling[20] or low-friction coatings,[21] in biomaterials,[22] for sensing, and for colloidal stabilization.[23−25]

■ MATERIALS AND METHODS

Proteins and Buffer. FG repeat domains of the yeast nucleoporin Nsp1p (amino acids 2−601; Nsp1p FGRDs) with and without a His$_{10}$-tag at the N-terminus (M_w = 65 and 63 kDa, respectively), and the nuclear transport receptor importin β from *Saccharomyces cerevisiae* (scImpβ, 95 kDa) were purified as described earlier.[3] Nsp1p FGRDs were stored at a concentration of 460 μM in 6 M guanidine hydrochloride, 1 mM iminodiacetic acid, 10 mM acetic acid, and 5 mM sodium acetate at −80 °C. scImpβ was stored at 100 μM concentration in 40 mM Tris pH 7.5, 260 mM NaCl, 4 mM magnesium acetate, 0.4 mM EDTA, 250 mM saccharose, and 10 mM β-mercaptoethanol at −80 °C. Proteins were diluted (1:300 Nsp1p FGRDs and 1:100 scImpβ) in working buffer (10 mM Hepes pH 7.4, 150 mM NaCl) prior to use. All chemicals were purchased from Sigma-Aldrich (Schnelldorf, Germany).

Surfaces. His-tag capturing QCM-D sensors with a fundamental resonance frequency $f_1 \approx 4.95$ MHz (QSX340; Biolin Scientific AB, Västra Frölunda, Sweden) were stored at −80 °C prior to use. The sensor surface functionalization is based on an approximately 3 nm thin passivating layer of poly(ethylene glycol) (PEG) that exposes divalent metal ions at a density of approximately 10^{13}/cm^2 for the capture of His-tagged molecules. Sensors were used as provided.

Quartz Crystal Microbalance with Dissipation Monitoring (QCM-D). QCM-D measures changes in resonance frequency, Δf, and dissipation, ΔD, of a sensor crystal upon interaction of (soft) matter with its surface. The QCM-D response is sensitive to the mass (including hydrodynamically coupled water) and the mechanical properties of the surface-bound layer.[6] To a first approximation, a decrease in Δf indicates a mass increase, while high (low) values of ΔD indicate a soft (rigid) film. Adsorption and interfacial processes were monitored in situ with subsecond time resolution. QCM-D measurements were performed with a Q-Sense E4 system (Biolin Scientific AB). The system was operated in flow mode with a flow rate of typically 20 μL/min using a syringe pump (KD Scientific, Holliston, MA, U.S.A.). The working temperature was 23 °C. Δf and ΔD were measured at the fundamental ($n = 1$) and six overtones ($n = 3, 5, ..., 13$), corresponding to resonance frequencies of $f_n \approx 5, 15, 25, ..., 65$ MHz. Changes in dissipation and normalized frequencies, $\Delta f_n/n$, are presented. Only the data from the overtones were used for further quantitative analysis, as at the fundamental frequency, the QCM-D response tends to be significantly affected by the mounting of the sensor, small air bubbles that are trapped at the sensor periphery and/or pressure waves.

Viscoelastic Modeling. Thickness and viscoelastic properties of FGRD films were estimated by fitting the QCM-D data to a continuum viscoelastic model.[26,27] The model relates the measured QCM-D responses, Δf and ΔD as a function of n, to the viscoelastic properties of the adsorbed layer and the surrounding solution. For time-resolved fitting of the data, we used the software QTools (version 3.0, Biolin Scientific AB; options "extended viscoelastic model" and "Voigt" viscoelastic representation). Data at selected time points were also fitted with the software QTM[28] (D. Johannsmann, Technical University of Clausthal, Germany; option "small load approximation"[29,30]). The FGRD film was modeled as a homogeneous viscoelastic layer with acoustic thickness d, density ρ, storage modulus $G'(f)$, and loss modulus $G''(f)$. The storage modulus is a measure for the elasticity of the film. The loss modulus is related to the film's viscosity $\eta(f)$ by $G''(f) = 2\pi f\eta(f)$. Both G' and G'' (and η) are frequency-dependent. The frequency dependence of G' and G'' was assumed to follow power laws, with exponents α' and α'', respectively (see Results section for details; the exponents for "shear" and "viscosity" in QTools correspond to α' and $\alpha'' - 1$, respectively). The semi-infinite bulk solution was assumed to be Newtonian with a viscosity of $\eta_l = 0.89$ mPa·s, and a density of $\rho_l = 1.0$ g/cm^3.

The fit results were obtained by minimizing $\chi^2(t) = \sum_{i=1}^{l}\{[y_i^{\text{theory}}(t) - y_i^{\text{experiment}}(t)]/\sigma_i\}^2$, where y_i^{theory} and $y_i^{\text{experiment}}$ represent the theoretically predicted and experimentally measured values of Δf or ΔD for the different overtones n = 3, 5, 7, 9, 11 and 13, respectively. The number of input parameters l at any given time point t is hence 12. σ_i is the noise in the data. In QTools, we set $\sigma_f = 0.5$ Hz for the normalized frequency shifts $\Delta f_n/n$. This value accounts for the noise in the data acquisition (the standard deviation was typically around 0.1 Hz) and drifts (estimated to reach at most a few Hz over the duration of the measurement). For ΔD, we set $\sigma_D = 0.2 \times 10^{-6}$, consistent with data acquisition noise and drifts. We note in passing that with these choices of σ_f and σ_D the shifts in resonance frequency and in bandwidth ($\Delta\Gamma_n$) of the dampened harmonic oscillator are weighted equally, because bandwidth shift relates to dissipation shift by $\Delta\Gamma_n/n = f_n/(2n) \times \Delta D_n \approx f_1/2 \times \Delta D_n \approx 2.5\text{ MHz} \times \Delta D_n$.[6] For a perfect agreement between experimental data and theoretical model, the normalized χ^2, that is, $\chi^2_{\text{norm}} = \chi^2/(l - p)$, where p is the number of fit parameters, would be expected to scatter around one. In QTM, $\sigma_f = 1$ Hz/n and $\sigma_D = 0.4 \times 10^{-6}/n$ are preset.

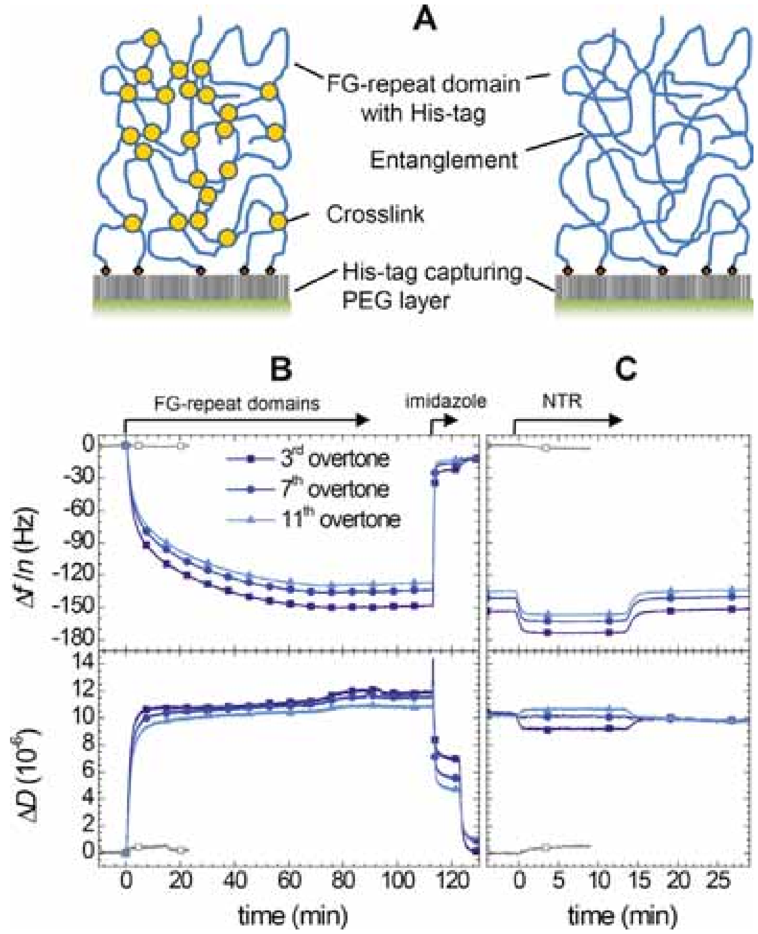

Figure 1. Formation of a surface-grafted monolayer of nucleoporin phenylalanine−glycine repeat domains (FGRDs). (A) Scheme illustrating the film architecture. The FGRD of Nsp1p was grafted through an N-terminal His_{10}-tag to a QCM-D His-tag Capturing Sensor. Attractive interactions between the flexible chains would generate a cross-linked meshwork (left); without such interactions, an entangled meshwork is expected to form (right). (B, C) Formation of the FGRD film and binding of the nuclear transport receptor (NTR) scImpβ followed by QCM-D (n = 3, 7, and 11 are shown as indicated). Start and duration of the incubation with different samples is indicated (arrows); remaining times correspond to buffer washes. Strong changes in frequency and dissipation upon addition of 100 μg/mL His-tagged FGRDs (B) reflect the formation of a flexible and hydrated film. FGRDs lacking a His-tag did not bind (gray lines with open squares, n = 3 is shown; incubation was limited to 15 min), and FGRDs with His-tag could be eluted rapidly by washing with 500 mM imidazole, demonstrating specificity of binding. Changes in Δf and ΔD at about 124 min do not reflect any changes on the surface but result from changes in the viscosity and density of the surrounding solution, owing to the presence of imidazole. The NTR scImpβ was added to an FGRD film at 1 μM bulk concentration (C). NTRs hardly bound to a bare His-tag Capturing Sensor in a control measurement (gray lines with open squares, n = 3 is shown; incubation was limited to 5 min).

QTools and QTM gave consistent results. Simulations with QTools and QTM of the responses in $\Delta f_n/n$ and $\Delta\Gamma_n/n = f_n/(2n) \times \Delta D_n$ for an arbitrarily chosen set of film parameters agreed to within 1 μHz with the predictions of eq 14 in ref 30 (setting $f_n = 2\pi f_1$), confirming that both methods are built on the same theoretical model. When fitting our data with the two methods, we observed minor discrepancies. Presumably these are due to different implementations of the χ^2-minimization algorithms, and differences in the choice of σ_f, σ_D, and the acoustic impedance of quartz (8.7694×10^6 kg/(m^2 s) in QTools and 8.8×10^6 kg/(m^2 s) in QTM).

Atomic Force Microscopy (AFM). Imaging and nanoindentation measurements were performed with a NanoWizard II AFM (JPK, Berlin, Germany) using oxide-sharpened Si_3N_4 probes (NP-S, Veeco, CA, U.S.A.) with a nominal cantilever spring constant of 0.06 N/m. The real spring constant, determined through the thermal noise method,[31] was 0.11 N/m. The coating of His-tag Capturing Sensors with FGRD films was first monitored by QCM-D, and the samples were then transferred for analysis by AFM. AFM images were acquired in tapping mode in solution. The drive frequency was typically around 50 kHz, and the free amplitude of the cantilever was set to 1 V. To ensure a soft approach to the sample, the set point amplitude was decreased manually, in steps of a few 10 mV, until the surface could be tracked. Scan speeds of 6−30 μm/s were employed. Nanoindentation assays were performed in working buffer solution. Deflection versus displacement curves were acquired at approach speeds between 0.1 and 20 μm/s and maximal loads of typically 2.5 nN and converted into force versus distance curves with JPK data processing software. A force curve was considered representative when it could be reproduced upon repeated indentation at the same spot and at different spots on the same sample.

In Situ Ellipsometry. Spectroscopic ellipsometry (M2000 V, Woollam, NE, U.S.A.) on QCM-D sensors was performed using an open fluid cell, as previously described.[32] The optical properties of the His-tag Capturing Sensor coating were first calibrated by fitting of ellipsometric data in air and in solvent, at a 70° angle of incidence, to a multilayer model. The coating of the His-tag Capturing Sensor consists of a few nm thin PEG layer, followed by a several 10 nm silica layer, a few nm thin titanium layer, and an opaque gold layer (~100 nm). We modeled the first two layers as a single transparent Cauchy medium and the two metal layers as a single B-Spline substrate. The resulting optical properties of the Cauchy layer (Cauchy parameters $A = 1.495$, $B = -0.00227$, and $C \approx 0$) were within the range typically observed for silica, the thickness (29.0 nm) was within the range provided by the manufacturer, and the mean square error (1.4) was close to 1.0, indicating a good fit. Furthermore, data acquired in air at additional angles of incidence (50°, 55°, 60°, and 65°) were consistent with the results, confirming that the model is appropriate. The FGRD film was treated as a transparent Cauchy medium and fitted as described previously.[32] The areal FGRD mass density was determined through de Fejter's equation,[33] using a refractive index increment of $dn/dc = 0.18$ cm^3/g.[3]

RESULTS

Immobilization of FG Repeat Domains on a His-Tag Capturing Sensor. We used the natively unfolded FG repeat domain of the yeast nucleoporin Nsp1p (Nsp1p FGRD) to test the performance of the His-tag Capturing Sensor (Figure 1A). To this end, we exposed the sensor surface to a solution of 1.5 μM FGRDs with an N-terminal His$_{10}$-tag and monitored the immobilization by QCM-D (Figure 1B). Strong changes in frequency and dissipation indicated binding of FGRDs to the sensor surface. The signals reached plateaus after 80 min of incubation, yielding overall changes in frequency and dissipation of −150 Hz and 12×10^{-6} (values are given for the third overtone), respectively. This suggests the successful formation of a soft and hydrated film. Upon rinsing in buffer, the signals remained virtually unchanged, demonstrating that the FGRDs were stably immobilized. In contrast, FGRDs lacking a His-tag did not bind (Figure 1B, gray lines with open squares), indicating that the proteins bound exclusively via the histidine tag and that the poly(ethylene glycol) layer on the His-tag Capturing Sensor provides appropriate passivation.

To evaluate the quality of the FGRD film, we compared our results with an earlier report in which the same Nsp1p FGRD construct was immobilized on a different support, made of a supported lipid bilayer (SLB) containing Ni^{2+}-loaded bis-nitrilotriacetic-acid-functionalized lipids.[3] The film formation kinetics and the maximal shifts in frequency were very similar. The maximal shifts in dissipation were also comparable, yet 15% smaller than on the SLB. Apparently, both immobilization methods yield similar FGRD films. The slight difference in the dissipation shifts might suggest that the FGRD film properties exhibit some sensitivity to subtleties in the mode of immobilization, such as the lateral mobility of the anchor points.

Immobilized proteins could be eluted by competition with imidazole: after washing with 500 mM imidazole for 10 min, shifts in frequency and dissipation reached levels close to the baseline (−12 Hz and 1.0×10^{-6}, respectively). The sensors could be regenerated when protein elution was followed by a loading step with 5 mM $CuSO_4$ solution. The binding curves for Nsp1p FGRDs agreed to within 10% between subsequent film preparation cycles on the same surface (data not shown), indicating that surfaces can be reused multiple times.

Interaction of NTRs with the FGRD film. To study the interaction between the FGRD film and NTRs, we created a fresh Nsp1p FGRD film on a His-tag Capturing Sensor and exposed it to a 1 μM solution of importin β from *Saccharomyces cerevisiae* (scImpβ), an NTR that is known to interact with Nsp1p FGRDs.[3,12,34] A decrease in frequency concomitant with a spreading of the dissipation values as a function of the overtone upon addition of scImpβ confirmed interaction (Figure 1C). Equilibrium was reached rapidly, and the frequency and dissipation signals rapidly returned to their original values after rinsing in buffer, indicating that the binding of scImpβ into the FGRD film is fast and completely reversible. To ascertain that the changes in frequency and dissipation were due to interaction between the NTR and FGRDs, we incubated a bare His-tag capturing surface with the NTR. The results (Figure 1C, gray lines with open squares) confirmed that nonspecific binding of the NTR to the sensor surface is small. These observations demonstrate that the His-tag capturing surface can be readily used to study the interaction between FGRDs and NTRs.

Viscoelastic Modeling of FGRD Films. In what follows, we will demonstrate how quantitative time-resolved information about the thickness and viscoelastic properties of FGRD films can be obtained from the QCM-D data. Viscoelastic models are increasingly used to extract quantitative information from QCM-D data.[3,26,30,35−38] Because we anticipate that the method will be of practical interest for forthcoming studies by others and us, and because the application of the model requires a certain amount of care,[6] we provide a detailed description of the data analysis procedure.

To start, we remind that lateral homogeneity is a prerequisite for the applicability of the viscoelastic model, because, as discussed in detail elsewhere (ref 6 and references therein), an additional energy dissipation mechanism can occur in laterally heterogeneous films that is not captured by the continuum viscoelastic model. Imaging by atomic force microscopy (AFM, Figure 2) revealed the FGRD film to be about as flat as the bare His-tag capturing QCM-D sensor surface. This indicates that the film is indeed laterally homogeneous, at least down to a length scale of ~10 nm, in agreement with earlier observations for Nsp1p FGRD films on SLBs.[3]

Second, we have no exact a priori knowledge about the frequency dependence of the film's viscoelastic properties. Over a rather narrow frequency range, the QCM-D data covers less than 1 order of magnitude, the viscoelastic properties of polymer solutions or gels are typically well approximated by power laws,[39,40] and we therefore use the expressions $G' = G'_0(f/f_0)^{\alpha'}$ and $G'' = G''_0(f/f_0)^{\alpha''}$. G'_0 and G''_0 are the shear storage and loss moduli at an arbitrarily chosen reference frequency f_0. We set $f_0 = 15$ MHz, which is close to the resonance frequency at the third overtone.

Third, an assumption about the film density ρ is required because thickness and viscoelastic properties enter as ρd, $\rho G'_0$, and $\rho G''_0$ into the model and the density can hence not be determined together with the five free fitting parameters d, G'_0, G''_0, α', and α''.[6] In many practically relevant cases, the density of the polymer of interest is quite similar to that of the solvent, and the mean film density can then be well approximated by the solvent density. Alternatively, the film density can be determined by separately quantifying the areal polymer mass density, for example, through optical mass-sensitive techniques, and correlation with QCM-D data.[6] In our case, we monitored the buildup of an FGRD film on a His-tag capturing QCM-D sensor surface by in situ ellipsometry (Figure 3). The maximal grafting density obtained from the ellipsometric data was $\Gamma_{max} = 10$ pmol/cm^2, corresponding to a surface area of 17 nm^2 per molecule, or a mean distance of about 4 nm between neighboring anchor points. These values are in excellent

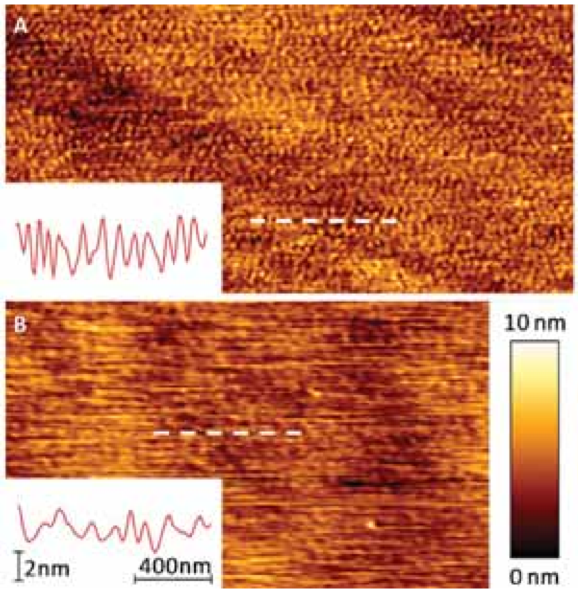

Figure 2. Characterization of the FGRD film morphology by AFM. Representative AFM images of the surface topography of a bare His-tag capturing surface (A) and an FGRD film on a His-tag capturing surface (B). Image size: 3 × 1.5 μm; color bar: false color coding of relative heights. Insets show height profiles of parts of selected scan lines (white dashed lines). The bare sensor surface (A) has a granular topography, with grains of 50−100 nm diameter and up to ∼4 nm height. The QCM-D sensor coating contains an evaporated gold film, and the observed topography is characteristic for such a film.[57] A silica layer and the organic His-tag capturing coating are deposited on top of the gold. Both top layers conform to the topography of the gold surface and do not add appreciable roughness.[57] The image with an FGRD film (B) was acquired at minimum load required for tracking the surface. The surface topography is overall similar yet slightly smoother than for the bare surface. Within the accessible resolution of the images (∼10 nm), we conclude that the FGRD film is laterally homogeneous.

agreement with previously reported results on an SLB-bound FGRD film.[3] Correlation with the QCM-D data[6] gave ρ = 1.05 g/cm^3. For simplicity, we assume the film density to be constant throughout the film formation procedure. In reality, the density will continuously increase from 1.0 g/cm^3 (the density of the buffer solution) to 1.05 g/cm^3, and we therefore underestimate d, G'_0, and G''_0 slightly, by a few percent.

Fourth, we remind that the viscoelastic model assumes that the film is homogeneous in the direction normal to the surface, implying that the polymer density is constant at distances smaller than d from the solid support and then drops instantaneously to zero ("box profile"). In reality, the film is likely to exhibit a density gradient of unknown shape. As a consequence, G'_0, G''_0, α', and α'' represent mean parameters, and the acoustic thickness d represents an equivalent box-profile thickness.[26,29,41]

Figure 4 displays the results of the best fits (i.e., the parameter set generating the lowest χ^2) for the time-resolved data set in Figure 1B,C. The values of χ^2 normalized by the number of degrees of freedom, that is, the number of input parameters l minus the number of fit parameters p, $\chi^2_{\mathrm{norm}} = \chi/(l - p)$, were of order unity, indicating a good fit. χ^2_{norm} increased slightly over time, indicating a systematically increasing error.

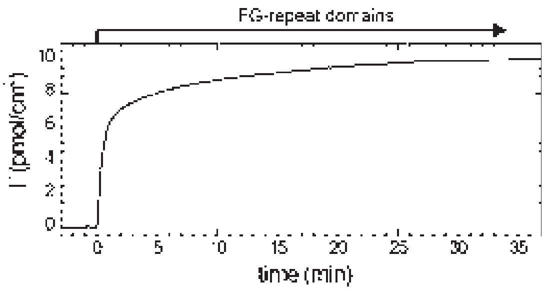

Figure 3. Quantification of FGRD grafting density by in situ ellipsometry. Evolution of the grafting density Γ during FGRD film formation on a His-tag Capturing Sensor. 100 μg/mL His-tagged FGRDs were exposed to the sensor surface from 0 to 35 min.

Most likely, these variations result from minor drifts in the frequency and/or dissipation: their magnitude is indeed consistent with typical drift rates. Figure 5 provides a visual impression of the excellent agreement between experimental and simulated data at selected time points. Importantly, the fit was unique: depending on the chosen range of starting values for the fit parameters, the nonlinear regression algorithm sometimes converged on other solutions, but these exhibited much larger χ^2_{norm} values (i.e., on the order of 10 and beyond). Furthermore, the exponents remained within the ranges $0 \leq \alpha' \leq 2$ and $-1 \leq \alpha'' \leq 1$, which are physically reasonable according to polymer theory.[39,40]

With regard to the results of the fit, the fitting software that is currently available does not provide means to automatically compute confidence intervals. Instead, we adopted a semi-automated procedure. One by one, each parameter was fixed while the other four parameters were kept as free-fitting parameters (α' and α'' were constrained to $-0.05 < \alpha' < 2.05$ and $-1.05 < \alpha'' < 1.05$, that is, the physically reasonable ranges plus a small noise margin). In a sequence of fitting runs, the evolution of χ^2 was monitored while the fixed parameter was set to values that differed increasingly from the optimal value. The joint confidence region was then defined by the range within which χ^2 did not increase by more than 2-fold from the value obtained for the best fit. If we assume that the model fits the data ideally, the joint confidence region can be estimated as $\chi^2 \leq \chi^2_{\mathrm{min}}[1 + p/(n - p)F_{1-\alpha}(p,n - p)$, where $F_{1-\alpha}$ is the F-distribution with confidence level $1 - \alpha$.[42] For a confidence level of one standard deviation ($1 - \alpha = 0.683$) and with $n = 12$ and $p = 5$, the term in the brackets becomes 2.0.

Because this procedure is time-consuming, it was only performed for a selected number of time points. The confidence limits in Figure 4 illustrate that all fitting parameters were typically well constrained by the data above a certain surface coverage. For coverages below the half maximal frequency shift, the thickness was not well constrained, but reasonable estimates of the viscoelastic properties could still be obtained. The facts that we found a unique solution with low χ^2_{norm} and that most or all fitting parameters were well-constrained, provide good indications that the extracted values are reliable.

Thickness and Viscoelastic Properties of FGRD Films. From Figure 4, it can be seen that the acoustic thickness increased during film formation, that is, as a function of grafting density, reaching 30 ± 4 nm at maximal coverage. The maximal thickness was comparable to the value determined via an AFM nanoindentation assay and to previously reported data for

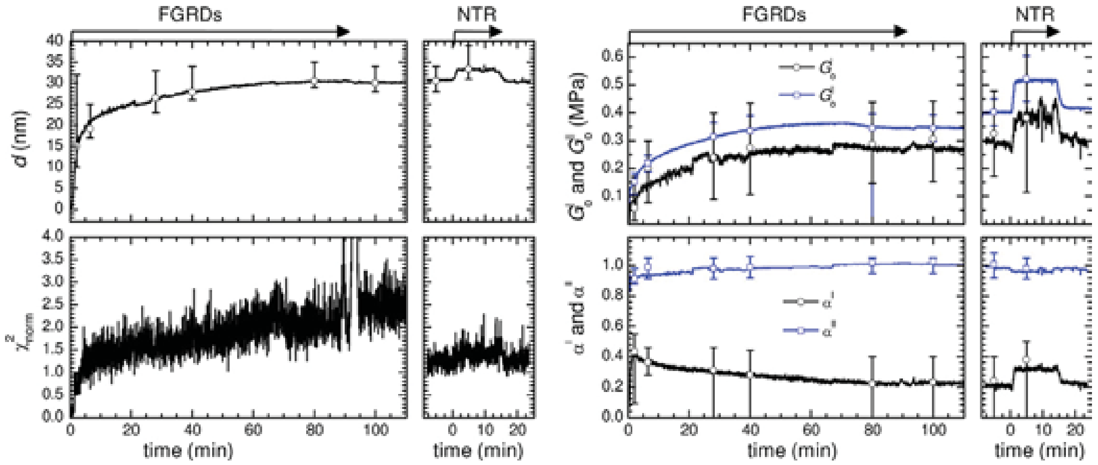

Figure 4. Viscoelastic modeling of the QCM-D data. The evolution of thickness d, viscoelastic properties (shear elastic modulus G'_0 and shear loss modulus G''_0 at f_0 = 15 MHz, and the frequency dependence α' and α'' of G' and G'', respectively) and χ^2_{norm} are shown for the data in Figure 1B,C. Error bars at selected time points correspond to the range of solutions within which χ^2 does not increase by more than 2-fold above the minimal value obtained at the given time point.

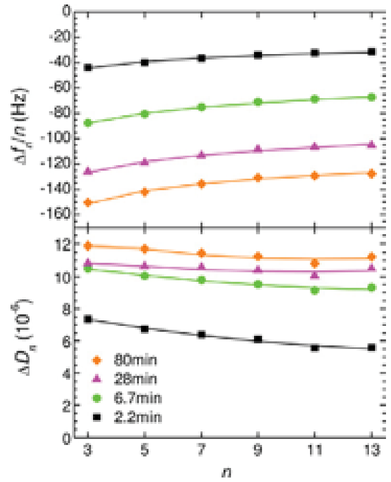

Figure 5. Quality of the fit. Experimental data (symbols) for selected time points (as indicated) during FGRD film formation (Figure 1B) are shown with the best fits by the viscoelastic model (lines). All measured overtones (n = 3−13) are presented.

Nsp1p FGRD films on SLBs (Table 1),[3,58] lending further support to the results of the fit. Binding of the NTR induced a marginal increase in film thickness, by approximately 4 nm, also in accordance with earlier experiments.[3] We note that the increase in film thickness is smaller than the size of the NTRs (Stokes diameter 7.8 nm[43]), consistent with swelling of the film upon absorption of NTRs (i.e., penetration into the film, as previously demonstrated with Nsp1p FGRD films on SLBs[3]) but inconsistent with the formation of a dense NTR monolayer by plain adsorption of NTRs on the film's surface.

With regard to viscoelastic properties, both the storage modulus G'_0 and the loss modulus G''_0 increased with coverage. At maximal coverage, they attained 0.30 ± 0.15 MPa and 0.35 ± 0.05 MPa, respectively. Incubation of the FGRD film with NTRs led to an increase in both moduli by about 0.1 MPa, indicating moderate film rigidification. α' decreased from about 0.4 to 0.2 during film formation, while α'' increased slightly, from 0.9 to 1.0. The NTR induced an increase of α' from 0.2 to 0.3, while α'' remained around 1.0. The viscoelastic parameters at maximal coverage compare well with the values reported for Nsp1p FGRD films on SLBs (Table 1).[3]

Both α' and α'' were nonzero, that is, the viscoelastic properties are frequency-dependent. In Figure 6A,B, this frequency dependence is illustrated graphically, in a double-logarithmic plot, for the fitting results corresponding to 2.2 and 100 min after the start of FGRD incubation. The two graphs reveal that, over the experimentally accessible frequency range, the storage modulus (i.e., the elastic component) remained

Table 1. Properties of Nsp1p FGRD Films at High Surface Coverage, as Determined from QCM-D Data through the Viscoelastic Model and from AFM Nanoindentation Assays

analysis method	d (nm)	G'_0 (MPa)	α'	G''_0 (MPa)	α''
		FGRD Film Built on His-Tag Capturing Sensor			
QCM-D[a]	30 ± 4	0.30 ± 0.15	0.2 ± 0.2	0.35 ± 0.05	1.00 ± 0.05
AFM[b]	30 ± 5[d]/∼40[e]	0.15 ± 0.05[e]	0		
		FGRD Film Built on SLB[c]			
QCM-D[a]	34 ± 4	0.18 ± 0.08	0.15 ± 0.15	0.29 ± 0.05	0.94 ± 0.03
AFM[b]	35 ± 5[d]/∼45[e]	0.15 ± 0.05[e]	0		

[a] G'_0 and G''_0 at f_0 = 15 MHz, α' and α'' for f = 15−65 MHz. [b] G'_0 at $f_0 \approx 10$ Hz, α' for $f \approx 1$ to 1000 Hz. [c] Data taken from ref 3. [d] Distance at which a force of 25 pN is reached, above which the interaction between the film and the indenter is considered significant. [e] Determined through fits to force curves, as described in Figure 7, and using $G' = 0.5E/(1 + \nu)$ with $0 \leq \nu \leq 0.5$.

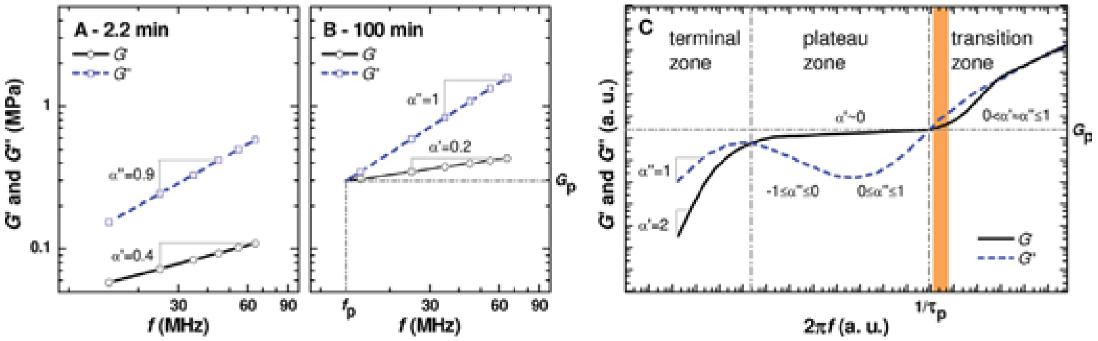

Figure 6. Frequency dependence of the viscoelastic properties of FGRD films and theoretical predictions. G' and G'' vs frequency are displayed in double-logarithmic plots. (A, B) Experimental results for an Nsp1p FGRD film at low (2.2 min after start of incubation; A) and maximal (100 min; B) grafting density. When extrapolated, the lines in B meet at f_p = 13 MHz and G_p = 0.3 MPa. (C) Theoretical predictions for a solution of entangled long-chain polymers (adapted from Figure 3 in ref 44; curves for a densely cross-linked polymer meshwork would be similar but lack the terminal zone[40]). Characteristic zones are indicated (see manuscript text for details). The results for the magnitude of G' relative to G'', and for the magnitudes of α' and α'', would be consistent with an evolution of the FGRD film's mechanical properties from the transition zone (at low grafting density) toward the plateau zone (at high grafting density) within the frequency range accessible by QCM-D (the frequency range shaded in orange in C would correspond to high grafting density). The relaxation time of entanglement or network strands, τ_p, and the plateau modulus, G_p, at the corresponding frequency are indicated.

below the loss modulus (i.e., the viscous component). Both moduli were of the same order of magnitude, that is, the film appeared viscoelastic within the frequency range accessible by QCM-D. With increasing surface coverage, the relative difference between G' and G'' decreased, that is, the film became increasingly elastic.

It is instructive to compare our experimental results with theoretical predictions for the viscoelastic properties of entangled polymer solutions or cross-linked polymer gels (Figure 6C).[40,44] In long-chain polymers, stress relaxation processes fall into two classes: segmental relaxations (fast) and disentanglement processes (slow). The frequencies of these relaxations define zones. On long time scales (terminal zone), the material flows like a viscous liquid ($G' \ll G''$, $\alpha'' = 1$). The terminal zone is only observed if the material is not permanently cross-linked. Because in our case the molecules were permanently linked to the surface, this zone is unlikely to occur. In the plateau zone (also called "rubber plateau"), the mechanical response is dominated by cross-links/entanglements. Here, the material appears predominantly elastic ($G' \gg G''$). Ideally, the storage modulus would be constant ($\alpha' = 0$), though in reality, α' is usually observed to be slightly larger than 0 because some relaxations do also occur in this frequency regime.[39,40] Hydrogen bonds, for example, tend to relax on a wide range of time scales. The magnitude of the storage modulus in the rubber plateau, G_p, contains information about the degree of cross-linking/entanglement. In the transition zone, the viscoelastic response is dominated by the dynamics of individual network strands. Here, $G' \approx G''$ and both moduli increase with frequency at a rate that depends on the details of the relaxation processes at play (typically $0 < \alpha' \approx \alpha'' < 1$).[40] Comparison with these theoretical predictions suggests that, for the FGRD film, the frequency range accessible by QCM-D (Figure 6A,B) is situated at the border between the plateau and transition zone (Figure 6C, region shaded in orange). In particular, G' and G'' have about the same magnitude, and α' approaches 0 while α'' is approximately 1. In this context, the decrease in α' from 0.4 to 0.2 with increasing grafting density (Figures 4 and 6A,B) suggests that the plateau zone approaches the QCM-D frequency range, as the coverage increases. By extrapolation of the curves in Figure 6B, we can estimate that, at maximal coverage, G' equals G'' at the frequency f_p = 13 MHz, corresponding to a time $\tau_p = 1/(2\pi f_p)$ = 12 ns, with the magnitude G_p = 0.3 MPa.

The comparison between theory and experiment would suggest that τ_p marks the time scale at which the plateau zone appears and that G_p, as determined through the viscoelastic model, is representative of the plateau modulus (i.e., the storage modulus in the plateau zone) of the entangled (and likely even transiently cross-linked[18]) meshwork that is formed by the monolayer of FGRDs. A rigorous test of this conjecture would require measurement of the viscoelastic properties of FGRD films at frequencies that are below those accessible by QCM-D. Accurate measurements of the viscoelastic properties of thin films remain challenging, but we can estimate the film's elasticity from its response to compression by an AFM indentation probe (Figure 7A). AFM approach speeds between 100 nm/s and 20 μm/s, and indentation depths on the order of 10 nm in these assays correspond to frequencies between 1 Hz and 1 kHz, whereas the QCM-D covers 15−75 MHz, that is, a difference between 4 and 8 orders of magnitude. In contrast to QCM-D, which is sensitive to shear deformation, AFM indents the film and hence measures the Young modulus E. Variations in the approach speed did not affect the force curves appreciably (data not shown), that is, α' = 0 across the frequency range covered by AFM, and $E \approx$ 0.3 MPa (Figure 7A). Assuming that the film is isotropic, the shear elastic modulus can be calculated from Young's modulus as $G' = 0.5E/(1 + \nu)$.[39] With typical Poisson ratios ν between 0 and 0.5,[39] G' would be between 0.1 and 0.2 MPa. Interestingly, the estimate based on the AFM data is only slightly inferior to the value obtained by QCM-D, as predicted by theory. This indicates that QCM-D can provide a reasonable estimate of the plateau modulus of FGRD films and that the plateau zone of Nsp1p FGRDs covers at least 7 orders of magnitude. Analysis of the previously reported[3] QCM-D and AFM data (Figure 7B) for Nsp1p FGRD films on SLBs gave similar results (Table 1). We infer that the QCM-D probes the viscoelastic properties at the border between the plateau zone and the transition zone for both immobilization platforms.

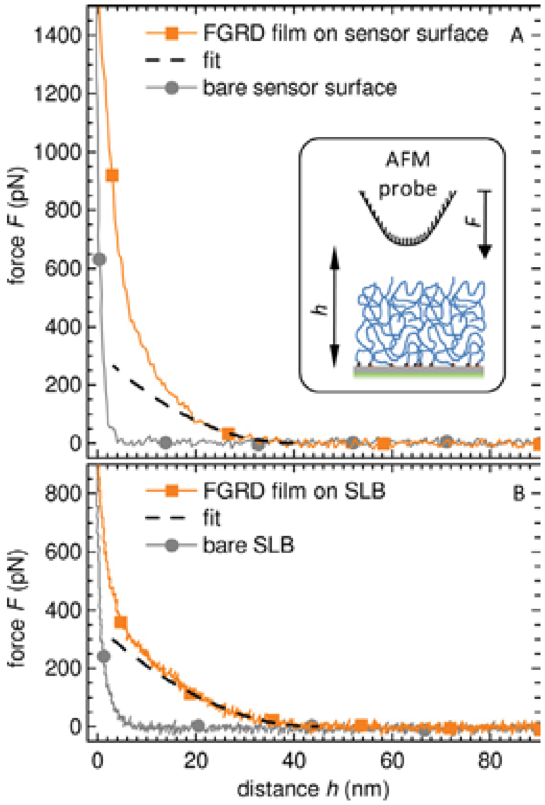

Figure 7. Compression of FGRD films by an AFM probe. (A) Representative force vs distance curve acquired at an approach rate of 500 nm/s on an Nsp1p FGRD-coated His-tag capturing surface (orange line with squares). Controls on a bare His-tag capturing surface before and after the compression assay (gray line with circles) demonstrate that the interaction of these surfaces with the AFM probe remained short-ranged (less than 5 nm). The black dashed line is an extrapolated fit with $F = \pi RdE \times (1 - h/d)^2$ over the range of h = 20–38 nm, providing estimates of d = 40 nm for the thickness of the uncompressed film and E = 0.3 MPa for Young's modulus in the linear compression regime (i.e., in which E is constant). (B) Force vs distance curve on an SLB-bound Nsp1p FGRD film (orange line with squares) and an SLB without FGRD (gray line with circles). The data was taken from Figure 4A in ref 3. The fit gave d = 45 nm and E = 0.3 MPa. The numbers for E are estimates due to the small probe size and uncertainties in the shape and radius of the indentation probes. The indentation probe was approximated by a sphere with radius R = 10 nm. The fitting formula is derived in the following way. Young's modulus is defined as $E = P/\sigma$ with the pressure (or stress) P and the strain $\sigma = 1 - h/d$. According to Derjaguin's approximation, the compression energy between two coplanar surfaces can be derived from the compression forces between a sphere and a plane as $W = F(h)/(2\pi R)$. Pressure is $P = \mathrm{d}W/\mathrm{d}h$. In the linear regime, E = constant. The fitting formula can be obtained by integrating both sides of $E\sigma = P$ with respect to h, with the boundary condition that $F(d) = 0$.

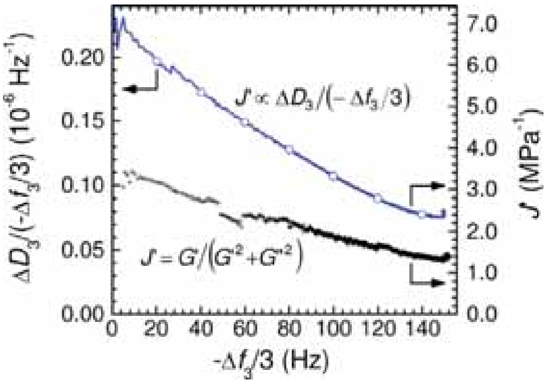

Figure 8. D/f plot and elastic compliance. $\Delta D_3/(-\Delta f_3/3)$ vs $-\Delta f_3/3$ (blue line with circles) for the Nsp1p FGRD film formation in Figure 1B. The right axis indicates the elastic compliance J', which to a first approximation is proportional to $\Delta D_3/(-\Delta f_3/3)$ according to ref 45. More accurate values for J', obtained through full viscoelastic modeling, are also shown (black crosses). Comparison of both methods reveals that the simple approximation overestimates the J' values by up to 2-fold.

Simple Approach To Estimate Elastic Compliance. Du and Johannsmann[45] recently proposed an alternative approach to estimate mechanical properties from QCM-D data. It is worthwhile to compare our results with their approach, which is attractive by its simplicity yet does not provide a full characterization of the viscoelastic properties. According to Du and Johannsmann,[45] the elastic compliance $J' \equiv G'/(G'^2 + G''^2)$ can be estimated from the ratio of the shifts in dissipation and frequency as $\Delta D_n/(-\Delta f_n/n) = 4\pi n\eta_1\rho_1/\rho \times J'(f)$, if the film is stiffer than the surrounding liquid and much thinner than the penetration depth, $\delta_1 = (\eta_1/(\pi n f_1 \rho_1))^{1/2}$, of the shear wave generated by the QCM-D sensor in that liquid. The experimental data of $\Delta D_3/(-\Delta f_3/3)$ and the resulting estimates for J' at $f \approx 15$ MHz as a function of frequency shift are displayed in Figure 8 (blue line with circles). For comparison, values of J' that were derived from G' and G'' through the full viscoelastic modeling are also shown (black crosses). The two different data sets for J' show values of the same order of magnitude, indicating that simple calculation of $\Delta D_n/(-\Delta f_n/n)$ can provide a reasonable order-of-magnitude estimate of J'. The exact values, however, are overestimated by up to 2-fold in this simplified approach. The deviation is not surprising if one notes that the FGRD film thickness is smaller yet on the same order of magnitude as δ_1, which is 137 nm for n = 3.[6,46] The decrease in $\Delta D_n/(-\Delta f_n/n)$ and in J' as a function of $-\Delta f$ nicely illustrates the gradual stiffening of the film. This response is consistent with a gradual increase in the concentration of proteins and transient cross-links (e.g., via inter-FG repeat interactions) in the film as the grafting density increases.

■ DISCUSSION

We have investigated the performance of a His-tag Capturing Sensor by studying an Nsp1p FGRD film as a model system. The main findings of this study are: (1) the model proteins could be immobilized stably, specifically and with high grafting densities; (2) the sensor surfaces could be successfully regenerated; (3) the viscoelastic properties of the supramolecular assembly of Nsp1p FGRDs could be quantified from fits with a viscoelastic model that explicitly considers the frequency dependence of viscoelastic properties to the QCM-D data.

Molecules equipped with a His-tag bound stably to the sensor surface, whereas the surface was inert to binding of proteins that lacked a His-tag. Immobilization of FGRDs on a surface is an appealing approach to characterize properties of FGRD assemblies and their interaction with NTRs, as it enables immobilization at controlled orientation and tunable densities, and application of surface-sensitive characterization techniques (here QCM-D, ellipsometry and AFM).[3,47−50] The His-tag capturing surface is attractive by its simplicity compared to other common methods for surface grafting of molecules such as SLBs. It can be used as provided without any further surface modification and regenerated after each measurement. From the estimated FGRD grafting density, we conclude that the surface can accommodate at least 10 pmol/cm^2 His-tagged molecules. Considering the size range of proteins, this density of binding sites should be sufficient to form dense monolayers of most, if not all, proteins. The His-tag capturing surface, hence, represents a generic platform for the immobilization of biomolecules in a well-controlled and functional orientation, for conformational, interaction, or mechanical studies using the QCM-D technique.

Viscoelasticity of FGRD and Other Ultrathin Polymer Films. Using Nsp1p FGRDs as an example, we have demonstrated that viscoelastic properties of ultrathin polymer films can be extracted from QCM-D data and AFM indentation assays. Consideration of the frequency ranges covered by both techniques, and the frequency dependence of G' and G'' observed within these ranges, suggests that both techniques can provide information about the viscoelastic properties in the plateau zone including the border between the plateau and transition zones (Figure 6C).

Because the viscoelastic properties in and the extension of the plateau zone arise from entanglements and cross-links, their characterization is of particular interest: they provide information about the dynamics and the morphology of polymer films.[39,40,51] A few simple estimates shall illustrate this for the FGRD film. The apparent molecular mass M_p of network or entanglement strands can be deduced from the plateau modulus using the relation $G_p \approx cN_AkT/M_p$, where c is the polymer concentration (in mass per volume), $N_A = 6.0 \times 10^{23}$ mol^{-1} is Avogadro's constant, and $kT = 4.1 \times 10^{-21}$ J is the thermal energy.[40,51] The estimated grafting density of $\Gamma_{max} = 10$ pmol/cm^2, a film thickness of 30 nm (Table 1) and the Nsp1p FGRD mass of 63 kDa give $c = 0.21$ g/mL. With $G_p = 0.3$ MPa, we obtain $M_p \approx 1.7$ kDa. The Nsp1p FGRD contains 600 amino acids, that is, the average mass per amino acid is 105 Da. Each strand hence contains about 16 amino acids. Interestingly, this value is comparable to the mean number of amino acids on the Nsp1p chain per each of its 33 FG repeats (18.2). With a length per amino acid of 0.35 nm, we can estimate the contour length of each strand to about 6 nm. Moreover, $\tau_p \approx 12$ ns is a measure of the relaxation time of these strands.[40,44]

We remind that the above estimates should be considered apparent values, because we assumed that the meshwork is homogeneous and we did not distinguish between entanglements and cross-links. Cross-links (Figure 1A, left) or entanglements (Figure 1A, right) are expected to dominate the meshwork properties if the FGRDs do or do not interact attractively with each other, respectively. Because inter-FG repeat interactions might be functionally important,[17,18,54,55] we do now consider these two scenarios explicitly.

We have previously reported that Nsp1p FGRDs form macroscopic gels even at concentrations that are 25-fold below those attained in our grafted film.[18] With the good correlation between the size of meshwork strands in our film and the mean number of amino acids per FG repeat unit on the Nsp1p chain, and considering that the confinement of one chain end to the surface should decrease the entropic penalty for interchain interactions compared to a mobile chain in a macroscopic solution, it is likely that our film is indeed a cross-linked gel. For a homogeneous meshwork that is dominated by cross-links, the correlation length ξ, corresponding to the distance between cross-links, is the measure for the mesh size. In this case, the plateau modulus is given by $G_x \approx kT/\xi^3$ and occurs at times larger than the relaxation time of network strands $\tau_\xi \approx \eta_1\xi^3/(kT)$.[40] Values of 2 and 4 nm for ξ are obtained from $G_p \approx 0.3$ MPa and $\tau_p \approx 12$ ns, respectively. The two values are in reasonable agreement, if one considers the error bars on our data and that the relations for G_x and τ_ξ are based on scaling approximations and, hence, accurate to within a numerical prefactor of order unity.[40] The viscoelastic data, therefore, is consistent with the picture of a densely cross-linked gel.

To test if our data can discriminate between entanglements and cross-links, we consider also the other extreme, that is, a meshwork that is dominated by entanglements. This situation would arise if the end-grafted peptide chains do not interact attractively with each other. Due to their mutual repulsion, the chains tend to stretch away from the surface. However, as the chains are flexible, they resist complete stretching and thus also explore the lateral dimensions, leading to entanglements with neighboring chains. In the nucleocytoplasmic transport field, the scenario of end-grafted, noninteracting chains is commonly, though imprecisely, termed a "brush-like, entropic barrier"[15,50] or "entropic bristles"[52] and opposed to a cross-linked gel.[15,50] More generally, in polymer physics, a polymer brush is defined as a dense arrangement of end-grafted polymer chains.[53] Within this definition, both entangled and cross-linked polymer films can be considered brushes, provided that they are end-grafted to a surface at sufficient density (i.e., the average distance between adjacent grafting points is smaller than the size that free polymer coils would adopt in dilute solution). Films of end-grafted, purely entangled polymer chains (Figure 1A, right) are, hence, a special case of a brush as are films of end-grafted, densely cross-linked polymer chains (Figure 1A, left). For purely entangled meshworks, two characteristic length scales are important: (1) the correlation length ξ, now more generally defined as the average distance from a monomer on one polymer chain to the nearest monomer on another chain, and (2) the entanglement tube diameter a, that is, the end-to-end distance of an entanglement strand. In this case, the plateau modulus is $G_e \approx kT/(a^2\xi)$ and starts at the entanglement relaxation time $\tau_e \approx \eta_1 a^4/(kT\xi)$.[40,44] $G_p \approx 0.3$ MPa and $\tau_p \approx 12$ ns give $\xi \approx 1.5$ nm and $a \approx 3.0$ nm, that is, $a > \xi$, yet both are of the same order of magnitude, as predicted by theory and found in experiments for entangled polymer solutions.[40] The viscoelastic data are, hence, also consistent with the picture of an entangled meshwork.

In entangled meshworks, both ξ and a determine the diffusion of noninteracting particles as a function of particle size, as described by Cai et al.[44] In cross-linked meshworks, ξ is the only relevant parameter. Within the accuracy of the scaling arguments, the values for ξ in a cross-linked gel and for a in an entangled meshwork, respectively, agree well with the size exclusion limit measured for the NPC's permeability barrier (5 nm).[8] This supports the conjecture that the polymer meshwork nature of FGRD assemblies in the nuclear pore complex is sufficient to explain their resistance to translocation of (sufficiently large) noninteracting particles, as proposed in several models of nucleo-cytoplasmic transport.[17,52,54,55]

The nuclear pore permeability barrier contains many different types of FGRDs, and inter-FG repeat interactions have been proposed to be functionally important.[17,18,54,55] Even though, for the reasons outlined above (i.e., Nsp1p forms stable macroscopic gels, the size of meshwork strands correlates with the mean number of amino acids per Nsp1p FG repeat unit, and confinement to the surface should enhance attractive interactions), we favor the notion that the Nsp1p film represents a densely (yet perhaps transiently) cross-linked polymer meshwork, the here-presented methodology does per se not allow to unambiguously exclude alternative models when based on an isolated data set because of the limited frequency range accessible by QCM-D. Future experiments by QCM-D and complementary surface-sensitive techniques on different FGRD films, including mutants of FGRDs, should enable quantitative comparison of the interaction strength and provide insight about variations in the degree of cross-linking/entanglement. Because the film thickness, the mode of chain attachment, and the FGRD grafting density can be controlled and matched to the conditions in the NPC, such measurements are likely to correspond more closely to the native conditions than measurements in macroscopic FGRD gels or solutions.[18] In this context, the $\Delta D/-\Delta f$ ratio as a first estimate of the elastic compliance J' (Figure 8) represents a simple and robust parameter to be used for comparison between different films, while the full viscoelastic modeling provides more detailed and accurate information.

The discussion above highlights that, by considering G'_0 and G''_0, as well as α' and α'', novel insight into the morphology and dynamics of ultrathin polymer films can be obtained. To our knowledge this application of QCM-D has so far not been fully appreciated. There is increasing evidence that the mechanical properties of biomolecules and their assemblies are functionally important in many biological processes.[56] Also, thin polymer films are becoming increasingly popular for a range of technological and sensing applications.[24,25] Therefore, the methodological approach presented here should be of interest to many other biomolecular or synthetic polymer films.

CONCLUSIONS

We have demonstrated that the His-tag Capturing Sensor presents a platform to create dense monolayers of His-tagged FGRDs and, by extension, other His-tagged proteins or peptides, in a simple way for QCM-D protein interaction studies. The formation of the FGRD layer and its interaction with NTRs could be followed label-free and in real-time by QCM-D. The QCM-D response compared very well to our earlier report of Nsp1p FGRDs grafted to a functionalized supported lipid bilayer.

Moreover, we showed how frequency-dependent viscoelastic properties and the acoustic thickness of the FGRD monolayer can be extracted from the QCM-D data. The presented data analysis method is not restricted to the immobilization platform used here, but can be readily applied to other surfaces that are covered with a laterally homogeneous polymer film. The QCM-D data together with AFM data suggest that, for the film under study, QCM-D is sensitive to the viscoelastic parameters at the border between the plateau zone and the transition zone. As a consequence, QCM-D can provide access to information about the morphology (i.e., characteristic length scales) and dynamics (i.e., relaxation times), which is likely to be relevant for the function of nanoscale FGRD meshworks and of interest for many other ultrathin polymer films.

AUTHOR INFORMATION

Corresponding Author

*E-mail: rrichter@cicbiomagune.es. Phone: +34 943 0053 29. Fax: +34 943 0053 15.

Notes

The authors declare no competing financial interest.

ACKNOWLEDGMENTS

We thank D. Görlich (Göttingen, Germany) for discussions and support, and M. Schubert (Lincoln, U.S.A.) for discussions. R.P.R. acknowledges funding from the Spanish Ministry of Science and Innovation (MICINN, refs RYC2009-04275 and MAT2011-24306), and the Department of Industry of the Basque Government. N.B.E. was supported by the Göttingen Graduate School for Neuroscience, Biophysics and Molecular Biosciences (DFG Grant GSC 226/1).

REFERENCES

(1) Hutschenreiter, S.; Tinazli, A.; Model, K.; Tampe, R. *EMBO J.* **2004**, *23*, 2488−2497.

(2) Wolny, P. M.; Banerji, S.; Gounou, C.; Brisson, A. R.; Day, A. J.; Jackson, D. G.; Richter, R. P. *J. Biol. Chem.* **2010**, *285*, 30170−30180.

(3) Eisele, N. B.; Frey, S.; Piehler, J.; Görlich, D.; Richter, R. P. *EMBO Rep.* **2010**, *11*, 366−372.

(4) Celia, H.; Wilson-Kubalek, E.; Milligan, R. A.; Teyton, L. *Proc. Natl. Acad. Sci. U.S.A.* **1999**, *96*, 5634−5639.

(5) Lata, S.; Gavutis, M.; Piehler, J. *J. Am. Chem. Soc.* **2006**, *128*, 6−7.

(6) Reviakine, I.; Johannsmann, D.; Richter, R. P. *Anal. Chem.* **2011**, *83*, 8838−8848.

(7) Denning, D. P.; Rexach, M. F. *Mol. Cell Proteomics* **2007**, *6*, 272−282.

(8) Mohr, D.; Frey, S.; Fischer, T.; Güttler, T.; Görlich, D. *EMBO J.* **2009**, *28*, 2541−2553.

(9) Görlich, D.; Kutay, U. *Annu. Rev. Cell Dev. Biol.* **1999**, *15*, 607−660.

(10) Weis, K. *Curr. Opin. Cell Biol.* **2002**, *14*, 328−335.

(11) Denning, D. P.; Patel, S. S.; Uversky, V.; Fink, A. L.; Rexach, M. *Proc. Natl. Acad. Sci. U.S.A.* **2003**, *100*, 2450−2455.

(12) Bayliss, R.; Littlewood, T.; Stewart, M. *Cell* **2000**, *102*, 99−108.

(13) Bayliss, R.; Leung, S. W.; Baker, R. P.; Quimby, B. B.; Corbett, A. H.; Stewart, M. *EMBO J.* **2002**, *21*, 2843−2853.

(14) Bayliss, R.; Ribbeck, K.; Akin, D.; Kent, H. M.; Feldherr, C. M.; Görlich, D.; Stewart, M. *J. Mol. Biol.* **1999**, *293*, 579−593.

(15) Peters, R. *Bioessays* **2009**, *31*, 466−477.

(16) Ader, C.; Frey, S.; Maas, W.; Schmidt, H. B.; Gorlich, D.; Baldus, M. *Proc. Natl. Acad. Sci. U.S.A.* **2010**, *107*, 6281−6285.

(17) Frey, S.; Görlich, D. *Cell* **2007**, *130*, 512−523.

(18) Frey, S.; Richter, R. P.; Görlich, D. *Science* **2006**, *314*, 815−817.

(19) Milles, S.; Lemke, E. A. *Biophys. J.* **2011**, *101*, 1710−1719.

(20) Charnley, M.; Textor, M.; Acikgoz, C. *React. Funct. Polym.* **2011**, *71*, 329−334.

(21) Chen, M.; Briscoe, W. H.; Armes, S. P.; Klein, J. *Science* **2009**, *323*, 1698−1701.

(22) Gribova, V.; Crouzier, T.; Picart, C. *J. Mater. Chem.* **2011**, *21*, 14354−14366.

(23) Fleer, G. J.; Cohen Stuart, M. A.; Scheutjens, J. M. H. M.; Cosgrove, T.; Vincent, B. *Polymers at Interfaces*; Chapman & Hall: London, 1993.

(24) Senaratne, W.; Andruzzi, L.; Ober, C. K. *Biomacromolecules* **2005**, *6*, 2427−2448.

(25) Decher, G. *Science* **1997**, *277*, 1232−1237.

(26) Domack, A.; Prucker, O.; Rühe, J.; Johannsmann, D. *Phys. Rev. E* **1997**, *56*, 680−689.

(27) Voinova, M. V.; Rodahl, M.; Jonson, M.; Kasemo, B. *Phys. Scr.* **1999**, *59*, 391−396.

(28) Johannsmann, D. http://www2.pc.tu-clausthal.de/dj/software_en.shtml.

(29) Johannsmann, D. *Macromol. Chem. Phys.* **1999**, *200*, 501−516.
(30) Johannsmann, D. *Phys. Chem. Chem. Phys.* **2008**, *10*, 4516−4534.
(31) Hutter, J. L.; Bechhoefer, J. *Rev. Sci. Instrum.* **1993**, *64*, 1868−1873.
(32) Carton, I.; Brisson, A. R.; Richter, R. P. *Anal. Chem.* **2010**, *82*, 9275−9281.
(33) De Feijter, J. A.; Benjamins, J.; Veer, F. A. *Biopolymers* **1978**, *17*, 1759−1772.
(34) Seedorf, M.; Damelin, M.; Kahana, J.; Taura, T.; Silver, P. A. *Mol. Cell. Biol.* **1999**, *19*, 1547−1557.
(35) Höök, F.; Kasemo, B.; Nylander, T.; Fant, C.; Sott, K.; Elwing, H. *Anal. Chem.* **2001**, *73*, 5796−5804.
(36) Larsson, C.; Rodahl, M.; Hook, F. *Anal. Chem.* **2003**, *75*, 5080−5087.
(37) Tsortos, A.; Papadakis, G.; Mitsakakis, K.; Melzak, K. A.; Gizeli, E. *Biophys. J.* **2008**, *94*, 2706−2715.
(38) Iruthayaraj, J.; Olanya, G.; Claesson, P. M. *J. Phys. Chem. C* **2008**, *112*, 15028−15036.
(39) Ferry, J. D. *Viscoelastic Properties of Polymers*, 3rd ed.; Wiley & Sons: New York, 1980.
(40) Rubinstein, M.; Colby, R. H. *Polymer Physics*; Oxford University Press: Oxford, 2003.
(41) Johannsmann, D. Studies of Viscoelasticity with the QCM. In *Piezoelectric Sensors*; Steinem, C., Janshoff, A., Eds.; Springer: Berlin, Heidelberg, 2007; Vol. *5*, pp 49−109.
(42) Draper, N. R.; Smith, H. *Applied Regression Analysis*, 2nd ed.; John Wiley and Sons Ltd.: New York, 1981.
(43) Jovanovic-Talisman, T.; Tetenbaum-Novatt, J.; McKenney, A. S.; Zilman, A.; Peters, R.; Rout, M. P.; Chait, B. T. *Nature* **2008**.
(44) Cai, L. H.; Panyukov, S.; Rubinstein, M. *Macromolecules* **2011**, *44*, 7853−7863.
(45) Du, B.; Johannsmann, D. *Langmuir* **2004**, *20*, 2809−2812.
(46) Tellechea, E.; Johannsmann, D.; Steinmetz, N. F.; Richter, R. P.; Reviakine, I. *Langmuir* **2009**, *25*, 5177−5184.
(47) Lim, R. Y. H.; Huang, N.-P.; Köser, J.; Deng, J.; Lau, K. H. A.; Schwarz-Herion, K.; Fahrenkrog, B.; Aebi, U. *Proc. Natl. Acad. Sci. U.S.A.* **2006**, *103*, 9512−9517.
(48) Lim, R. Y. H.; Köser, J.; Huang, N.-P.; Schwarz-Herion, K.; Aebi, U. *J. Struct. Biol.* **2007**, *159*, 277−289.
(49) Lott, K.; Bhardwaj, A.; Mitrousis, G.; Pante, N.; Cingolani, G. *J. Biol. Chem.* **2010**, *285*, 13769−13780.
(50) Lim, R. Y. H.; Fahrenkrog, B.; Köser, J.; Schwarz-Herion, K.; Deng, J.; Aebi, U. *Science* **2007**, *318*, 640−643.
(51) de Gennes, P.-G. *Scaling Concepts in Polymer Physics*; Cornell University Press: Ithaca; London, 1979.
(52) Rout, M. P.; Aitchison, J. D.; Magnasco, M. O.; Chait, B. T. *Trends Cell Biol.* **2003**, *13*, 622−628.
(53) Jones, R. A. L.; Richards, R. W. *Polymers at Surfaces and Interfaces*; Cambridge University Press: Cambridge, U.K., 1999.
(54) Ribbeck, K.; Görlich, D. *EMBO J.* **2001**, *20*, 1320−1330.
(55) Ribbeck, K.; Görlich, D. *EMBO J.* **2002**, *21*, 2664−2671.
(56) Discher, D.; Dong, C.; Fredberg, J. J.; Guilak, F.; Ingber, D.; Janmey, P.; Kamm, R. D.; Schmid-Schonbein, G. W.; Weinbaum, S. *Ann. Biomed. Eng.* **2009**, *37*, 847−859.
(57) Richter, R. P.; Brisson, A. *Langmuir* **2003**, *19*, 1632−1640.
(58) It should be born in mind that, for films that exhibit a density gradient along the surface normal, the thickness will depend on the method by which it is measured and, therefore, only an approximate comparison is warranted. The acoustic thickness determined by QCM-D relied on the box-profile approximation. The thickness from the AFM indentation assay reported in ref 3 (see also footnote [d] in Table 1) was based on the definition of a threshold force above which an interaction between the film and the indenter is considered significant. The thickness estimates provided in Figure 6 (see also note [e] in Table 1), even though extracted from the same AFM indentation data, give a somewhat larger value because they rely on a model for film elasticity instead of a force threshold.

5 Cohesiveness tunes assembly and morphology of FG repeat domain meshworks

This chapter constitutes a manuscript which will be submitted soon as:

Cohesiveness tunes assembly and morphology of FG nucleoporin domain meshworks – Implications for nuclear pore permeability

Authors: **Nico B. Eisele**[a,b], Aksana A. Labokha[b], Steffen Frey[b], Dirk Görlich[b], Ralf P. Richter[a,c,d]

[a] Biosurfaces Unit, CIC biomaGUNE, Paseo Miramon 182, 20009 San Sebastian, Spain
[b] Department of Cellular Logistics, Max Planck Institute for Biophysical Chemistry, Am Faßberg 11, 37077 Göttingen, Germany
[c] I2BM, Department of Molecular Chemistry, J. Fourier University, 570 Rue de la Chimie, 38041 Grenoble Cedex 9, France
[d] Max Planck Institute for Intelligent Systems, Heisenbergstraße 3, 70569 Stuttgart, Germany

Contribution of authors: Nico B. Eisele, Steffen Frey, Dirk Görlich and Ralf P. Richter designed research. Nico B. Eisele performed QCM-D, ellipsometry, and FRAP measurements and analyzed data. Aksana A. Labokha and Steffen Frey purified proteins. Ralf P. Richter performed AFM measurements and analyzed data.

5.1 Abstract

Nuclear pore complexes (NPCs) control the exchange of macromolecules between the cytoplasm and the nucleus. A selective permeability barrier which arises from a supramolecular assembly of intrinsically unfolded nucleoporin domains rich in phenylalanine-glycine dipeptides (FG domains) fills the nuclear pore. There is increasing evidence that selective transport requires cohesive FG domain interactions. To understand the functional roles of cohesiveness, we studied monolayers of end-grafted FG domains as a bottom up nanoscale model system of the permeability barrier. Based on detailed physico-chemical analysis of the model films and comparison of the data with polymer theory, we propose that cohesiveness is tuned to promote rapid assembly of the permeability barrier and to generate a stable and compact pore-filling meshwork with a small mesh size. Our results highlight the functional importance of weak interactions, typically a few $k_{\mathrm{B}}T$ per chain, and contribute important information to understand the mechanism of size-selective transport.

Bulk macromolecular transport between the cytosol and the nucleus of eukaryotic cells is gated through nuclear pore complexes (NPCs) [1, 2, 3, 4], large protein assemblies that perforate the nuclear envelope. To form an NPC, several types of nucleoporin proteins self-assemble in multiple copies into a ring-like structure with a central channel of 35-40 nm in diameter [5]. Specialized nucleoporin domains that are natively unfolded and rich in FG dipeptides (FG domains) are grafted at high density to the channel walls [6] and constitute a selective permeability barrier: molecules smaller than 5 nm in diameter [7] can diffuse efficiently through the channel, whereas larger molecules are delayed or blocked, unless they are bound to nuclear transport receptors (NTRs) [1, 2, 3, 8].

The physical mechanism behind transport selectivity remains poorly understood. Several models have been proposed [9, 10, 11, 12, 13]. They share the idea that the permeability barrier of NPCs arises from the supramolecular assembly of FG domains. The structure of the FG domain meshwork inside the NPC remains elusive, presumably because it is highly dynamic and exhibits a low degree of order. There is, however, increasing evidence that FG domains can interact attractively with each other [14, 15, 16, 17], and that these interactions are essential for the formation of a functional permeability barrier [14, 18].

We hypothesize that the combination of flexible chains, their confinement through grafting, and their cohesiveness determines the functionality of the permeability barrier. Cohesiveness is heterogeneously distributed within FG domain chains: cohesive patches, made of FG, FxFG, or GLFG motives but also other amino acids, are interspaced with repulsive sequences [17, 19, 20, 21, 22]. The balance of these interactions, together with the confinement of the chains, will ultimately determine the organization and dynamics of the nanoscale FG domain meshwork in a way that is crucially important for function, yet, not well understood.

To explore experimentally how the balance of interactions affects the morphology and dynamics of FG domain assemblies, we exploited a recently developed nanoscale model system of the permeability barrier: planar films of FG domains that are end-grafted to supported lipid bilayers (SLBs) (see figure 5.1 A) [23, 24]. The films reproduce the native permeability barrier in the following aspects: the FG domains are end-grafted, the film thickness is comparable to the dimensions of the nuclear pore, and the FG repeat densities are comparable. Compared to the native pore or reconstituted systems that reproduce the pore-like topology [18, 25], the choice of a planar geometry provides excellent control on film formation and greatly facilitates a detailed and quantitative characterization of the film morphology and dynamics.

To rationalize the behavior of our films, we took advantage of classical theoretical concepts of polymer physics. We hypothesized that the average degree of cohesiveness, rather than the exact distribution of cohesive elements along the chain, determines ensemble physico-chemical properties of FG domain assemblies. Figure 5.1 schematically shows theoretical predictions about the morphology of end-grafted and flexible, regular polymers of varying cohesiveness [26, 27]. Within this theoretical framework, cohesive-

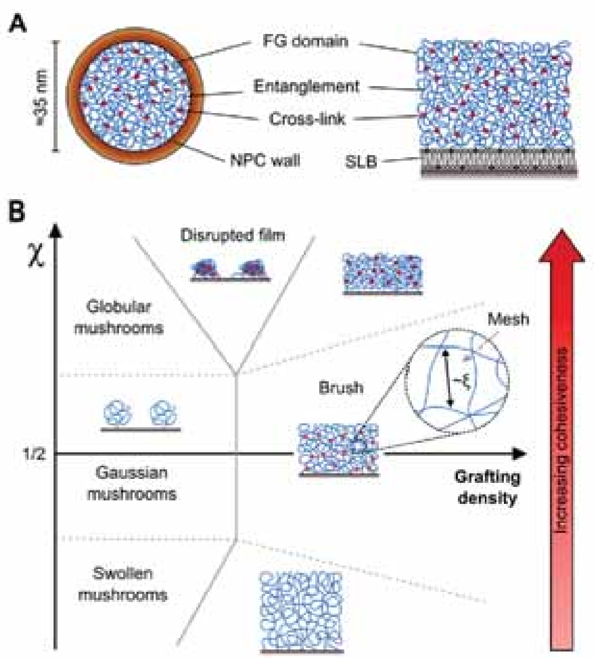
A
≈35 nm
FG domain
Entanglement
Cross-link
NPC wall
SLB
B
χ
Disrupted film
Globular mushrooms
Mesh
Brush
~ξ
1/2
Gaussian mushrooms
Grafting density
Swollen mushrooms
Increasing cohesiveness

Figure 5.1: ***Supramolecular assembly of FG domains, and predictions by polymer theory:*** *(A) Schematic cross section of the yeast NPC perpendicular to its axis. FG domains are anchored to the NPC wall at high density. The flexible, intrinsically disordered chains explore the NPC channel, interpenetrate, and may form cross-links (red circles) to form the permeability barrier. (A, right) Monolayers of SLB-grafted FG domains are used as model systems of the permeability barrier, to study the impact of cohesiveness on the organization and dynamics of FG domain assemblies at the nm scale. (B) Schematic phase diagram, summarizing simple theoretical predictions for films of flexible, regular, end-grafted polymers as a function of the Flory interaction parameter* ξ *(or cohesiveness) and grafting density. The brush and disrupted film phases are of particular interest for this study. Boundaries between phases are drawn qualitatively. The interpenetration of chains in the brush (insets) gives rise to the correlation length* ξ*, a measure of the average mesh size.*

ness receives a precise physical meaning. It is identical to the so-called Flory interaction parameter χ, which is determined by the (average) relative strength of polymer-polymer, polymer-solvent and solvent-solvent interactions. In the absence of cohesive interactions, a sufficiently high grafting density entails the formation of a so-called brush, in which the film is laterally homogeneous and its chains are partially stretched away from the grafting surface. When the chains become weakly cohesive, the stretching will decrease and an increasingly dense film is expected to form. As the overall cohesiveness increases further, lateral phase separation occurs, driven by the maximization of inter-chain interactions. Depending on the grafting density and cohesiveness, different morphologies can arise [27, 28]: a continuous film perforated by pores, an array of isolated clusters of several polymer chains, or an array of globules of individual chains. Flexible chains in a brush do also explore the lateral dimensions, implying that they show some degree of interpenetration. This aspect is frequently neglected when sketching polymer brushes (e.g. in Refs. [13] and [29]) yet it might be functionally important. On a local scale, the film forms a meshwork of interpenetrating chains, and the so-called correlation length ξ is a measure for the mean mesh size [30, 31, 32].

In this paper, we provide evidence that FG domains, despite their heterogeneous primary structure, faithfully reproduce the basic theoretical predictions for regular, flexible polymers. To this end, we compared different types of FG domains, including mutants. The FG domains were selected for their difference in cohesiveness, based on their propensity to form macroscopic hydrogels. ”Nup98-glyco” is an O-GlcNAc-modified, 485 amino acid long FG domain from *Xenopus tropicalis* Nup98. This domain forms tight macroscopic hydrogels and is essential for forming a selective permeability barrier in NPCs reconstituted from *Xenopus* egg extracts [18, 22]. Nsp1-WT, a 600 amino acid FG domain from *Saccharomyces cerevisiae*, consists of a highly cohesive N-terminal domain and a less cohesive C-terminal domain [17, 29] but still forms tight macroscopic hydrogels [14, 15]. Nsp1-FILV→S, a mutant Nsp1 FG domain in which all hydrophobic amino acids were exchanged by the hydrophilic serine, does not form macroscopic hydrogels [17]. We demonstrate that the morphologies outlined in figure 5.1b can be generated if the cohesiveness is adjusted appropriately. We argue that the self-organization phenomena that we observe on planar surfaces are relevant for the NPC topology, and discuss the broad implications for the assembly and function of the permeability barrier.

5.2 Results

5.2.1 FG domain film assembly and its kinetics

Specific and stable end-grafting of FG domains with different cohesiveness (Nup98-glyco, Nsp1-WT, and Nsp1-FILV→S) through terminal His-tags to SLBs doped with Ni^{2+}-NTA functionalized lipids [33] was confirmed by quartz crystal microbalance with dissipation monitoring (QCM-D; Supplementary figure 5.9 and 5.10).

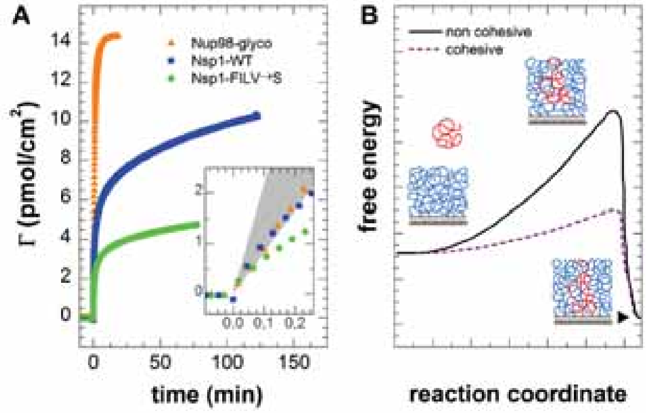

Figure 5.2: ***Kinetics of FG domain film assembly and maximal grafting density depend strongly on FG domain type:*** *(A) Film formation was monitored by ellipsometry. At 0 min 0.9 μM FG domains were added to SLBs containing 10 mol-% bis-NTA functionalized lipids. All FG domains were incubated under identical stirring conditions. Initial adsorption (inset) is similar for all FG domains and limited by mass transport (the gray shaded area represents theoretically estimated mass transport rates, see Methods for details). At higher coverage, adsorption rates differ significantly between FG domains. (B) Schematic free energy profiles for the binding of FG domain molecules to an FG-domain-covered SLB. The barrier due to entropically unfavorable partitioning of new molecules into the existing FG domain film (black curve) is lowered through weak, attractive inter-chain interactions (purple curve).*

Grafting density and film formation kinetics were quantified by spectroscopic ellipsometry (SE; figure 5.2 A). The different FG domains initially adsorbed with similar rates, consistent with mass-transport-limited binding. Clearly, all FG domains can bind rapidly to a sparsely covered SLB, i.e. binding of the His-tag to the Ni^{2+}-NTA group is not rate limiting. The adsorption rates decreased with increasing surface density, and the decrease in rate differed drastically between FG domains: it was very pronounced for

Nsp1-FILV→S, less pronounced for Nsp1-WT, and barely noticeable for Nup98-glyco up to $\Gamma = 10\,\text{pmol/cm}^2$. The grafting densities of both Nsp1 constructs remained well below this density during the first hour of incubation, indicating that availability of Ni^{2+}-NTA anchor groups did not limit binding of Nsp1 constructs within this time.

A strongly coverage-dependent decrease in the binding rate, as observed for the Nsp1-FILV→S mutant, is consistent with theoretical predictions for the formation of polymer brushes made from non-interacting polymers: the brush-forming polymers constitute an entropic barrier (figure 5.2 B) against the access of free polymers from solution to the SLB, entailing a coverage-dependent reduction in the binding rate [34]. Cohesiveness would be predicted to facilitate entry and partitioning of polymers into the surface-confined film, and we propose that this is the reason why Nsp1-WT and Nup98-glyco continue to bind rapidly at surface coverages that are inhibitory for Nsp1-FILV→S. The entropic penalty associated with the partitioning of polymers from the solution into the film increases with coverage, and differences in the cohesiveness would readily explain why Nup98-glyco retained a high binding rate longer than Nsp1-WT.

5.2.2 Thickness, concentration, and mechanical properties of FG domain meshworks

To test how different degrees of cohesiveness affect FG domain film thickness, we prepared and compared different FG domain films at grafting densities close to the maximal coverage attainable with Nsp1-FILV→S (i.e. $5.1 \pm 0.3\,\text{pmol/cm}^2$, or one molecule per $31 \pm 2\,\text{nm}^2$; Supplementary figure 5.11). These values compare well with the estimated average surface area per FG domain chain in a yeast NPC which would be 24 - $32\,\text{nm}^2$, assuming a channel of $35 - 40\,\text{nm}$ in diameter and $30 - 35\,\text{nm}$ in length [5], and approximately 136 FG domains per channel [6, 35].

AFM indentation assays with a nanosized probe (figure 5.3) revealed film thicknesses in the range of a few 10 nm, consistent with the formation of a monolayer of weakly extended polypeptide chains. The Nsp1-FILV→S mutant formed the thickest films (35 ± 5 nm), Nsp1-WT a film of intermediate thickness (25 ± 8 nm), and Nup98-glyco the thinnest film (17 ± 3 nm). Thickness values determined from QCM-D (by fitting the QCM-D to a visco-elastic model, see figure 5.12) and SE data of films prepared under identical conditions showed the same trend (figure 5.3b), corroborating the AFM data. From the thickness determined by AFM and the grafting density, we can estimate the concentration of FG domains in the films to be 85 ± 13 mg/ml for Nsp1-FILV→S, 146 ± 47 mg/ml for Nsp1-WT, and 191 ± 34 mg/ml for Nup98-glyco. Clearly, increasing FG domain cohesiveness promotes the formation of more compact films with higher FG domain concentration.

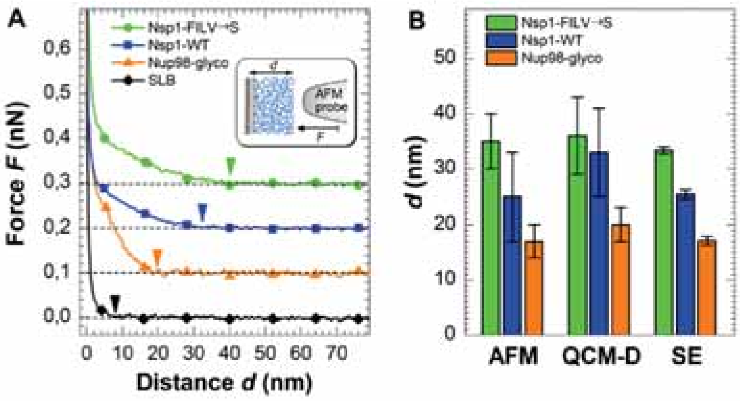

Figure 5.3: *The strength of inter-FG repeat interactions affects the thickness and concentration of FG domain films:* *(A) AFM indentation assays (schematically described in the inset) on FG domain films with a grafting density of 5.4, 5.1, and 4.8 pmol/cm^2 for Nup98-glyco, Nsp1-WT, and Nsp1-FILV→S, respectively, were carried out to estimate the film thickness. The thickness was determined by the distance between the onset of repulsive forces (arrowheads) and the hard-wall compression limit ($d = 0$). Control curves on SLB-covered silica before and after the indentation assays were taken to validate that the interaction with the probe remained short-ranged. AFM measurements were performed by Ralf Richter, CIC BiomaGUNE, San Sebastian, Spain. (B) Film thicknesses determined by AFM indentations assays, and independently through viscoelastic modeling of QCM-D data (Supplementary figure 5.12) and optical modeling of ellipsometry data on identically prepared FG domain films. The stronger the cohesiveness the thinner and denser the film.*

A polymer meshwork should become stiffer when increasing the concentration or interaction strength. For thin, homogeneous films, the elastic compliance (or inverse of

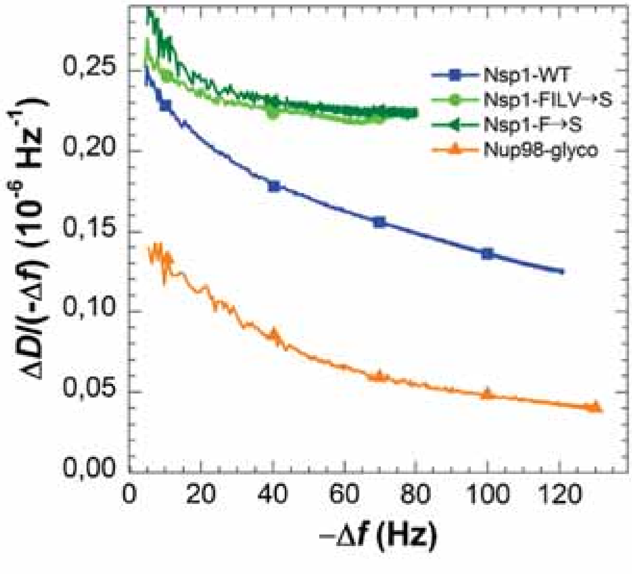

Figure 5.4: ***Cohesiveness leads to stiffer FG domain films:*** *A parametric plot of $\Delta D/-\Delta f$ vs. $-\Delta f$ monitored by QCM-D during film formation, provides an estimate of the evolution of the elastic compliance (inverse of stiffness) of FG domain monolayers with coverage. Differences in the mechanical properties of the FG domain films can be clearly discriminated by this plot. To evaluate the contribution of phenylalanines to the stiffness of Nsp1-WT meshworks, we included additionally an Nsp1 construct in which exclusively phenylalanines were mutated to serines (Nsp1-F→S). Nsp1-F→S and Nsp1-FILV→S exhibited very similar curves, indicating that the F→S mutation is sufficient for the loss of cohesivity compared to Nsp1-WT.*

stiffness), J', can be estimated directly from QCM-D data [24, 36]. Figure 5.4 displays the evolution of the ratio of QCM-D dissipation and frequency shifts, $\Delta D/-\Delta f$, which is proportional to J'/ρ, where ρ is the film density, during the process of film formation. All curves exhibited a monotonous decrease in $\Delta D/-\Delta f$ with increasing absolute frequency shifts (or surface coverage), consistent with a gradual increase in protein concentration and perhaps even attractive interactions within the films [24]. The magnitudes of the $\Delta D/-\Delta f$ values varied significantly between FG domain types, indicating that film stiffness indeed depends on the quality of the respective FG domain. Nup98-glyco and Nsp1-FILV→S formed the most rigid and soft films, respectively, while Nsp1-WT formed films of intermediate rigidity, consistent with the trends observed for film compaction and film formation kinetics. Interestingly, we could not find any difference in stiffness between Nsp1-FILV→S and another Nsp1 construct in which exclusively phenylalanines were mutated to serines (Nsp1-F→S). This indicates that F is essential for formation of the cross-links that make Nsp1-WT stiffer than its mutant forms, whereas I, L and V, which together contribute only 19 % of the total content in hydrophobic amino acids of the Nsp1 FG domain, only play a subordinate role.

5.2.3 Lateral homogeneity of and chain mobility in FG domain meshworks

To test how the nature of the FG domains affects the supramolecular organization along the surface plane, we imaged FG domain films at selected grafting densities by AFM (figure 5.5). Nup98-glyco films at grafting densities of 12 and 9 pmol/cm^2 (figure 5.5 A and B) appeared overall homogeneous. Small-scale surface corrugations with a characteristic lateral length scale of about 20 nm could be clearly imaged, whereas any feature of smaller size eluded imaging. When decreasing the surface density to 5.4 pmol/cm^2 (figure 5.5 C), depressions appeared. The depressions were shallow yet their diameter of typically about 100 nm was already several times wider than the transport channel of NPCs. When further decreasing the grafting density, the film became very heterogeneous, showing holes of several 100 nm in diameter (figure 5.5 D). We believe that these holes traverse the film completely, even though the apparent depth of the holes in figure 5.5 D (approximately 5 nm) is likely to be smaller than the unperturbed thickness of the surrounding film. Most likely, the discrepancy arises because the FG domain film is transiently compressed upon encounter with the AFM probe, even under the gentlest imaging conditions. Indeed, we observed the measured depth of the holes to sensitively depend on the imaging conditions, i.e. a subtle decrease in the AFM cantilever's set-point amplitude, which is a measure of the pressure that the AFM probe exerts on the film, entailed a significant further reduction (by a few nm) in apparent depth (data not shown).

Despite the films' compliance, the lateral surface features of all Nup98-glyco films varied only little, if at all, upon repeated imaging for extended times (up to one hour). Measurements by fluorescence recovery after photobleaching (FRAP; figure 5.6 A) confirmed that SLB-bound Nup98-glyco domains have no detectable lateral mobility.

The stability of film morphology is direct evidence that inter-chain interactions within end-grafted Nup98-glyco assemblies are sufficiently strong to drive self-organization into temporally stable and rather dense hydrogel phases at the nm scale. If the grafting density is too low, the hydrogel phase is disrupted. In contrast, if the density is sufficiently high, a laterally homogeneous hydrogel can form. Nsp1-WT films, formed at 6.6 pmol/cm^2, were laterally homogeneous but exhibited some apparent roughness (figure 5.5 E). In contrast to Nup98-glyco, the surface features varied strongly upon repeated imaging, indicating that the grafted Nsp1-WT molecules retain sufficient mobility to reorganize rapidly. Images of Nsp1-WT and Nsp1-FILV→S films at 5.5 pmol/cm^2 appeared so smooth that they were indistinguishable from images of a pure SLB (figure 5.5 F), i.e. they were too soft to be imaged and readily penetrated by the AFM tip. Complementary FRAP measurements provided direct evidence that lateral mobility is retained for Nsp1-WT and Nsp1-FILV→S (figure 5.6 B and C). Clearly, the cohesiveness of Nsp1-WT (as well as Nsp1-FILV→S) is too weak to drive the formation of stable aggregates in FG domain monolayers. This result is in obvious contrast with the observation of stable Nsp1-WT hydrogels at the macroscopic level [14, 15].

Figure 5.5: ***Grafting density and cohesiveness influence the morphology of FG domain assemblies*** *(right page)***:** *Images by AFM of different FG repeat domain films. The left column shows low magnification images ($2.5 \times 1.25\,\mu m^2$). The right column shows images at higher magnification ($1 \times 0.5\,\mu m^2$), which were either obtained by digital zoom (from zones encased by orange solid lines in the left column) or by imaging at a higher resolution. Nup98-glyco films at a grafting density of (A) 12 and (B) 9 pmol/cm^2 show a homogeneous surface with a distinct and stable small-scale morphology. (C) At 5.4 pmol/cm^2 shallow depressions of typically 100 nm width and a few nm in depth appear. (D) At 4.0 pmol/cm^2 the film becomes highly heterogeneous, with holes of several 100 nm in width that are likely to fully traverse the film. (E) Nsp1-WT films at 6.6 pmol/cm^2 appear homogeneous with some apparent roughness that could not be imaged stably. (F) Control image of a pure SLB. Color bar: false color coding of relative heights; scale bars: 200 nm; insets show height profiles of selected scan lines (white dashed lines). AFM measurements were performed by Ralf Richter, CIC biomaGUNE, San Sebastian, Spain.*

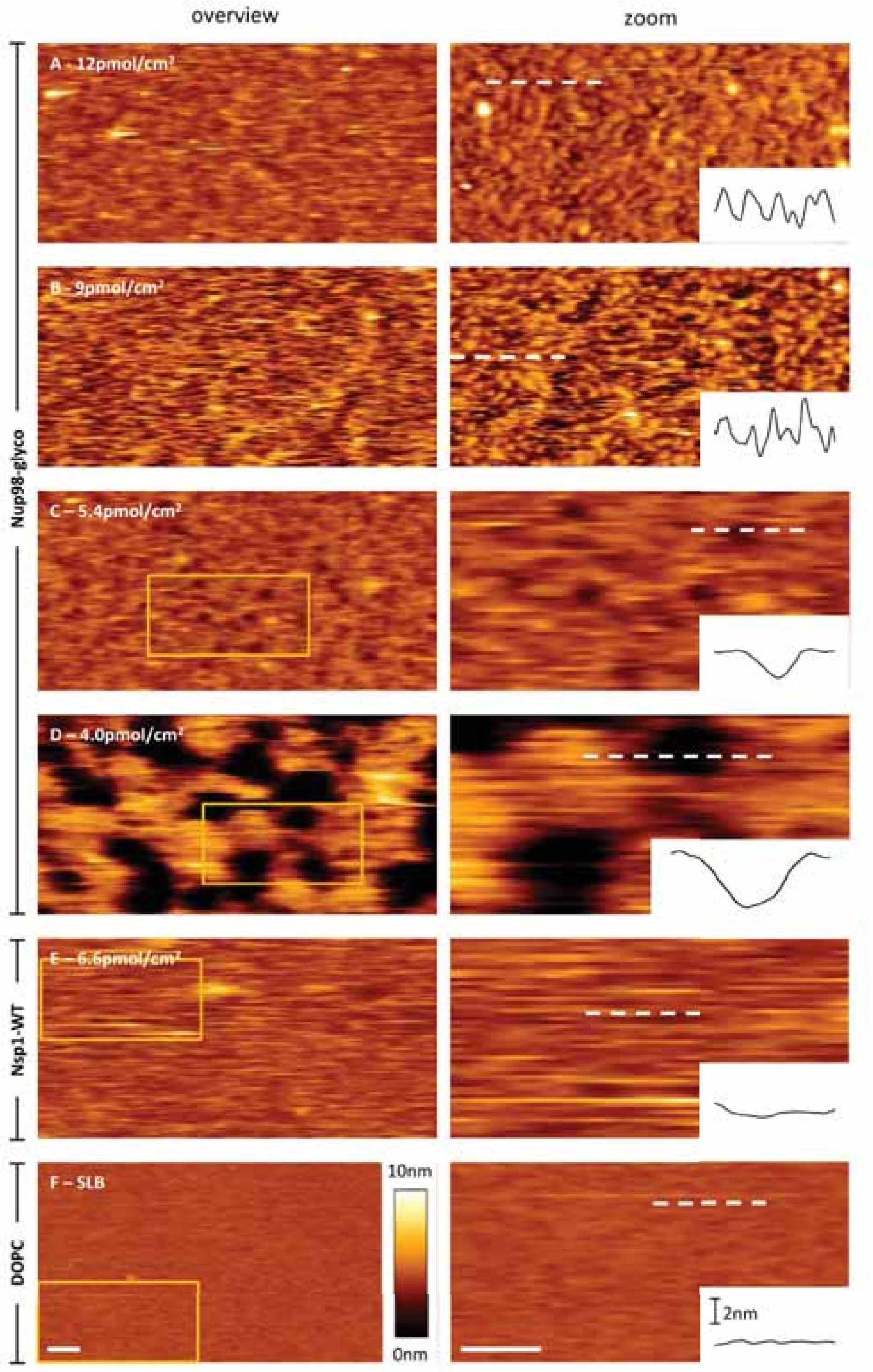
overview
zoom
A - 12pmol/cm²
B - 9pmol/cm²
C – 5.4pmol/cm²
D – 4.0pmol/cm²
E – 6.6pmol/cm²
F – SLB
Nup98-glyco
Nsp1-WT
DOPC
10nm
0nm
2nm

Figure 5.5

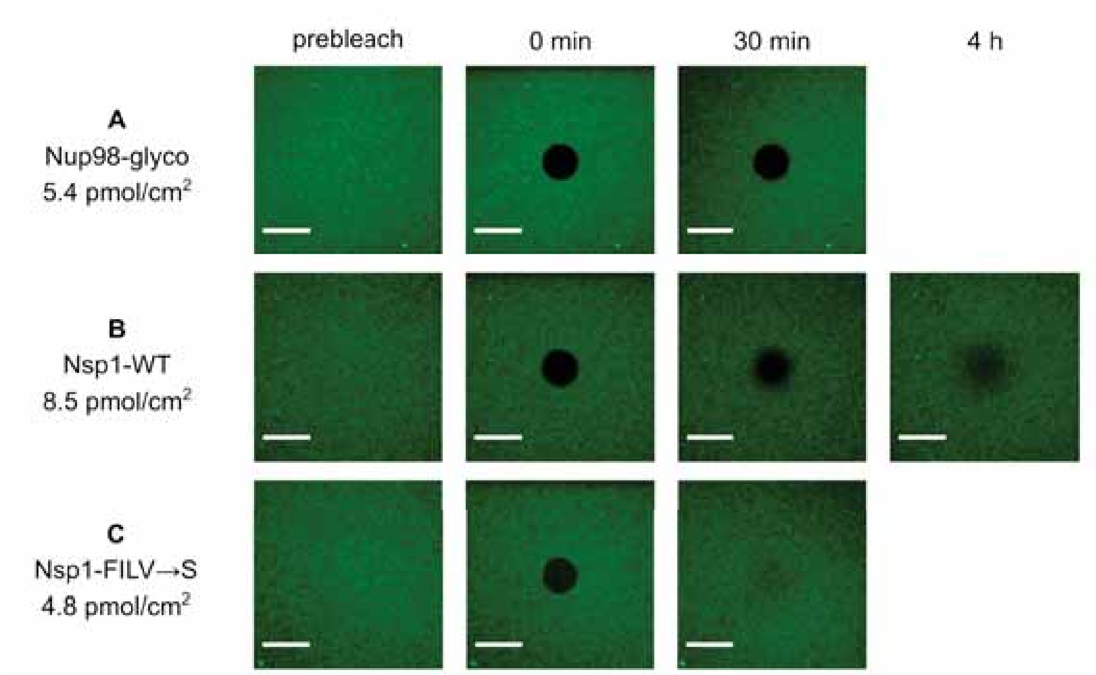

Figure 5.6: ***Lateral mobility of FG domain films:*** *Measurements by fluorescence recovery after photobleaching (FRAP). (A) Nup98-glyco, even at a relatively low surface coverage (5.4 pmol/cm^2), did not show any significant recovery of the bleached central spot within 30 min. (B) In contrast, a slow yet significant recovery, was observed for Nsp1-WT even at close-to-maximal surface density, demonstrating that the FG domains are laterally mobile within the film. (C) Also Nsp1-FILV→S showed recovery, which was quicker and almost complete within 30 min. Scale bar: 30 μm.*

5.2.4 Energy of film compaction

Cohesive interactions effectively lower the free energy of grafted FG domain chains. In the cases of no or weak cohesiveness (i.e. $\chi \geq 0.5$), mean field theory [37] predicts a free energy increase (in units of thermal energy $k_\mathrm{B}T$) of $E \approx 2h^2/(Nb^2)$ upon confinement of a chain in the brush, where b is the statistical (Kuhn) segment length ($b = 0.76\,\mathrm{nm}$, i.e. twice the contour length of an amino acid in polypeptides) and N is the number of segments (or half the number of amino acids) per chain. The AFM results for h (figure 5.3 B) correspond to free energies of 14 ± 5, 8 ± 5 and $4 \pm 2\,k_\mathrm{B}T$, respectively, for Nsp1-FILV→S, Nsp1-WT and Nup98-glyco. The value for Nup98-glyco should be considered an upper bound, because this FG domain forms only a weak brush, i.e. at the borderline to a disrupted film, under the employed surface coverage (figure 5.5 C).

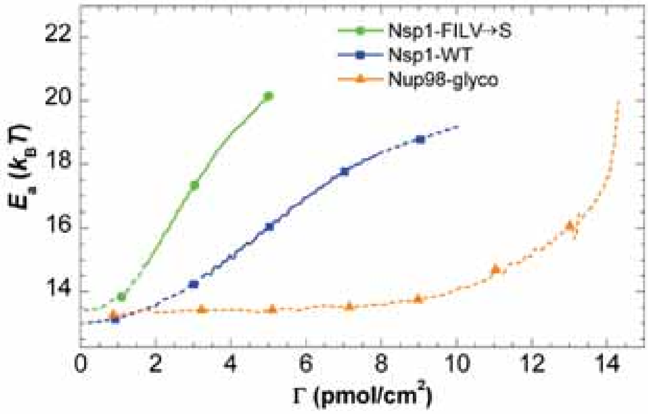

Figure 5.7: *Quantification of the energy for FG domain film compaction from binding rates:* *Activation energies E_a were determined from the FG domain binding rates $d\Gamma/dt$ in figure 5.2 as a function of grafting density Γ through $d\Gamma/dt = cA\exp(E_A/k_BT)$, where $c = 0.9\mu M$ is the concentration of FG domains in the bulk solution. Following the theoretical considerations for the formation of brushes by Ligoure and Leibler [34], we set $A = 6\pi^2/2^{1/3} \times k_BTM_W/\left(\eta_0 N_A \rho b^5 N^2\right) \approx 4.13\,mol\ m\ s^{-1}\ g^{-1}\ M_W/N^2 \cdot \eta_0 = 0.9\,mPa\,s$ is the solution viscosity, $N_A = 6.02 \times 10^{-23} mol^{-1}$ is Avogadro's number, $\rho = 1.3\,g/cm^3$ is the protein partial specific volume [38], $b = 0.76nm$ is the statistical (Kuhn) segment length (or twice the contour length of an amino acid), N is the number of segments (or half the number of amino acids) per FG domain chain, and M_w the FG domain molecular weight. As long as binding is limited by the permeation of an incoming molecule through the FG domain film (solid lines), the activation energy is equivalent to the free energy increase associated with partitioning and stretching of the chain in the film. In the limits of low and high coverage (dashed lines), mass transport limitations and saturation of the Ni^{2+}-NTA binding sites on the SLB, respectively, impose an upper limit on the experimentally accessible activation energies. The differences between the activation energies for Nsp1-FILV→S on one hand, and Nsp1-WT or Nup98-glyco on the other, correspond to the energies of film compaction due to cohesiveness. At $5\,pmol/cm^2$, it amounts to $3\,k_BT$ for Nsp1-WT and $\geq 7\,k_BT$ for Nup98-glyco.*

Provided that binding is limited by the FG domain film, the free energy increase can also be related to binding rates (figure 5.2 A) through Arrhenius' law, $d\Gamma/dt = A\exp(E/k_{\mathrm{B}}T)$ [34]. The pre-factor A depends only weakly on the FG domain type, and we estimate energy gains of 3 and $7\,k_{\mathrm{B}}T$ for Nsp1-WT and Nup98-glyco, respectively, compared to Nsp1-FILV→S, at $\Gamma = 5\,\mathrm{pmol/cm^2}$ (figure 5.7). The value for Nup98-glyco is a lower limit, because binding of this FG domain remained mass transport limited until higher grafting densities. Both approaches for the estimation of energy gains produce similar results. They reveal that the average free energy cost per amino acid, or per FG unit of typically 15 to 20 amino acids, for film compaction is rather small, typically on the order of 0.01, or 0.1 $k_\mathrm{B}T$, respectively.

5.3 Discussion

We have used monolayers of selected types of FG domains to study the effect of cohesiveness on the morphology of FG domain assemblies at the nanoscale. The monolayers mimic the conditions in the native NPC as FG domains are end-grafted to a surface at comparable densities. Under these conditions, cohesiveness drastically affected various film properties, i.e. formation kinetics, morphology (thickness and lateral homogeneity), chain mobility and mechanical properties. Importantly, the observed morphologies, and their dependence on cohesiveness, are in good qualitative agreement with theoretical predictions for regular, flexible polymer chains (figure 5.1 B). Our study provides evidence that theoretical concepts for regular, flexible polymers are pertinent to predict the self-organization behavior of FG domains. We propose that such concepts are useful to better understand the permeability barrier's mechanism of function.

5.3.1 Impact of cohesiveness on the morphology and implications for the size selectivity of the permeability barrier

Applying these theoretical concepts to the topology of the NPC transport channel - a cylinder that is short, i.e. the diameter roughly equals the length - and considering that the grafting density in our planar systems is comparable to that in the native NPC, different morphologies would be expected as a function of cohesiveness between polymer chains (figure 5.8). Without cohesiveness, a continuous polymer meshwork would occupy the entire channel and pervade a rather large space around the channel entrances (figure 5.8 A). Balanced inter-chain interactions induce compaction into a denser meshwork (figure 5.8 B). If the cohesiveness becomes too strong, i.e. at free energy gains well beyond a few $k_\mathrm{B}T$ per chain, the continuity of the meshwork is disrupted. Polymer chains may form a collapsed phase near the wall (figure 5.8 C), as experimentally observed on planar surfaces (figure 5.5 C and D), or become partially stretched close to the wall and collapsed at the channel's center [28, 39, 40].

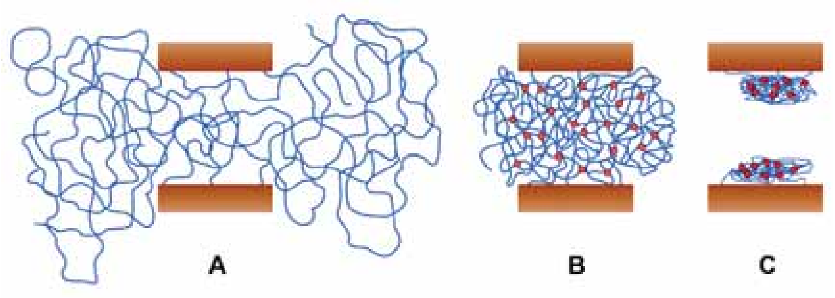

Figure 5.8: *Impact of cohesiveness on the supramolecular FG domain assembly in the NPC topology:* *Scheme of a cross section along the channel axes, based on predictions from polymer theory for flexible, grafted polymers. (A) If the inter-chain interactions are only weakly attractive or repulsive, an extended brush forms, and chains entangle into a meshwork with a characteristic mesh size. (B) With moderate inter-FG-domain interactions, the meshwork becomes denser; the characteristic mesh size and the size-exclusion limit decrease. (C) Strong inter-chain interactions generate a discontinuous and leaky meshwork that fails to fill the entire channel. Tuning the cohesiveness of FG domains hence provides a robust strategy to optimize the size-selectivity of the nuclear pore permeability barrier.*

The performance of these morphologies as permeability barriers would differ drastically. Size selectivity would be almost completely lost in the scenario shown in figure 5.8 C, because even rather large molecules can rapidly diffuse through spaces that are not occupied by the FG domain meshwork. The assemblies sketched in figure 5.8 A and B should both feature size-selective permeability, albeit to a different extent [24, 31, 32]. To a first approximation, both assemblies can be characterized by an average mesh size. Molecules smaller than the mesh can readily permeate the FG domain assembly, whereas the diffusion of larger molecules is slowed down [31, 32]. In meshworks of flexible polymers, the mesh size is predicted to decrease with polymer concentration with a power between 3/4 and 1, depending on χ [30, 31, 32]. Consequently, the roughly two-fold increase in FG domain concentration that we observed between non-cohesive

Nsp1-FILV→S and strongly cohesive Nup98-glyco (at identical grafting density) would translate into a decrease in the mesh size by 40 % or more. This simple estimate illustrates that a compaction of the FG domain meshwork through inter-chain interactions (figure 5.8 B) can decrease the size-exclusion limit for inert proteins considerably. We would like to stress that the improvement in size selectivity through film compaction is expected to persist even if the individual inter-chain interactions (or cross-links) are very short lived. In such a ”compacted meshwork”, the size-exclusion limit arises predominantly from the mutual confinement of interpenetrating polymer chains [31, 32]. With increasing stability, cross-links can add another quality to the meshwork, i.e. they improve size selectivity further, because they enhance the spatial confinement of chains and thereby stabilize the meshes [31]. Whether compaction alone is sufficient or stable cross-links, as they are formed in a hydrogel, are also required to accomplish the degree of size-selective permeability that is characteristic for the NPC remains an open question to be addressed in future work.

Based on our experimental results and polymer theory concepts, we conjecture that the formation of a dense and continuous pore-filling phase of FG domains is a viable strategy to create a barrier that effectively excludes inert molecules based on their size. Tuning of the overall cohesiveness emerges as a robust and efficient way to generate such architecture for the grafting densities and FG domain contour lengths that are typical in NPCs. At the same time, such a phase would enable translocation of NTRs, according to the selective phase model, as previously demonstrated *in vitro* with macroscopic FG domain hydrogels [15, 22, 41] and reconstituted NPCs [18]. In the presence of NTRs, FG domain meshworks were found to have enhanced size selectivity [25, 42]. Further studies on FG domain monolayers should aim at understanding how NTRs affect the morphology [23, 43], size selectivity, and mechanical properties [24] of FG domain meshworks.

5.3.2 FG domains can form nanoscopic hydrogels

Structural characterization by AFM (figure 5.5 A – C) and FRAP analysis (figure 5.6 C) provide strong evidence that, in physiological buffer, end-grafted Nup98-gyco assembles into stable hydrogels. This implies that certain FG domains can retain hydrogel properties even in assemblies with dimensions comparable to the NPC, where the size of the assembly is only a few times larger than the native extension of the individual molecules in isolation. This is, however, not the case for all FG domains, and Nsp1 is a case in point: films of end-grafted Nsp1-WT remained fluid - irrespective of whether they were grafted through the C-terminus (figure 5.5 E and figure 5.6 B) or the N-terminus [23] - even though this FG domain forms stable macroscopic hydrogels [14]. Amyloid type structures [17] and a hierarchical structural organization [44] have been reported in the macroscopic Nsp1-WT hydrogels. The distinct physical state of Nsp1-WT films suggests that these complex structural features may not be retained in nanoscale Nsp1-WT assemblies. Constraints in molecular orientation imposed by grafting and/or effects of scale might inhibit their development. Future studies with other FG domain types should be useful to test how widespread the formation of stable hydrogels in end-grafted films is, and if the contrast between macroscopic and nanoscopic behavior is unique to Nsp1. The recent finding that Nup98-glyco but not Nsp1 FG domains can restore a selective permeability barrier in NPCs reconstituted from partially FG-domain-depleted *Xenopus* egg extracts [18], whereas both FG domains form highly selective macroscopic hydrogels [14, 15, 18, 22], suggests that the ability to form a nanoscopic hydrogel might well have functional significance.

5.3.3 Impact of cohesiveness on NPC biogenesis and stability

Figure 5.2 demonstrates that cohesiveness can greatly facilitate the assembly of end-grafted FG domain meshworks. Because the NPC is a self-assembled architecture, this effect might be important for the rate of NPC biogenesis. Moreover, stretching of grafted chains in a brush at NPC-relevant grafting densities entails entropic penalties that can readily amount to $10\,k_{\mathrm{B}}T$ or more. Unless equilibrated by cohesive inter-chain interactions, this penalty decreases the stability of FG domain anchorage. We therefore propose that cohesiveness facilitates (and might even be essential for) the correct and timely assembly and for the stability of the permeability barrier. Indeed, a non-cohesive Nup98-FIL→S mutant, were F, I and L residues were mutated to serines, was found to require higher concentrations for efficient incorporation into reconstituted NPCs than wild type Nup98-glyco [18].

5.3.4 Impact of heterogeneities on the performance of the permeability barrier

We argued above that a continuous pore-filling meshwork is required for the correct function of the permeability barrier. This meshwork, however, may not be entirely homogeneous. For example, it is well known that the density of polymers in planar brushes exhibits a parabolic profile in the direction normal to the surface [45, 46]. Spatial variations in the FG repeat density might very well occur inside the NPC, both along and perpendicular to the channel axis, owing to the geometrical constraints of the channel [39, 47]. Variations in FG repeat density and cohesiveness within [17, 29] and between [16] individual FG domains might contribute further heterogeneities, as illustrated by a recent simulation study [47].

In particular, such variations could explain the results by Ma et al. (2012) who proposed preferred transport paths for inert molecules and NTRs, respectively, that were spatially separated yet interdependent [48]. Recent simulations by Osmanovic et al. (2012) suggest that tuning of cohesiveness sensibly affects the distribution of FG repeats perpendicular to the channel axis [40]. We conclude that the results by Ma et al. (2012) do not represent firm evidence against the selective phase model, as had been proposed by the authors. Instead, we conjecture that the location of transport paths may vary between cellular species as a function of the fine tuning of cohesive interactions, but that the existence of a preferred path at a precise location is not essential for the functionality of the permeability barrier.

Cohesiveness of FG domains and the position of FG domains in the NPC might also be interconnected to further optimize size and species selectivity of the permeability barrier. For example, FG domains that are located at the periphery of the permeability barrier might be less cohesive, to occupy a larger volume for catching NTRs from solution, while FG domains in the center could show stronger cohesion to form a tight and highly size selective meshwork [16].

Clearly, such heterogeneity effects cannot be captured by simple theories of flexible polymers. Their understanding is likely to require more sophisticated theoretical [40, 49] and experimental approaches that consider explicitly the heterogeneous primary structure of FG domains and/or the topology of NPCs. We have therefore intentionally chosen to keep our comparison between theory and experiment largely on a qualitative level. However, we propose that the simple conceptual approach presented here captures essential features underlying the function of the permeability barrier.

To summarize, we have demonstrated that FG domain monolayers show different film formation kinetics, morphologies, dynamics, and mechanical properties depending on the type of employed FG domain. In agreement with predictions from polymer theory we attribute these findings to different degrees of cohesiveness between FG domains. Based on the analysis of our data in terms of simple theoretical concepts for assemblies of flexible polymers, we propose the formation of a compact FG domain assembly that fills the entire pore - a compacted meshwork - as a key design principle for a functional permeability barrier. Tuning of inter-chain interactions, within the range of a few $k_{\mathrm{B}}T$ of free energy per chain, emerges as a robust and effective tool to optimize functionality. It should be beneficial for the biogenesis and stability of NPCs, and useful as a design rule for the engineering of man-made species-selective filtering devices.

5.4 Methods

5.4.1 Proteins and buffer

We used the following FG domains: Nsp1-WT (amino acids 2 to 601; 62.1 kDa), Nsp1-F→S (58.8 kDa), Nsp1-FILV→S (57.9 kDa), and Nup98-glyco (amino acids 1 to 485, with about 30 O-GlcNAc modified Ser and Thre residues per chain (2); 55.3 kDa) without His-tag; Nsp1-WT (64.1 kDa), Nsp1-F→S (60.8 kDa), and Nsp1-FILV→S (60.4 kDa) with C-terminal His_{10}-tag; and Nup98-glyco (58.8 kDa) with N-terminal His_{14}-tag. FG domains with and without a His-tag were purified as described earlier [22, 23]. To obtain fluorescently labeled FG domains, the N-terminal cysteine of the Nsp1 FG domain constructs and the C-terminal cysteine of Nup98-glyco were reacted with Atto488-maleimide and purified by high-performance liquid chromatography as described previously [15]. All FG domains were stored at a concentration of 10 mg/ml in 50 mM Tris pH 8 and 6 M guanidine hydrochloride (GuHCl) at -80 °C. Prior to use, the FG domains were diluted in working buffer (10 mM Hepes, pH 7.4, 150 mM NaCl) to desired concentrations. The dilutions were chosen such that the residual concentration of GuHCl in the final solution was below 75 mM.

5.4.2 Surfaces

Silica-coated QCM-D sensors (QSX303, Biolin Scientific, Vaestra Froelunda, Sweden) and silicon wafers with a native oxide layer of less than 2 nm thickness (University Wafers, South Boston, MA, USA) were cleaned by immersion in a 2 % sodium dodecyl sulfate solution for 30 min, rinsing with ultrapure water, blow-drying with nitrogen, and exposure to UV/ozone (BioForce Nanosciences, Ames, IA, USA) for 30 min. Glass cover slips (#1.5, $24 \times 24\,\text{mm}^2$; Menzel Glaeser, Thermo Scientific, Germany) were immersed in freshly prepared piranha solution, i.e. a 1:3 (*v*/*v*) mixture of 50 % H_2O_2 and concentrated H_2O_2 for 1 h, rinsed with ultrapure water, and blow-dried with nitrogen. Cleaned substrates were stored in air and again exposed to UV/ozone (30 min) prior to use.

5.4.3 Preparation of lipids and lipid vesicles

Lyophilized dioleoylphosphatidylcholine (DOPC) was purchased from Avanti Polar Lipids (Alabaster, AL, USA). Lipid analogues with chelator headgroups comprising either two or three nitrilotriacetic acid moeieties (bis-NTA or tris-NTA, respectively) [33] were kindly provided by J. Piehler (University of Osnabrueck, Germany). Lipid vesicles were prepared as described earlier [33, 50]. Before use, vesicle suspensions were diluted to 50 µg/mL in working buffer containing 10 mM $NiCl_2$.

5.4.4 Quartz crystal microbalance with dissipation monitoring (QCM-D)

QCM-D measures changes in resonance frequency, Δf, and dissipation, ΔD, of a sensor crystal upon interaction of (soft) matter with its surface. The QCM-D response is sensitive to the mass (including hydrodynamically coupled water) and the mechanical properties of the surface-bound layer [51]. To a first approximation, a decrease in Δf indicates a mass increase, while high (low) values of ΔD indicate a soft (rigid) film. Adsorption processes were monitored *in situ* with sub-second time resolution. QCM-D measurements were performed with a Q-Sense E4 system (Biolin Scientific). The system was operated in flow mode with a flow rate of typically 20 µL/min using a syringe pump (KD Scientific, Holliston, MA, USA). The working temperature was 23 °C. Δf and ΔD were measured at the fundamental ($n = 1$) and typically 6 overtones ($n = 3, 5 \ldots 13$), corresponding to resonance frequencies of $f_n \approx 5, 15, 25 \ldots 65$ MHz. Changes in dissipation and normalized frequencies, $\Delta f_n/n$, for $n = 5$ are presented.

5.4.5 Spectroscopic ellipsometry (SE)

SE (M2000V, Woollam, NE, USA) on silicon wafers was performed using an open fluid cell with continuously stirred sample solution, and data were fitted with the software CompleteEASE (Woollam, NE, USA) using a model of multiple optically homogeneous layers, as previously described [23, 52]. The FG domain film was treated as a transparent Cauchy medium with optical thickness d_{opt} and wavelength-dependent refractive index n. The FG domain grafting density was determined through de Fejter's equation [53], $\Gamma = d_{opt}\Delta n/M_W \times dn/dc$, where M_W is the molecular weight, and Δn the (approximately wavelength-independent) difference in refractive index between film and buffer solution. We used a refractive index increment of $dn/dc = 18\,\mathrm{cm}^3/\mathrm{g}$. Error bars for d_{opt} in figure 5.3 B correspond to 90 % confidence intervals, as automatically calculated by the fit algorithm implemented in the CompleteEASE software.

5.4.6 Quantification of mass transport limited FG domain adsorption rates

In our experimental *in situ* ellipsometry setup, i.e. a flat surface opposite a rotating stirrer, transport of molecules to the film can be adequately described by diffusion through an unstirred layer next to the surface [54]. The mass transport limited adsorption rate of FG domains can be estimated from a reference measurement of an adsorption process that is limited by mass transport and that occurs under identical stirring conditions [54]:

$$\left(\frac{\partial\Gamma}{\partial t}\right)_{\mathrm{FG}} = \left(\frac{R_{\mathrm{ref}}}{R_{\mathrm{FG}}}\right)^{2/3} \frac{[\mathrm{FG}]}{[\mathrm{ref}]} \left(\frac{\partial\Gamma}{\partial t}\right)_{\mathrm{ref}}.$$

We chose the adsorption of avidin with a concentration of 0.1 µM to a biotinylated SLB [55] as the reference and measured an adsorption rate of $(\partial\Gamma/\partial t)_{\mathrm{ref}} = 2.07 \pm 0.12\,\mathrm{pmol/cm^2/min}$ (mean ± standard deviation from three measurements). The Stokes radius for avidin is $R_{\mathrm{ref}} = 3.4\,\mathrm{nm}$, and we estimate R_{FG} to be between 3.5 and 8.7 nm, based on reported values for other FG domains [20, 29] and other intrinsically disordered or chemically denatured proteins [56, 57]. These considerations lead to a mass transport limited adsorption rate for FG domains between 7.6 and 21.5 $\mathrm{pmol/cm^2/min}$ at a bulk concentration of $0.9 \pm 0.1\,\mu\mathrm{M}$. This range is represented as a gray-shaded area in figure 5.2 A.

5.4.7 Atomic force microscopy (AFM)

Imaging and nanoindentation measurements were performed on a NanoWizard II AFM (JPK, Berlin, Germany) using oxide-sharpened Si_3N_4 probes (NP-S, Veeco, CA, USA) with a nominal cantilever spring constant of 0.06 N/m. The real spring constant, determined through the thermal noise method, was 0.10 N/m. Sample films were prepared on silicon wafers, following the same incubation steps as previously established by SE (figure 5.2 and supplementary figure 5.11), although in still solution. Complementary SE measurements confirmed that stirring does not significantly affect the final adsorbed amounts for the incubation times used (1 h or more).

AFM images were acquired in tapping mode in solution. The drive frequency was typically between 10 and 20 kHz, and the free amplitude of the cantilever was set to about 30 nm. To ensure a soft approach to the sample, the setpoint amplitude was decreased manually, in steps of a few Å, until the surface could be tracked. Scan speeds of 2 to 20 µm/s were employed.

Nanoindentation assays were performed in working buffer solution. Deflection *vs.* displacement curves were typically acquired at approach speeds of 500 nm/s and maximal loads of 1 nN, and converted into force vs. distance curves with JPK Data Processing software. We compared only force curves that were acquired with the same tip, in order to minimize the effect that variations in the shape of the AFM probe may have on indentation. Reference force curves were acquired on a control surface – an SLB that lacked FG domain coating - before and after indentation of each FG domain film. Only indentation series which reproducibly showed a small interaction distance (≤ 5 nm) on bare SLBs were accepted. A force curve was considered representative, when it could be reproduced upon repeated indentation at the same spot and at different spots on the same sample. For further analysis, and display in figure 5.3a, 6 to 12 curves were taken with the same AFM probe on the same or different spots on a given FG domain film and averaged. To quantify the onset of repulsive forces, data around the estimated contact point were fitted with a polynomial; the onset was then taken as the distance at which the force exceeded baseline level by 15 pN.

5.4.8 Fluorescence recovery after photobleaching (FRAP)

FRAP measurements were performed with a confocal laser scanning microscope (LSM 510, Zeiss, Germany) using an argon laser ($\lambda = 488$ nm), a plan-apochromat 63 ×/1.4 oil immersion objective and a completely opened pinhole (1 mm diameter). FG domain films were assembled on glass cover slips, from protein solutions containing approximately 1 mol-% Atto488-labeled FG domains. The image size was set to $119 \times 119\,\mu\text{m}^2$. After acquiring several pre-bleach images of the fluorescently labeled FG domain monolayer, a circular region with a radius of 10 µm in the center of the imaged area was bleached through brief exposure (3 to 8 s) to high laser intensity. More than 60 % bleaching in the center of the exposed region was achieved. Fluorescence recovery due to lateral diffusion of bleached (unbleached) FG domains out of (into) the bleached region was then monitored through acquisition of post-bleach images over a period of up to 4 h.

Acknowledgements

We thank Jacob Piehler (Osnabrueck, Germany) for providing NTA-functionalized lipids, and Oleg Borisov (Pau, France) for fruitful discussions. R.P.R. acknowledges funding from the Spanish Ministry of Science and Innovation (MICINN, refs RYC2009-04275 and MAT2011-24306), and the Department of Industry of the Basque Government. N.B.E. was supported by the Goettingen Graduate School for Neuroscience, Biophysics and Molecular Biosciences (DFG Grant GSC 226/1).

5.5 Supplementary Information

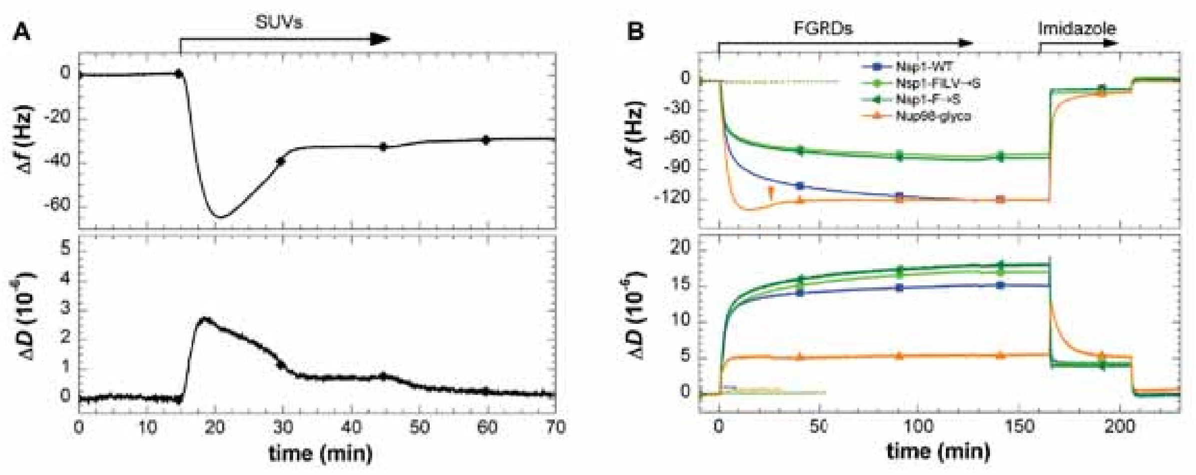

Figure 5.9: ***FG domains are anchored specifically and stably through their terminal His-tags to NTA-functionalized SLBs:*** *(A) SLB formation monitored by QCM-D. Silica surfaces in working buffer were exposed to 50 μg/mL SUVs made of 90 mol-% DOPC and 10 mol-% bis-NTA-functionalized lipids. Start and duration of the incubation is indicated by an arrow. The two-phase behavior together with the final changes in frequency and dissipation of Δf = -28 Hz and $\Delta D < 0.3 \cdot 10^{-6}$, respectively, characterizes the formation of an SLB of good quality [58]. The minor shifts in Δf and ΔD at about 44 min are due to the removal of $NiCl_2$ from the solution during rinsing in working buffer. (B) Formation of FG domain films was monitored by QCM-D on SLBs formed from SUVs containing either a mixture of 90 mol-% DOPC and 10 mol-% bis-NTA-functionalized lipids (solid lines), or only DOPC (dotted lines). Baselines (i.e. $\Delta f = \Delta D = 0$) correspond to the responses for bare SLBs. Start and duration of incubation steps with different samples are indicated with solid arrows on top of the plot. After each incubation step, the solution phase was replaced by working buffer. Strong changes in frequency and dissipation upon incubation with different His-tagged FG domain species (listed in the legend) at 45 μg/mL (i.e. 0.7 μM Nsp1-FILV→S, Nsp1-F→S and Nsp1-WT and 0.8 μM Nup98-glyco) on NTA-functionalized SLBs reflect the formation of soft and hydrated films. No changes in Δf and ΔD for Nsp1-derived FG domains and minor changes for Nup98-glyco upon rinsing in buffer (rinsing of Nup98-glyco was performed at 25 min, i.e. earlier than for the other species; orange arrowhead) indicate stable grafting. After exposure to 500 mM imidazole at pH 7.4, Δf and ΔD return to baseline levels, demonstrating specificity of binding. Changes in Δf and ΔD upon exchange from imidazole containing solution to pure working buffer do not reflect any changes on the surface but result from a change in the viscosity and/or density of the surrounding solution owing to the presence of imidazole. When exposed at 90 μg/mL (i.e. 1.5 μM Nsp1-FILV→S, Nsp1-F→S, and Nup98-glyco and 1.4 μM Nsp1-WT) to SLBs made of pure DOPC, none of the His-tagged FG domains induced appreciable QCM-D responses, confirming that the FG domains do not bind to SLBs that lack NTA functionality.*

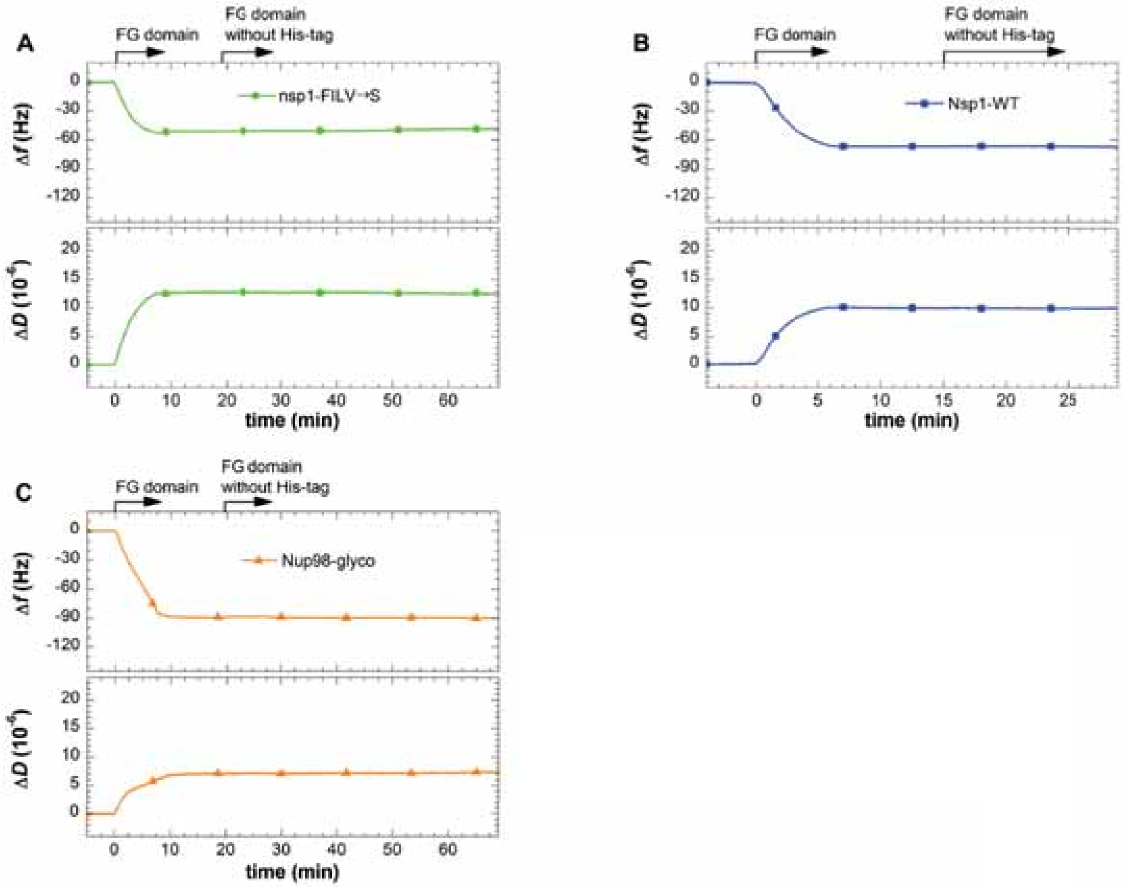

Figure 5.10: ***All FG domains in the films are anchored to the SLB:*** *SLBs with 10 mol-% bis-NTA functionalized lipids were formed and incubated with His-tagged FG domains at a concentration of 23 μg/mL (0.4 μM). Incubation was interrupted, by rinsing in working buffer, when frequency shifts reached between 50 and 70 % of the maximal frequency shifts observed in figure 5.9 B. No changes in Δf and ΔD were observed when the films were subsequently incubated with the same FG domain types lacking the His-tags at identical concentration. We conclude that homophilic interactions or entanglements are not sufficient to entrap individual FG domains stably in the films. All stably bound FG domain molecules must hence be anchored to the SLB.*

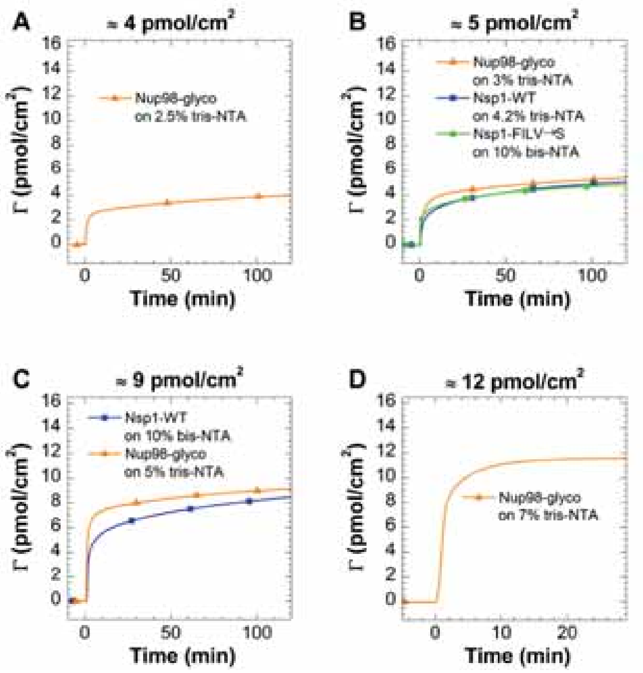

Figure 5.11: ***Tuning FG domain surface density:*** *FG domain films with defined and reproducible grafting densities (indicated on top of each plot) were obtained by tuning the valency (bis or tris) and fraction (in mol-%) of NTA-functionalized lipids in the SUVs from which the SLBs were formed (indicated in each plot). FG domains were incubated at concentrations of 56 µg/mL (1.0 µM) for Nup98-glyco and 113 µg/mL (1.8 µM) for Nsp1-WT and (1.9 µM) Nsp1-FILV→S.*

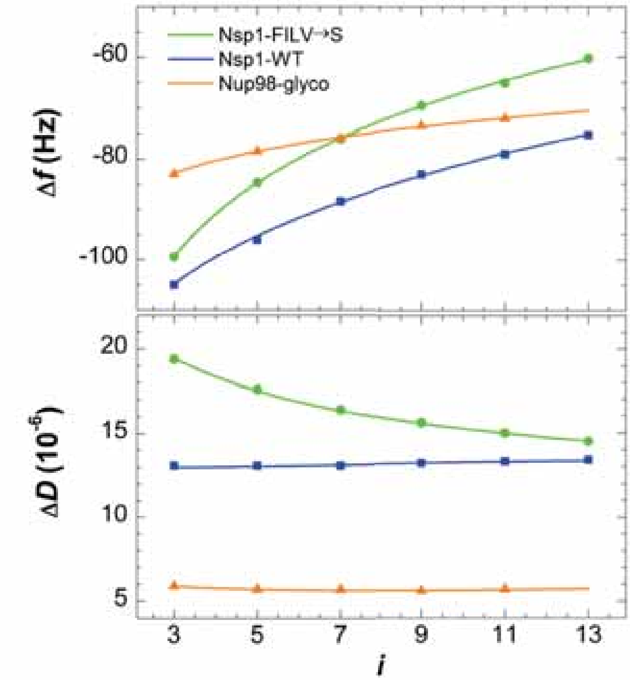

Figure 5.12: ***FG domain film thickness determination from QCM-D data:*** *Film thickness was estimated by fitting the QCM-D data for all overtones to a continuum viscoelastic model [59] with the software QTM (D. Johannsmann, Technical University of Clausthal, Germany [60]; option "small load approximation"), as described in detail elsewhere [24]. The model relates the measured QCM-D responses, Δf and ΔD as a function of the overtone number, to the viscoelastic properties and the thickness of the surface-confined film [24, 51]. The figure shows the final QCM-D responses (symbols) for the formation of FG domain films of about 5 pmol/cm^2 (see figure 5.11 B for film formation conditions; FG domain type is indicated in the plot) together with the best fits (lines) as a function of overtone i. Resulting film thicknesses are shown in figure 5.3 B, where error bars correspond to joint confidence regions with a confidence level of one standard deviation, and were determined as described in Ref. [24].*

References

[1] D. Görlich and U. Kutay. 1999. “Transport between the cell nucleus and the cytoplasm.” In: *Annu. Rev. Cell. Dev. Biol.* 15, pp. 607–660.

[2] I. G. Macara. Dec. 2001. “Transport into and out of the nucleus.” In: *Microbiol. Mol. Biol. Rev.* 65 (4), 570–94, table of contents.

[3] H. Fried and U. Kutay. Aug. 2003. “Nucleocytoplasmic transport: taking an inventory”. In: *Cell. Mol. Life Sci.* 60 (8), pp. 1659–1688.

[4] M. A. D’Angelo and M. W. Hetzer. 2008. “Structure, dynamics and function of nuclear pore complexes”. In: *Trends Cell Biol.* 18 (10), pp. 456–66.

[5] Q. Yang, M. P. Rout, and C. W. Akey. Jan. 1998. “Three-dimensional architecture of the isolated yeast nuclear pore complex: functional and evolutionary implications.” In: *Mol. Cell* 1 (2), pp. 223–234.

[6] L. A. Strawn, T. Shen, N. Shulga, D. S. Goldfarb, and S. R. Wente. Mar. 2004. “Minimal nuclear pore complexes define FG repeat domains essential for transport.” In: *Nat. Cell Biol.* 6 (3), pp. 197–206.

[7] D. Mohr, S. Frey, T. Fischer, T. Güttler, and D. Görlich. Sept. 2009. “Characterisation of the passive permeability barrier of nuclear pore complexes.” In: *EMBO J.* 28 (17), pp. 2541–2553.

[8] A. Cook, F. Bono, M. Jinek, and E. Conti. 2007. “Structural biology of nucleocytoplasmic transport”. In: *Annu. Rev. Biochem.* 76, pp. 647–71.

[9] K. Ribbeck and D. Görlich. Mar. 2001. “Kinetic analysis of translocation through nuclear pore complexes.” In: *EMBO J.* 20 (6), pp. 1320–1330.

[10] K. Ribbeck and D. Görlich. June 2002. “The permeability barrier of nuclear pore complexes appears to operate via hydrophobic exclusion.” In: *EMBO J.* 21 (11), pp. 2664–2671.

[11] M. P. Rout, J. D. Aitchison, M. O. Magnasco, and B. T. Chait. Dec. 2003. “Virtual gating and nuclear transport: the hole picture.” In: *Trends Cell Biol.* 13 (12), pp. 622–628.

[12] R. Peters. Mar. 2005. “The nanopore connection to cell membrane unitary permeability.” In: *Traffic* 6 (3), pp. 199–204.

[13] R. Y. H. Lim, B. Fahrenkrog, J. Köser, K. Schwarz-Herion, J. Deng, and U. Aebi. Oct. 2007. “Nanomechanical basis of selective gating by the nuclear pore complex.” In: *Science* 318 (5850), pp. 640–643.

[14] S. Frey, R. P. Richter, and D. Görlich. Nov. 2006. “FG-rich repeats of nuclear pore proteins form a three-dimensional meshwork with hydrogel-like properties.” In: *Science* 314 (5800), pp. 815–817.

[15] S. Frey and D. Görlich. Aug. 2007. “A saturated FG-repeat hydrogel can reproduce the permeability properties of nuclear pore complexes.” In: *Cell* 130 (3), pp. 512–523.

[16] S. S. Patel, B. J. Belmont, J. M. Sante, and M. F. Rexach. Apr. 2007. “Natively unfolded nucleoporins gate protein diffusion across the nuclear pore complex.” In: *Cell* 129 (1), pp. 83–96.

[17] C. Ader, S. Frey, W. Maas, H. B. Schmidt, D. Görlich, and M. Baldus. 2010. “Amyloid-like interactions within nucleoporin FG hydrogels”. In: *Proc. Natl. Acad. Sci. U.S.A.* 107 (14), pp. 6281–6285.

[18] B. B. Hülsmann, A. A. Labokha, and D. Görlich. 2012. “The permeability of reconstituted nuclear pores provides direct evidence for the selective phase model”. In: *Cell* 150 (4), pp. 738–51.

[19] M. P. Rout and S. R. Wente. Oct. 1994. “Pores for thought: nuclear pore complex proteins.” eng. In: *Trends Cell Biol.* 4 (10), pp. 357–365.

[20] D. P. Denning, S. S. Patel, V. Uversky, A. L. Fink, and M. Rexach. Mar. 2003. “Disorder in the nuclear pore complex: the FG repeat regions of nucleoporins are natively unfolded.” In: *Proc. Natl. Acad. Sci. U.S.A.* 100 (5), pp. 2450–2455.

[21] D. P. Denning and M. F. Rexach. Feb. 2007. “Rapid evolution exposes the boundaries of domain structure and function in natively unfolded FG nucleoporins”. In: *Mol. Cell. Proteomics* 6 (2), pp. 272–82.

[22] A. A. Labokha, S. Gradmann, S. Frey, B. B. Hulsmann, H. Urlaub, M. Baldus, and D. Gorlich. Jan. 2013. “Systematic analysis of barrier-forming FG hydrogels from Xenopus nuclear pore complexes”. In: *EMBO J.* 32 (2), pp. 204–218.

[23] N. B. Eisele, S. Frey, J. Piehler, D. Görlich, and R. P. Richter. May 2010. “Ultrathin nucleoporin phenylalanine-glycine repeat films and their interaction with nuclear transport receptors.” In: *EMBO Rep.* 11 (5), pp. 366–372.

[24] N. B. Eisele, F. I. Andersson, S. Frey, and R. P. Richter. 2012. “Viscoelasticity of Thin Biomolecular Films: A Case Study on Nucleoporin Phenylalanine-Glycine Repeats Grafted to a Histidine-Tag Capturing QCM-D Sensor”. In: *Biomacromolecules* 13 (8), pp. 2322–32.

[25] T. Jovanovic-Talisman, J. Tetenbaum-Novatt, A. S. McKenney, A. Zilman, R. Peters, M. P. Rout, and B. T. Chait. 2008. “Artificial nanopores that mimic the transport selectivity of the nuclear pore complex”. In: *Nature* 457 (7232), pp. 1023–1027.

[26] O. V. Borisov, Y. B. Zhulina, and T. M. Birshtein. 1988. “Constitutional diagram and collapse of grafted chain layers”. In: *Polymer Science U.S.S.R.* 30 (4), pp. 772–779.

[27] E. B. Zhulina, T. M. Birshtein, V. A. Priamitsyn, and L. I. Klushin. 1995. “Inhomogeneous Structure of Collapsed Polymer Brushes Under Deformation”. In: *Macromolecules* 28 (25), pp. 8612–8620.

[28] M. Tagliazucchi and I. Szleifer. 2012. “Stimuli-responsive polymers grafted to nanopores and other nano-curved surfaces: structure, chemical equilibrium and transport”. In: *Soft Matter* 8 (28), pp. 7292–7305.

[29] J. Yamada, J. L. Phillips, S. Patel, G. Goldfien, A. Calestagne-Morelli, H. Huang, R. Reza, J. Acheson, V. V. Krishnan, S. Newsam, A. Gopinathan, E. Y. Lau, M. E. Colvin, V. N. Uversky, and M. F. Rexach. 2010. “A bimodal distribution of two distinct categories of intrinsically disordered structures with separate functions in FG nucleoporins”. In: *Molecular & Cellular Proteomics* 9 (10), pp. 2205–2224.

[30] P.-G. de Gennes. 1979. “Scaling Concepts in Polymer Physics”. Ithaca and London: Cornell University Press.

[31] M. Rubinstein and R. H. Colby. 2003. “Polymer Physics”. Oxford: Oxford University Press.

[32] L. H. Cai, S. Panyukov, and M. Rubinstein. Oct. 2011. “Mobility of Nonsticky Nanoparticles in Polymer Liquids”. In: *Macromolecules* 44 (19), pp. 7853–63.

[33] S. Lata, M. Gavutis, and J. Piehler. Jan. 2006. “Monitoring the dynamics of ligand-receptor complexes on model membranes”. In: *J. Am. Chem. Soc.* 128 (1), pp. 6–7.

[34] C. Ligoure and L. Leibler. 1990. “Thermodynamics and kinetics of grafting end-functionalized polymers to an interface”. In: *J. Phys. France* 51 (12), pp. 1313–1328.

[35] M. P. Rout, J. D. Aitchison, A. Suprapto, K. Hjertaas, Y. Zhao, and B. T. Chait. Feb. 2000. “The yeast nuclear pore complex: composition, architecture, and transport mechanism.” In: *J. Cell Biol.* 148 (4), pp. 635–651.

[36] B. Du and D. Johannsmann. Mar. 2004. “Operation of the quartz crystal microbalance in liquids: derivation of the elastic compliance of a film from the ratio of bandwidth shift and frequency shift”. In: *Langmuir* 20 (7), pp. 2809–12.

[37] E. B. Zhulina, O. V. Borisov, and V. A. Priamitsyn. 1990. “Theory of steric stabilization of colloid dispersions by grafted polymers”. In: *J. Colloid Interface Sci.* 137 (2), pp. 495–511.

[38] H. Zhao, P. H. Brown, and P. Schuck. 2011. “On the Distribution of Protein Refractive Index Increments”. In: *Biophys. J.* 100 (9), pp. 2309–2317.

[39] O. Peleg, M. Tagliazucchi, M. Kröger, Y. Rabin, and I. Szleifer. 2011. “Morphology Control of Hairy Nanopores”. In: *ACS Nano* 5 (6), pp. 4737–4747.

[40] D. Osmanovic, J. Bailey, A. H. Harker, A. Fassati, B. W. Hoogenboom, and I. J. Ford. 2012. “Bistable collective behavior of polymers tethered in a nanopore”. In: *Phys. Rev. E* 85 (6), p. 061917.

[41] S. Milles and E. A. Lemke. 2011. “Single molecule study of the intrinsically disordered FG-repeat nucleoporin 153”. In: *Biophys. J.* 101 (7), pp. 1710–1719.

[42] S. Frey and D. Görlich. 2009. “FG/FxFG as well as GLFG repeats form a selective permeability barrier with self-healing properties”. In: *EMBO J.* 28 (17), pp. 2554–2567.

[43] R. L. Schoch, L. E. Kapinos, and R. Y. Lim. 2012. “Nuclear transport receptor binding avidity triggers a self-healing collapse transition in FG-nucleoporin molecular brushes”. In: *Proc. Natl. Acad. Sci. U.S.A.* 109 (42), pp. 16911–16916.

[44] M. Petri, S. Frey, A. Menzel, D. Görlich, and S. Techert. 2012. “Structural Characterization of Nanoscale Meshworks within a Nucleoporin FG Hydrogel”. In: *Biomacromolecules* 13 (6), pp. 1882–1889.

[45] Y. Zhulina, V. Pryamitsyn, and O. Borisov. 1989. “Structure and conformational transitions in grafted polymer chain layers. A new theory”. In: *Polymer Science U.S.S.R.* 31 (1), pp. 205–216.

[46] S. T. Milner. Feb. 1991. “Polymer brushes.” In: *Science* 251 (4996), pp. 905–914.

[47] M. Tagliazucchi, O. Peleg, M. Kröger, Y. Rabin, and I. Szleifer. 2013. “Effect of charge, hydrophobicity, and sequence of nucleoporins on the translocation of model particles through the nuclear pore complex”. In: *Proc. Natl. Acad. Sci. U.S.A.* 110 (9), pp. 3363–3368.

[48] J. Ma, A. Goryaynov, A. Sarma, and W. Yang. 2012. “Self-regulated viscous channel in the nuclear pore complex”. In: *Proc. Natl. Acad. Sci. U.S.A.* 109 (19), pp. 7326–31.

[49] J. S. Mincer and S. M. Simon. 2011. “Simulations of nuclear pore transport yield mechanistic insights and quantitative predictions”. In: *Proc. Natl. Acad. Sci. U.S.A.* 108 (31), E351–8.

[50] S. Lata, A. Reichel, R. Brock, R. Tampé, and J. Piehler. July 2005. “High-affinity adaptors for switchable recognition of histidine-tagged proteins.” In: *J. Am. Chem. Soc.* 127 (29), pp. 10205–10215.

[51] I. Reviakine, D. Johannsmann, and R. P. Richter. Dec. 2011. “Hearing what you cannot see and visualizing what you hear: interpreting quartz crystal microbalance data from solvated interfaces”. In: *Anal. Chem.* 83 (23), pp. 8838–48.

[52] I. Carton, A. R. Brisson, and R. P. Richter. 2010. “Label-free detection of clustering of membrane-bound proteins”. In: *Anal. Chem.* 82 (22), pp. 9275–81.

[53] J. A. De Feijter, J. Benjamins, and F. A. Veer. 1978. “Ellipsometry as a tool to study the adsorption behavior of synthetic and biopolymers at the air-water interface”. In: *Biopolymers* 17 (7), pp. 1759–1772.

[54] W. T. Hermens, M. Benes, R. Richter, and H. Speijer. 2004. “Effects of flow on solute exchange between fluids and supported biosurfaces”. In: *Biotechn. Appl. Biochem.* 39 (3), pp. 277–284.

[55] P. Bingen, G. Wang, N. F. Steinmetz, M. Rodahl, and R. P. Richter. 2008. “Solvation effects in the QCM-D response to biomolecular adsorption - a phenomenological approach”. In: *Anal. Chem.* 80 (23), pp. 8880–8890.

[56] J. E. Kohn, I. S. Millett, J. Jacob, B. Zagrovic, T. M. Dillon, N. Cingel, R. S. Dothager, S. Seifert, P. Thiyagarajan, T. R. Sosnick, et al. 2004. “Random-coil behavior and the dimensions of chemically unfolded proteins”. In: *Proc. Natl. Acad. Sci. U.S.A.* 101 (34), pp. 12491–12496.

[57] O. Tcherkasskaya, E. A. Davidson, and V. N. Uversky. 2003. “Biophysical constraints for protein structure prediction”. In: *J. Proteome Res.* 2 (1), pp. 37–42.

[58] R. Richter, R. Berat, and A. Brisson. 2006. “The formation of solid-supported lipid bilayers - an integrated view”. In: *Langmuir* 22 (8), pp. 3497–3505.

[59] A. Domack, O. Prucker, J. Rühe, and D. Johannsmann. July 1997. “Swelling of a polymer brush probed with a quartz crystal resonator”. In: *Phys. Rev. E* 56 (1), pp. 680–.

[60] D. Johannsmann. N.d. In: *internet, link: http://www2.pc.tu-clausthal.de/dj/software_en.shtml.*

6 Towards construction of FG repeat domain pores as a model system

6.1 Introduction

In the preceding chapters, we demonstrated that continuous FG repeat domain films constitute, despite their simplicity, a valuable model system of the interior of the permeability barrier of NPCs. A more elaborated model system of NPCs, however, would be artificial FG repeat domain pores, i.e. pores that have the dimensions of an NPC (diameter and length around $30-50\,\text{nm}$) and which are selectively functionalized with FG repeat domains (as illustrated in figure 6.1). Such a model system would allow to access other parameters such as flux of inert proteins and NTRs across the pores. Moreover, in this model system the pores could be entirely functionalized with selected types of FG repeat domains, including artificially generated FG repeat domains or mutants. This could would give further insights into the mechanism of selectivity of NPCs.

There are only a few studies in which work with artificial FG repeat domain pores was reported. One of them is the study by Jovanovic-Talisman et al. (2008) [1]. Briefly, a commercially available porous polycarbonate membrane served as the porous substrate. A thin gold layer was sputtered onto this substrate and Nsp1-WT was bound to the gold via a C-terminal Cys. The polycarbonate membrane was then dried. A double-sided sticky tape with a hole was attached to a microscope cover slip and the hole was filled with a solution of permeation probes. Then the functionalized polycarbonate membrane was sandwiched between the double-sided sticky tape and the open top compartment.

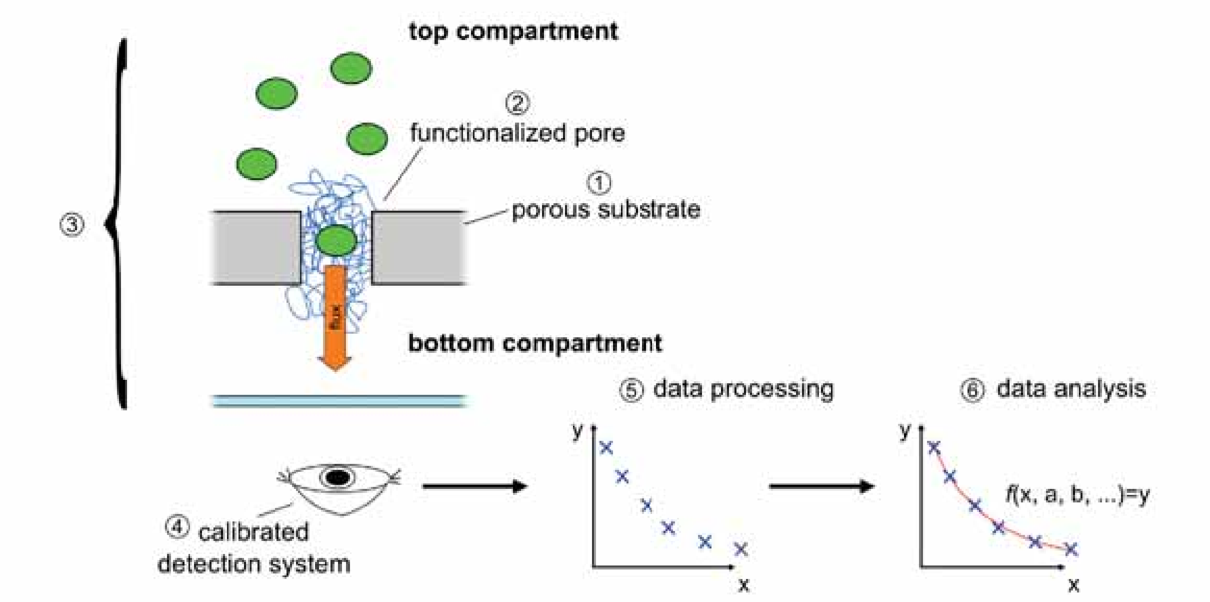

Figure 6.1: Schematic illustration of a measurement setup with artificial FG-repeat domain pores: *In general, the measurement setup for the detection of transport processes across artificial FG-repeat domain pores would consist of the following core items: (1) A porous substrate separates a top and a bottom compartment. (2) The pores of the substrate have dimensions of the transport channel of an NPC (30 - 50 nm) and are functionalized with FG-repeat domains. (3) The porous substrate, the top compartment, and the bottom compartment are part of a measurement chamber. If permeation probes are added to one of the compartments, transport across the pore will occur. (4) A calibrated detection system is needed to quantify this transport. (5) The complex data needs to be processed before (6) it can be fitted to a theoretical model and the parameters of interest can be extracted.*

Finally, the top compartment was filled with buffer solution. The flux of fluorescent proteins across the pores was monitored by confocal microscopy as a decrease in fluorescence intensity in the bottom compartment.

Although, from the bio-inspired engineering point of view, the report by Jovanovic-Talisman et al. (2008) was impressive and a mile-stone in creation of artificial model systems of the NPC's permeability barrier, the reported protein selectivity of the artificial pores was far below to the selectivity properties of a native NPC. Hence, it remains a task for the future to create a measurement setup with artificial FG repeat domain pores that prove to have a protein selectivity comparable to native NPCs. In this thesis chapter, we will report important steps towards this goal.

To start with, the introduction will be followed by a section about the theoretical predictions for the flux across artificial FG repeat domain pores and mathematical formulae, relevant for determination of the selectivity of artificial pores, will be elaborated. Moreover, we will consider two different kind of measurement chambers (see figure 6.2). One will be a simple measurement chamber with stagnant solutions in two compartments which are separated by a porous membrane. The other one will be a more elaborated measurement chamber, were two channels, to which flow can be applied, are separated by a porous membrane. In addition, from this chapter we will learn, that there are intrinsic limitations in such measurement setups. Plans to circumvent these limitations in the future will be presented.

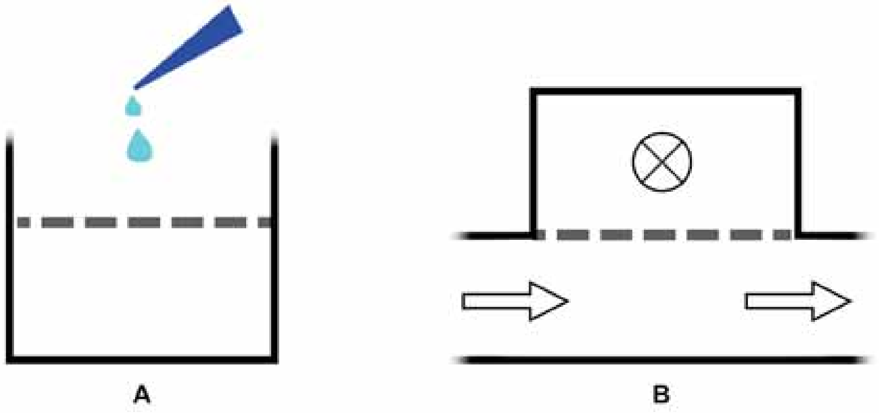

Figure 6.2: Schematic illustration of two designs for measurement chambers: *Provided are two cross sections of two different measurement chambers that could be designed for the measurement set-up of artificial FG repeat domain pores. (A) A simple chamber with stagnant solution in which no flow can be applied (here illustrated with an open top compartment that allows for solution exchange by pipetting). (B) A measurement chamber which allows to (temporarily) apply a flow to one or both compartments (flow is illustrated by arrows in the bottom compartment and with a crossed circle in the top compartment).*

As a second step towards the construction of artificial FG repeat domain pores, we created measurement setups with pores that are not yet functionalized. This was an important step and allowed to experimentally verify some of the predictions about the net flux across a porous substrate made by theory. In addition, we will demonstrate that we established a well aligned measurement setup and a data processing routine. These results are important prerequisites for future measurements with a setup with pores that are functionalized with FG repeat domains.

In order to have pores which are filled with FG repeat domains, we will present our advancement in functionalizing the porous substrate, in section 6.4. As an alternative to the work of Jovanovic-Talisman et al., we chose to sputter a thin layer of SiO_2 and to functionalize it with a His-tag capturing layer. Our data suggests that sputtering SiO_2 to the substrate lead to circular pores of the desired diameter. Moreover, Nsp1-WT could be grafted specifically via its His-tag at sufficient grafting density. Also the effect of drying and rehydration of an Nsp1-WT film immobilized onto the substrate (a step which might be necessary in the measurement assembly) was tested.

6.2 Theoretical predictions for the diffusion across a porous membrane

In our measurement chamber, a porous membrane will divide a top and a bottom compartment. Initially, the bottom compartment is filled with a solution of permeation probes (i.e. proteins) and the top compartment is filled with a solution without permeation probes. As a consequence of the concentration gradient, there will be a net flux of permeation probes across the pores until the concentrations of the permeation probes in both compartments is equal. If the pores are equipped with a permeability barrier, diffusion across the pores may be slowed down or blocked. In the following, we will elaborate on the theoretical description of this phenomenon. The implications of the design of the porous substrate for the sensitivity of the measurement setup will be analyzed, and effective measures to improve the sensitivity for the selectivity of the permeability barrier will be proposed.

Recapitulation of simple diffusion phenomena

Our measurement setup will be sensitive for the concentration of permeation probes in the bottom compartment. It will be, thus, important to derive a mathematical function $c(t, z)$ to describe the evolution of probes concentration in time and space. To this end, we start by recapitulating the description of simple diffusion for a concentration gradient along the z-dimension without a porous membrane. Fick's first law in its one dimensional form describes the mass flux, F, as follows:

$$F = D\frac{\partial c}{\partial z}\,, \tag{6.1}$$

where D is the diffusion coefficientand c is the concentration of the permeation probe.

Fick's second law describes how concentration distribution changes over time, t, as follows:

$$\frac{\partial c}{\partial t} = D\frac{\partial^2 c}{\partial z^2}\,. \tag{6.2}$$

The solution for equation (6.2) will depend on the design of the measurement chamber which will ultimately define the boundary conditions for the differential equation.

6.2.1 Simple chamber with stagnant solutions

Flux across an unfunctionalized porous membrane

In a simple chamber with stagnant solutions, we have the following conditions (see figure 6.3 A): (*i*) the height of the bottom compartment is confined between 0 and z_0; (*ii*) there is a porous membrane perpendicular to the z-axis at $z = z_0$ with thickness l_m and a void fraction ϵ_m; (*iii*) the membrane spans over the hole bottom compartment, i.e. the membrane is connected to the walls of the measurement chamber. Moreover, we assume that the pore channels are perpendicular to the surface of the membrane, i.e., the void fraction, which is generally defined as the total volume of the pores divided by the volume of the entire membrane, can be calculated by dividing the total area of the

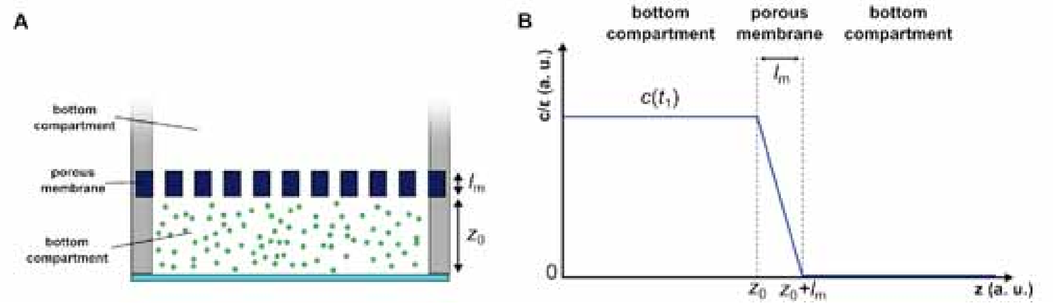

Figure 6.3: Illustration of permeation probe distribution in a simple chamber: *(A) Schematic side view of the simple chamber. A porous membrane will be spanned between the walls, confining the bottom compartment. The height of the bottom compartment is* z_0 *and the thickness of the membrane is* l_m. *(B) The concentration profile of the permeation probe for an arbitrarily chosen time* t_1 *is shown under the conditions that the bottom compartment is relatively small, the transport across the membrane is limiting, and the dilution capacity of the top compartment is infinite. The concentration is normalized against* ϵ *which is the void fraction, i.e.* $\epsilon = 1$ *for the top and the bottom compartment and* $\epsilon = \frac{\text{total volume of pores}}{\text{total volume of membrane}}$ *for the membrane (we assume that the pore channels are perpendicular to the surface of the membrane). The concentration of the permeation probe* $c(t_1)$ *in the bottom compartment will be equilibrated (since the transport across the membrane is the limiting step) while in the top compartment it will be zero (perfect sink condition). For a thin membrane, the concentration of the permeation probe will approximately decrease linearly between* z_0 *and* $z_0 + l_m$.

pores by the area of the entire membrane.

Next, we make the following assumptions, which will simplify the mathematical description of $c(t, z)$: (*i*) the bottom reservoir sufficiently small, so that mass transport within it is not a limiting factor; (*ii*) the top compartment is large (i.e. the dilution is unlimited); and (*iii*) the flux across the porous membrane is rate limiting.

As consequences of these conditions and assumptions: (1) the permeation probes will be homogeneously distributed in the bottom reservoir at all times, and (2) the top compartment will present a perfect sink (i.e. the concentration of permeation probes is always zero here). A graph of $c(t = t_1, z)$ is illustrated in figure 6.3 for an arbitrarily chosen moment t_1 (such a graph is called a "z-profile" in the following).

Conditions (1) and (2) are the boundary conditions, which are necessary to derive, $c(t, z)$. They can be mathematically expressed as:

$$c(t,z) = c(t, z = z_0), \quad \text{for } 0 < z \leq z_0 \text{ and } t > 0; \tag{6.3}$$

$$c = 0, \quad \text{for } z \geq z_0 + l_\mathrm{m} \text{ and } t > 0. \tag{6.4}$$

Note, equation (6.3) implies that the concentration in the bottom compartment is only a function of t and independent from z. We will henceforth write only $c^*(t)$, instead of $c(t,z)$ for the concentration in the bottom compartment.

If the porous membrane is sufficiently thin, equation (6.1) for the flux across the membrane, F_m, can be simplified as follows:

$$F_\mathrm{m} = \epsilon_\mathrm{m}\, D\, \frac{\partial c}{\partial z} = \epsilon_\mathrm{m}\, D\, \frac{c^*(t)}{l_\mathrm{m}}, \quad \text{for } z_0 \leq z \leq z_0 + l_\mathrm{m}. \tag{6.5}$$

The amount of molecules removed from the bottom compartment, m, can be calculated by:

$$m(t) = A \int_0^t F_\mathrm{m}(\phi)\, d\phi, \tag{6.6}$$

where A is the area of the membrane.

The total amount of molecules available, m_tot can be calculated by:

$$m_\mathrm{tot} = c_0\, A\, z_0. \tag{6.7}$$

With equation (6.6) and (6.7) the differential equation for $c^*(t)$ can be expressed as follows:

$$c^*(t) = \frac{m_\mathrm{tot} - m(t)}{A\, z_0} = c_0 - \frac{1}{z_0} \int_0^t F_\mathrm{m}(\phi)\, d\phi = c_0 - \frac{\epsilon_\mathrm{m}\, D}{z_0\, l_m} \int_0^t c^*(\phi)\, d\phi. \tag{6.8}$$

The following equation is a solution of equation (6.8) under the boundary conditions (6.3) and (6.4):

$$c^*(t) = c_0\, e^{-t/\tau_\mathrm{m}}, \tag{6.9}$$

with

$$\tau_\mathrm{m} = \frac{z_0\, l_\mathrm{m}}{\epsilon_\mathrm{m}\, D}, \tag{6.10}$$

as the characteristic time scale of the diffusion process. From equation (6.10) it becomes evident, that the characteristic time scale depends strongly on the thickness of the membrane.

In section 6.3.4, it will be shown that experimental data obtained for flux experiments with our simple chamber can be well fitted to the equations derived above. The extracted parameter for τ_m does compare well with the theoretical value, validating the assumption made above.

Flux across a porous membrane functionalized with FG repeat domains

If we had a porous SiO_2 layer (i.e. without underlying polycarbonate membrane) with thickness l_{SiO_2}, a void fraction ϵ_{SiO_2}, and without FG repeat domains (i.e. without a permeability barrier) we could calculate the flux F_0 of a permeation probe across this membrane and determine the characteristic time scale τ_0 as described above. If we equip the pores with FG repeat domains, we could repeat the permeation experiment and would measure another flux, F^*, and another characteristic time scale, τ^*, since the FG repeat domains would influence the permeation of the probes across the pore. From these two experiments, we could determine a selectivity factor κ which we define as:

$$\kappa \,:=\, F_0/F^* \,=\, \tau^*/\tau_0. \tag{6.11}$$

Note, all other parameters, in particular thickness and ϵ, are kept equal in the two experiments. If we solve equation (6.11) after F^*, we derive:

$$F^*(t) \;=\; \epsilon_{SiO_2}\kappa^{-1}D\frac{c(t)}{l_{SiO_2}}. \tag{6.12}$$

From equation (6.12) we see, that κ can be understood as a factor that adjusts D for the exit rate, the entry rate, and the changed diffusion coefficient in the artificial pore, i. e. $\kappa^{-1}D = D_{\text{effective}}$.

If we solve equation (6.11) after τ^*, we derive an equation for the characteristic time scale τ^*:

$$\tau^* \;= \kappa\frac{z_0 l_{SiO_2}}{\epsilon_{SiO_2}D}. \tag{6.13}$$

It is interesting to note here that a 30 nm thick layer functionalized with FG-repeat domains must have a κ of 200 to lead to the same τ_m as an unfunctionalized polycarbonate membrane of a thickness of 6 µm (if $\epsilon_m = \epsilon_{SiO_2}$, i.e. if the diameter of the unsputtered and the sputtered pores are equal).

Above, we considered the case of an isolated SiO_2 layer without underlying polycarbonate membrane. Our initial design of the measurements chamber, however, is not based on an isolated SiO_2 layer to measure τ^*. Instead, the substrate will be a 30 nm thin SiO_2 layer functionalized with FG-repeat domains above a 6 µm thick polycarbonate membrane. The flux across the porous membrane, hence, will be limited by both the 6 µm thick polycarbonate membrane and the 30 nm thin SiO_2 layer functionalized with FG-repeat domains. In a simple approximation, the characteristic time scale τ in this system will be additive [2]:

$$\tau \;=\; \tau_{\mathrm{m}} + \tau^*. \tag{6.14}$$

τ is accessible to experiment and τ_{m} can be determined from a reference measurement of the net flux across an unfunctionalized membrane (as outlined above). With the experimentally accessible parameter $\alpha \;=\; \tau_{\mathrm{m}}/\tau$ one finds:

$$\tau^* = \tau(1 - \alpha). \tag{6.15}$$

The approximation that led to equation (6.14) and (6.15), respectively, overestimates τ^* by less than 15 % if the flux is predominantly limited by the functionalized pores ($\alpha < 0.5$, i. e., $\tau^*/\tau_{\mathrm{m}} > 1$). For $\alpha < 2/3$ (i.e. $\tau^*/\tau_{\mathrm{m}} > 1/2$), the error is still smaller than 20 % [2].

Methods to improve the sensitivity of the setup for the selectivity of the artifical permeability barrier

As a consequence from the theoretical considerations above τ^*/τ_{m} should be high (>1) to extract τ^* accurately by this approach. It is instructive to rewrite τ^*/τ_{m} with equation (6.10) and (6.13) to:

$$\frac{\tau^*}{\tau_{\mathrm{m}}} = \kappa \frac{l_{SiO_2}\,\epsilon_m}{l_m\,\epsilon_{SiO_2}}. \tag{6.16}$$

In the following, we will itemize, which parameters could be possibly tuned in the setup to improve the sensitivity for τ^*:

- Increasing l_{SiO_2}. On the other hand, this would influence the selectivity between an NTR and an inert probe. Our values for the selectivity of the artificial pore may then deviate from values in pores of the dimension of the permeability barrier of NPCs.

- Increasing $\frac{\epsilon_m}{\epsilon_{SiO_2}}$. This may be reached by adjusting the sputtering process (e. g. to obtain pores in the SiO_2 with 30 nm diameter on a membrane with pores with a diameter of 100 nm). Alternatively, the pores underneath the SiO_2 layer could be increased by removing the polycarbonate partly via plasma (SiO_2 is more resistant to plasma then organic material). Both attempts may not be straight forwardly achievable.

- Increasing κ. κ reflects the qualities of the permeability barrier itself, it depends e. g. on the FG-repeat domain composition and concentration in the artificial permeability barrier. Since this is the parameter that we want to study, tuning of it to enhance sensitivity is not advisable.

- Decreasing l_m. This could be achieved, for instance, by plasma etching. Alternatively, entirely new porous substrates may be used in the future.

6.2.2 Microfluidic flow chamber

The microfluidic chamber consists basically of two channels which are separated by a porous membrane at a crossing section (see figure 6.4). The geometry is, hence, different from the simple chamber. The most important difference in the following considerations will be that the bottom compartment is not confined, yet, continuous.

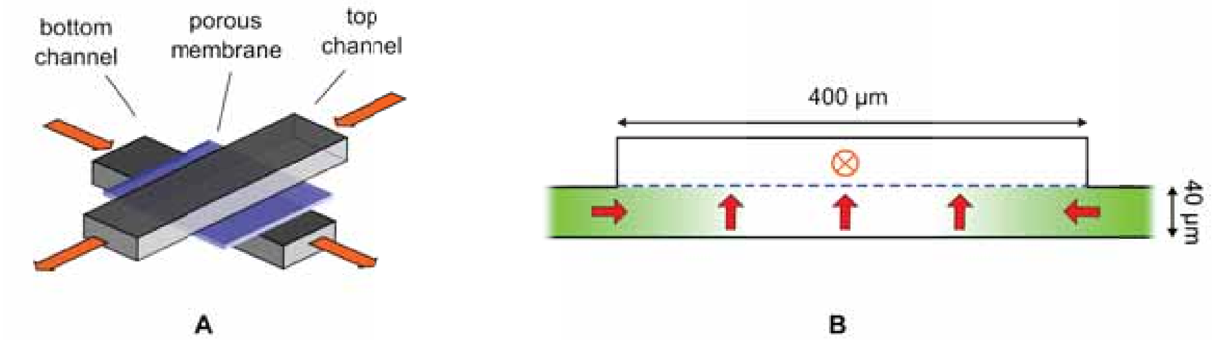

Figure 6.4: Illustration of the flux in the microfluidic chamber: *(A) The microfluidic chamber will basically consist of two channels which are separated by a porous membrane at a crossing section. Flow can be applied to both compartments independently (indicated by orange arrows). The figure is not drawn to scale for the sake of illustration. (B) A cross section of the crossing between top and bottom compartment is shown (drawn to scale). The bottom channel is filled with permeation probes (green color) and no flow is applied. In the top compartment there is a continues flow (orange crossed circle) creating a perfect sink. This will induce a net flux (red arrows) of the permeation probes (from the bottom to the top channel) which, as a consequence, will create also a net flux within the bottom channel.*

A flux experiment could be performed the following way: the bottom channel is filled with a solution of permeation probes and then the flow is switched off. In the top compartment a continuous flow of buffer solution without permeation probes is applied and maintained (which creates a perfect sink). The permeation probes from the bottom channel will diffuse across the membrane and will be transported away by the flow in the top compartment. As a consequence, permeation probes will be depleted in the bottom channel at the position of the crossing section. Additional to the concentration gradient between the bottom and the top compartment, a lateral concentration gradient and lateral flux within the bottom channel need to be considered.

The theoretical predictions for the microfluidic chamber are, thus, more complex compared to the simple chamber. It is yet unclear if a general analytical approximation can be found for this scenario.

Numerical approximation

Instead of deriving a general analytical solution, the expected concentration profiles were approximated numerically. To this end, I wrote a Matlab routine which accounts for our envisaged chamber geometry (i.e. a channel width of 400 µm and a channel height of 40 µm) under the conditions (*i*) that there is a perfect sink in the top compartment (experimentally achievable by a continues flow of buffer in the top channel); (*ii*) that the bottom compartment is thin; and (*iii*) that the flux in z-direction is limited by the transport across the membrane (i.e. there is no concentration gradient along z within the bottom compartment). The results of the numerical calculations are shown in figure 6.5 (A). The measured intensity is remarkably robust towards lateral displacement of the microscope objective (or the acquired z-stacks, respectively) from the center, as shown in figure 6.5 (B). This Matlab routine would also allow to extract the characteristic time scale of the diffusion process from experiments, e.g. by a grid fit of the experimental data to a set of numerically derived solutions (shown in figure 6.5 (C)).

The scenario of a wide upper compartment/channel

The shape of the intensity profiles, in the bottom compartment, will strongly depend on the width of the upper channel and on κ as demonstrated by numerical solutions in figure 6.6. If the upper channel is sufficiently wide, the intensity minima become

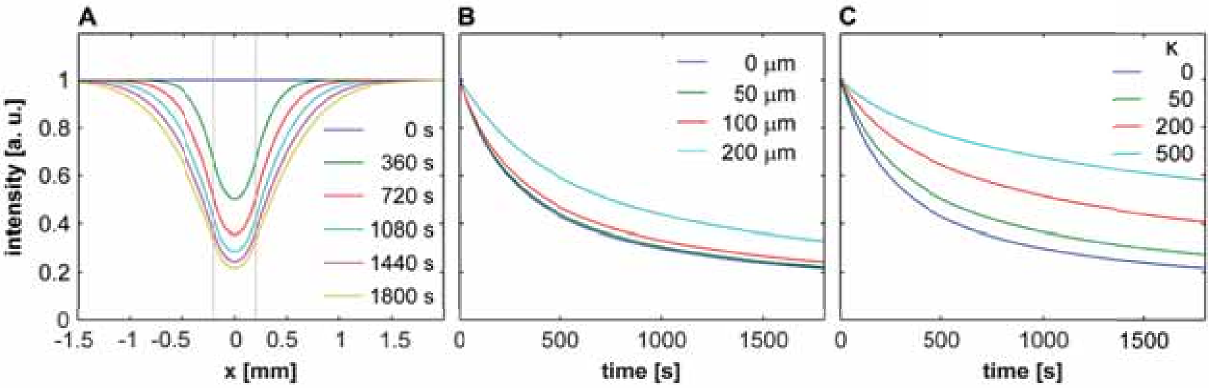

Figure 6.5: Simulated intensity profiles for the current design of the microfluidic chamber: *(A) The concentration profiles in the lower compartment of a microfluidic chamber were simulated for a flux experiment with eGFP and a polycarbonate membrane with a nominal pore diameter of 30 nm, a pore density of 9.2 pores/μm^2, and a thickness of 6 μm. The width of the top channel was set to 400 μm and its lateral position is indicated by gray, dotted lines. (B) The intensity as a function of time is shown at x positions as indicated in the figure legend. The curves overlap sufficiently well for a x-displacement from the center of up to 100 μm. (C) The concentration decrease at the center, i.e. $x = 0$, was simulated for the same conditions as in (A), yet, with the additional condition that there is a 30 nm thin layer of SiO$_2$ functionalized with FG repeat domains with a selectivity quality of κ as indicated in the legend. Note, for all numerical solution τ was calculated according to equation (6.14). As a consequence, the prediction for the intensity decrease in (C) for $\kappa = 50$ (i.e., $\alpha = 0.8$) may be an overestimation (see text for more information).*

plateaus and remain plateaus even for long measurement times (see figure 6.6 top row, right column), because the permeation probes from the laterals of the lower channel need more time to diffuse to the center. As a consequence, the concentration decrease as a function of time ($c^*(t)$), at the plateaus, can be derived exactly the same way as for the simple chamber. Hence, all the equations derived in section 6.2.1 are also valid for the microfluidic chamber, in this special case.[1] As demonstrated in figure 6.6, a width of e.g. 2 mm would be sufficient to achieve this, if the pores are not functionalized. However, with increasing κ the width of the upper channel would need to be increased further to achieve plateaus. For instance, if κ is higher than 200, a width of 2 mm of the upper channel would not be sufficient to achieve plateaus.

---

[1] On a side remark, a wide upper compartment can also be constructed as an open compartment, instead of a channel.

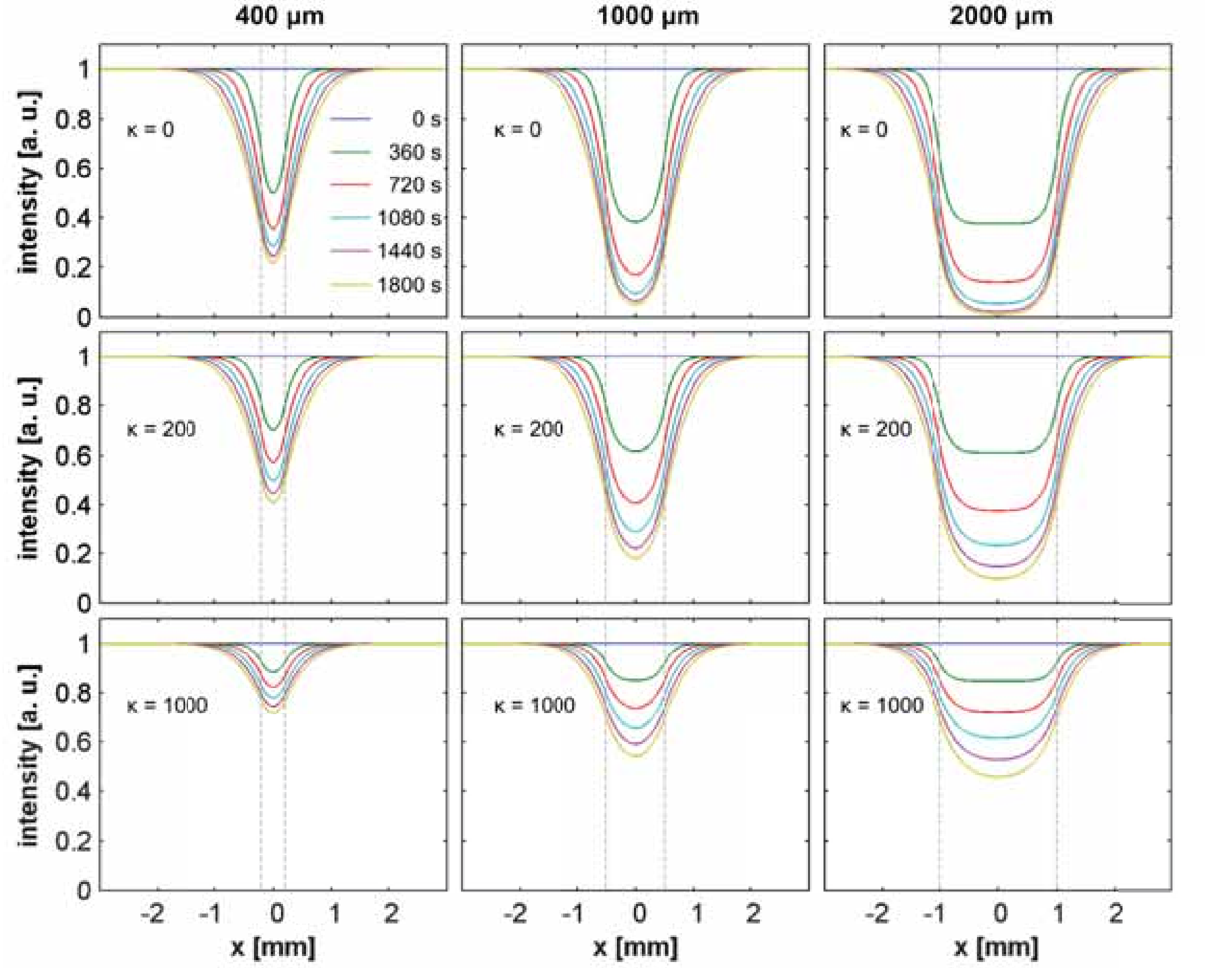

Figure 6.6: Dependance of the intensity profiles on the top channel width and κ: *This array of intensity profiles in the lower compartment was simulated for a flux experiment with eGFP and a polycarbonate membrane with a nominal pore diameter of 30 nm, a pore density of 9.2 pores/μm^2, and a thickness of 6 μm, and a 30 nm thin layer of functionalized SiO$_2$. The two parameters that were varied to span the array were the width of the top channel and the selectivity factor of the artificial permeability barrier κ. The width was set to 400 μm (left column), 1000 μm (middle column), and 2000 μm (right column) and κ was set to 0 (top row), 200 (middle row), and 1000 (bottom row). With increasing width of the top channel, the intensity profiles reach more pronounced plateaus. An increasing κ shrinks the intensity profiles, on the one hand, and makes the plateaus disappearing for long measurement times.*

6.3 Creation of a setup with unfunctionalized pores

6.3.1 Characterization of porous polycarbonate membranes

Our approach to create FG-repeat domain pores was based on commercially available nucleopore track-etched membranes made of polycarbonate, which are available with different nominal pore sizes (e.g. 30, 50, and 100 nm). We sought to characterize their morphology by SEM.

Beam damage

When we took the first scanning electron microscopy (SEM) images of uncoated polycarbonate membranes, we noticed that the membrane can become easily damaged by the electron beam of the SEM, as illustrated in figure 6.7. When taking SEM images, hence, we tried to reduce the beam power as much as possible and to avoid taking SEM images repetitively from the same position.

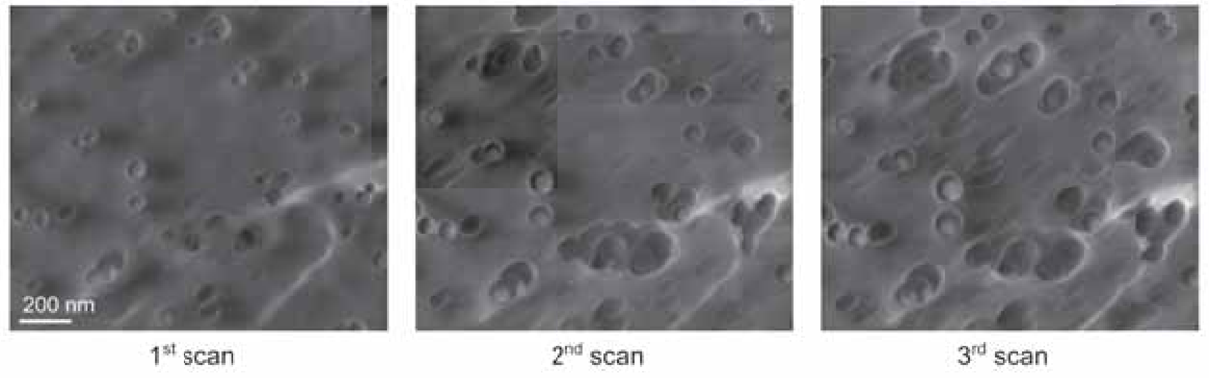

Figure 6.7: Beam damage of polycarbonate membranes induced by SEM: *SEM images were taken repetitively at the same position on the dull side of polycarbonate membrane (nominal diameter 100 nm). The surface becomes easily damaged by the electron beam during the scan. Images were taken by Christopher Tollan (CIC nanoGUNE, San Sebastian, Spain).*

The two sides of a polycarbonate membrane

The two sides of a membrane could be distinguished by eye, one was shiny and the other one was dull. This was also observed by others and seems to stem from the polycarbonate membrane production [3]. We imaged both faces with identical conditions with the

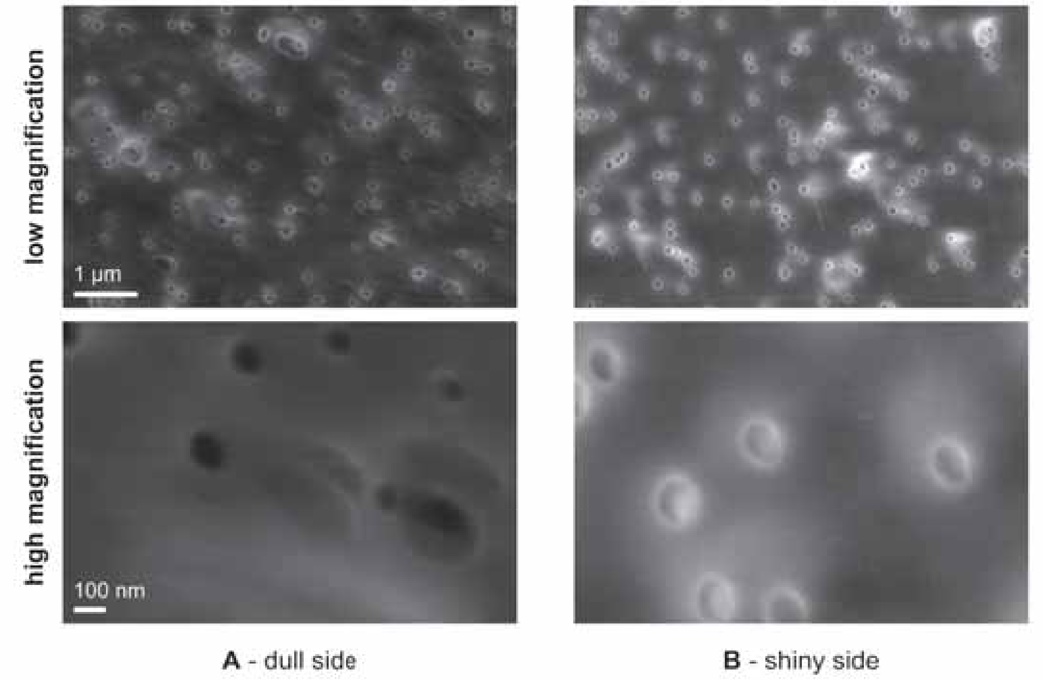

Figure 6.8: SEM images of the two side of a polycarbonate membrane: *SEM images were taken from the dull (A) and shiny (B) side of a polycarbonate membrane (nominal pore diameter 100 nm). Overview images are shown on the top while on the bottom magnifications are shown. The images clearly show that the shiny side was more homogeneous and that the distribution of the pore entrances was narrower than for the dull side. Images were taken by Christopher Tollan (CIC nanoGUNE, San Sebastian, Spain).*

SEM (see figure 6.8). All taken SEM images indicate that the shiny side was more homogeneous and showed a narrower size distribution of the entrance of the pores. Currently, we cannot exclude that the observed difference between two sides of a polycarbonate membrane may be an artifact caused by beam damage – the two sides of the membrane may simply be differently sensitive towards beam damage.

The pore diameter and the void fraction

We took SEM images to characterize the shape and diameter of the pore entrances (see figure 6.9). Several observations could be made frome these images: (1) the pore entrances were quite circular; (2) the measured pore diameter was similar to the numbers provided by the manufacturer (30, 50, and 100 nm); (3) and sometimes two pores overlapped and formed a bigger pore. From such SEM images, we counted the amount of pores per area unit and estimated the void fraction, ϵ, under the assumption, that the pore channels are circular and that they are perpendicular to the planar membrane. The results are summarized in table 6.1.

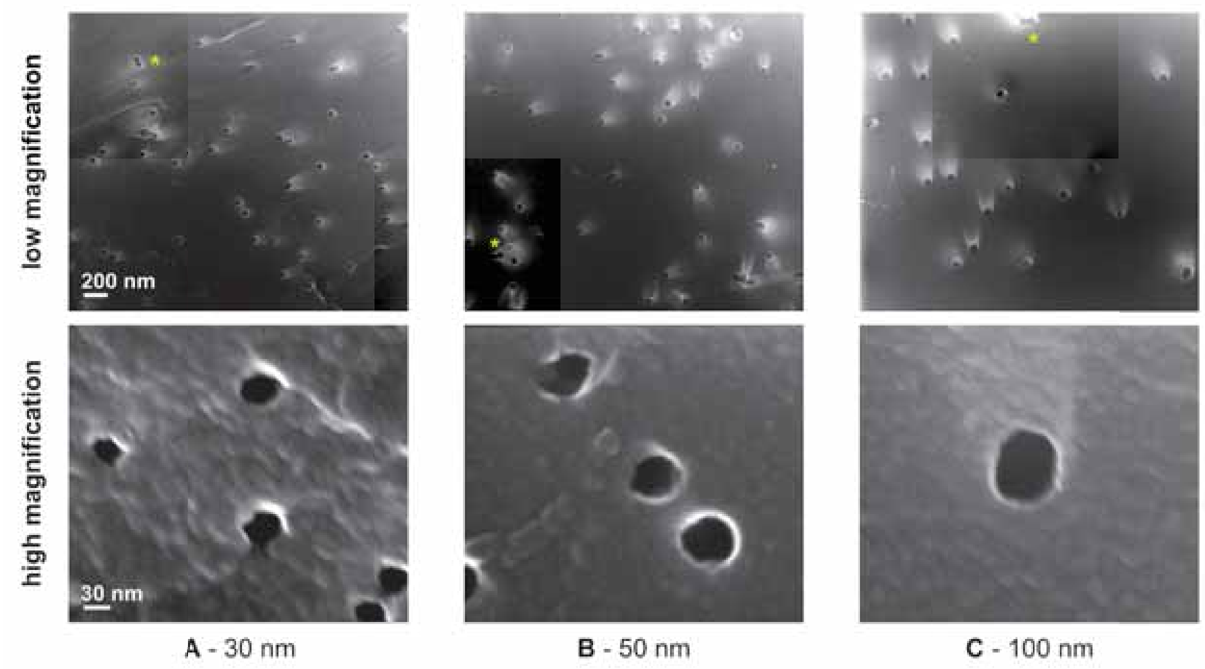

Figure 6.9: SEM images of polycarbonate membranes: *SEM images were taken from uncoated polycarbonate membranes with different nominal pore diameter, i.e. (A) 30 nm, (B) 50 nm, or (C) 100 nm. The top row provides overview images at low magnification. It can be seen that pores are mainly randomly distributed and have apparently a similar size. However, sometimes two pores almost coincide, thereby, forming a double pore (as indicated with yellow asterisks). Images of pores at high magnification are shown on the bottom row. These images indicate that the pores were quite circular and that the diameter matches the nominal diameter provided by the manufacturer quite well. Images were taken by Ixaskun Carton (CIC biomaGUNE, San Sebastian, Spain).*

Table 6.1: *Areal pore density and void fraction of unsputtered polycarbonate membranes*

nominal pore diameter	pores/µm^2	ϵ
30 nm	9.2	0.0065
50 nm	7.6	0.0149
100 nm	3.4	0.0267

Thickness

We determined the thickness of the membrane with a high precision film thickness gauge (Hahn and Kolb, Germany) to be 6 µm and confirmed, thereby, the value from the manufacturer.

6.3.2 Setup alignment and testing of the data processing routine

We adjusted the laser power and the detector settings of the confocal LSM to obtain a linear correlation between fluophore concentration and intensity read out. To this end, we acquired z-stacks of eGFP or MBP-mCherry solutions of different concentrations (0.5 – 5 µM) by confocal LSM in reference measurements (see figure 6.10 A). The data was then processed with a self-written Matlab routine. The Matlab routine calculated the average intensity for each z-plane and subtracted a value for the background (buffer without fluophores). Then z-profiles of the average intensity were produced by plotting the average intensity against z (figure 6.10 B). Here, the z-axis of the z-profiles was offset such that the half maximum of the intensities was at the z-position $z = 0$. This allowed to correct for focus drifts during the measurements. It can be observed that after reaching a maximum (i.e. the focal plane is completely in the solution) the measured intensity decreased with increasing z-distance although the concentration is homogeneously distributed in the whole solution. This effect is due to refractive index mismatch between the layers (oil, glass plate, solution) and scatter effects and can be commonly observed. After background subtraction and normalization against the maximal acquired intensity, the z-profiles overlapped to a master curve (see figure 6.10 (C). The intensities at a z-position 20 µm away from the glass slide (red line in figure 6.10 (A)) correlated linearly with the concentrations (figure 6.10 (D)).

Since we showed above that the z-profiles overlapped to a master curve, the linear correlation between intensity and concentration remain over the complete z-range and also for averages of the intensity calculated over z-intervals. This allows to rewrite equation (6.9) (see section 6.2, p. 124) by replacing concentration with intensity, leading

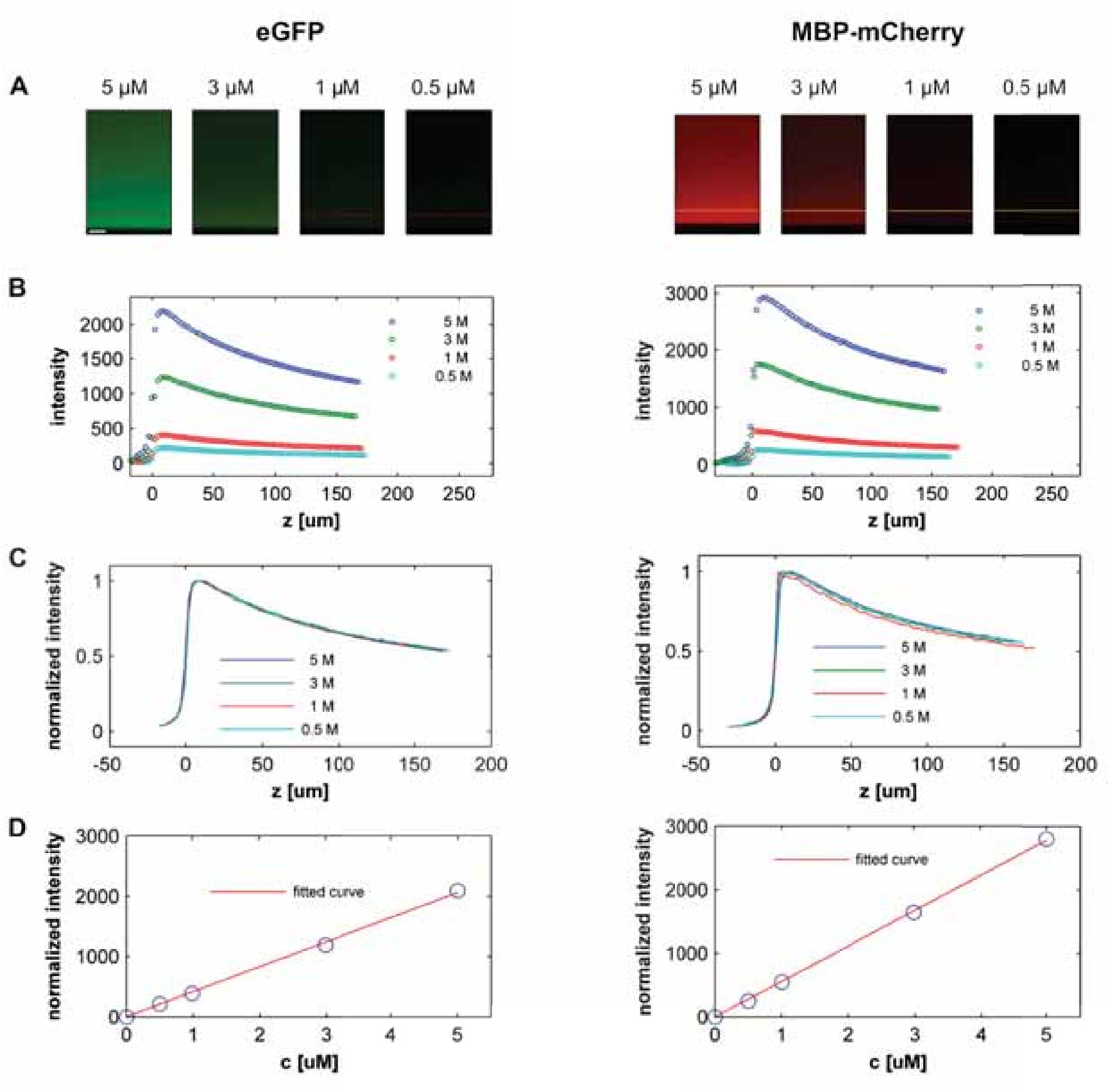

Figure 6.10: Correlation between intensity and concentration of fluorescent probes: *z-stacks of eGFP (left) and MBP-mCherry (right) solutions of different concentrations were acquired. (A) z-stacks are shown (x-z dimension is shown, the pixels in y-dimensions are averaged). (B) The average intensity per x-y plane was plotted against its z-position to obtain z-profiles. (C) The z-profiles were corrected for focus drift and background intensity, and were normalized against the maximal intensity value. The z-profiles overlay nicely and form a master curve. (D) The intensity (here measured at a z-position 20 μm above the glass slide, as indicated with a red line in (A)) correlated linearly with the concentration. Scale bar in (A) is 25 μm.*

to:

$$I(t) \;=\; I_0 \exp\left(-\frac{\epsilon_m D}{l_c l_m} t\right) \;=\; I_0 \exp\left(-\frac{1}{\tau_m} t\right), \tag{6.17}$$

where I is the measured intensity and I_0 is the initially detected intensity.

These settings allowed a z-plane spacing of 2.5 µm and a time resolution of 10 s for a series of z-stacks. We did not observe bleaching effects with these settings. On a side remark, the signal-to-noise ratio is extremely high with these settings. If a quicker z-stack acquisition is needed in the future, the pixel resolution of the images could be easily reduced while maintaining the excellent signal-to-noise ratio.

6.3.3 Construction of a simple chamber

The construction of a simple chamber was inspired by the chamber design reported by Jovanovic-Talisman et al. (2008) [1]. The construction steps are illustrated in figure 6.11.

Briefly, the bottom compartment was composed of a double sided sticky tape with a hole (diameter approximately 2 mm) which was attached to a passivated glass slide. The top compartment was made of the lid of an 2 mL laboratory reaction tube. Both compartments were filled with a solution of the permeation probe before they were assembled to a measurement chamber. The porous polycarbonate membrane separates both compartments. For the experiments presented in this section we used porous membranes with a nominal pore diameter of 30 nm. The membranes were not coated with SiO_2.

6.3.4 Permeability experiments with the simple chamber

We performed permeation experiments in our simple chamber, in order to test (1) the theoretical predictions for the flux across unfunctionalized membranes derived in section 6.2 (p. 124) and (2) the measurement setup. The chambers were equipped with

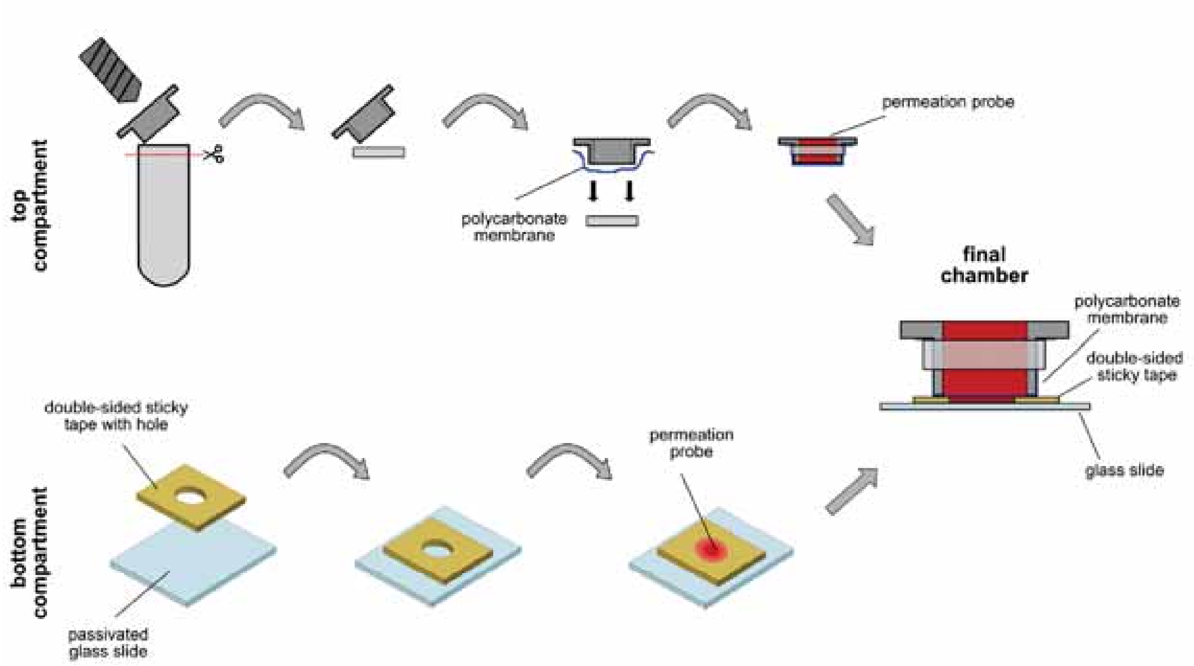
top compartment
permeation probe
polycarbonate membrane
final chamber
polycarbonate membrane
double-sided sticky tape
glass slide
double-sided sticky tape with hole
permeation probe
bottom compartment
passivated glass slide

Figure 6.11: Scheme for the construction of a simple chamber: *The bottom compartment was composed of a passivated glass slide to which a double sided sticky tape with a 2 mm hole was attached. In a next step the hole was filled with buffer containing the permeation probe. The top compartment was made of the lid of an ordinary laboratory 2 mL plastic reaction tube to which the polycarbonate membrane was clipped. Buffer containing the permeation probe was also added to the top compartment before it was quickly attached to the bottom compartment.*

polycarbonate membranes with a nominal pore diameter of 30 nm and were not functionalized.

Initially, both compartments were filled with a 5 µM solution of either eGFP or MBP-mCherry. Then the solution in the top compartment was quickly exchanged with a solution of pure buffer without permeation probes. This induced a gradient in concentration which led to a flux of permeation probes across the polycarbonate membrane, from the bottom to the top compartment. The flux was measured by acquiring a series of z-stacks via confocal LSM. In figure 6.12 (A), the raw data for four selected time points are shown. From the pre-rinsing image, two observations could be made: (1) the membrane could be seen as a dip in intensity; and (2) the membrane was partly transparent and allowed to measure fluorescence in the top compartment as well. After

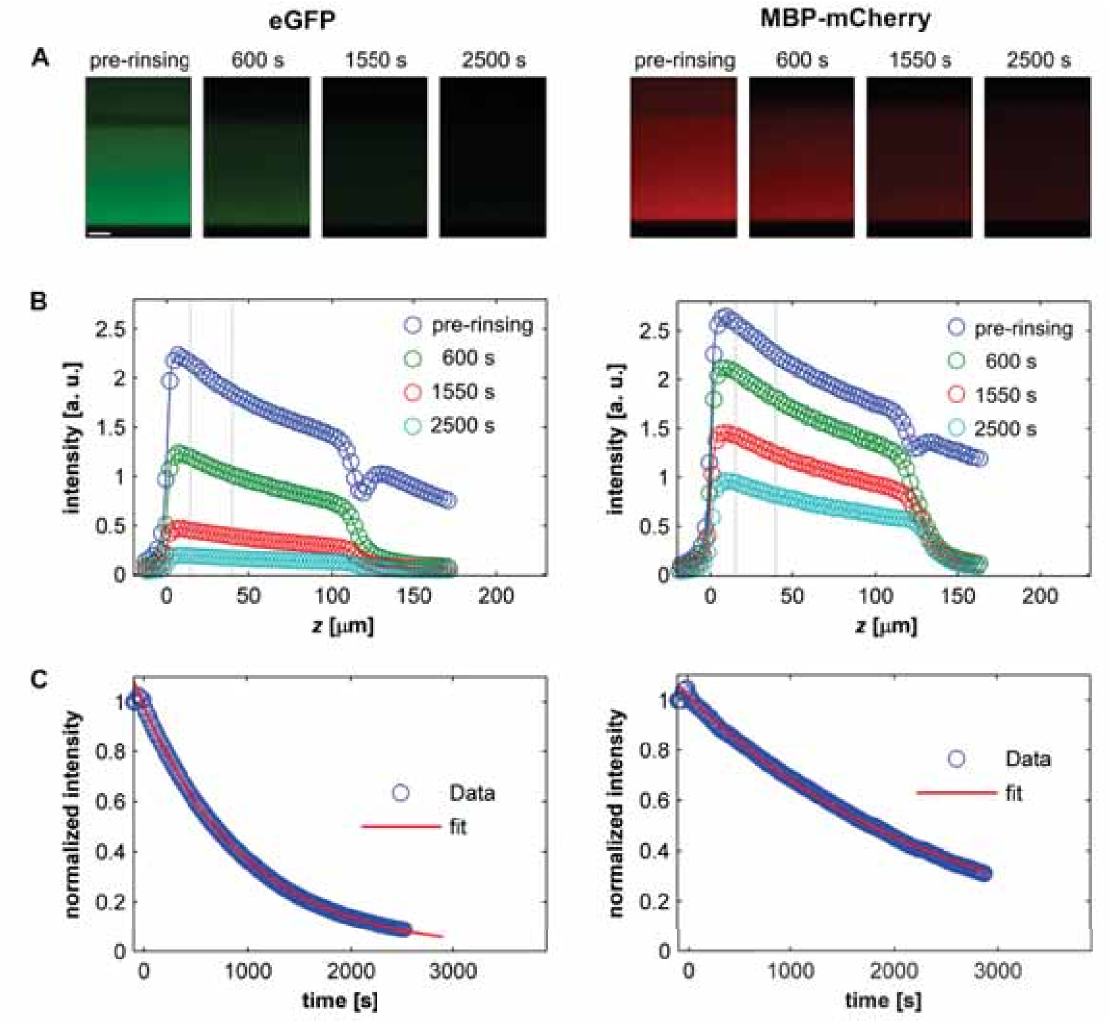

Figure 6.12: Permeation control experiments with the simple chamber: *Permeability experiments were carried out with a blank polycarbonate membrane, nominal pore diameter 30 nm, in the simple chamber. Both compartments were filled with a solution of either eGFP (left column) or MBP-mCherry (right column) at a concentration of 5 μM. After acquiring a base line, the solution of the permeation probes in the top compartment was exchanged with buffer. (A) A series of z-stacks for selected time points is shown. (B) z-profiles of the intensity are shown for the z-stacks in (A). (C) The intensity was averaged over the z-range confined by the gray lines in (B), normalized, and then plotted against the time. A fit of an exponential function (equation (6.17)) to the data was done (red line). The scale bar in (A) is 25 μm.*

exchanging the protein solution in the top compartment with buffer, the intensity in the bottom compartment was decreasing and thereby demonstrated protein depletion in the bottom compartment.

In a next step, the average intensity for each z-plane was calculated with a matlab routine and plotted against its z-position to obtain a z-profile. In figure 6.12 (B) four exemplary z-profiles are presented, corresponding to the raw data shown in figure 6.12 (A). The intensity dip in the pre-rinsing z-profile corresponded to the polycarbonate membrane. Its position was used to determine the height of the bottom compartment, z_0, which was 118 µm for the chamber with eGFP and 125 µm for the chamber with MBP-mCherry.

In a next step, the intensity was averaged within a $z-$interval from 15 to 40 µm, as indicated by gray lines in figure 6.12 (B). The averaged and normalized intensities were plotted against acquisition time (see figure 6.12 (C)), and fitted to equation (6.17) to obtain the characteristic time scale of the diffusion process. The error bars represent the boundaries of a 95 % confidence interval for the fit. For comparison, we also calculated the theoretical values using equation (6.10). To this end, the thickness of the membrane, l_m, was measured to be 6 µm and the diffusion coefficients for the permeation probes were estimated by using the Stokes-Einstein equation ($D = k_{\mathrm{B}}T/(6\pi\eta_{\mathrm{s}}R_{\mathrm{S}})$, where η_{s} is the viscosity of the solvent and R_{S} the stokes radius of the probe) and a stokes radius of 2.4 and 3.6 nm for eGFP [4] and MBP-mCherry [5], respectively. The results of the fits and the theoretical predictions are summarized in table 6.2.

The excellent fit with an exponential as well as the quantitative agreement between the experimentally found $\tau_{\mathrm{m}}^{\mathrm{exp.}}$ and the theoretical predicted $\tau_{\mathrm{m}}^{\mathrm{theo.}}$ (see equation (6.10)) suggest that the assumptions made in section 6.2 were reasonable. Furthermore, the experimentally measured characteristic time scales were very close to the theoretical predictions for eGFP and at least within the same order of magnitude for MBP-mCherry.

Table 6.2: *Characteristic time scales τ_m determined experimentally and by theory.*

	eGFP	**MBP-mCherry**
$\boldsymbol{\tau}_{\mathrm{m}}^{\mathrm{exp.}}$ [s]	1020 ± 2	2479 ± 12
$\boldsymbol{\tau}_{\mathrm{m}}^{\mathrm{theo.}}$ [s]	1096	1741

6.3.5 Construction of a prototype of a microfluidic chamber

We sought to purpose-design a microfluidic chamber where a top channel and a bottom channel are separated by a porous polycarbonate membrane at a crossing section. The chamber would allow for flow to be applied independently in both of the compartments and, thereby, for: (1) sample exchange after a permeation experiment, i.e. for a series of measurements with the same membrane; and (2) for creation of a perfect sink (or a continuous source) at the exit (entry) side of the membrane.

To this end, we created two compartments, made of PDMS, both with a channel (see materials and methods for more details). The channel was designed to have a nominal width of 400 µm and height of 40 µm. The total volume of one channel in the chamber was about 0.5 µL. The assembling of the two compartments to one chamber with a membrane at the crossing section of the channels was done as described in Ref. [6] and is illustrated in figure 6.13. Briefly, a thin mortar layer of uncured PDMS was applied to both compartments and to the edges of the polycarbonate membrane. Then, the membrane was embedded between the two compartments and the mortar layer was cured. In a next step, the channels were connected to tubes. Needles were used as adapters between the PDMS chamber and the tubing.

We checked whether the two compartments were glued together in a leakage free manner after curing the mortar layer. To this end, we applied air pressure to one inlet after the other and maintaining the other inlets closed. No air escape was observed, suggesting that the compartments were indeed tightly assembled. We also checked by microscopy, whether uncured mortar had crept into the channels, before the curing step. The channels were unblocked and no obstacles could be seen. Moreover, air and buffer solution could be easily pressed through the channels.

We then connected the inlet tubings to a peristaltic pump (ISM953C, Ismatec, Germany) and filled the channel with buffer solution at a typical flow rate of 20 µL/min. In a next step, we took an x-y-scan with confocal LSM of the crossing section of a cham-

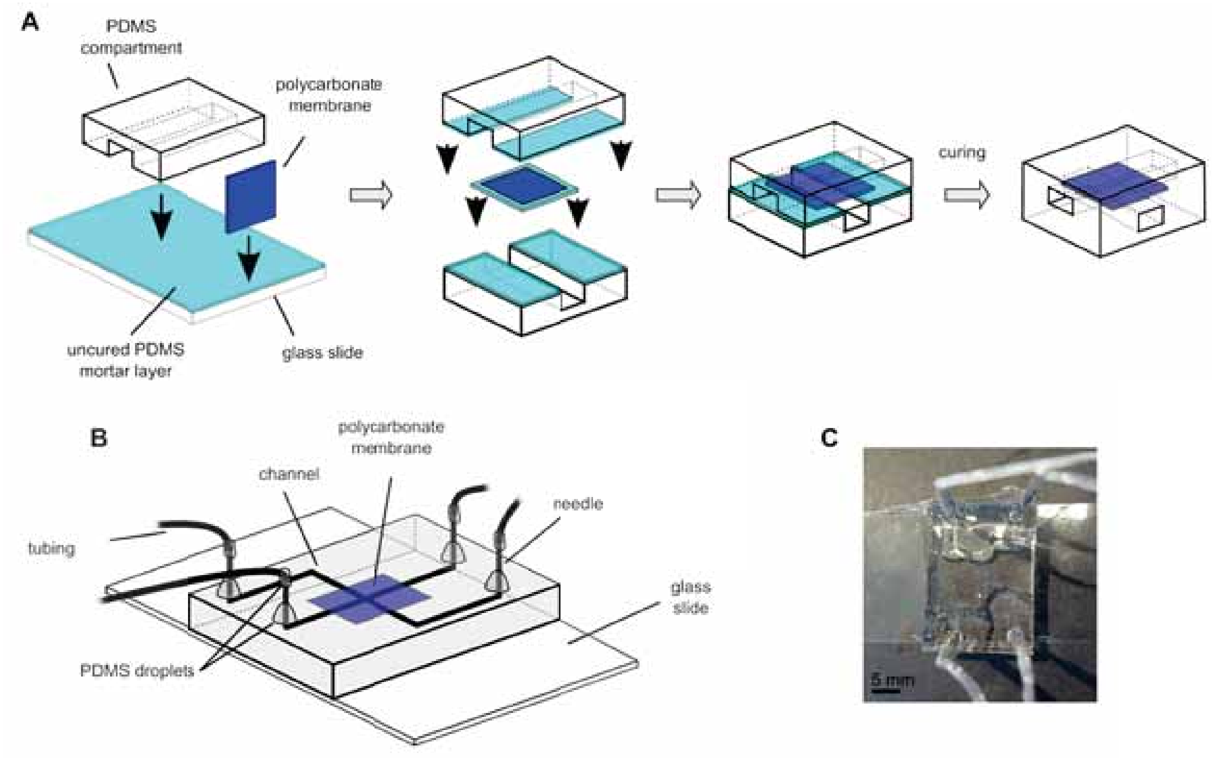
A
PDMS compartment
polycarbonate membrane
curing
uncured PDMS mortar layer
glass slide
B
polycarbonate membrane
channel
needle
tubing
glass slide
PDMS droplets
C
5 mm

Figure 6.13: Construction of a microfluidic flow chamber: *(A) Construction scheme: A thin layer of uncured PDMS (mortar layer) was spin coated to a glass slide. The bottom and top compartment were quickly dipped into this mortar layer, as well as the edges of the polycarbonate membrane. Then, the membrane was embedded between the two compartments, before the mortar layer was cured. (B) A schematic view of a constructed chamber is shown. To attach tubings to the chamber, needles were pushed through the PDMS to the ends of the channels. Then tubes were connected to the other end of the needles. The connection between the needles and (1) the PDMS chamber on one end and (2) the tube on the other end was sealed by a droplet of PDMS which was then cured at room temperature. The dimensions of the chambers are about 0.5 cm × 1 cm × 2 cm. (C) A photograph (top view) of a constructed cell is shown. (A) was adapted from [6].*

ber which lower channel was filled with a 5 µM eGFP solution (see figure 6.14 left and middle). In this scan, the channels and the membrane were clearly visible. The image confirms the width of the channel to be 500 µm. Fluorescence read out of the image (see figure 6.14 right) suggests, that the polycarbonate membrane was embedded crevice and leakage free, since no fluorescence around the membrane could be observed.

In a next step, we sought to measure the height of our channels. To this end, we filled both channel with eGFP and carried out a z-stack of the crossing section (see figure 6.14 (B)). The membrane was clearly visible as a dip in intensity between the two channels. The height of the channels was measured to be 50 µm.

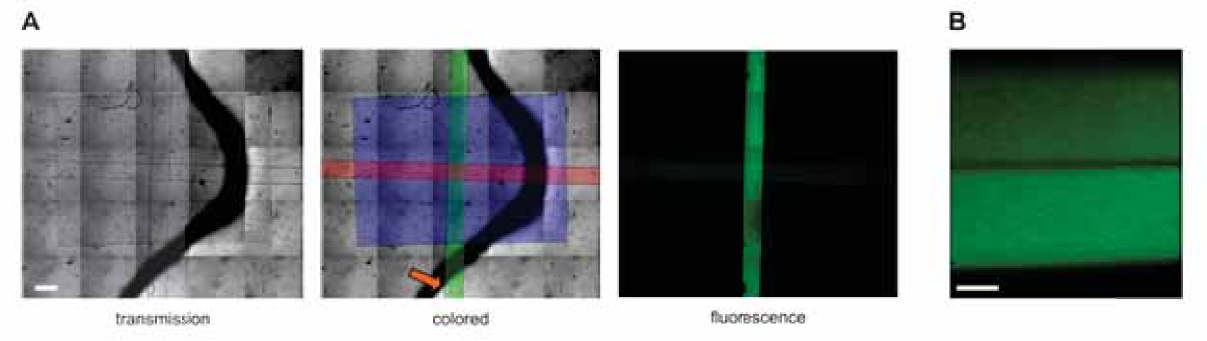

Figure 6.14: Characterization of a constructed microfluidic chamber: *(A) An x-y-scan of the crossing section of the channels was taken. The lower channel was filled with eGFP. The left image shows the read out of the transmission channel. The microfluidic channels and the membrane can be observed. The channel width was measured to be about 500 μm. The thick, black line on the right side of the image stems from PDMS (which was used to seal the tubings) on the top of the chamber and has no impact onto the channels below. In the middle image, the position of important elements was digitally colored for a better visibility: lower channel (green, vertical), upper channel (red, horizontal) and the membrane (blue). The orange arrow is pointing to a bubble that formed in the lower channel during imaging. The right image shows the fluorescence read out of the image. Green fluorescence was observed in the bottom channel which was filled with eGFP. No green fluorescence could be observed around the membrane suggesting leakage free bonding. A very weak green florescence was detected in the top channel which stems from eGFP that diffused across the membrane during the experiment. (B) A z-stack of the crossing section was acquired by confocal LSM after filling both channels with eGFP. The membrane is clearly visible as a decrease in intensity. The channel height was measured to be around 50 μm. The scale bar is 500 μm in (A) and 20 μm in (B).*

Although the buffer with the eGFP was degassed extensively before the experiment, air bubbles appeared in the channels, within short time. We speculate, that the buffer becomes quickly enriched with gas since (1) air can permeate through PDMS and the silicon tubing (which were about 20 cm long) and (2) the surface to volume ratio in a microfluidic system is large. In addition, bubble formation in the channel walls may be catalyzed since the PDMS is hydrophobic.

The formation of bubbles in the channels will have important implications for permeation experiments. Growing of a bubble would induce a flow which would perturb a permeability experiment.

6.3.6 Permeability experiments with the microfluidic chamber

We performed a permeability experiment in our microfluidic chamber with an unfunctionalized polycarbonate membrane with pores of a diameter of 30 nm. The bottom compartment was filled with a solution of eGFP (5 µM) as a permeation probe. Then the flow in the bottom compartment was switched off, while the flow of buffer in the top compartment was maintained. After about 50 s the tubings of the top compartment were blocked close to the tube inlet and outlet to prevent flow due to relaxation of the tubing.

We expected the created concentration gradient between the bottom and the top channel to induce permeation of eGFP across the membrane. A series of z-stacks by confocal LSM was acquired to measure this permeation as a decrease in intensity in the bottom compartment. The raw data is presented in figure 6.15 (A). Hardly a change in intensity could be observed by eye. The processed data of the z-stacks is shown in figure 6.15 (B) as intensity change during time. The jump in the intensity between 50 s and 90 s is likely to stem from switching off the flow and blocking the tubing. A decrease in intensity in the bottom compartment was observed from 90 s to about 450 s and demonstrates the depletion of eGFP in the bottom compartment. Around 450 s, however, the intensity started to increase. We suspect this perturbation of the experiment to be created by a growing bubble, which was found in the lower channel after the experiment. While the bubble was forming and growing, it might have induced a flow in the bottom channel which, as a consequence, was exchanging the depleted eGFP in the confocal volume with fresh eGFP from the laterals of the channel.

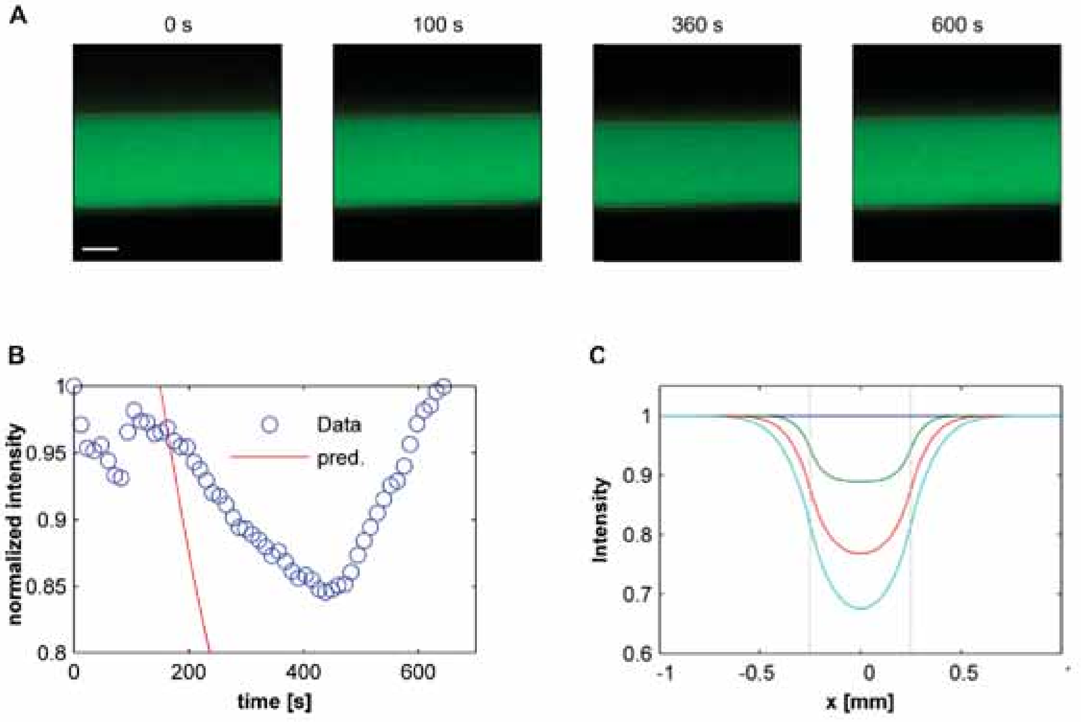

Figure 6.15: Flux experiment with microfluidic chamber: *In a flux experiment with the microfluidic chamber, the bottom compartment was filled with a solution of 5 μM eGFP. Flow of buffer was maintained in the top channel. The membrane had pores with a diameter of 30 nm which where not functionalized. (A) A series of z-stacks for selected time points is shown. (B) The normalized, average intensity in the lower channel was plotted against time. For the first 150 s the intensity is slightly unstable due to work with the tubing (see text). From 150 to 450 s the intensity in the bottom compartment was decreasing, due to eGFP flux from the bottom to the top compartment. Around 450 s, however, the intensity is increasing due to a bubble that formed in the bottom channel. Growth and moving of the bubble induced a flow which lead to perturbation of the experiment. (C) The concentration profiles in the lower compartment of a microfluidic chamber were simulated for the flux experiment. The simulated data from (C) was overlapped in (B) with the experimental data as a red line. The numerically predicted intensity decrease (at the center position of the lower compartment, i. e. $x = 0$ in (C)) had the same order of magnitude as the decrease in intensity in the experiment between 180 and 400 s. Scale bar is 20 μm in (A).*

We numerically calculated the concentration profiles for our experiment (see figure 6.15 (C)) and overlapped the results (red line in figure 6.15 (B)) with the experimentally measured decrease in intensity. The predicted decrease was similar in magnitude to the experimentally observed decrease. An explanation for this could be the flow induced by the bubble which perturbed the experiment already before the intensity increase around 450 s.

6.4 Functionalization of porous polycarbonate membranes

6.4.1 Characterization of SiO_2 coated polycarbonate membranes

We sputtered a 30 nm thin SiO_2 layer onto the shiny side of the polycarbonate membranes with a nominal diameter of 100 nm. SEM images showed that the SiO_2 coating decreased the pore size to 50 – 30 nm (see figure 6.16 (A) and (B)). We tested the coating stability via a so called ”scotch test”, i.e. an adhesive scotch tape was attached to the silica coated membrane and then removed. No traces of the SiO_2 could be observed by eye on the adhesive tape demonstrating that the coated SiO_2 layer was stable and that a TiO_2 contact layer was not necessary to ensure tight adhesion. To obtain a side view of a section of the coated membrane, transmission electron microscopy (TEM) images (silica mapping mode) were taken of cut slices of the sputtered membrane (see figure 6.16 (C)). We observed that the sputtered SiO_2 layer had indeed a thickness of around 30 – 50 nm. Furthermore, the SiO_2 covered the walls along the entrance of the pores without plugging the pore channel. We speculate that the diameter of the pore entrance and depth of the coating along the pore walls may be further adjusted to desired values by tuning the sputtering parameters (such as the sputtering angle and the SiO_2 thickness) and/or using polycarbonate membranes with another pore diameter as a starting substrate. Since we, however, achieved a pore entrance of 30 – 50 nm, which is sufficiently close to the dimensions of the NPC transport channel, we did not undertake further attempts to investigate the tuning possibilities.

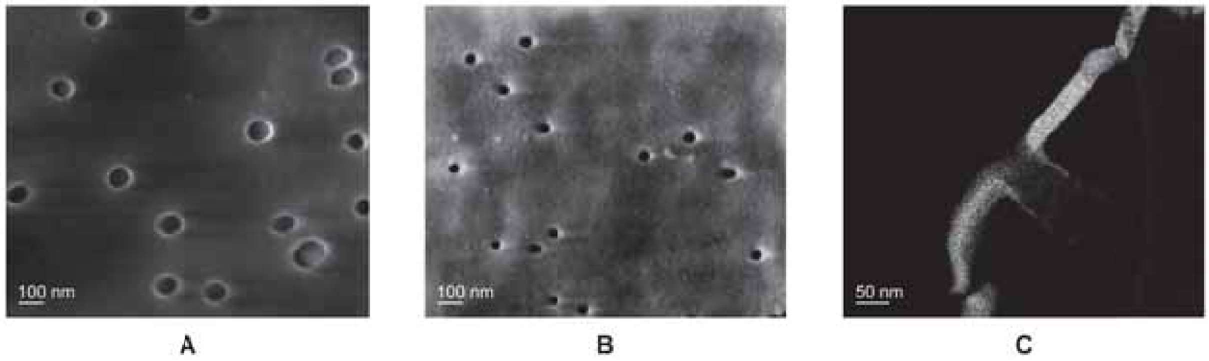

Figure 6.16: Electron microscopy images of SiO_2 coated polycarbonate membranes: *A polycarbonate membrane with pores of a diameter of 100 nm was coated with 30 nm SiO_2. (A) An SEM image of a part of the membrane which was not coated is shown. The pores were circular and had a diameter of around 100 nm. (B) An SEM image of the coated part of the membrane is shown. The diameter of the pores was approximately reduced to 30 – 50 nm after the sputtering process. (C) Side-view by TEM of a membrane slice with a pore (silica mapping mode). The image demonstrates that the sputtered SiO_2 layer had indeed a thickness of around 30 nm, the pores remained unplugged and circular, and the SiO_2 coating easily deposited down to a depth of a pore diameter or more into the channel. Image (A) and (B) were taken by Leire Diaz (CIC biomaGUNE, San Sebastian, Spain); image (C) was taken by Birgit Bußmann and Kersten Hahn, MPI for Intelligent Systems, Stuttgart, Germany*

6.4.2 Functionalization of the SiO_2 layer on polycarbonate membranes

We functionalized the SiO_2 layer by a two step reaction (see Materials and Methods, p. 164, for details). First an amino-silane reacted with the SiO_2 and in a second step the Ni^{2+} chelating EDTA group was coupled to the amino-silane in the presence of EDC. The incubation time of the amino-silane step needed to be limited to 5 min. Otherwise, the membrane became brittle and could not be used further. The EDTA coupling was done by incubating the silica for 1×4 h, 2×2 h followed by 1×15 h. We monitored binding of Nsp1-WT with either a C-terminal His_{10}-tag (Nsp1-WT-H_{10}) or an N-terminal His_{10}-tag (H_{10}-Nsp1-WT) to the functionalized SiO_2 wafer by ellipsometry (see figure 6.17). Binding was stable upon rinsing in buffer and a grafting density of at least 3.9 pmol/cm^2 was reached. Only 20 % of the reached mass stayed bound upon rinsing in imidazole suggesting that most of the Nsp1-WT molecules were grafted *via* their His-tag. We also tested the background binding of the functionalized surfaces by incubating it with Nsp1-WT without His-tag and detected a mass increase of 1.1 pmol/cm^2 during incubation, yet, upon rinsing in buffer only 0.6 pmol/cm^2 stayed bound. This suggests that the background binding was acceptably low.

The total mass of FG repeat domains for a yeast NPC is estimated to be about 5.5 MDa [7]. Assuming NPC dimensions of a diameter of about 30 – 50 nm and a length of 50 nm this translates a nominal grafting density of ca. 3 pmol/cm^2. This is very similar to the Nsp1-WT grafting density achieved in our films.

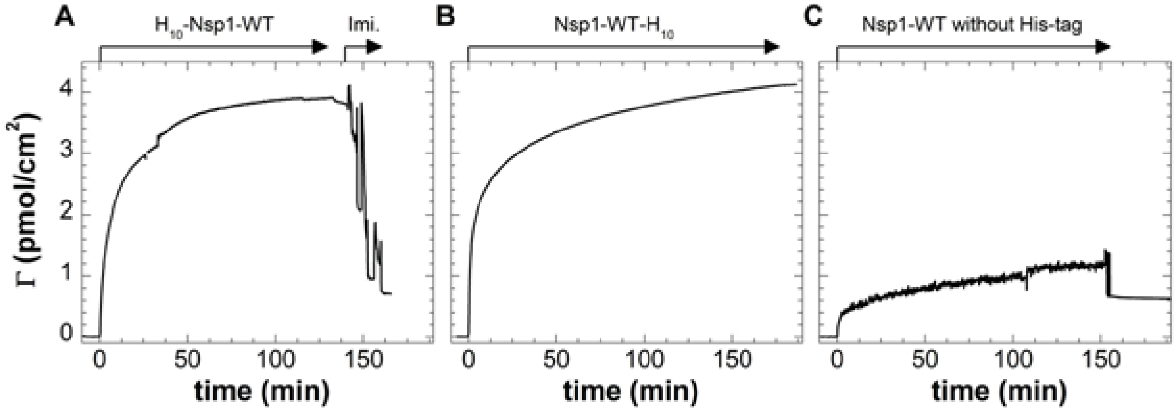

Figure 6.17: Binding of FG-repeat domains to functionalized SiO_2 wafers: *SiO_2 wafers were functionalized with a EDTA group which was loaded with Ni^{2+} and then incubated with either (A) 190 µg/mL His_{10}-Nsp1-WT, or (B) 125 µg/mL Nsp1-WT-His_{10} (incubation steps are indicated by arrows). Both His-tagged Nsp1-WT constructs bound to the functionalized wafers. The final surface mass was in both cases about 4 pmol/cm^2. Binding was stable upon rinsing in buffer. As a control for specific binding via the His-tag, the His_{10}-Nsp1-WT1 film in (A) was rinsed stepwise with 2 M imidazole (Imi.) resulting in elution of more than 80 % of the bound molecules. (C) As an additional control, we also incubated a functionalized wafer with 60 µg/mL Nsp1-WT without His-tag yielding to a mass of about 80 ng/cm^2. However, the bound mass was reduced to less than 50 ng/cm^2 upon rinsing in buffer.*

Moreover, we sought to estimate the achievable grafting density on functionalized polycarbonate membranes by fluorescence measurements by confocal LSM. As a reference, we formed Nsp1-WT films of known grafting density on SLBs as a standard. The Nsp1-WT films contained 2 mol-% atto-488 labeled Nsp1-WT tracers.To this end, we formed SLBs with either 4.2 mol-% tris-NTA or 10 mol-% bis-NTA functionalized lipids on glass slides. The SLBs were incubated with a solution of 125 µg/mL Nsp1-WT-His$_{10}$, containing 2 mol-% atto-488 labeled Nsp1-WT tracers, for 2 h to create labeled Nsp1-WT films of different grafting densities (see figure 6.18 (A)). The grafting densities were determined in a parallel measurement with SLBs on wafers by ellipsometry to be 4.5 and 7.5 pmol/cm^2, respectively (see chapter 5). After subtracting the background intensity, the measured intensities from the LSM measurement were plotted against the grafting density determined by ellipsometry (see figure 6.18 (B)). The correlation between fluorescence intensity and grafting density was approximately linear.

Next, we carried out confocal LSM measurements to determine the fluorescence of a blank, functionalized membrane before incubation it with atto-488 labeled Nsp1-WT-His$_{10}$ (see figure 6.18 (C), left) and found a low fluorescence of the substrate.

When incubating the functionalized polycarbonate membrane with 125 µg/mL atto-488 labeled Nsp1-WT-His$_{10}$ for 2 h, a strong increase of the fluorescence intensity was observed. Moreover, the intensity signal did not change upon rinsing in buffer (see figure 6.18 (C), middle). This demonstrated stable binding of the labeled Nsp1-WT-His$_{10}$ molecules to the functionalized polycarbonate membrane. After subtracting the background intensity and using the standard curve (figure 6.18 (B)), we determined a grafting density of approximately 4.8 pmol/cm^2 (indicated in figure 6.18 (B) with blue, dotted lines). This value was in agreement with the predicted achievable grafting density from ellipsometry measurements on functionalized SiO_2 wafers.

The attached Nsp1-WT film could be almost completely washed off from the functionalized polycarbonate membrane by incubation in 2 M imidazole for 10 min (see figure 6.18 (C), right), suggesting that binding of the Nsp1-WT-His$_{10}$ molecules was mainly specific via their His-tags.

As an additional control, we incubated unfunctionalized membranes, with and without SiO_2 layer, in a solution of 125 µg/mL atto-488 labeled Nsp1-WT-His$_{10}$ molecules and did not observe an increase in intensity (see figure 6.18 (D) and (E)).

We note, the Nsp1-WT film on the functionalized polycarbonate membrane (figure 6.18 (C), middle) appears slightly less homogeneous than the Nsp1-WT films on SLBs. It is currently an open question, whether this is due to inhomogeneities of the Nsp1-WT film itself or whether the confocal intensity read out is hampered by the polycarbonate membrane. In order to answer this question, complementary techniques, such as imaging AFM, might be carried out in the future.

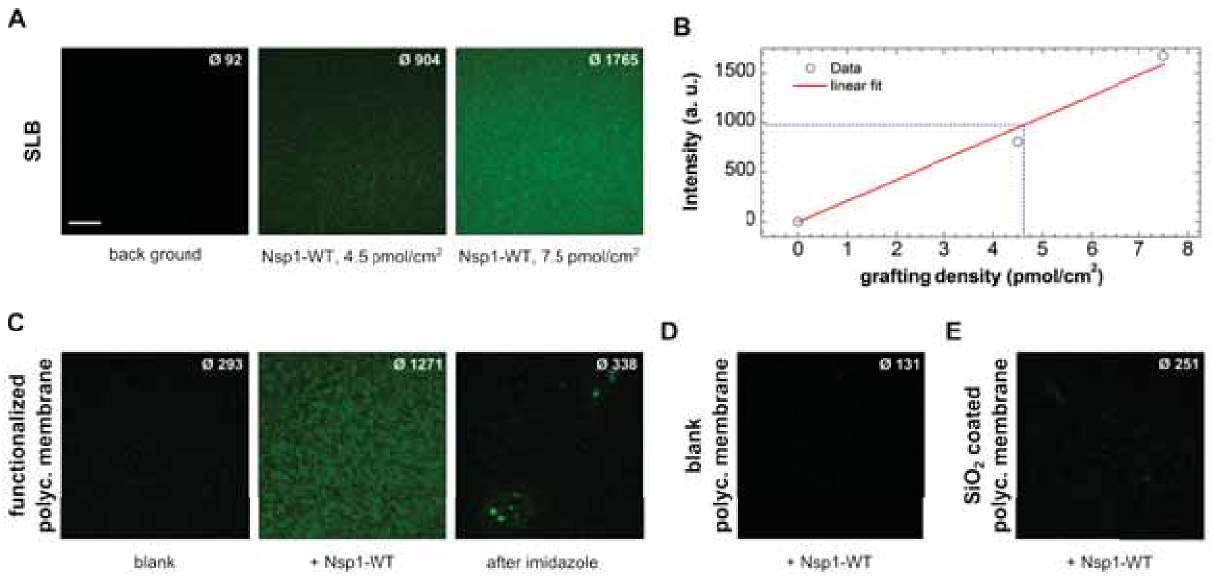

Figure 6.18: Estimation of Nsp1-WT grafting density on functionalized polycarbonate membranes by LSM: *LSM images of different substrates were taken under identical settings to estimate grafting density of Nsp1-WT on functionalized polycarbonate membranes. The average intensity (∅) of the images is indicated in the images. (A) atto-488 labeled Nsp1-WT films with a grafting density of 4.5 and 7.5 pmol/cm^2 were formed on SLBs as a reference. (B) A standard curve was obtained by plotting the average intensity value (corrected for background intensity) against the grafting density determined by ellipsometry in parallel measurements on wafers. (C) Confocal image of a functionalized polycarbonate membrane before and after incubation with atto-488 labeled Nsp1-WT were taken. The average intensity corresponds to a grafting density of 4.8 pmol/cm^2 on the standard curve (indicated with blue lines in (C)). Upon incubation with imidazole, the intensity of the fluorescence read out dropped close to the background. (D) No fluorescence increase could be measured on a blank, polycarbonate membrane incubated atto-488 labeled Nsp1-WT molecules. (E) Neither did a SiO$_2$ coated, yet not functionalized, membrane show a significant increase in intensity after incubation in atto-488 labeled Nsp1-WT molecules. Scale bar in (A) is 20 μm.*

6.4.3 Drying of an Nsp1 film

In the future, one has to decide at which step Nsp1-WT is grafted to the functionalized membrane when constructing the chambers. In the microfluidic chamber, this could be easily done by constructing first the chamber with a functionalized membrane, then fill the channels with a solution of Nsp1-WT and incubating the membrane thereby for a desired time. The remaining Nsp1-WT from the solution could then be easily removed by rinsing the channel with buffer.

In contrast, no flow can be applied in the simple chamber. The situation here would be thus quite different. One may think first of the following approach: first to construct the simple chamber, and then to add the FG repeat domains, then to remove unbound FG repeat domains by diluting the top compartment several times. However, the passage of unbound FG repeat domains across the pore might be hampered once a FG repeat domain meshwork is anchored in the pore. Furthermore, the addition of permeation probes to the bottom compartment would constitute another problem.

An alternative approach is to first immobilize the FG repeat domains to the membrane. Then the membrane with the FG repeat domains could dried before constructing a chamber [1]. After assembling of the chamber, the membrane could be exposed again to liquid and the FG repeat domains on the membrane were thereby rehydrated.

An important question, which arises when following this protocol, is whether drying and rehydration of an Nsp1 film immobilized onto a functionalized SiO_2 substrate had an effect onto the properties of the Nsp1 film. We sought to answer this question with a control measurement. To this end, we functionalized a SiO_2 coated QCM-D sensor and measured the adsorption of Nsp1-WT-His_{10} molecules to the surface by QCM-D (see figure 6.19). Changes in frequency and dissipation showed that the Nsp1-WT-His_{10} molecules bound to the functionalized SiO_2 sensor upon incubation with 100 µg/mL Nsp1-WT-His_{10}. Binding was stable upon rinsing in buffer and final shifts in Δf and ΔD of -78 Hz and 10.8×10^{-6}, respectively, were reached (values are given for the third overtone). The sensor with the grafted Nsp1-WT-His$_{10}$ film was then rinsed in mQ water, blow dried with nitrogen, and resuspended in buffer. The QCM-D response of the rehydrated film differed significantly from the values obtained before. Also, the visco-elastic properties, obtained by fitting the QCM-D values to a visco-elastic model (see chapter 4 on p. 71 for details) before and after the drying step, differed significantly (see table 6.3). This demonstrated that the film would be indeed affected from being dried during the chamber assembly and we speculate that this also affects the qualities of the permeability barrier to some extend.

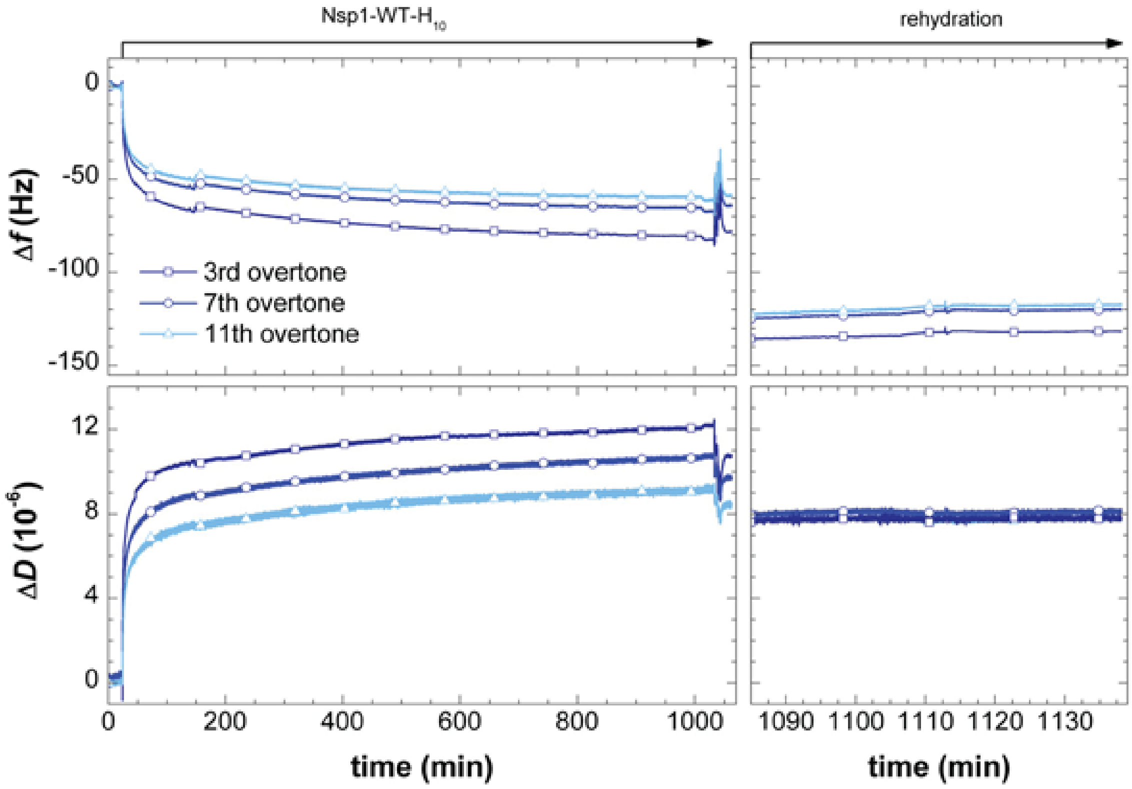

Figure 6.19: Effect of drying and rehydrating an Nsp1 film: *(A) Adsorption of Nsp1-WT molecules to an functionalized* SiO_2 *QCM-D sensor followed by QCM-D (overtones 3, 7, and 11 are shown as indicated). Strong changes in frequency and dissipation demonstrate binding of the Nsp1-WT-His*$_{10}$ *molecules to the surface. Binding is stable upon rinsing in hepes (the peak at the beginning of the rinsing step is due to temperature difference effects). (B) The sensor with the immobilized Nsp1 film on it was rinsed with water, blow dried with nitrogen, and resuspended in buffer. Both, frequency and dissipation shifts changed significantly compared to the values obtained before the drying step.*

Table 6.3: *Results from viscoelastic modeling*

	before drying			**after drying**		
$\boldsymbol{d}$ [nm]	21	±	5	27	±	2
$\boldsymbol{G_0'}$ [kPa] [a]	162	±	105	392	±	222
$\boldsymbol{\alpha'}$	0.40	±	0.20	0.17	±	0.17
$\boldsymbol{G_0''}$ [kPa] [a]	203	±	15	423	±	58
$\boldsymbol{\alpha''}$	0.94	±	0.06	0.96	±	0.04

---

[a] G_0' and G_0'' are given at $f = 15\,\mathrm{MHz}$.

Since the experiment above indicates that drying of the immobilized FG repeat domain film should be avoided, another option is necessary to construct the simple chamber. We, hence, tried whether a membrane, with the immobilized FG repeat domains, which is still wet, i.e. not dried after the immobilization of the FG repeat domains, could be used for the construction of the simple chamber. In our hands, however, a wet, functionalized polycarbonate membrane with immobilized Nsp1-WT molecules did not adhere with any of its sides to our double-sided sticky tape. To circumvent this issue in the future, either a double-sided sticky tape with improved adhesion would be needed or the design/construction plan of the simple chamber could be changed. Alternatively, the microfluidic chamber might be used instead of the simple chamber.

6.5 Discussion

In the preceding sections, we presented our achievements in constructing a measurement setup to measure the permeability of porous polycarbonate membranes. We characterized the porous polycarbonate membranes which were used as a permeability barrier by SEM. Moreover, we aligned the setup to allow for a linear correlation between the fluorescence intensity and the concentration of the fluorescent permeation probes. The construction of two types of measurement chambers was presented: (1) a simple chamber with stagnant solutions in both compartments and (2) a microfluidic chamber in which a flow could be applied independently to each compartment. Finally, we demonstrated that permeation experiments with these chambers equipped with yet unfunctionalized pores could be successfully performed and that experimental data matched the theoretical predictions.

In addition to the achievements summarized above, we also functionalized SiO_2 substrates to capture His-tagged FG repeat domains. The functionalization allowed to graft His-tagged Nsp1-WT molecules with a grafting density of at least 3.9 $\mathrm{pmol/cm^2}$ to functionalized silica wafers or functionalized silica coated polycarbonate membranes. Our measurements demonstrate that the grafting was specific via the His-tag.

6.5.1 The porous substrate

Pore diameter of the porous SiO_2 layer

The concentration of FG repeat domain grafted to the walls of a functionalized pore depends strongly on the diameter of the pore. Hence, if we perform experiments, in the future, with functionalized pores to which FG repeat domains are grafted, it will become crucial to have a detailed picture about the pore's mean diameter and its distribution.

The manufacturer provided the information that the mean pore size is held to a tolerance of +0 %/-20 % of the rated pore size [8]. It is complicated to measure the pore sizes of the porous polycarbonate exactly by SEM since beam damage occurs, especially at high magnification. AFM imaging assays may be an alternative, yet, due to the shape of the AFM tip, it may be difficult to obtain an unambiguous information of the pore size, as well with this technique. Yet, if the pore entrance is only used to estimate the FG repeat domain concentration, it may be merely sufficient to characterize the pore size distribution of the porous SiO_2 layer. The SiO_2 layer may be well accessed by SEM imaging since the metal is less sensitive for beam damage.

On a side remark, the SEM images of the two sides of the polycarbonate membrane indicated that the size distribution of the pore entrance was more homogeneous at the shiny side of the membrane than on the dull side. We could not exclude that this observation was due to an artifact caused by beam damage. To improve the size distribution of the functionalized pore entrances it may be recommendable to sputter the SiO_2 simply on the shiny side of the polycarbonate membrane.

Pore channel

As pointed out in section 6.2, the underlying polycarbonate membrane itself already constitutes a permeability barrier since it is 200 times thicker than the envisaged 30 nm thick layer of functionalized SiO_2. The shape and orientation of the complete pore channel will influence the permeation experiment significantly. When deriving the theoretical predictions, we assumed (1) that the pores have a cylindrical shape, (2) that the diameter of all cylinders is the same, (3) and that they are oriented perpendicular to the membrane. This is likely to be an oversimplified picture of the true conditions.

Indeed, several studies have been carried out to investigate the shape of the pore channel in commercially available and self made track etched polycarbonate membranes [9, 10, 11, 12, 13]. The studies had in common that the angle of the channels usually scatters between -30° to +30° to the normal. Moreover, the channel diameter was two to three times wider in the center than at the entrances. The reasons for these findings are discussed in reference [3] and references therein. Since the shape and orientation of the channel will have important implications onto the flux across the membrane these details should be considered in the future to refine the theoretical predictions.

The porous substrate in the future

On the long run, however, it would be attractive to remove the polycarbonate substrate partly around the pores, thereby increasing ϵ_m and hence the sensitivity of the measurements for κ. The organic polycarbonate material could be straight forwardly removed by chemical solutions and/or plasma [13]. In addition, self-made porous substrates could have a better size-distribution than the comercially available porous substrates [14].

6.5.2 Discrepancy between the experimentally measured and the theoretically predicted characteristic time scales

We could successfully perform permeation experiments with the simple chamber and eGFP and MBP-mCherry as permeation probes. The data could be fitted very nicely to our theoretical derived equation as an exponential decay of the decrease of the intensity. The experimentally measured characteristic times scales matched almost precisely the theoretical predictions in the case of eGFP as a permeation probe. However, the experimentally measured characteristic time scale for the permeation experiment with MBP-mCherry was about 45 % higher than the theoretical predictions, i.e. the permeation across the pore was slower than predicted. Several fine details have not been taken into account when deriving the theoretical prediction of the characteristic time scales: (1) not all pore cylinders may be perpendicular to the membrane surface; (2) there is a size distribution of the pore entrances; (3) the walls of the pores may have an effect onto the diffusion of the particles; (4) there might be a steric hindrance at the entrance to the pores. The first and second aspects are likely to be simplifications of the true conditions as discussed above. The latter two aspects, are studied in literature [15, 16, 17, 18] and may be included to tune the theoretical predictions in the future. In practice, however, merely control measurements with pores without FG repeat domains may already constitute a suitable reference system to determine the selectivity factor of the artificial permeability barrier of functionalized membranes.

6.5.3 Permeability experiments with the microfluidic chamber

In this thesis, we reported the creation of a microfluidic measurement chamber which may be used in the future to measure the flux of permeation probes across a porous membrane. We were able to embed a porous membrane between two PDMS compartments and, thereby, to separate two microfluidic channels from each other by this membrane at a crossing section. The dimensions of the microfluidic channels were 500 µm in width and

50 µm in height. The total volume of one measurement channel was below 1 µL. First permeation experiments suggest that permeability experiments might be possible with this device in the future.

To this end, several problems need to be solved in the future. The main problem was the appearance of bubbles in the measurement channels which severely perturbed the measured concentration decrease of the permeation probe. To counteract bubble formation, vacuum channels could be embedded close to the liquid channels. The vacuum applied and maintained in this channels would avoid the formation of bubbles [19, 20, 21, 22, 23]. In addition, if the crossing section is increased, for instance by making the top compartment wide, the intensity profiles at the crossing section will become flatter and which, as a consequence, will reduce the effect of the bubbles.

Another issue, that we observed during the permeation experiments with the microfluidic chamber was that flow in the compartments due to relaxation of the tubes after switching the pump off needs to be avoided. To this end, we blocked the inlet and outlet tubes close to the entrances and exits to the microfluidic chamber. We used here simple tube clamps. Closing them, however, produced jumps in the monitored intensity. More elaborated systems, such as valves at the entrances, may be implemented into the construction plan of microfluidic chambers in the future.

In addition, we did not test, whether part of the PDMS mortar crept onto the edges of the membrane at the crossing section, before curing it. If this happened a part of the membrane would be blocked and the actual area of the permeable membrane would be reduced. As a consequence, the protein flux across the membrane at the crossing section would be decreased. Such an effect might have further contributed to the discrepancy between the initially measured and the theoretical predicted flux across the membrane. It will be, thus, an important experiment for the future to prove, whether the membrane is (partly) blocked or not, by the mortar PDMS. This might be easily checked, for instance by labeling the mortar PDMS with a fluorescent label and checking the position of the mortar after curing with a fluorescence microscope.

6.5.4 Functionalization strategy of the substrate

We functionalized SiO_2 layer in a two step reaction first with an amino-silane to which in a second step EDTA was coupled. After loading the EDTA with Ni^{2+} we could bind Nsp1-WT specifically via its His-tag to the surface with a maximal grafting density of at least $3.9\,\mathrm{pmol/cm^2}$. If the same grafting density can be achieved at functionalized pores the Nsp1-WT concentration will be about $200\,\mathrm{mg/mL}$. This concentration would be similar to the estimated FG repeat domain concentration in native yeast NPCs. However, Nsp1-WT is a rather long FG repeat domain. If the pores are equipped with shorter FG repeat domains in the future we may achieve a lower concentration (mass per volume). In this case, the surface functionalization might need to be improved. One option to tune the grafting density might be to use another chelating polycarboxylic acid, such as NTA, DTPA, or TTHA [24].

6.5.5 Drying of the FG repeat domain film

In the future, the measurement chamber should be equipped with functionalized membranes to which FG repeat domains are grafted. In case of the simple chamber, we sought to bind the FG repeat domains first to the membrane, then to dry the membrane with the FG repeat domains before assembling the chamber. Since both compartments are filled with liquid solutions, the FG repeat domain film should rehydrate after the chamber assembly.

We investigated the effect of drying and rehydrating an Nsp1-WT film grafted to our SiO_2 surface by QCM-D. We found that the QCM-D response of the Nsp1-WT film was significantly different before and after the drying and rehydration step. We could not observe a reversibility of this effect over the monitored time range of 2 h. This demonstrates that the film properties were changed by the drying and rehydration step.

In addition, we fitted the QCM-D data to a viscoelastic model to extract information about its viscoelastic properties. The results of the fit suggested that film became more rigid after drying and rehydration. It might be interesting to investigate in the future whether this treatment triggers a gel-formation of the Nsp1-WT film on the surface. This could be investigated by FRAP measurements, as done in chapter 5.

Jovanovic-Talisman et al. also dried and rehydrated the Nsp1-WT film on the membranes during the assembly process of their chamber [1]. Although the grafting Nsp1-WT was achieved via binding of the terminal Cys to a gold layer on the membrane, we suspect that the Nsp1-WT film was also affected by the drying and rehydration step. This might have influenced the measurements in their study.

In order to avoid the drying and rehydration step, another assembly strategy for the simple chamber should be found. In this context, the microfluidic flow chamber becomes an attractive alternative to circumvent these issues.

6.6 Conclusions

We presented important intermediate steps towards the development of a nanoscale model system of the permeability barrier of NPCs with a pore like topology mimicking the topology of the native systems. The construction plan of the model system was based on a porous polycarbonate membrane which divides to compartments which allows for flux measurements of fluorescent permeation probes across the pore.

Our achievements included the elaboration of a theoretical framework which allows to quantify the flux of permeation probes across the pores and the pore's selectivity once it is equipped with a permeability barrier. Moreover, we reported the construction of two different types of measurement chambers, a simple one with stagnant solutions and a microfluidic chamber which allows to apply flow independently to the two compartments. Furthermore, we calibrated a detection setup for detection of net flux of fluorescent probes in the chambers and a Matlab data processing and analysis routine. These steps allowed to perform successfully flux measurements in the simple chamber, with a porous membrane which was not functionalized with FG repeat domains. The experimentally observed flux was close to the theoretical predictions. In order to equip the pores with FG repeat domains in the future, we worked on a functionalization strategy of the polycarbonate membrane. The strategy was based the functionalization of a sputtered SiO_2 layer, on one side of the polycarbonate membrane, with a His-tag capturing layer. We reported stable and mainly specific binding of His-tagged Nsp1-WT to the functionalized membranes with a grafting density close the estimated grafting density in the NPC.

Combining our achievements in construction of a measurement chamber with a detection system for flux measurements and functionalizing polycarbonate with FG repeat domains may allow to perform flux measurement across pores equipped with FG repeat domains in the near future. The flux of NTRs and inert proteins of different size across pores equipped with single types of FG repeat domains or mutants would contribute to our understanding of the working mechanism and efficiency of the permeability barrier of NPCs.

6.7 Materials and methods

6.7.1 Materials and buffer preparation

Chemicals were purchased from Sigma-Aldrich, Germany, if not mentioned otherwise. For the experiments described in this chapter we used a buffer containing 10 mM HEPES pH 7.4 and 150 mM NaCl. The buffer was degassed under vacuum for 30 min. PDMS and PDMS curing agent (Dow Corning, U.S.A.) were mixed in a ratio of 9:1 and degassed for 30 min under vacuum.

6.7.2 Substrate functionalization

Substrates

Control experiments were performed on silicon wafers (University Wafers, U.S.A.) with a native SiO_2 layer and QCM-D sensors (Biolin Scientific, Sweden) coated with SiO_2.

Permeation experiments were performed with nucleopore track-etch filter membranes (Whatman plc, UK). These membranes are made of polycarbonate and are perforated with pores of a certain diameter (indicated in the text). One face of the membranes is shiny while the other is dull. A thin SiO_2 layer of approximately 30 nm was directly sputtered onto the shiny side of the polycarbonate membrane (sputtering was done by Olatz Idigoras, CIC nanoGUNE, San Sebastian, Spain).

Functionalization strategy

The protocol for functionalization of SiO_2 layers with NTA-groups is based on Ref. [24]. The substrates were activated by exposing them either to UV/ozone for 30 min (in the case of SiO_2 wafers and QCM-D sensors) or to O_2 plasma for 5 min (in the case of polycarbonate membranes with a sputtered layer of SiO_2). The activated substrates were then incubated in a mixture containing 88 % (*v*/*v*) ethanol, 2 % (*v*/*v*) water, and 10 % (*v*/*v*) 3-aminopropyltriethoxysilane (Thermo Scientific, U.S.A.), which was previously filtered with a 0.2 µm polytetrafluoroethylene membrane filter (VWR, U.S.A.). The incubation time was kept to 5 min, to prevent the polycarbonate membrane from becoming brittle. After incubation, the substrates were thoroughly rinsed with ethanol followed by rinsing with a 10 mM EDTA pH 7.8 solution. After these rinsing steps, the substrates were incubated in a solution containing 0.5 M EDTA pH 8.0 and 25 mM EDC for 4 h. The EDC incubation was repeated four times. Then the substrates were thoroughly rinsed with water and stored in 10 mM EDTA pH 7.8 at 4 °C for no more than one week.

6.7.3 Construction of simple chambers (stagnant solutions)

The design and construction of our simple chamber with stagnant solution in bottom and top compartment is based on the chamber design reported by Jovanovic-Talisman et al. [1]. To construct the bottom compartment, a glass slide (Menzel, Germany) was exposed to O_2 plasma for 5 min and then passivated by incubation in 100 µg/mL PLL-g-PEG (Susos, Switzerland) for 5 min. Then the glass slide was rinsed in mQ water, blow dried with nitrogen, and a double-sided sticky tape with a 2 mm hole in it was attached. In a next step 0.5 µL of buffer containing the permeation probe was added to the bottom compartment. The top compartment was made of the lid of an ordinary laboratory 2 mL plastic reaction tube (Eppendorf, Germany) to which the polycarbonate membrane was clipped. The top reservoir was also filled with buffer containing the permeation probe before it was quickly attached to the bottom compartment.

6.7.4 Construction of microfluidic chambers

Photo masks

Photo masks of the axial projection of both the top and the bottom compartment were made with AutoCAD (AutoDesk Inc., U.S.A.) and printed at a resolution of 25 000 dpi (BVM, Germany).

Creation of master wafers

For the creation of a microfluidic PDMS chamber, negative imprints of the channels of the micro fluidic compartments were produced. These so called “master wafers” served as a casting mold for the fabrication of the PDMS bottom and top compartment of the microfluidic chambers. To this end, we followed the protocol of the SU-8 photo resist (Micro Chem, U.S.A.). The creation steps of these wafers are illustrated in figure 6.20 and are briefly described in the following:

A new silica wafer was dried in an oven at 200 °C for 1 h. After cooling it to room temperature, we used a spin coater (WS-400B-6NPP-LITE, Laurell technologies corporation, U.S.A.) to coat the wafer with a 40 µm thin layer of SU-8 50 photo resist (Micro Chem,U.S.A.) by running 3000 rpm for 30 s. Next, the photo resist solvent was evaporated by soft baking the wafer at 65 °C for 5 min followed by 95 °C for 15 min. The photo mask was put on top of the photo resist layer and the uncovered parts were then exposed four times to UV (350 – 400 nm) light (intelli-Ray 400, Uvitron International, U.S.A.) for 5 s, thereby inducing cross-linking in the exposed parts of the photo resist. The cross-linking needs to be further improved by post exposure baking at 65 °C for 1 min followed by 95 °C for 4 min. The parts of the photo resist that were not cross-linked were removed by incubating the photo resist in SU-8 developer (Micro Chem, U.S.A.) for 5 min. The developer was rinsed off with acetone, followed by isopropanol, followed by mQ water and was then blow dried with nitrogen. Then, the wafer with photo resist was hard baked at 200 °C for 1 h to further cross-link the material. Finally, the wafer was coated with an anti adhesive layer of (Tridecafluoro-1,1,2,2-tetrahydrooctyl)trichlorosilane (ABCR, Germany) by gas phase evaporation. To this end, the wafer and a small droplet of (Tridecafluoro-1,1,2,2-tetrahydrooctyl)trichlorosilane were kept for 2 h in a desiccator under vaccuum.

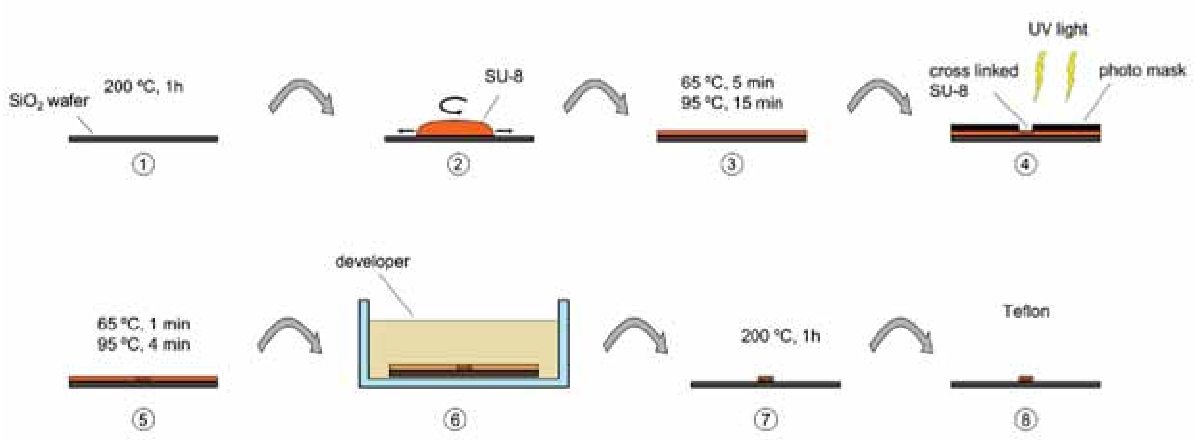

Figure 6.20: ***Scheme for the construction of a master wafer:*** *Step 1: Drying of the substrate. Step 2: Spin coating of a thin layer of SU-8 photo resist onto the substrate. Step 3: Soft baking. Step 4: Cross linking of photo resist. Step 5: Post exposure bake. Step 6: Removal of photo resist that was not cross linked by developer. Step 7: Hard bake. Step 8: Teflon coating.*

Creation of PDMS top and bottom compartments

Top and bottom compartment were constructed as summarized in figure 6.21.

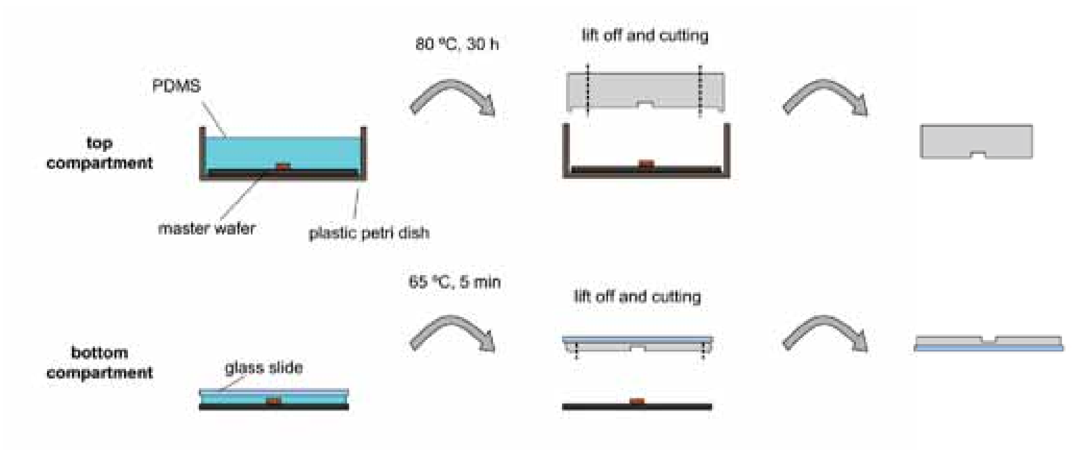

Figure 6.21: ***Scheme for the construction of top and bottom compartments of the microfluidic chamber:*** *Top compartment (top row): A plastic petri dish with the master wafer lying in it was filled with PDMS. Then, the PDMS was cured at 80°C for 30 min. The cured PDMS with the imprint of the channels of the master waver was lifted off and cut at the edges. Bottom compartment (bottom row): A small amount of PDMS was poured over the master wafer and a microscope glass slide was then gently pressed onto the PDMS. The PDMS was cured on a heating plate at 65°C for 5 min, before it was lifted off from the master wafer together with the microscope slide. Finally, the edges of the PDMS layer were cut.*

Microfluidic chamber assembly

The assembly of the microfluidic chamber with the polycarbonate membrane embedded between top and bottom compartment was performed as described in [6]. First, PDMS was mixed with curing agent in a ratio 9:1 (w/w). This mixture was then further mixed with toluene in a ratio of 1:2 (w/w) to make the PDMS less viscous. A glass slide was then spin coated with this mixture at 1500 rpm. This leads to a thin PDMS layer on the glass slide. The coated glass slide was then put into an oven at 80 °C, to evaporate the toluene, for 5 min. This PDMS layer was transferred to the top and bottom compartments by placing them onto the PDMS layer for 5 s. Also the edges of the polycarbonate membrane were dipped into the PDMS layer. Then, the membrane was carefully placed onto the channel of the top compartment and the bottom compartment was placed onto them using a micromanipulator (Scientifica, UK). Finally, the mortar PDMS layer was cured at 80 °C for 5 min.

6.7.5 Confocal microscopy imaging

The permeation experiments were performed with a confocal laser scanning microscope (LSM 510, Zeiss, Germany) equipped with an argon and a DPPS laser. A plan-apochromat 63x/1.4 oil immersion objective was used if not stated otherwise. The pinhole was set to 0.68 mm diameter allowing for a z-resolution of 2.5 µm. The x-y planes were imaged at a size of 120 µm × 120 µm and a resolution of 32×32 pixels. The pixel depth was set to 12 bit. z-stacks were acquired with a z-step size of 2.5 µm every 10 s. eGFP was excited at a wavelength of 488 nm with a laser power of 0.3 % and a master gain of 650. mCherry was excited at a wavelength of 516 nm with a laser power of 1 % and a master gain of 720.

6.7.6 Data processing and analysis routine

A program script was written for Matlab (The Mathworks, U.S.A.) allowing for a quick and convenient processing and analysis of the confocal microscopy data. The Matlab program loads the confocal data and adjusts it for background intensity and axial focus drifts. The average intensity in a desired confocal volume is calculated and normalized to the starting conditions. The Matlab routine is available upon request.

6.7.7 Protein purification and labeling

Proteins were provided by Steffen Frey, MPI for biophysical chemistry, Göttingen, Germany. Information about protein expression and purification can be found in chapter 3 supplementary information (fluorescent probes) and chapter 5 materials and methods (Nsp1-WT and atto488-Nsp1-WT).

References

[1] T. Jovanovic-Talisman, J. Tetenbaum-Novatt, A. S. McKenney, A. Zilman, R. Peters, M. P. Rout, and B. T. Chait. 2008. “Artificial nanopores that mimic the transport selectivity of the nuclear pore complex”. In: *Nature* 457 (7232), pp. 1023–1027.

[2] P. Déjardin and E. Vasina. 2004. “An accurate simplified data treatment for the initial adsorption kinetics in conditions of laminar convection in a slit: application to protein adsorption”. In: *Colloids and Surfaces B: Biointerfaces* 33 (2), pp. 121–127.

[3] P. Y. Apel, I. Blonskaya, S. Dmitriev, O. Orelovitch, and B. Sartowska. 2006. “Structure of polycarbonate track-etch membranes: Origin of the ”paradoxical” pore shape”. In: *J. Membr. Sci.* 282 (1), pp. 393–400.

[4] D. Mohr, S. Frey, T. Fischer, T. Güttler, and D. Görlich. Sept. 2009. “Characterisation of the passive permeability barrier of nuclear pore complexes.” In: *EMBO J.* 28 (17), pp. 2541–2553.

[5] S. Frey and D. Görlich. 2009. “FG/FxFG as well as GLFG repeats form a selective permeability barrier with self-healing properties”. In: *EMBO J.* 28 (17), pp. 2554–2567.

[6] B. Chueh, D. Huh, C. Kyrtsos, T. Houssin, N. Futai, and S. Takayama. 2007. “Leakage-free bonding of porous membranes into layered microfluidic array systems”. In: *Anal. Chem.* 79 (9), pp. 3504–3508.

[7] L. A. Strawn, T. Shen, N. Shulga, D. S. Goldfarb, and S. R. Wente. Mar. 2004. “Minimal nuclear pore complexes define FG repeat domains essential for transport.” In: *Nat. Cell Biol.* 6 (3), pp. 197–206.

[8] “Whatman Nucleopore Membranes - Microfiltration Membrane Characteristics”. N.d. Whatman International Ltd.

[9] J. Calvo, A. Hernandez, G. Caruana, and M. L. 1995. “Pore Size Distributions in Microporous Membranes I. Surface Study of Track-Etched Filters by Image Analysis”. In: *J. Colloid Interface Sci.* 175 (1), pp. 138–150.

[10] D. S. Cannell and F. Rondelez. 1980. “Diffusion of polystyrenes through microporous membranes”. In: *Macromolecules* 13 (6), pp. 1599–1602.

[11] G. Guillot and F. Rondelez. 1981. “Characteristics of submicron pores obtained by chemical etching of nuclear tracks in polycarbonate films”. In: *J. Appl. Phys.* 52 (12), pp. 7155–7164.

[12] A. Hernandez, F. Martinez-Villa, J. Ibanez, J. Arribas, and A. Tejerina. 1986. “An experimentally fitted and simple model for the pores in nuclepore membranes”. In: *Sep. Sci. Technol.* 21 (6-7), pp. 665–677.

[13] C. Schönenberger, B. Van der Zande, L. Fokkink, M. Henny, C. Schmid, M. Krüger, A. Bachtold, R. Huber, H. Birk, and U. Staufer. 1997. “Template synthesis of nanowires in porous polycarbonate membranes: electrochemistry and morphology”. In: *J. Phys. Chem. B* 101 (28), pp. 5497–5505.

[14] E. Ferain and R. Legras. 2001. “Efficient production of nanoporous particle track etched membranes with controlled properties”. In: *Radiat. Meas.* 34 (1), pp. 585–588.

[15] R. Ladenburg. 1907. “Über den Einfluss von Wänden auf die Bewegung einer Kugel in einer reibenden Flüssigkeit”. In: *Annalen der Physik* 328 (8), pp. 447–458.

[16] J. Pappenheimer, E. Renkin, and L. Borrero. 1951. “Filtration, diffusion and molecular sieving through peripheral capillary membranes”. In: *Am. J. Physiol.* 167 (13), p. 2578.

[17] J. Pappenheimer. 1953. “Passage of molecules through capillary walls”. In: *Physiol. Rev.* 33 (3), pp. 387–423.

[18] E. Renkin. 1954. “Filtration, diffusion, and molecular sieving through porous cellulose membranes”. In: *J. Gen. Physiol.* 38 (2), pp. 225–243.

[19] M. Johnson, G. Liddiard, M. Eddings, and B. Gale. 2009. “Bubble inclusion and removal using PDMS membrane-based gas permeation for applications in pumping, valving and mixing in microfluidic devices”. In: *J. Micromech. Microeng.* 19 (9), p. 095011.

[20] C. Lochovsky, S. Yasotharan, and A. Günther. 2012. “Bubbles no more: in-plane trapping and removal of bubbles in microfluidic devices”. In: *Lab Chip* 12 (3), pp. 595–601.

[21] A. Skelley and J. Voldman. 2008. “An active bubble trap and debubbler for microfluidic systems”. In: *Lab Chip* 8 (10), pp. 1733–1737.

[22] J. Sung and M. Shuler. 2009. “Prevention of air bubble formation in a microfluidic perfusion cell culture system using a microscale bubble trap”. In: *Biomed. Microdevices* 11 (4), pp. 731–738.

[23] W. Tan and S. Takeuchi. 2007. “A trap-and-release integrated microfluidic system for dynamic microarray applications”. In: *Proc. Natl. Acad. Sci. U.S.A.* 104 (4), pp. 1146–1151.

[24] D. Görlich and S. Frey. May 2010. “Immobilisation of chelating groups for immobilised metal ion chromatography (IMAC). EP Patent 2,183,049”.

7 Concluding remarks and perspectives

7.1 Achievements

The aim of this thesis was to create and study nanoscale model systems of the NPC's permeability barrier and, by doing so, to shed light on the permeability barrier's mechanism of selectivity. In the following, main achievements will be summarized.

7.1.1 Creation of planar model systems

One of the developed model systems were planar films of end-grafted FG-repeat domains which mimic the interior of the NPC. The grafting surfaces had His-tag capturing properties and were either: (1) custom made SLBs doped with bis- or tris-NTA modified lipids (see chapter 3 and 5), or (2) commercially available His-tag capturing QCM-D sensors (see chapter 4), or (3) SiO_2 layers which were functionalized with EDTA (see chapter 6).

Despite their simplicity, this type of model system is attractive, because it can be characterized quantitatively and in detail by a toolbox of biophysical techniques such as QCM-D, ellipsometry, AFM, and FRAP.

7.1.2 FG repeat domain films resemble the permeability barrier in the NPC

The planar model systems reproduce important properties of the native systems. The mode of FG repeat domain attachment is end-confined anchoring in the NPC and in our model systems. In addition, the achieved maximal grafting densities (ca. 5 – 10 pmol/cm^2) and FG repeat domain concentrations (ca. 200 mg/mL) for wild type FG repeat domains were similar to the currently available estimate of grafting density and concentration of FG repeat domains in the NPC [1]. Moreover, the thickness of our films (about 30 nm) was similar to the diameter and length of the of the NPC's transporter channel [2].

7.1.3 NTR binding to FG repeat domain films

We exploited our planar model system to study the interaction of NTRs with FG repeat domain assemblies. In chapter 3, we used Nsp1 as FG repeat domain and scImpβ, scImpβ• eGFP, and scImpβ• Gsp1p• GTP as model NTR (with and without cargo). We could demonstrate that the model NTR interacted selectively with the Nsp1 film, and that the Nsp1 film was permeable for scImpβ. Moreover, we could provide quantitative estimates for the affinity between Nsp1 and the model NTR (and its complexes). A key finding of our study was that scImpβ binding to Nsp1 films induced only a moderate change (of a few nanometers) in thickness. This result strongly contrasted previous reports of a collapse for hsNup153 brushes upon interaction with hsImpβ [3, 4], calling into question the reversible collapse model. In order to investigate under which circumstances a collapse or a brush stretching appears, our model system may, in future, be extended to other FG repeat domains and NTRs.

7.1.4 Connecting biological function of the FG repeat domain meshwork with theoretical predictions from polymer physics

A major contribution to extend our understanding of the properties of the permeability barrier was to apply concepts of polymer theory to our FG repeat domain films.

Quantification of characteristic length and time scales

In chapter 4, we extracted estimates for the correlation length and the characteristic time scale for relaxation of meshwork strands in the Nsp1-WT meshwork *via* a rheological approach. This information is important to understand the mechanism of selectivity of the permeability barrier, since the mobility of a permeation probe in the meshwork is expected to strongly depend on these two parameters [5]. In the future, this approach might be extended to films consisting of other types of FG repeat domains.

The morphology of FG repeat domain meshworks is influenced by the cohesiveness of the FG repeat domains

The key finding of chapter 5 was that cohesiveness substantially influences the morphology of FG repeat domain meshworks. By applying concepts of polymer theory, we connected the morphology of a meshwork with its size selectivity qualities for permeation probes. This led to the hypothesis that cohesiveness may be tuned, in the native NPC, to obtain a compactified meshwork with exquisite permeability barrier properties.

7.1.5 First steps towards creating a model system comprising the NPC topology

In chapter 6, we reported intermediate steps towards the development of a nanoscale model system of the NPC that reproduces, in addition to the features of the planar systems, the pore-like topology of the NPC transport channel. The envisaged model system was based on artificial pores with FG repeat domains grafted to the pore walls.

Theoretical predictions for flux of solutes across nanoporous substrates

We elaborated a detailed, theoretical framework about the flux of permeation probes across a porous substrate. The results provided valuable predictions about the detection limits of the setup and guidelines for optimizing the experimental design.

Creation of a measurement setup

We also reported the creation of two measurement chambers in which a porous polycarbonate membrane separated two compartments. In one of the measurement chambers, the solutions in both compartments were stagnant, while in the second measurement chamber, flow could be applied to both compartments independently. The simple measurement chamber with stagnant solutions could be used to demonstrate a working (1) detection system for net flux of fluorescent permeation probes across the pores and (2) data processing and analysis routine (implemented in Matlab).

Grafting of FG repeat domains to functionalized porous membranes

In order to graft FG repeat domains specifically with one end to the walls of the pores, we sputtered a 30 nm thin layer of SiO_2 onto one side of the membrane. The sputtered SiO_2 layer was stably connected to the polycarbonate and also deposited a few 10 nm down the channels. Pore diameters of $30-50$ nm could be achieved readily. We demonstrated that the SiO_2 layers can be coated with a His-tag capturing layer and that His-tagged FG repeat domains can be specifically grafted to the functionalized surfaces at densities that are estimated to be present in NPCs.

In the future, our achievements will be combined to create artificial FG repeat domain pores as a nanoscale model system of the NPC.

7.2 Outlook

The achievements of this thesis can be extended to further study the mechanism of selectivity of the NPC's permeability barrier. A brief outline of possible perspectives is given.

7.2.1 Affinity studies

We exploited our planar model system to study the interaction of Nsp1-WT with scImpβ (alone, with a cargo, and coupled to Ran• GTP). This approach can be straightforwardly extended to study the interaction between other types of FG repeat domains and NTRs. For instance, a systematic and accurate determination of the binding affinities for a set of FG repeat domains and a set of NTRs could further contribute to a better understanding of the transport across the NPC and might allow to refine some of the concepts such as the idea of an affinity gradient [6, 7]. Furthermore, NTRs could be replaced by other binding partners, such as virus proteins [8, 9, 10], that may interact with FG repeat domains in our model system.

In this regard, our films represent an interesting *in vitro* model of FG repeat domain assemblies for the study of interactions that are crucial for nuclear import and export.

7.2.2 Role of NTRs for the morphology of the meshwork

We studied in detail the morphology of FG repeat domain meshworks in the absence of NTRs (see chapter 5). However, the FG repeat domain meshwork *in vivo* is likely to always comprise NTRs since their concentration in the cell is typically in the micro molar range. Furthermore, an improved size selectivity was reported for *in vitro* model systems of the NPC when NTRs were present [11, 12]. Hence, it would be interesting to exploit our model system in the future to study in detail the morphology of the FG repeat domain films when NTRs are bound to it.

Such a study would be important given that we make a connection between the morphology of the FG repeat domain meshwork and its selectivity quality. In addition, this could contribute to our understanding of the role of NTRs – they may not only serve as shuttles for cargo, yet, also could play an active role in improving the selectivity qualities of the permeability barrier.

7.2.3 Role of spacers for cohesiveness

Our experiments confirmed the findings by Frey et al. that FG repeat motives are crucial for cohesiveness of FG repeat domains [13]. However, there is evidence that the spacers between the FG-motives also play an important role either as repulsive elements to prevent a collapse of the meshwork or as a cohesive element, further tightening the meshwork [14, 15, 16]. In order to study the contribution of the spacer elements to the cohesiveness, it would be interesting to work with artificial FG repeat domains that have well controlled spacers. Planar films of such artificial FG repeat domains would constitute a valuable model system allowing to readily investigate the role of spacers for cohesiveness.

Such studies may allow to design polymers which reproduce properties of FG repeat domains and assemble into meshwork with filter properties. Equipping a porous substrate with such a filtering meshwork may then be used as a man-made bio-inspred filter device.

7.2.4 Different types of FG repeat domains at different locations

We studied FG repeat domain films that consisted only of one type of FG repeat domain. The FG repeat domain meshwork in the NPC, however, consists of a mixture of FG repeat domains. There is evidence that this mixture is crucial for viability [1] and that certain FG repeat domains interact preferentially with each other thereby forming subcomplexes which may reflect physiologically relevant structures (reviewed in Ref. [17]).

Our model systems could be further developed to allow for studying mixtures of FG repeat domains. Such a study would be crucially important to answer the question, why the permeability barrier consists of different types of FG repeat domains rather than of a single one with an appropriate balance of cohesive elements.

7.2.5 Exploiting the compartmentalization in the artificial FG repeat domain pore system

The artificial pore model system is similar to the native conditions with respect to having two separated compartments. This could be exploited to imbed asymmetric distributions of other proteins involved in the nucleo-cytoplasmic transport. An example is the Ran• GTP gradient which is important for the nucleo-cytoplasmic molecule transport in the cell (reviewed in Ref. [18]).

In this respect, the artificial FG repeat domain pore system could constitute a beneficial (minimalistic) tool to study transport pathways across the NPC *in vitro* and to improve our understanding of nucleo-cytoplasmic transport phenomena.

References

[1] L. A. Strawn, T. Shen, N. Shulga, D. S. Goldfarb, and S. R. Wente. Mar. 2004. “Minimal nuclear pore complexes define FG repeat domains essential for transport.” In: *Nat. Cell Biol.* 6 (3), pp. 197–206.

[2] Q. Yang, M. P. Rout, and C. W. Akey. Jan. 1998. “Three-dimensional architecture of the isolated yeast nuclear pore complex: functional and evolutionary implications.” In: *Mol. Cell* 1 (2), pp. 223–234.

[3] R. Y. H. Lim, B. Fahrenkrog, J. Köser, K. Schwarz-Herion, J. Deng, and U. Aebi. Oct. 2007. “Nanomechanical basis of selective gating by the nuclear pore complex.” In: *Science* 318 (5850), pp. 640–643.

[4] R. L. Schoch, L. E. Kapinos, and R. Y. Lim. 2012. “Nuclear transport receptor binding avidity triggers a self-healing collapse transition in FG-nucleoporin molecular brushes”. In: *Proc. Natl. Acad. Sci. U.S.A.* 109 (42), pp. 16911–16916.

[5] L. H. Cai, S. Panyukov, and M. Rubinstein. Oct. 2011. “Mobility of Nonsticky Nanoparticles in Polymer Liquids”. In: *Macromolecules* 44 (19), pp. 7853–63.

[6] I. Ben-Efraim and L. Gerace. Jan. 2001. “Gradient of increasing affinity of importin beta for nucleoporins along the pathway of nuclear import.” In: *J. Cell Biol.* 152 (2), pp. 411–417.

[7] B. Pyhtila and M. Rexach. Oct. 2003. “A gradient of affinity for the karyopherin Kap95p along the yeast nuclear pore complex.” In: *J. Biol. Chem.* 278 (43), pp. 42699–42709.

[8] R. A. Fouchier, B. E. Meyer, J. H. Simon, U. Fischer, A. V. Albright, F. González-Scarano, and M. H. Malim. July 1998. “Interaction of the human immunodeficiency virus type 1 Vpr protein with the nuclear pore complex.” In: *J. Virol.* 72 (7), pp. 6004–6013.

[9] S. Popov, M. Rexach, G. Zybarth, N. Reiling, M.-A. Lee, L. Ratner, C. M. Lane, M. S. Moore, G. Blobel, and M. Bukrinsky. 1998. “Viral protein R regulates nuclear import of the HIV-1 pre-integration complex”. In: *EMBO J.* 17 (4), pp. 909–917.

[10] Y. Jenkins, M. McEntee, K. Weis, and W. C. Greene. 1998. “Characterization of HIV-1 vpr nuclear import: analysis of signals and pathways”. In: *J. Cell Biol.* 143 (4), pp. 875–885.

[11] S. Frey and D. Görlich. 2009. “FG/FxFG as well as GLFG repeats form a selective permeability barrier with self-healing properties”. In: *EMBO J.* 28 (17), pp. 2554–2567.

[12] T. Jovanovic-Talisman, J. Tetenbaum-Novatt, A. S. McKenney, A. Zilman, R. Peters, M. P. Rout, and B. T. Chait. 2008. “Artificial nanopores that mimic the transport selectivity of the nuclear pore complex”. In: *Nature* 457 (7232), pp. 1023–1027.

[13] S. Frey, R. P. Richter, and D. Görlich. Nov. 2006. "FG-rich repeats of nuclear pore proteins form a three-dimensional meshwork with hydrogel-like properties." In: *Science* 314 (5800), pp. 815–817.

[14] S. S. Patel, B. J. Belmont, J. M. Sante, and M. F. Rexach. Apr. 2007. "Natively unfolded nucleoporins gate protein diffusion across the nuclear pore complex." In: *Cell* 129 (1), pp. 83–96.

[15] J. Yamada, J. L. Phillips, S. Patel, G. Goldfien, A. Calestagne-Morelli, H. Huang, R. Reza, J. Acheson, V. V. Krishnan, S. Newsam, A. Gopinathan, E. Y. Lau, M. E. Colvin, V. N. Uversky, and M. F. Rexach. 2010. "A bimodal distribution of two distinct categories of intrinsically disordered structures with separate functions in FG nucleoporins". In: *Molecular & Cellular Proteomics* 9 (10), pp. 2205–2224.

[16] C. Ader, S. Frey, W. Maas, H. B. Schmidt, D. Görlich, and M. Baldus. 2010. "Amyloid-like interactions within nucleoporin FG hydrogels". In: *Proc. Natl. Acad. Sci. U.S.A.* 107 (14), pp. 6281–6285.

[17] T. U. Schwartz. 2005. "Modularity within the architecture of the nuclear pore complex". In: *Curr. Opin. Struct. Biol.* 15 (2), pp. 221–226.

[18] M. Stewart. 2007. "Molecular mechanism of the nuclear protein import cycle". In: *Nat. Rev. Mol. Cell Biol.* 8 (3), pp. 195–208.

Author's contribution

Work of this thesis was performed in collaboration. Wherever collaborators have assisted in data acquisition, data interpretation, data analysis and data simulations their contributions have been acknowledged: in the form of co-authorship on published or prepared manuscripts; in the acknowledgment of published or prepared manuscripts; or in figures presented in this thesis. In the following, I will summarize my own contribution.

Chapter 3: Ultrathin nucleoporin FG repeat films and their interaction with NTRs

This chapter was published in EMBO Reports, 2010, 11: 366–372, as: *"Ultrathin nucleoporin phenylalanine-glycine repeat films and their interaction with NTRs"*. Authors: **Nico B. Eisele**, Steffen Frey, Jacob Piehler, Dirk Görlich, Ralf P. Richter.

I co-designed research (together with Steffen Frey, Dirk Görlich and Ralf P. Richter). I performed all QCM-D and ellipsometry measurements and analyzed the data. I contributed to data interpretation, figure preparation, and writing the article.

Chapter 4: Viscoelasticity of Thin Biomolecular Films

This chapter was published in Biomacromolecules, 2012, 13: 2322–2332 as: *"Viscoelasticity of Thin Biomolecular Films: A Case Study on Nucleoporin Phenylalanine-Glycine Repeats Grafted to a Histidine-Tag Capturing QCM-D Sensor"*. Authors: **Nico B. Eisele**, Fredrik I. Andersson, Steffen Frey, and Ralf P. Richter

I co-designed research (together with Ralf Richter). I performed all QCM-D and ellipsometry measurements and analyzed the data. I contributed to data interpretation. All figures were prepared by myself, except figures displaying data from AFM measurements (i.e. figure 2 and figure 7 in this publication, which were prepared by Ralf Richter). I wrote the first draft of the article and helped to complete the article for publication.

Chapter 5: Cohesiveness tunes assembly and morphology of FG repeat domain meshworks

This chapter constitutes a manuscript which will be submitted soon as: *"Cohesiveness tunes assembly and morphology of FG nucleoporin domain meshworks – Implications for nuclear pore permeability"*. Authors: **Nico B. Eisele**, Aksana A. Labokha, Steffen Frey, Dirk Görlich and Ralf P. Richter.

I co-designed research (together with Steffen Frey, Dirk Görlich and Ralf P. Richter). I preformed all QCM-D, ellipsometry, FRAP measurements and analyzed the data. I contributed to data interpretation. I prepared all figures, except figure 5.1 (which was prepared with the help of Ralf Richter) and figures displaying AFM data (i.e. figures 5.3 A and 5.5, which were prepared by Ralf Richter). I wrote the first draft of the article and helped to complete the paper for submission.

Chapter 6 Towards construction of FG repeat domain pores as a model system

The results in this chapter have not yet been published or prepared for an article manuscript. Nevertheless this work was performed in collaboration with others. If data from collaborators were used for a figure, I clearly acknowledged the collaborator in the figure caption (this concerns essentially all shown SEM/TEM images). If collaborators have contributed material or protocols they were acknowledged in the text. I contributed to the derivation of the theoretical framework, concerning net flux across the porous membrane working with Ralf Richter. All QCM-D, ellipsometry, and CLSM measurements were performed by myself. The construction of the measurement chambers was done by myself. All Matlab routines were also independently programmed by myself.

N. Eisele

Nico Eisele
March, 2013
San Sebastian, Spain

List of publications

N. B. Eisele, Frey, J. Piehler, D. Görlich, R. P. Richter. 2010. ”Ultrathin nucleoporin FG repeat films and their interaction with nuclear transport receptors”. In: *EMBO reports*, 11(5), pp. 366 – 372.

N. B. Eisele, F. I. Andersson, S. Frey, R. P. Richter. 2012. ”Viscoelasticity of thin biomolecular films: a case study on nucleoporin phenylalanine-glycine repeats grafted to a histidine-tag capturing QCM-D sensor”. In: *BioMacromolecules*, 13, pp. 2322 – 2332.

N. B. Eisele, A. A. Labokha, S. Frey, D. Görlich, R. P. Richter, ”Cohesiveness tunes assembly and morphology of FG nucleoporin meshworks – Implications for nuclear pore permeability”, *in preparation*.

R. P. Richter, K. B. Rodenhausen, **N. B. Eisele**, M. Schubert. In press. ”Coupling Spectroscopic Ellipsometry and Quartz Crystal Microbalance to Study Organic Films at the Solid-Liquid Interface”. In: K.-J. Eichhorn and K. Hinrichs (Eds.), *Ellipsometry of Functional Organic Surfaces and Films*, Springer.

Acknowledgment

It would not have been possible to do the research for this doctoral thesis without the help and support of the people around me, to only some of whom it is possible to give particular mention here.

First of all, I would like to express my sincere gratitude to Ralf Richter for giving me the opportunity to carry out an exciting PhD project under your supervision in your laboratory in San Sebastián. Throughout my PhD project you have been a huge source of knowledge and inspiration. You always encouraged me to further develop my scientific knowledge and my ability to critically examine scientific issues.

I also would like to express my sincere gratitude to Dirk Görlich for providing me with the opportunity to carry out this PhD project in an interdisciplinary and international collaboration with his laboratory. This collaboration led to inspiring and stimulating discussions and, furthermore, strongly supported my research with the supply of essential material.

I am grateful to Claudia Steinem for joining my thesis committee, supporting my thesis, and fruitful discussions.

Another thanks goes to Dirk Görlich and Claudia Steinem for reviewing my thesis and to Ralf Richter, Detlef Doenecke, Jörg Enderlein, and Sarah Köster for being members of my examination board.

Moreover, I would like to express my gratitude to Steffen Frey for many fruitful discussions and for supplying me with proteins for my project.

Special thanks to Jürgen Schünemann, who always helped with purifying proteins.

I also would like to thank Thomas Burg for offering me the possibility to gain practical experience in the field of micro-fluidics in his laboratory.

Another thanks goes to many of the collaborators already mentioned in my thesis: Ixaskun Carton, Leire Diaz and Chris Tollan for SEM images, Olatz Idigoras and Andreas Berger for sputtering membranes, Birgit Bußmann and Kersten Hahn for TEM Images, Aksana Labokha for proteins, Jacob Piehler for lipids, and Fredrik Andersson for His-tag Capturing Sensors.

The work would have been less pleasant and more difficult without the support of my fellow group members: a special thanks to my current and former colleagues at the CIC biomaGUNE (Spain) and the Department of Cellular Logistics (MPI, Göttingen).

Cornelia Paz and the GGNB office have been a great help at coordinating the administrative tasks related to this project.

This thesis would not have been possible without the financial support from the GGNB and the CIC biomaGUNE.

Meinen Eltern möchte ich für ihre uneingeschränkte Unterstützung, die sie mir all die Jahre entgegen gebracht haben, herzlich danken. Ohne dies wäre diese Arbeit sicherlich nicht möglich gewesen.